2019

Efficient modeling of latent thermal energy storage systems for optimal design and operational research

Chunjian Pan
Lehigh University, chp313@lehigh.edu

Efficient modeling of latent thermal energy storage systems for optimal design and operational research

by

Chunjian Pan

Presented to the Graduate and Research Committee
of Lehigh University
in Candidacy for the Degree of
Doctor of Philosophy

in

Mechanical Engineering

Lehigh University

January, 2019

DISSERTATION SIGNATURE SHEET

Approved and recommended for acceptance as a dissertation in partial fulfillment of the requirements for the degree of Doctor of Philosophy.

Student Name: Chunjian Pan

Dissertation Title: Efficient modeling of latent thermal energy storage systems for optimal design and operational research

_____
Date

_____
Dr. Natasha Vermaak, Dissertation Advisor

_____
Accepted Date

Committee Members:

_____
Dr. Natasha Vermaak, Committee Chairman

_____
Dr. Carlos E. Romero, Committee Member

_____
Dr. Sudhakar Neti, Committee Member

_____
Dr. Mayuresh V. Kothare, Committee Member

Acknowledgements

Firstly, I would like to thank my advisor, Prof. Natasha Vermaak, for her patient and professional guidance during my doctoral work. Her mentoring my research and my technical writing greatly improved my academic skill.

My greatest thanks go to Dr. Carlos E. Romero, Director of the Energy Research Center, for the support during my entire PhD. He is the nicest professor to work with, more like being a friend. I gained a great deal of research knowledge from him.

Many thanks to Dr. Sudhakar Neti for providing his expertise and guidance on the PCM project and on my research work. I also thank Dr. Mayuresh V. Kothare for being my committee member and for giving me valuable suggestions to improve my research work.

Greats thanks to Prof. Edward K. Levy, who believed in me and accepted me to the Energy Research Center of Lehigh University.

I deeply thank Dr. Carlos Rubio Maya, who enabled valuable collaboration opportunities and I acknowledge the Mexican National Council of Science and Technology for funding support. In addition I acknowledge the Advanced Research Projects Agency-Energy of US Department of Energy for funding the PCM project.

I would like to thank Mrs. Colleen Munion, who maintains a good working environment at the ERC. Thanks also go to all my lab mates and visiting scholars from China; because of you, I had a wonderful time and experience at the ERC. Special thanks to Dr. Xingchao Wang, Dr. Zhongliang Qiao and Dr. Shaojun Ren for your companionship and friendship. It was a great pleasure to get to know many friends at Lehigh.

Lastly, I am grateful for my parents for bringing me into this world, for raising me and seeing that I grow into a responsible man in society.

Table of Contents

List of Tables

List of Figures

Abstract

As a booming economy drives the need for more electricity, demands on freshwater for thermoelectric power generation also grow. Facing limited freshwater resources, alternative dry cooling technologies such as air cooled condensers (ACCs) that reduce water consumption are becoming more prevalent. However, the performance of ACCs dramatically decreases at ambient temperatures. This project proposes a novel application of a Phase Change Material (PCM) based cooling system for supplementary cooling of ACCs. One of the engineering challenges that prevents the commercial application of latent thermal energy storage (LTES) systems is the lack of computationally efficient methods to model the transient nonlinear behavior of the system. In this dissertation, efficient modeling approaches for LTES systems are proposed at different scales for optimal design and operational research.

Chapter 1 Introduction

As a booming economy drives the need for more electricity, demands on freshwater for thermoelectric power generation also grow. However, freshwater is already limited in many locations and is becoming scarcer for a growing global population. This constraint will affect future electricity generation. Thus, alternative dry-cooling technologies, i.e., air-cooled-condensers (ACC's) that reduce water consumption are needed. In particular, this dissertation focuses on systems with ACCs that employ a power generation loop of the kind illustrated in Figure 1.1. However, the performance of ACCs is very sensitive to wind conditions and ambient temperatures [1]. ACCs become less effective when the ambient temperature is higher (See Figure 1.2). Consequently, the existing ACCs may fail to condense all the steam.

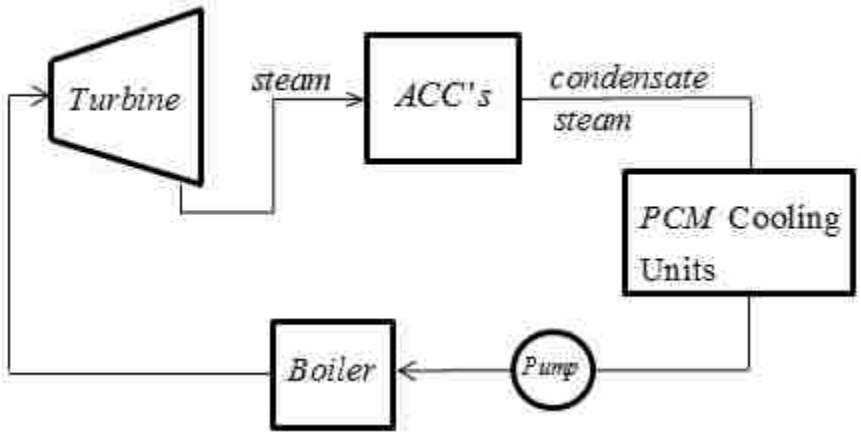

Figure 1.1 Schematic incorporation of the PCM based supplementary cooling system in a power generation loop [1]

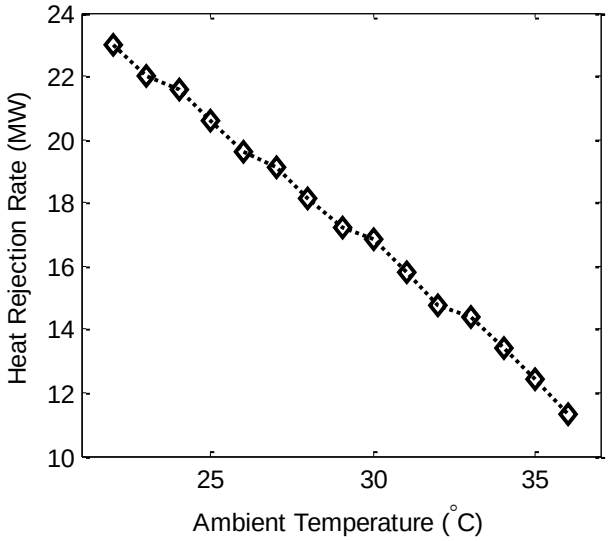

Figure 1.2 ACC heat rejection under fluctuations of ambient temperatures [2]

To address these challenges facing ACCs, a novel cooling concept that incorporates the use of phase change materials (PCMs) is proposed. The goal is to provide supplemental cooling when the ACC performance is limited. ACC performance is most affected during hot summer daytimes. During the night, temperatures can be more than 10 ℃ lower than daytime temperatures, especially in relatively dry regions. Thus the idea is to turn the night-time lower temperature into cooling energy that can be used for cooling during the daytime. The proposed approach is to use a PCM reservoir to store the cooling resource (via freezing) during the night-time and to provide cooling energy (via melting) during the daytime. Figure 1.1 shows a schematic incorporating the proposed PCM based supplemental cooling system in the power generation loop. A conceptual sketch of the PCM Cooling Units in Figure 1.1 is shown in Figure 1.3. The PCM candidate used for investigations in this dissertation is $CaCl_2 \cdot 6H_2O$, which has a melting temperature that is relevant for the application of interest and also has a low cost. In addition $CaCl_2 \cdot 6H_2O$ is nonflammable and nontoxic.

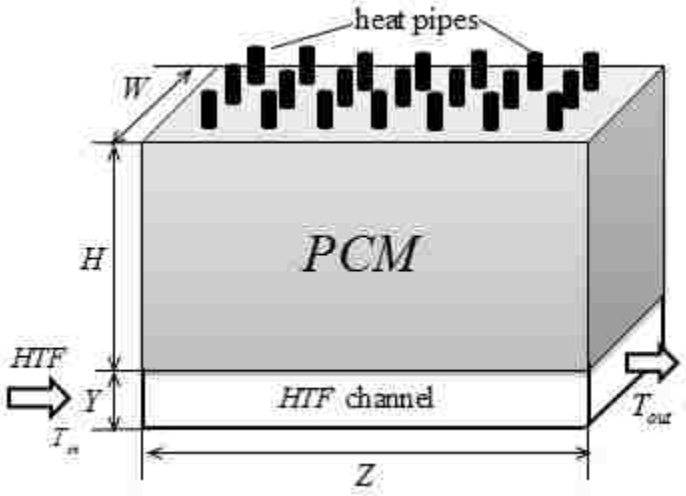

Figure 1.3 Conceptual sketch of the LTES cooling system [3]

1.1 **Design challenges of a LTES system and main aims of the dissertation**

Sensible thermal energy storage relies on temperature gradients that can be difficult to achieve. Even if large temperature gradients can be obtained; large temperature variation can also be an obstacle during usage. Latent thermal energy storage (LTES) systems based on PCMs have two obvious advantages over sensible thermal energy storage. One is higher energy density, resulting in smaller equipment size and less investment cost. The other is that PCM-based LTES systems release or absorb heat isothermally, resulting in efficient temperature management. Despite these advantages, only a few commercial applications employ LTES due to several engineering challenges. One major problem is the lack of computationally efficient models to resolve the transient and nonlinear freezing behavior of a PCM-based LTES system. The low conductivity of PCMs is another engineering challenge preventing the commercial application of LTES systems. To address the low conductivity of PCMs, typically finned

heat pipes are embedded in the PCM to increase the heat transfer performance and guarantee that all of the PCM can be solidified within the typical 10-hour window during the night-time. However, the finned heat pipes also present optimal design challenges of their own due to their increased cost, more complex geometries, and associated computational costs (See Figure 1.4).

As a result, while the optimal design of finned PCM-based heat pipe structures is necessary to lower system cost, currently the available computational approaches for design and optimization are severely limited and mostly involve the solution of transient nonlinear systems of partial differential equations. In many cases, parametric optimizations have been reported based on computational fluid dynamics (CFD) simulations [4-8]. In these cases, multiple simulations need to be carried out for variations of the design parameters of interest. This is computationally expensive and can only guarantee near-optimal solutions. Similarly, at the full-scale system-level, CFD models are the usual, computationally expensive, design tool [9]. However, a large scale system simulated in this way is often not useful for operational research (for example, to determine dynamic flow rate control). Thermal network models were reported in [10, 11] for full scale system simulation. These models require solving large coupled systems of governing equations. As a result, the computational efficiency of these models is not sufficient for operational research purposes.

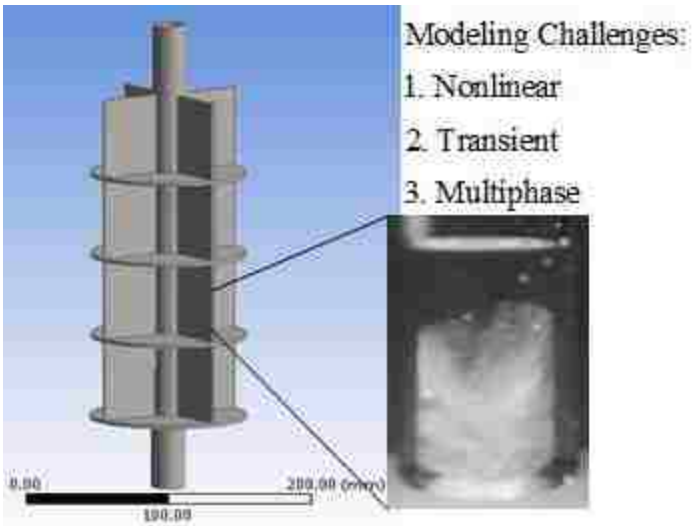

Figure 1.4 Finned heat pipe structure and modelling challenges. On the left is a plot of the finned heat pipe. On the right is an image of a piece of solid PCM under melting conditions

This dissertation is focused on developing efficient modeling methods for (i) the structural optimization of a PCM tank, and (ii) the full (large) scale model of a LTES system for operational research. The main content of the dissertation can be divided into two parts that ultimately aim to provide a reliable full-scale PCM-LTES system level model and design tool for field applications. The first part, which includes Chapter 2 - 4, is on the optimal sizing design of a finned heat pipe unit in a representative LTES system. The second part, Chapters 5-6, builds on and incorporates Chapters 2-4, in order to perform system-level modeling for operational research. Operational research includes the topics of (a) selecting parallel or in-series arrangements of the LTES units and (b) optimal heat transfer fluid (HTF) mass flow rate control. Chapter 7 is a supplementary study related to Chapter 6. In Chapter 7, an experimentally validated analytical model of the melting behavior of a PCM is presented as an alternative module that can be incorporated in the full scale system-level model of Chapter 6. The structure of the

dissertation is summarized in Figure 1.5 and the contribution of each chapter is highlighted below:

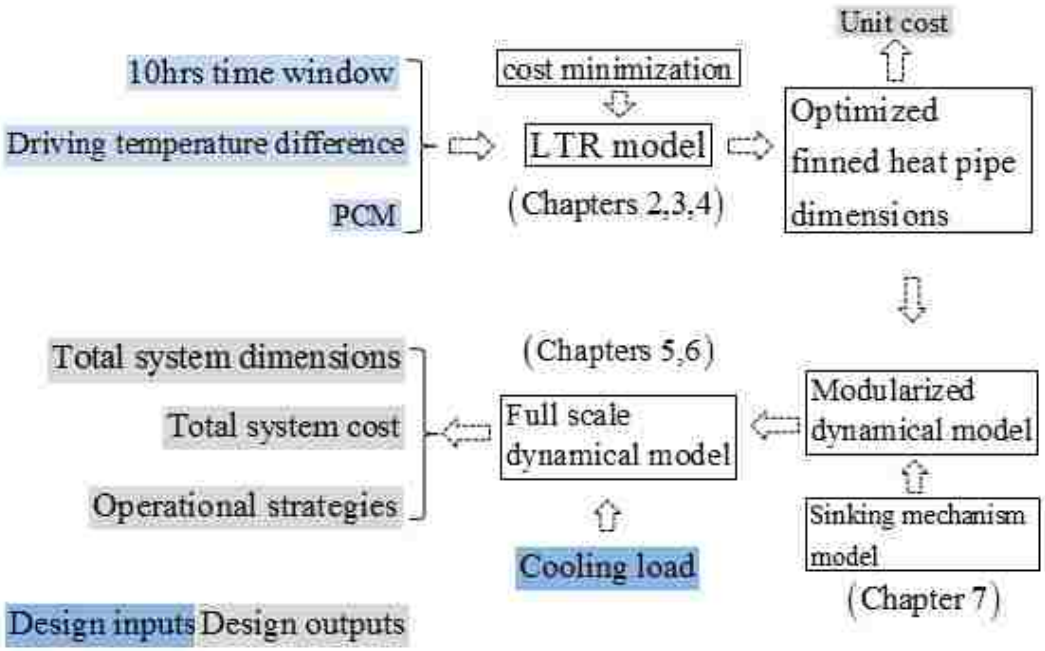

Figure 1.5 Structure of the dissertation

- Chapter 2 proposes an efficient modeling method for PCM solidification enhanced with multidimensional fins in rectangular coordinates.
- Chapter 3 extends the methods in Chapter 2 to cylindrical coordinates and a benchmark optimization example is provided to illustrate the computational advantages the proposed model.
- Chapter 4 further extends the modeling approach developed in Chapters 1-2 to 3-D cylindrical coordinates. The modified model is applied to the optimal design of a finned heat pipe unit for a representative LTES system.
- Chapter 5 develops an explicit 1-D analytic solution for the problem of annular PCM solidification, which captures the transient nonlinear behavior.

- Chapter 6 applies the modeling method developed in Chapter 5 to build a numerical model for the tank structure (See Figure 1.2).
- Chapter 7 introduces an experimentally validated analytical model to capture the sinking behavior of PCM during melting in a tube geometry. This chapter serves as preliminary work identifying directions to increase the fidelity of the modeling approach in Chapter 6 (which is based on an assumption of conduction-dominated heat transfer in the finned heat pipe module).

Verification for Chapters 2-7 is performed via comparison with computational fluid dynamics (CFD) simulations, energy balance checks, and experimental results where available.

References

[1] Pan C., Vermaak N., Romero C., Neti S., et al. Cost estimation and sensitivity analysis of a latent thermal energy storage system for supplementary cooling of air cooled condensers. Applied Energy, 2018, (224): 52-68.

[2] http://nuicone.org/site/common/proceedings/Mechamical/oral/ME-15.pdf

[3] Pan C., Vermaak N., Romero C. Neti S., et al. Efficient optimization of a longitudinal finned heat pipe structure for a latent thermal energy storage system, *Energy Conversion and Management* 2017, (153): 93-105.

[4] Xie J, Yuan C. Parametric study of ice thermal storage system with thin layer ring by Taguchi method. Appl Therm Eng 2016 ; 98: 246-55.

[5] Zhao R, Gu J, Liu J. Optimization of a phase change material based internal cooling system for cylindrical Li-ion battery pack and a hybrid cooling design. Energy 2017;135:811-822.

[6] Shinde A, Arpit S, Pramod K M, et al. Heat Transfer Characterization and Optimization of Latent Heat Thermal Storage System Using Fins for Medium Temperature Solar Applications. J Sol Energy Eng 2017; 139(3): 031003.

[7] Song H, Zhang W, Li Y, et al. Exergy analysis and parameter optimization of heat pipe receiver with integrated latent heat thermal energy storage for space station in charging process. Appl Therm Eng 2017; 119: 304-11.

[8] Saffari M, de Gracia A, Fernández C, et al. Simulation-based optimization of PCM melting temperature to improve the energy performance in buildings. Appl Energy 2017; 202: 420-34.

[9] https://www.sharcnet.ca/Software/Fluent6/html/ug/node973.htm

[10] Hamidreza Shabgard, Christopher W. Robak, Theodore L. Bergman, Amir Faghri. Heat transfer and exergy analysis of cascaded latent heat storage with gravity-assisted heat pipes for concentrating solar power applications. Sol Energy 2012; 86(3):816-30.

[11] K. Nithyanandam, R. Pitchumani. Design of a latent thermal energy storage system with embedded heat pipes. Appl Energy 2014; 126: 266-80.

Chapter 2

Efficient modeling of phase change material solidification with multidimensional fins

(Pan C**.**, Hoenig S., Chen C. H., et al. Efficient modeling of phase change material solidification with multidimensional fins. *International Journal of Heat and Mass Transfer*, 2017, (115): 897-909.)

Efficient modeling of phase change material solidification with multidimensional fins

Chunjian Pan[1], Sean Hoenig [2], Chien-Hua Chen[2] , Sudhakar Neti[1]
Carlos Romero[1], Natasha Vermaak[1]
[1]Lehigh University, Bethlehem, PA 18015, USA
[2]Advanced Cooling Technologies, Inc., Lancaster, PA 17601, USA

Abstract

Phase Change Materials (PCMs) are gaining importance in energy storage applications. Many PCM are poor thermal conductors and thus can gain from the optimal use of appropriate fins. Phase change process is inherently nonlinear in behavior due to the latent heat, thus simulations are usually based on finite difference or finite element approaches, which can be computationally inefficient for optimal design of latent energy storage systems. A novel modeling approach called Layered Thermal Resistance (LTR) model is proposed for the first time in this paper for efficient PCM simulations in multi-dimensions. The LTR model can be coupled with multidimensional fins for PCM-fin structure optimal design. Compared with CFD results, the results by the LTR model are high accurate in estimating the solidification time and the highlight is it has negligible simulation cost. Moreover, accurate heat flux of a finned PCM system is also obtained. The LTR model represents the nonlinear solidification process in a finned latent energy storage structure with analytic equations, thus it has bright applications in PCM heat sink optimization with internal fins.

Key words: Latent energy storage, Efficient PCM modeling, PCM with internal fins, optimal fin design

Nomenclature

T_m	The exact PCM solidification temperature
T_w	Cooling temperature at the boundary
t_{Neu}	PCM solidification time for Neumann's solution
t_{LTR}	PCM solidification time estimated by the LTR model
t_{CFD}	PCM solidification time estimated by the CFD model
ε	Percent error
s	Distance of solidification front
Δs	Thickness of each discrete layer for a 1-D PCM bar
N	Number of discrete PCM layers
A	Cross section area of a 1-D PCM bar
ΔV	Volume of each discrete layer for a 1-D PCM bar
q	Heat flux
$R(i), R_i(i), R_{ij}(i)$	Thermal resistances for heat transfer to the PCM layer i
$t(i)$	Discrete solidification time for PCM layer i
t_s	Total solidification time
R_t	Total thermal resistance of a system
L_m	Latent energy of PCM
Cp_{pcm}	Heat capacity of PCM
k_{pcm}	Conductivity of PCM
ρ_{pcm}	Density of PCM
$\Delta v_l(i)$	Volume of each discrete layer for the 2-D and 3-D cases
T_{upper}	Upper PCM melting temperature
T_{lower}	Lower PCM melting temperature
H, H_{ref}	Specific PCM enthalpy and a referenced enthalpy value
T_{cell}	Temperature of a discrete element
ΔT	Driving temperature difference
φ	Liquid fraction of PCM

x, y, z	Locations of solidification fronts in x, y, z directions
a, b, c	Side lengths of a cuboid
$\mu, \gamma,$	Side length ratios of a rectangle or a cuboid
α	Resistance tuning factor value
δ	Thickness of fin
h	Heat transfer coefficient in the PCM side
L	Distance from the fin to the solidification front of PCM
k_{fin}	Conductivity of the fin
l	Length of a 1-D fin
η	Fin efficiency
ξ	Parameter for fin efficiency calculation
$\psi(0)$	Dimensionless superheating parameter
T_{ini}	Initial temperature of the PCM domain

1 Introduction

Abundant research has been devoted to thermal energy storage systems due to their important role in clean energy technologies and matching renewable energy to load patterns. A good example is the mismatch between supply and demand of solar energy and thermal energy storage systems can play a major role. 'Cold storage' produced at a lower costs during off peak hours of the day is a practical way to release utilities' burden to produce enough electricity during high demand hours [1-2].

Many mature and industrial applications of thermal energy storage systems use sensible energy. Phase Change Materials (PCMs) are receiving more attention due to their high-energy densities. PCM can store or release energy at near isothermal

conditions that are thermodynamically superior [3]. The thermal reliability and stability of the PCMs was reviewed by Rathod [4]. However, the low conductivity of PCM materials is a barrier for many practical applications [3], especially for large scale systems. Researchers are eager to resolve this issue by analyzing different heat transfer enhancement techniques, i.e., including high conductivity foams or metal matrices into the PCM [5], dispersing high conductivity particles in the PCM [6], or use microencapsulation of the PCM [7]. Work conducted by Lohrasbi [8-9] indicated that immersing innovative fin structures into PCM as a heat transfer enhancement technique is superior to nanoparticles dispersion. Plenty of research has been conducted to study the PCM system with fin structures since they can be simple and compact [10-12]. Sheikholeslami and Lohrasbi [13-15] studied the Nano-particle Enhanced PCM (NEPCM) and innovative fin structures in a combined way to increase the performance of the latent heat thermal energy storage system (LHTESS). Corrosion between PCM ($CaCl_2 \cdot H_2O$) and fin container was recently reported by Ren [16].

Mathematical modelling plays important role for analyzing the performance of energy storage systems with PCMs. Henry [17] reviewed major methods of mathematical modelling of solidification and melting. An elegant Neumann' solution is available for a one-dimensional semi-infinite region with simple initial and boundary conditions and constant thermal properties, as first presented by Stefan [18]. Many real world solidification problems are rarely one dimensional, and usually have complex initial and boundary conditions. Thus computational fluid dynamics (CFD) is widely employed in modeling PCMs. However, CFD is not always the efficient tool for optimal design of a LHTESS. Optimizations have been often based on parametric studies through

simulations [10]. Multiple simulations need to be carried out for variations of the design parameters of interest. More efficient modeling with high accuracy and smaller CPU time as discussed here can be immensely beneficial to the design and optimization of a LHTESS.

Though many finite difference or finite element based methodologies have been developed for modeling PCM and PCM with heat transfer enhancement techniques, very few simple and efficient modeling techniques for simulation of PCM are in vogue. Efficient modeling of PCM freezing thus has room for improvement and useful applications. An approximate analytical model is presented to model the solidification and solidification of a finned PCM in one and two dimensions [19-21]. A fast 1-D analytical model is proposed in [22] to simulate the behavior of a wallboard containing the PCM and good predication is achieved compared with CFD results. In this paper an efficient modeling approach called call Layered Thermal Resistance (LTR) model is proposed for the first time to model the solidification process that is applicable for 2-D and 3-D geometries with fins. The highlight of the method is its ease with which it can include extended fins. That enables the method to be efficient and useful in optimization and design of a LHTESS with fins. The model is conduction based, so it is suitable for the energy discharging process, as many studies have demonstrated that during solidification natural convection exits only in the very beginning and soon conduction dominates the whole process [23]. For many processes involving energy charging and discharging, the freezing is often the resistance dominated process, thus posing a harder design goal to achieve, i.e., solidify the PCM within required time period. So an efficient

coupled PCM-fin modeling method has useful applications for optimal design during the freezing process when fins are to be used.

The content of this paper is organized as follows. In section 2, the efficient PCM modeling approach called Layered Solidification Front model shorthand noted as LTR model is described in 1-D, 2-D and 3-D and its performance is compared with CFD results. In section 3, the construction of LTR models coupled with fins is given in 2-D and 3-D and their performance were tested against the CFD results. Section 4 summaries the efficient PCM modeling technique and suggests further study to develop and improve the method.

2. Layered Thermal Resistance model for PCM solidification

This section introduces the construction of the Layered Thermal Resistance (LTR) models for PCM solidification in multiple dimensions including 1-D, 2-D and 3-D.

2.1 1-D Layered Solidification Front Model for fast PCM modeling

In this section the novel approach for efficient PCM solidification modeling in 1-D is developed and its results were compared to the Neumann's solution. The idea for the proposed LTR model is assuming that the liquid PCM is solidified layer by layer and the final solidification time is estimated by adding together the solidification times of all the discrete layers.

A 1-D semi-infinite PCM bar is shown in Figure 2.1. Assuming its exact solidification temperature is T_m, cooled by constant Temperature T_w at one end and has zero flux for the remaining sides. The initial temperature of the bar everywhere is assumed to be T_m. It should be noted that when the initial temperature equals to the solidification temperature, there is no heat loss at the solidification interface for a semi-infinite bar, so the solidified distance given by the Neumann's solution is equivalent to a fixed bar. Thus given certain solidification time t_{Neu}, the solidification front s can be estimated by Neumann's solution [17]. Then the LTR model is applied to the solidification front s to estimate its solidification time t_{LTR}. The performance of the LTR model is evaluated by comparing the estimated solidification time to that was assigned to the Neumann's solution. Estimation accuracy in terms of percent error is defined as:

$$\varepsilon = \frac{(t_{LTR} - t_{Neu})}{t_{Neu}} \times 100\%. \tag{2.1}$$

To implement the LTR model, the solidification front s is equally divided into $N-1$ pieces, called layered solidification fronts. The volume for each piece is ΔV. The distance between the solidification front and cooling surface determines the thermal resistance to pass energy into the current layer, thus prescribing the magnitude of heat flux going into the layer. The solidification time for each of the discrete layer is then determined through dividing the total energy in the discrete layer by its current heat flux. The final solidification time is estimated by adding those solidification times of all the discrete layers. Eqns. (2.2-2.7) shows this process in 1-D. The heat flux (2.5) is also obtained for the entire solidification process.

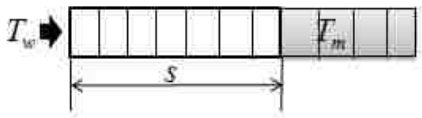

Figure 2.1 1-D PCM bar

$$\Delta s = \frac{s}{N-1}, \quad (2.2) \qquad \Delta V = \Delta s A \quad (2.3)$$

$$R(i) = \frac{i\Delta s}{Ak_{pcm}} \quad (2.4) \qquad q(i) = \frac{T_m - T_w}{R(i)} \quad (2.5)$$

$$t(i) = \frac{\Delta V \rho_{pcm}[L_m + 0.5 Cp_{pcm}(T_w - T_m)]}{q(i)} \quad (2.6) \qquad t_s = \sum_{i=1}^{N-1} t(i). \quad (2.7)$$

Given certain PCM properties which are used throughout this paper (see Table 2.1), different solidification times t_{Neu} and driving temperature difference $dT = T_m - T_w = 10℃$, the Neumann's solution [17] gives the distances of the solidification fronts. The LTR model was used to estimate the solidification time to reach those fronts. Table 2.2 shows that the LTR model has high accuracy. However, there is some constant overestimated error based on the LTR model. This means there is some small default error within the model itself. The most possible source for this constant deviation is that the average temperature difference $0.5(T_m - T_w)$ is used to account for the sensible energy in Eqn. (2.6) for each of the discretized layer, and it may overestimate the sensible energy compared with Neumann's solution. Grids sensitivity analysis is given in Table 2. 3. $t_{Neu} = 10hrs$ is the target solidification time to be achieved by the LTR model. Table 2.3 shows that more discrete layers will increase the accuracy of the LTR model, while insufficient number of layers will lead to large deviations.

Table 2.1 Thermal properties of certain PCM used in this paper

Density	Conductivity	Heat Capacity	Latent Heat
1600 kg/m^3	0.5 W/(mK)	2000 J/(kgK)	120kJ/kg

Table 2.2 Performance of the LTR model

Given solidification time t_{Neu} (hrs)	1	3	5	7	10
Solidification front distances by Neumann's solution (cm)	1.33	2.31	2.98	3.53	4.22
t_{LTR} (hrs)	1.0285	3.085	5.142	7.199	10.285
ε	2.85%	2.85%	2.85%	2.85%	2.85%

Table 2.3 Effect of number of discrete layers on the accuracy of the LTR model

Number of layers	9999	999	99	49	29	9	2
t_{LTR}	10.275	10.285	10.378	10.484	10.629	11.416	15.411
ε	2.75%	2.85%	3.78%	4.84%	6.29%	14.16%	54.12%

2.2 LTR Model for 2-D

This section introduces the LTR model to 2-D PCM solidification modeling with constant cooling temperature at boundaries. Extra tuning parameter has to be introduced to successfully apply the LTR model in 2-D. Figure 2.2 shows the layered solidification fronts in a rectangle. It is cooled on the two sides with constant temperature, and has zero heat flux at the other two sides. The modeling approach is shown in Eqns. (2.8-2.13), where a is the thickness of the domain out of the paper. Variables x and y denote the locations of the freezing front. Two heat paths with the two thermal resistances R_1 and R_2 are regarded to transfer heat to the freezing front. And average temperature difference $0.5(T_m - T_w)$ is used to account for the sensible energy.

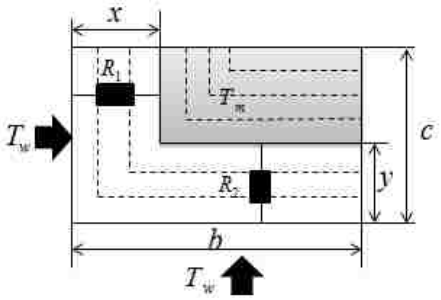

Figure 2.2 Layered moving fronts for a rectangular PCM

$$R_1(i) = \frac{x(i)}{a(c-y(i))k_{pcm}} \quad (2.8) \qquad R_2(i) = \frac{y(i)}{a(b-x(i))k_{pcm}} \quad (2.9)$$

$$R_t(i) = \frac{R_1(i)R_2(i)}{R_1(i)+R_2(i)} \quad (2.10) \qquad \mathrm{q}(i) = \frac{T_w-T_m}{R_t(i)} \quad (2.11)$$

$$\mathrm{t}(i) = \frac{\Delta V_l(i)\rho_{pcm}[L_m+0.5Cp_{pcm}(T_w-T_m)]}{q(i)} \quad (2.12) \qquad t_s = \sum_{i=1}^{N-1} t(i). \quad (2.13)$$

Computational Fluid Dynamics (CFD) simulation results are used to verify the LTR model. The Solidification & Melting Model [24] which is based on the enthalpy-porosity method [25] is implemented in Fluent (commercial CFD software) to obtain the numerical solutions. For the enthalpy-porosity method, three regions, solid, liquid, and mushy zones, are defined in the computational domain. Given a PCM's melting range (T_{lower}, T_{upper}) and a cell temperature T_{cell}, a liquid fraction ranging from 0 to 1 is defined by eqn. (2-14) and is used to identify the three regions.

$$\varphi = \begin{cases} 1, & T_{cell} > T_{upper} \\ \frac{T_{cell}-T_{lower}}{T_{upper}-T_{lower}}, & T_{lower} \le T_{cell} \le T_{upper} \\ 0, & T_{cell} > T_{upper} \end{cases} \quad (2\text{-}14)$$

As the solidification process is conduction dominated [18], the continuity and momentum equations were turned off in the Fluent setup. Thus energy balance is the main governing equation:

$$\frac{\partial}{\partial t}(\rho_{pcm}H) = \nabla \cdot (k_{pcm}\nabla T) \quad (2\text{-}15)$$

where specific enthalpy H is formulated according to enthalpy method [25],

$$H = H_{ref} + \int_{T_{ref}}^{T} Cp_{pcm}dT + \varphi L_{pcm}. \quad (2\text{-}16)$$

Validation of the solidification phenomenon by the enthalpy method [25] against the experimental data is available in Ismail's work [26]. Figure 2.3 directly cited from [26]

shows good comparison of solidification fronts between the numerical and experimental results. The $\psi(0)$ in the figure is a dimensionless superheating parameter defined as $\psi(0) = (T_{ini} - T_m)/(T_{ini} - T_w)$ to represent the system with different initial temperature, where T_{ini} is the initial temperature of the system. It should be noted that The exact solidification temperature to the used in the LTR model is defined as $T_m = \frac{1}{2}(T_{lower} + T_{upper})$.

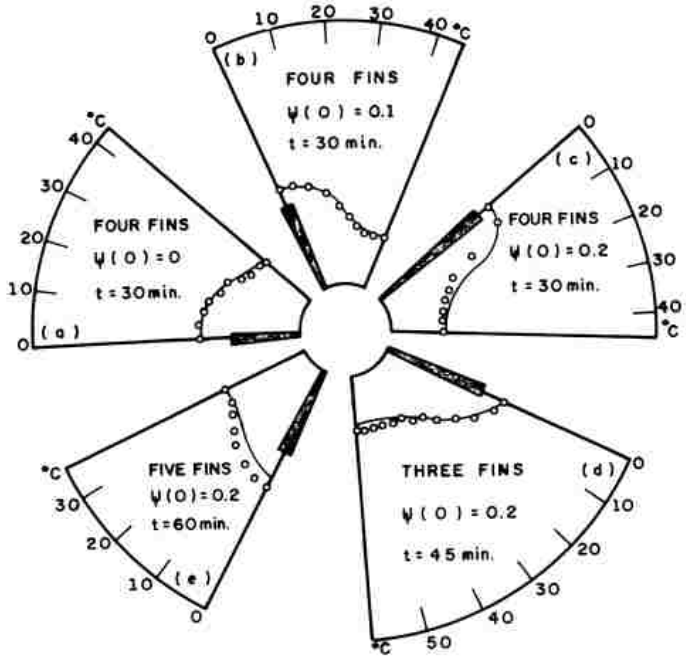

Figure 2.3 Comparison of numerical and experimental solidification fronts [26]

For the simulations in this study, the total number of elements is 10,000-40,000 and the time step is 3-6 s depending on the size of the geometry. Sensitivity studies were performed to confirm mesh and time-step independence of the results presented. The energy equation was discretized using the Second Order Upwind scheme. A pressure based solver with double-precision was chosen. The convergence was checked at every 2 time steps with the scaled absolute residual of 10^{-9} was used for the energy equation.

Table 2.4 Rectangle shape with different length ratios

c (cm)	0.1	0.3	0.5	1.0	2.0	3.0	4.0
b (cm)	4.0	4.0	4.0	4.0	4.0	4.0	4.0
Ratio c/b	0.025	0.075	0.125	0.25	0.5	0.75	1.

Table 2.4 shows the rectangular PCM domain with different aspect ratios to be used to test the LTR model. The ratios here range from 0.025 to 1. It should be noted that an aspect ratio 0.025 can also represent the ratio 40. The CFD results were treated as trusted reference to validate the LTR model. From left plot in Figure 2.4, it can be seen that the LTR model overestimates the solidification time for the 10 cases by around 50% to 60% compared with the CFD results. This means adjustment can be made to improve the accuracy of the LTR model. The right plot in Figure 2.4 shows a nice curve can be fitted between the solidification time ratios t_{CFD}/t_{LTR} of the two models and the aspect ratios c/b of a rectangle. The solidification time ratio of the two models actually indicates how much thermal resistance was overestimated by the LTR model. From this perspective, the ratio can be treated as a tuning parameter to adjust the total resistance in the LTR model. The LTR model modified with a tuning factor is then called the tuned LTR model in the following context.

A regression model was built by custom support vector regression (SVR) which is also available as MATLAB toolbox [27] to predict the resistance tuning factor for the LTR model. Other curve fitting techniques can also be employed such as simple linear fitting or spline interpolation [28]. Generally, SVR has more generalization ability with a small training sample [29] which means higher predication accuracy than other methods. In Eqns. (2.17-2.19), the aspect ratio μ is the independent variable for the SVR model f_1 while α is the output resistance tuning parameter (solidification time ratio of the LTR and

CFD models t_{LTR}/t_{CFD}), which is used to adjust the total resistance of the LTR model. The 7 cases' data is used to train and build the SVR model $\alpha = f_1(\mu)$. Figure 2.5 shows the regression curve. It is the reconstruction curve of the solidification time ratio versus aspect ratio of a rectangle. What needed to be emphasized is that the aspect ratio is covered from 0.025 to 1, which can also represent a ratio range from 1 to 40, so this aspect ratio range includes a large number of rectangular shapes. When estimating the solidification time of a new rectangle PCM, its aspect ratio should fall within this range.

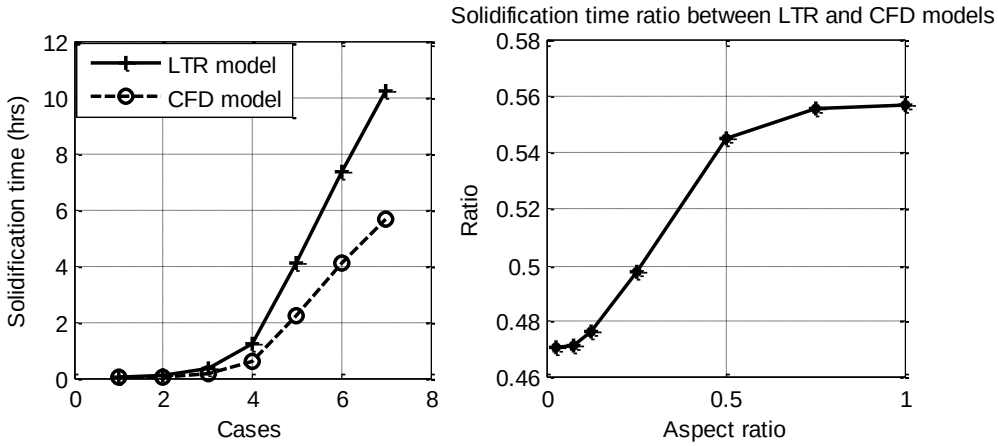

Figure 2.4 Solidification time estimated by LTR and CFD models

$$\alpha = f_1(\mu)\,, \quad (2.17) \qquad \mu = \frac{c}{b}\,, \quad (2.18) \qquad R_t(i) = \alpha \frac{R_1(i)R_2(i)}{R_1(i)+R_2(i)} \quad (2.19)$$

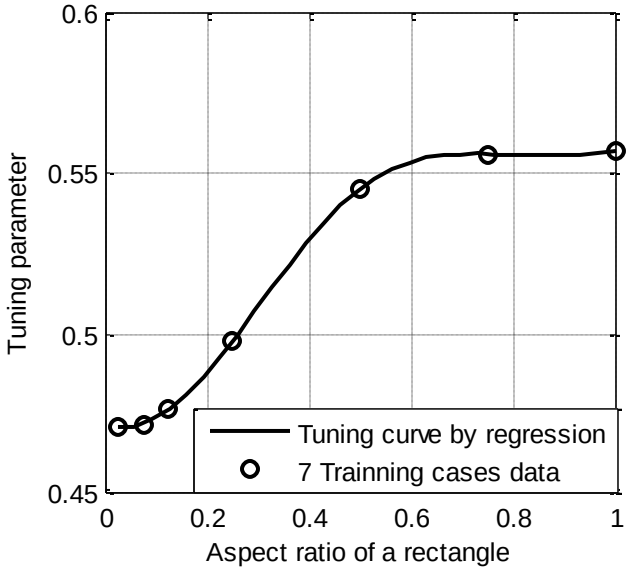

Figure 2.5 Regression curve of the tuning parameter for the tuned LTR model

For the 7 cases simulated by the CFD method in Fluent, a solidification temperature range $T_{upper} - T_{lower} = 2℃$ is set, the initial temperature is T_{upper} everywhere, $T_{upper} - T_w = 10℃$ and the conductivity of the PCM is $k_{pcm} = 0.5\, W/mK$. In the LTR model the driving temperature difference $\Delta T = T_m - T_w = 9℃$, as it is assumed that the exact freezing temperature is the mean temperature of the solidification temperature range. For the tuned LTR model to be more flexible in use, it is desired that the resistance tuning curve is independent of boundary conditions and material properties. Ideally, $\partial f_1/\partial \Delta T = 0$ and $\partial f_1/\partial k_{pcm} = 0$. Or at least the effect from those parameters on the accuracy of the tuned LTR model is negligibly small. Nine new cases shown in Table 2.5 are considered to test the accuracy of the tuned LTR model. The first 3 cases have different side lengths while keeping same driving temperature and PCM conductivity as the cases for building the resistance tuning curve. Cases 4 -5 have different driving temperatures. Cases 6 and 7 have different PCM conductivities. Case 8 has both different driving temperature difference and PCM conductivity as the training

cases. Case 9 has a much larger driving temperature difference than other cases. Additionally cases 4 to 9 both have different aspect ratios than the 7 training cases. The CFD results are treated as the trustful reference to judge the tuned LTR model. Estimation error is defined as:

$$\varepsilon = \frac{(t_{LTR} - t_{CFD})}{t_{CFD}} \times 100\%. \quad (2.20)$$

The performance of the tuned LTR model is shown in Figure 2.6. The accuracy is within 10% error as compared to the CFD results. It can be concluded that the resistance tuning curve is almost only depended on the aspect ratio of a rectangle. Once the tuned LTR model is developed, it can be applied to new temperature boundaries, different species of PCM and for various rectangles as long as their aspect ratios falling in the range of the tuning curve.

Grids independent study was performed and it was found that 30 and 150 discrete layers almost give same solidification time. Generally, the final solidification time estimated by the tuned LTR model is quite robust to the number of the discrete layers. 150 discrete layers are assigned to all the 7 training cases and the 9 predicting cases. It should also be pointed out that the solidification time for a certain case in CFD is determined when the solid fraction of PCM reaches 99.9%. Due to low PCM conductivity, there is a "tailing effect", referring to the situation when almost 70% of the PCM can be solidified within half of the total solidification time, and at the final stage, a small amount of PCM takes a relatively long time to solidify. The solidification time chosen at 99.9% liquid fraction could be 5% more than that chosen at 99.1%. If a new solidification time is chosen based on different solidified percentage fraction, the

resistance tuning curve needs to be rebuilt accordingly. And high prediction accuracy is still guaranteed. The CPU time involved with the use of the tuned LTR model is trivial compared to a full CFD prediction and therein lies the benefit for optimal design procedures.

Table 2. 5 New testing Cases

Cases	#1	#2	#3	#4	#5	#6	#7	#8	#9
ΔT ℃	10	10	10	20	7	10	10	20	50
k_{pcm} W/(mK)	0.5	0.5	0.5	0.5	0.5	1	0.3	2.0	0.5
c cm	1	3	5	3	1	3	1	5	6
b cm	5	5	5	5	5	5	5	6	6

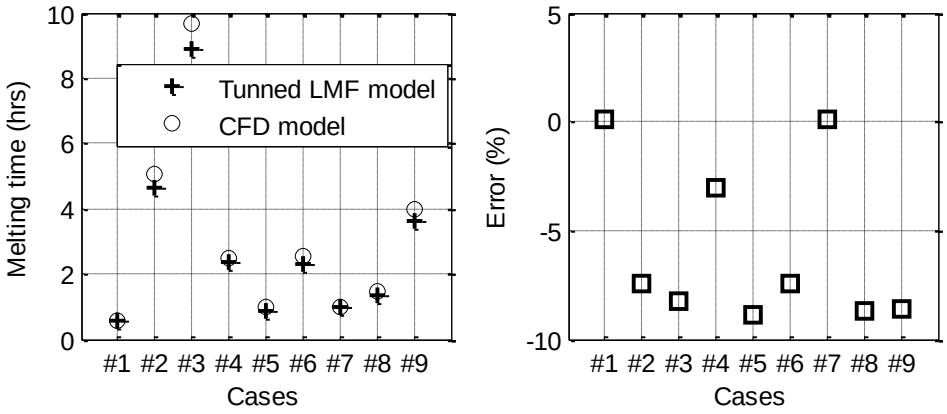

Figure 2.6 Predictions of 9 2-D cases using the tuned LTR model

2.3 LTR model for 3-D

The methods and procedures described thus far for the tuned LTR model can be generalized to 3-D. Figure 2.7 shows a cuboid PCM domain cooled at three surfaces with constant Temperature. a, b, c are the three side lengths and x, y, z are the locations of current solidification fronts along the Cartesian coordinates. The cuboid geometry can be defined by two geometric aspect ratios $\mu = a/b$ and $\gamma = c/b$. Consequently, the

resistance tuning parameter will be defined by a surface $\alpha = f_2(\mu, \gamma)$. To construct this tuning surface in the present example, 4 aspect ratios (0.1, 0.4, 0.7, 1) were assigned to μ, γ. Together there are 16 discrete samples, but due to symmetry, the distinct samples are 10. Table 2.6 shows specific points that cover the lengths ratios from 0.1 to 1. The Solidification & Melting model [24] In Fluent was used to obtain the numerical results. In the CFD model a solidification temperature range $T_{upper} - T_{lower} = 1℃$ was set, the initial temperature was T_{upper} everywhere and $T_{upper} - T_w = 10℃$. Eqns.(2.21-2.24) show the thermal resistances calculation procedures of the 3-D tuned LTR model, the heat flux and solidification calculations are same as the Eqns. (2.11-2.13) in Section 2.2. Figure 2.8 shows the solidification time surfaces of the 16 pointes estimated by CFD model and the LTR model without a resistance tuning factor. There is obvious deviation in amplitude but the shape of the surfaces by the two models shares similarity. This suggests that a resistance tuning surface can be constructed based on the solidification time ratios of the two models. A custom support vector regression was applied to build the resistance tuning surface. The two aspect ratios that cover the range (0.1, 1) are the input variables and the solidification time ratio t_{CFD}/t_{LTR} between the LTR model without tuning and CFD mode is the output of the SVR model f_2. As there are 16 discrete points, the data set is much sparse compared with having 10 data points in the one dimensional case. The regression parameter should indeed be optimized for the smallest possible overall predication error [29].

Figure 2.9 shows the tuning surface by the custom SVR model. Table 2.7 lists the 7 testing cases. Results presented in Figure 10 shows excellent prediction performance for the tuned LTR model in 3-D. The prediction error is within 4% percentage, which is

better than the 2-D case. A possible reason is a smaller solidification temperature range is used for the CFD cases. Analysis of around 150 layered solidification fronts were included in the cases considered. It also demonstrates that the resistance tuning surface and predictions are independent of boundary temperature and the PCM properties. So this tuning surface is applicable to new cuboid shapes and other PCMs.

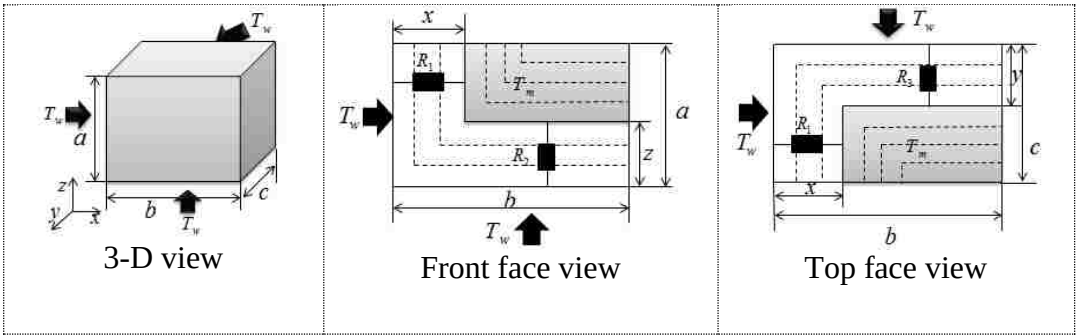

Figure 2.7 3-D cubic PCM cooling from 3 faces with constant Temperature

$$R_1 = \frac{x}{(a-z)(c-y)k_{pcm}} \quad (2.21) \qquad R_2 = \frac{z}{(a-z)(b-x)k_{pcm}} \quad (2.22)$$

$$R_2 = \frac{z}{(a-z)(b-x)k_{pcm}} \quad (2.23) \qquad R_t = \alpha \frac{R_1 R_2 R_3}{R_1+R_2+R_3} \quad (2.24)$$

Table 2.6 Cuboids with different side lengths ratios

a (cm)	5	5	5	5	5	5	5	5	5
b (cm)	0.5	2	3.5	5	2	3.5	5	3.5	5
c (cm)	0.5	2	3.5	5	0.5	0.5	0.5	2	3.5
b/a	0.1	0.4	0.7	1.0	0.4	0.7	1.0	0.7	1.0
c/a	0.1	0.4	0.7	1.0	0.1	0.1	0.1	0.4	0.7

Table 2.7 New cases for the tuned LTR model testing

Dimensions(cm)	(2,2,2)	(8,8,8)	(3,2,1)	(7,4,2)	(2,1,1)	(7,7,3)	(9,8,7)
ΔT ℃	10	10	7	20	10	20	15
k_{pcm} W/(mK)	0.5	0.5	0.5	0.5	0.3	1	3

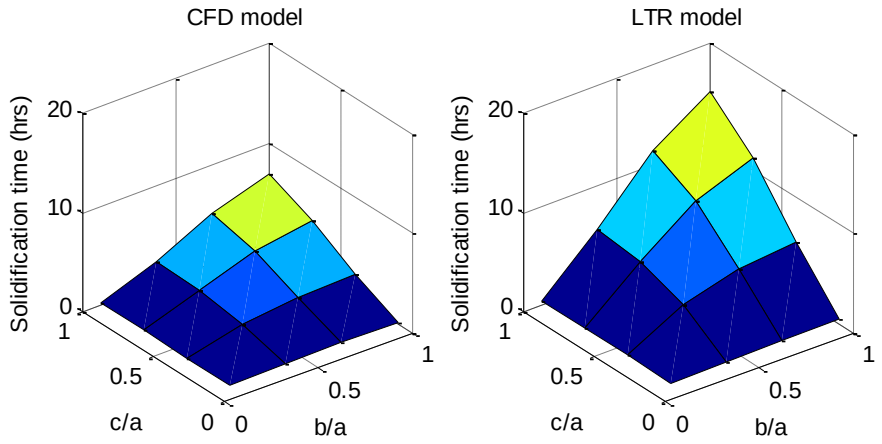

Figure 2.8 Solidification times estimation by CFD and LTR models without tuning

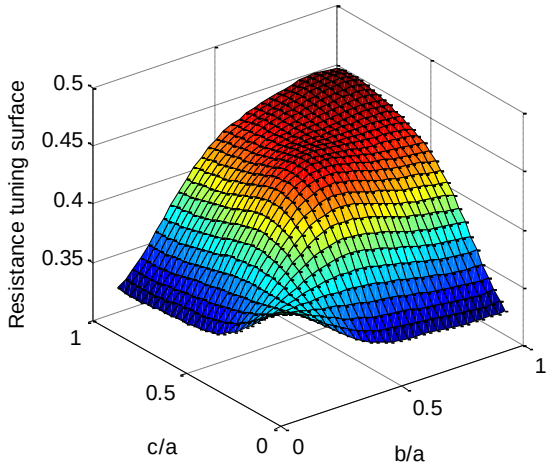

Figure 2.9 Resistance tuning surface by support vector regression

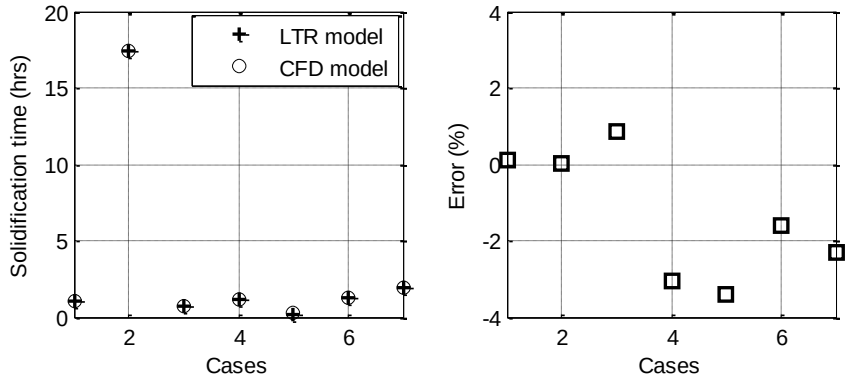

Figure 2.10 Predictions of the 7 new cases by the tuned LTR model

3 Coupled PCM with fins by Layered thermal resistance model

Many PCM's used for thermal energy storage are very poor thermal conductors thus posing impediments to energy transfer particularly during the energy retrieval (solidification) process. Fins, embedded graphite and other methods were used overcome this obstacle. Application of the tuned LTR model to a PCM domain containing fins would thus be a natural extension of the method. The discharging process is more difficult to complete as it is conduction controlled [23], while the melting process can be much easier to complete due to the solid sinking phenomenon induced by density differences between the solid and liquid PCM phases [30]. Thus an efficient coupled fin-PCM model based on conduction can prove to be critical and beneficial to the optimal design of an energy storage system with PCM. In this section the tuned LTR model is applied for modeling PCM systems that include plate fins. Note that in the following sections, the finned LTR model means the tuned LTR model that is coupled with fins.

3.1 Coupled PCM Fin modeling in 2-D

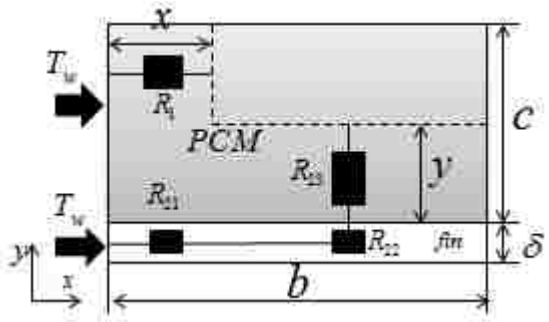

Figure 2.11 2-D coupled PCM fin sketch

A rectangular PCM domain with a plate fin on one side as shown in Figure 2.11 was studied. The PCM and the fin are cooled at the same end (the edge along the y-axis) with same constant temperature and the other boundaries have zero heat flux. There are two heat paths for energy transfer to the PCM. One path is through PCM with its thermal

resistance R_1 and the other one is through the fin, passing through multiple thermal resistances R_{21}, R_{22}, R_{23}. R_1 is the same as Eqns. (2.8) in Section 2.2 and R_{23} is a new name to be used in current description but it has the same definition as Eqn.(2.9) in Section 2.2. R_{21} and R_{22} are defined as:

$$R_{21} = \frac{x}{a\delta k_{fin}}, \qquad (3.1) \qquad R_{22} = \frac{\delta}{2a(b-x)k_{fin}}, \qquad (3.2)$$

where a is the thickness of the rectangular PCM domain and fin in z direction and x is the distance of the solidification front in x direction. R_{21} is the resistance in the fin from the cooling source to the solidification front in x-axis direction. The resistance in the fin for passing the heat from fin to the PCM is R_{22}. This resistance is rather small compared to the others and thus can be neglected. Besides the fin resistances to be incorporated into the tuned LTR model, fin efficiency is also a key factor that must be considered. The fin efficiency (3.3) was derived by solving the energy balance equation of the fin (presented in Appendix). Thus the thermal resistance passing through the fin needs to be increased by $1/\eta$. Eqn. (3.5) is the total resistance for the finned LTR model shown in Figure 10. The heat flux and solidification time calculations are the same as Eqns. (2.11-2.13) listed in Section 2.2.

$$\eta = \frac{T(x)-T_m}{T_w-T_m} = cosh(\xi x) - tanh(\xi b)sinh(\xi x), \qquad (3.3)$$

$$R_2 = 1/\eta(R_{21} + R_{22}) + R_{23}, \qquad (3.4) \qquad R_t = \alpha(R_1R_2/R_1 + R_2) \qquad (3.5)$$

To test the prediction capabilities of the finned LTR model, 4 different dimensions were considered as shown in Table 2.8. Three fin thickness (2mm, 1mm, 0.5mm) and two types of fin material (aluminum, carbon steel) were also considered, so together there

were 24 testing cases. The conductivity of the aluminum fin is 202.4 $\mathrm{W/(mK)}$ and that of carbon steel is 50 $\mathrm{W/(mK)}$.

Table 2.8 New cases for the finned LTR model testing

Cases	#1	#2	#3	#4
a (cm)	1	1	1	5
b (cm)	1	3	7	5

Figure 2.12 shows the solidification time of all the cases predicted by the finned LTR model (denoted by solid lines) and by CFD model (denoted by circles). Figure 2.12 shows the prediction errors as defined in Section 2 Eqn. (2-18). From left to right in sequence are the 4 cases; every three points represent the three fin thicknesses (0.5mm, 1mm, 2.0mm). For the aluminum fin cases with different thicknesses, the predication errors of all the cases are within 4% percentage. For the carbon-steel fin cases, most of them have prediction errors within 5%, except for Case 3 with fin thickness 0.5 mm as shown in Figure 2.13. Large prediction error occurs when the fin thickness is small, i.e. 0.5mm. It is possible that the fin's low efficiency causes the large prediction error, so extra cases were tested to verify this assumption as shown in Table 2.9 and 2.10. In the evaluation of fin efficiency, the heat transfer coefficient is an unknown variable and it is assumed to be the conductivity of PCM divided by the distance from the fin to the solidification front of PCM, $h = k_{pcm}/L$. The distance L in the fin efficiency calculation (Eqn.3.3) in the finned LTR model changes with the locations of the solidification front and, but here it is set as $L = 1cm$. The length of the fin, fin thickness and fin material are the dependent variables for the calculation of the fin efficiency. For the aluminum fin in Figure 2.14, when the fin efficiency is decreased to 0.2 either due to low fin thickness (comparison between #1 and #2), or the fin is too long (comparison between #3 and # 4),

the deviation in solidifying time estimation by the finned LTR model becomes large. The same also happens for the carbon-steel fin cases as shown in Figure 2.15. Thus it can be concluded that as long as the fin' efficiency is not lower than a certain value, the finned LTR model will always give high accurate solidification time estimation.

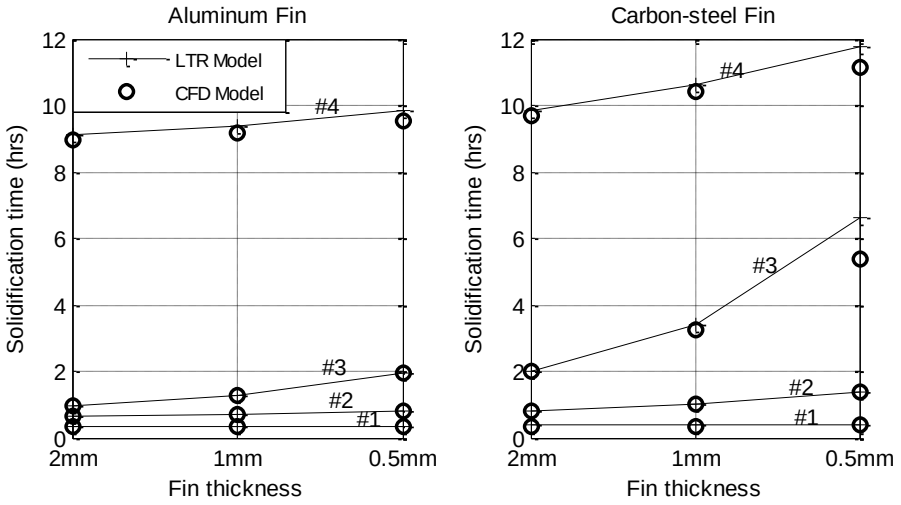

Figure 2.12 Predications of the testing cases by the 2-D Finned LTR model

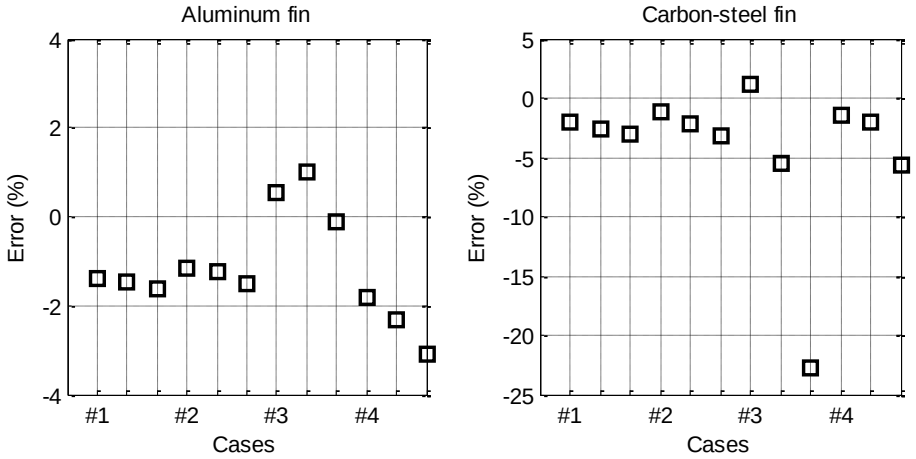

Figure 2.13 Predication errors by 2-D Finned LTR model
(Every 3 consecutive points represent fin thickness 0.5mm, 1.0mm and 2.0mm)

Table 2.9 Extra testing cases for aluminum fin

Cases	#1	#2	#3	#4
a (cm)	10	10	10	10
b (cm)	150	150	180	210
Fin thickness(mm)	2	1	2	2

Table 2.10 Extra testing cases for carbon steel fin

Cases	#1	#2	#3	#4
a (cm)	10	10	10	10
b (cm)	70	70	80	110
Fin thickness(mm)	2	0.5	2	2

(In the parentheses (aspect ratio b/c, fin thickness (mm))

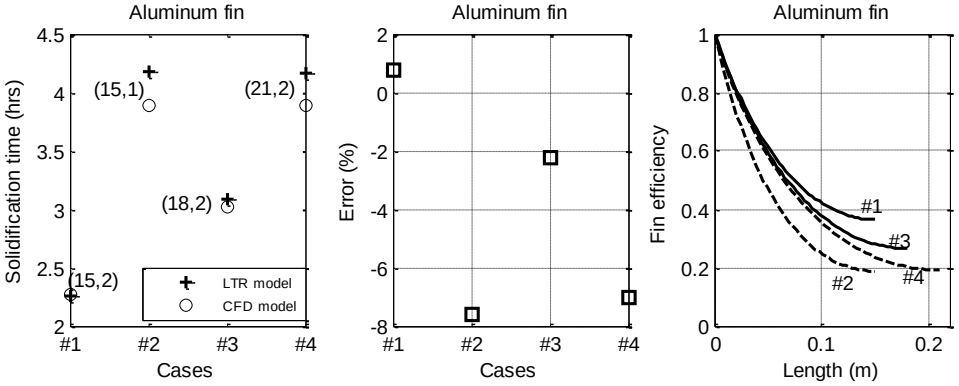

Figure 2.14 Solidification time prediction errors versus fin efficiency for aluminum fin

(In the parentheses (aspect ratio b/c, fin thickness (mm))

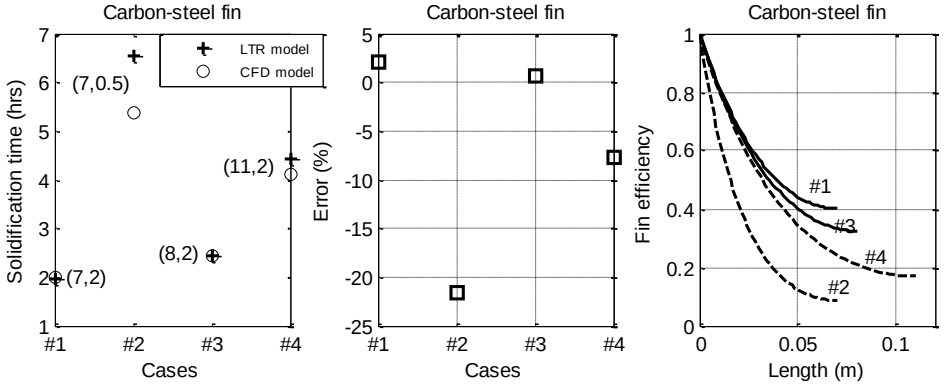

Figure 2.15 Solidification time prediction errors vs. fin efficiency for carbon-steel fin

For modeling PCM only, the heat flux during the solidification process was not considered, but for a finned PCM system it is an important parameter to study the performance of a fin. Figure 2.16 shows the solidification fraction curves given by the finned LTR and CFD models and Figure 2.17 shows the heat flux curves through the

cooling surfaces including both the PCM and fin faces. One case under comparison was Case 1 with 2mm thick aluminum fin and the other one was Case 4 with 0.5 mm thick carbon-steel fin. Respectively the two cases represent short-time solidification and solidification in a long time period. There is some discrepancy between the two solidification fraction curves predicted by the finned LTR and CFD models. However, the curvature trend for the heat flux matches quite well for both of the two cases. This implies that the finned LTR model also has a good ability to represent the heat flux dynamics during the entire solidification process. Thus the finned LTR model will be a reliable model to be employed in efficient optimal design of a finned PCM system.

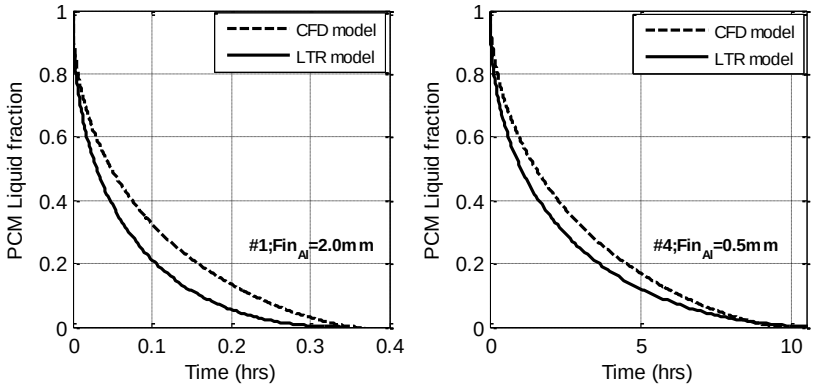

Figure 2.16 Solidification curves comparison between the finned LTR and CFD models for the 2-D cases

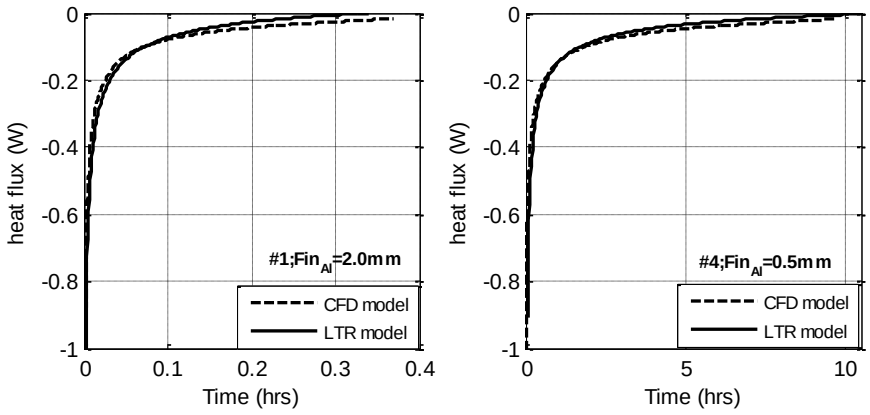

Figure 2.17 Heat flux curve comparison between the finned LTR and CFD models

3.2 Coupled PCM fin modeling in 3-D

The methods described above can be applied for a more general three dimensional PCM domain with fins. Figure 2.18 shows a cuboidal PCM wrapped by three plate fins. The fins were considered to have same thickness. And the system is cooled at the surface of the left plate fin; the remaining faces have zero heat flux. Though conduction paths through the PCM and fins are infinite in nature, it is assumed there are three principal heat paths, each passing through one plate fin and PCM. Based on Figure 2.18, the total thermal resistance for the heat path going through the left plate fin is R_1 and R_{11} is the resistance of the left plate fin, $R_{12}$is the resistance in the PCM for this heat path. The total thermal resistance of the heat path going through the bottom plate fin is R_2, and $R_{21}$is the resistance for the heat passing through the fin, $R_{22}$is the resistance in PCM of this heat path. Similarly R_3 is the total resistance for heat going through the back-plate fin in the figure, its component resistances are R_{31} for the fin and R_{32} for the PCM. It is assumed additionally that heat transfer in the fin only takes place along the length of the fin (say only along the x direction), so the fin efficiency (3.3) in the 2-D case can also be applied in the plate fins for the 3-D case. Then the heat flux, solidification time calculations are same as those (Eqns2.11-2.13) used in the LTR model without fins for the 2-D case. (Note that the names of R_{ij} in Eqns.(3.6-3.14) may already appears in the previous sections, but they are redefined under current context.)

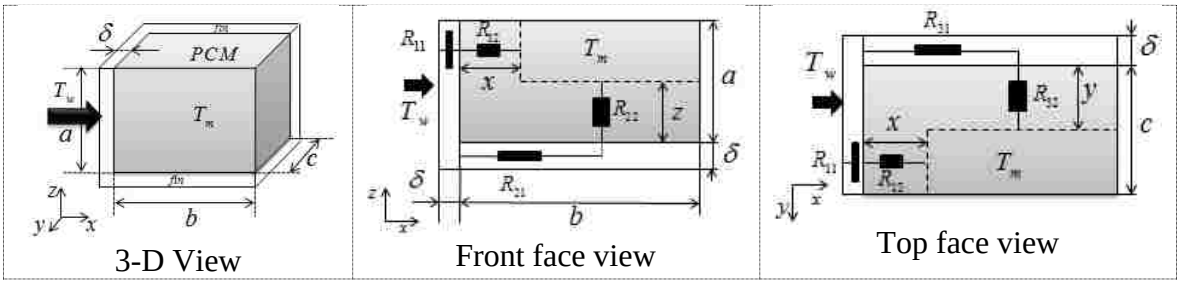

3-D View Front face view Top face view

Figure 2.18 PCM wrapped in a 3-D plate fins

$$R_{11} = \delta/cak_{fin} \quad (3.6)\ R_{12} = x/(a-z)(c-y)k_{pcm} \quad (3.7)\ \ R_1 = R_{11} + R_{12} \qquad (3.8)$$

$$R_{21} = x/c\delta k_{fin} \quad (3.9)\ R_{22} = z/(b-x)(c-y)k_{pcm} \quad (3.10)\ R_2 = 1/\eta\, R_{21} + R_{22} \ (3.11)$$

$$R_{31} = x/a\delta k_{fin} \ \ (3.12\ \ R_{22} = y/(b-x)(a-z)k_{pcm}\ (3.13)\ \ R_3 = 1/\eta\, R_{31} + R_{32}\ (3.14)$$

Nine cases as listed in Table 2.11 were used to test the performance of the 3-D finned LTR model. The geometries of the testing cases vary from a long bar shape (Case 4) to a plate shape (Case 6). Case 8 considers a different driving temperature difference and Case 9 considers a different PCM conductivity. The fin material is aluminum and its thickness is 1mm. CFD results were obtained by the Solidification & Melting model in Fluent [24]. The solidification time estimation is shown in Figure 2.19. Most of the cases have an error within 5%, except for the plate shape case which has an error close to 8%. The performance is not as good as the 2-D situation. The assumption that one-dimensional conduction takes place in the fin is the most possible cause to enlarge the error. The solidification fraction curves and the heat flux curves of Case 1 and Case 7 are shown in Figures 2.20 and 2.21. There are some discrepancy between the two solidification fraction curves predicted by CFD and the finned LTR models. However, the 3-D finned LTR model captures the trend of a heat flux curve very well for both of the cases. The 3-D finned LTR model promises to be an efficient and reliable modeling

approach for a finned PCM system considered in Figure 2.18 with almost no simulation cost after the tuning surface is built.

Table 2.11 Test cases for 3-D finned LTR model

Cases	#1	#2	#3	#4	#5	#6	#7	#8	#9
(a, b, c) cm	(2,2,2)	(1,3,1)	(1,5,1)	(1,7,1)	(5,1,5)	(7,1,7)	(6,6,6)	(6,6,6)	(6,6,6)
ΔT ℃	10	10	10	10	10	10	10	20	10
k_{pcm} W/mK	0.5	0.5	0.5	0.5	0.5	0.5	0.5	0.5	1.0

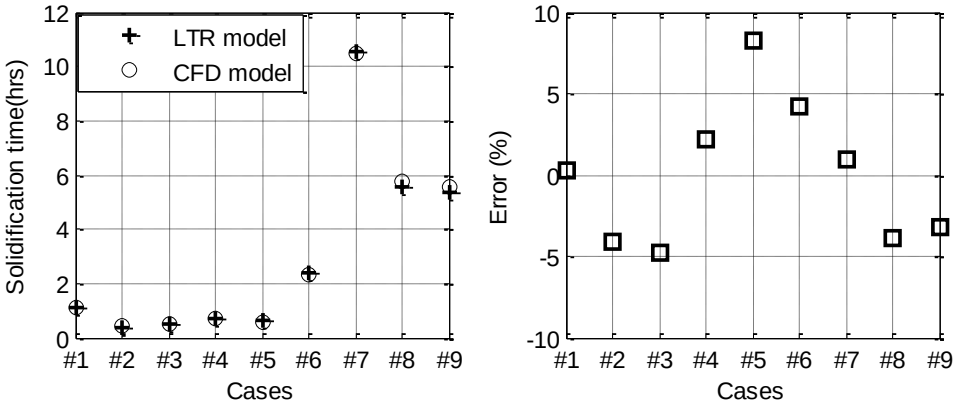

Figure 2.19 Solidification time predictions by 3-D finned LTR model

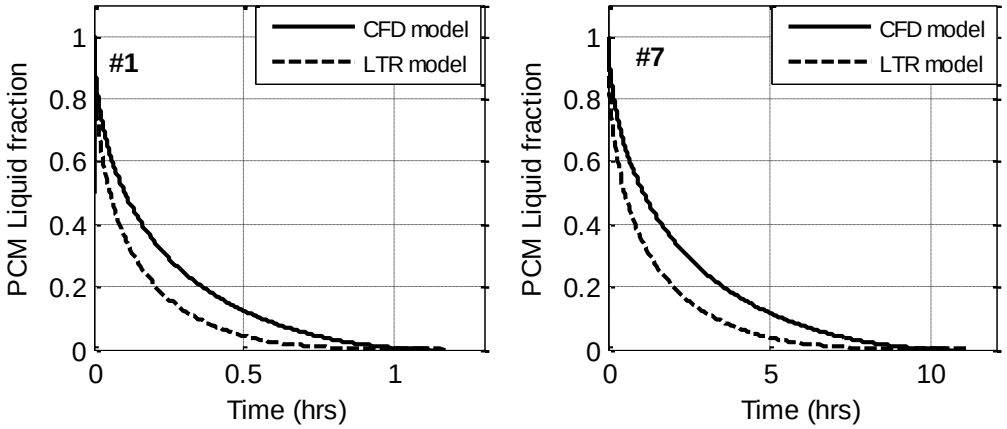

Figure 2.20 Solidification curve comparison between finned LTR and CFD models for the 3-D cases

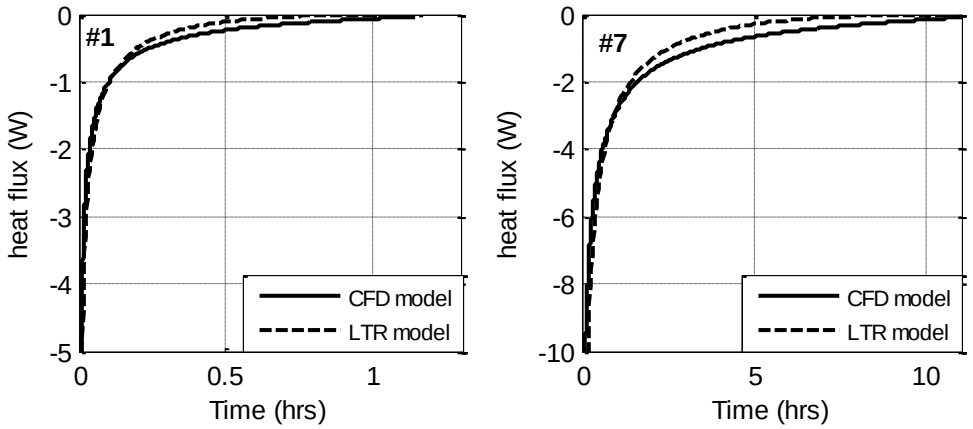

Figure 2.21 Heat flux curve comparison between finned LTR and CFD models

4. Conclusion

An efficient method to predict PCM behavior in three dimensions that could include fins is described in this paper. For most of the cases considered here results from the efficient LTR model compare well with those obtained using full scale transient three dimensional CFD methods. The key to successfully building the LTR model is to define the correct 'tuning curve /surface' for the geometry and shape of interest. The LTR model described here for Cartesian coordinates can readily be adapted for other complex geometries and coordinates such as cylindrical and/or curvilinear orthogonal coordinates. Then the tuning curve or surface will be dependent on the appropriate chosen ratios of independent parameters. As the finned LTR model represents a PDE described nonlinear transient freezing process into algebraic equations, thus a well-tuned LTR model can become the back-bone of an extensive yet efficient and inexpensive optimal design of a system that uses PCM and fins.

Acknowledgement

This research is sponsored by the ARPA-e ARID Program under Contract No. DE-AR0000582. Any opinions, findings, and conclusions or recommendations expressed in this article are those of the authors and do not necessarily reflect the views of the Advanced Research Projects Agency-Energy.

References

[12] Rahdar, Mohammad Hoseini, Abolghasem Emamzadeh, and Abtin Ataei. A comparative study on PCM and ice thermal energy storage tank for air-conditioning systems in office buildings. Appl. Therm. Eng. 96 (2016) 391-399.

[13] Ibrahim, Nasiru I., et al. "Experimental testing of the performance of a solar absorption cooling system assisted with ice-storage for an office space. Energy Convers. Manage. 148 (2017) 1399-1408.

[14] Agyenim F, Hewitt N, Eames P, et al. A review of materials, heat transfer and phase change problem formulation for latent heat thermal energy storage systems (LHTESS). Renew. Sustainable Energy Rev. 14 (2010) 615-628.

[15] Rathod M K, Banerjee J. Thermal stability of phase change materials used in latent heat energy storage systems: a review. Renew. Sustainable Energy Rev. (18) 2013 246-258.

[16] Fleming E, Wen S, Shi L, et al. Experimental and theoretical analysis of an aluminum foam enhanced phase change thermal storage unit. Int. J. Heat Mass Transfer (82) 2015 273-281.

[17] Khodadadi J M, Hosseinizadeh S F. Nanoparticle-enhanced phase change materials (NEPCM) with great potential for improved thermal energy storage. : Int. Commun. Heat Mass (34) 2007 534-543.

[18] Jamekhorshid A, Sadrameli S M, Farid M. A review of microencapsulation methods of phase change materials (PCMs) as a thermal energy storage (TES) medium. Renew. Sustainable Energy Rev. (31) 2014 531-542.

[19] Lohrasbi S, Sheikholeslami M, Ganji D D. Discharging process expedition of NEPCM in fin-assisted latent heat thermal energy storage system. J. Mol. Liq. (221) 2016 833-841.

[20] Lohrasbi S, Miry S Z, Gorji-Bandpy M, et al. Performance enhancement of finned heat pipe assisted latent heat thermal energy storage system in the presence of nano-enhanced H_2O as phase change material. Int. J. Hydrogen Energy (42) 2017 6526-6546.

[21] Peleg P. Levin, Avraham Schitzer, Gad Hetsroni. Numerical optimization of a PCM-based heat sink with internal fins. Int. J. Heat Mass Transfer 61 (2013) 638-645.

[22] Manish K. Rathod, Jyotirmay Banerjee. Thermal performance enhancement of shell and tube Latent Heat Storage Unit using longitudinal fins. Appl. Therm. Eng. 75 (2015) 1084-1092.

[23] Zhuo Li, Zhi-Gen Wu. Analysis of HTFs, PCMs and fins effects on the thermal performance of shell-tube thermal energy storage units. Sol. Energy 122 (2015) 382-395.

[24] Sheikholeslami M, Lohrasbi S, Ganji D D. Response surface method optimization of innovative fin structure for expediting discharging process in latent heat thermal energy storage system containing nano-enhanced phase change material. J. Taiwan Inst. Chem. Eng. (67) 2016 115-125.

[25] Sheikholeslami M, Lohrasbi S, Ganji DD. Numerical analysis of discharging process acceleration in LHTESS by immersing innovative fin configuration using finite element method. Applied Thermal Engineering. (107) 2016 154-66.

[26] Lohrasbi S, Sheikholeslami M, Ganji D D. Multi-objective RSM optimization of fin assisted latent heat thermal energy storage system based on solidification process of

phase change Material in presence of copper nanoparticles. Appl. Therm. Eng. (118) 2017 430-447.

[27] Ren S J, Charles J, Wang X C, et al. Corrosion testing of metals in contact with calcium chloride hexahydrate used for thermal energy storage. Mater. Corros. DOI: 10.1002/maco.201709432.

[28] Henry Hu, Stavros A Argyropoulos. Mathematical modelling of solidification and solidifying: a review. Modeling Simul. Mate. Sci. Eng. 4 (1996) 371-396.

[29] Stefan J.. S B Wien Akad. Mat. Natur.98 (1889) 473-484,965-983.

[30] Lamberg P, Siren K. Analytical model for solidification in a semi-infinite PCM storage with an internal fin. Heat and Mass Transfer (39) (2003) 167-176.

[31] Lamberg P, Siren K. Approximate analytical model for solidification in a finite PCM storage with internal fins. Appl. Math Model 27 (7) 2003 491-513.

[32] Lamberg P. Approximate analytical model for two-phase solidification problem in a finned phase change material storage. Appl. Energy 77 (2) (2004) 131-52.

[33] Parham A. Mirzaei, Fariborz Haghighat. Modeling of phase change materials for applications in whole building simulation. Renew. Sustainable Energy Rev. 16 (2012) 5353-62.

[34] Jegadheeswaran S, Pohekar S D. Performance enhancement in latent heat thermal storage system: a review. Renew. Sustainable Energy Rev. 13(9) (2009) 2225-2244.

[35] https://www.sharcnet.ca/Software/Fluent6/html/ug/node973.htm

[36] Brent AD. Voller VR, Reid KJ. Enthalpy-porosity technique for modeling convection-diffusion phase change: application to the solidifying of a pure metal. Num. Heat Tr. Part A (13) 1988 297-318.

[37] Ismail KAR, Alves CLF, Modesto MS. Numerical and experimental study on the solidification of PCM around a vertical axially finned isothermal cylinder. Appl. Therm. Eng. (21) 2001 53-77.

[38] https://www.mathworks.com/help/stats/support-vector-machine-regression.htm

[39] https://en.wikipedia.org/wiki/Spline_interpolation

[40] Smola, A.J., Schölkopf, B. A tutorial on support vector regression. Stat. Comput. 14 (2004) 199-222.

[41] Kozak Y, Rozenfeld T, Ziskind G. Close-contact melting in vertical annular enclosures with a non-isothermal base: Theoretical modeling and application to thermal storage. Int. J. Heat Mass Transfer 72 (2014) 114-127.

Appendix

Fin efficiency calculation

The fin extended from the heat pipe is approximated by a 1D conduction bar. As shown in Figure 2.22, it has a constant temperature at one end and heat flux boundary condition on the PCM side; the other end and side have zero heat flux. Based on an energy balance of the bar, the fin efficiency is:

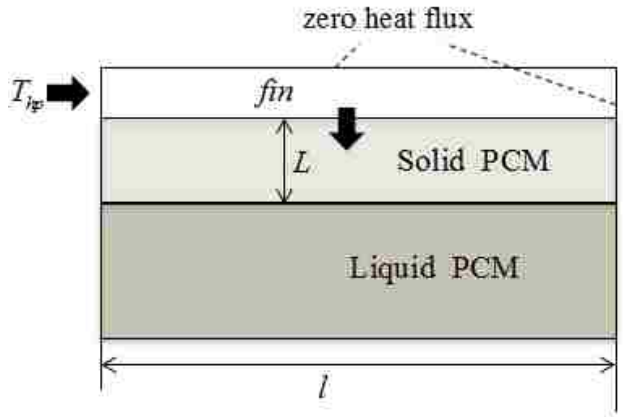

Figure 2. 22 Geometry and boundary conditions for the 1-D bar efficiency calculation

$$Q_x = Q_{x+\Delta x} + Q_c, \quad \Delta x \to 0 \Rightarrow Q_{x+\Delta x} = Q_x + \frac{dQ_x}{dx}\Delta x, \quad \frac{dQ_x}{dx}\Delta x + Q_c = 0 \qquad \text{(A.1)}$$

$$Q_x = -k_{fin} A \frac{dT}{dx}, \qquad Q_c = hS(T - T_{pcm}) \qquad \text{(A.2)}$$

$$A = cw, \qquad S = c\Delta x, \qquad h = \frac{k_{pcm}}{\boldsymbol{L}} \quad \text{(c: Thickness of the fin)} \qquad \text{(A.3)}$$

$$\frac{d}{dx}\left(-k_{fin} A \frac{dT}{dx}\right) + hS(T - T_{pcm}) = 0, \quad \text{assuming } \theta = T(x) - T_{pcm} \qquad \text{(A.4)}$$

$$\frac{d^2\theta}{dx^2} - \frac{k_{pcm}}{k_{fin} w d_m}\theta = 0, \qquad \theta\big|_{x=0} = T_{hp} - T_{pcm}, \qquad \left.\frac{\partial\theta}{\partial x}\right|_{x=l} = 0 \qquad \text{(A.5)}$$

$$\xi^2 = \frac{k_{pcm}}{k_{fin} w \boldsymbol{L}}, \qquad \text{(A.6)}$$

$$\theta = \left(T_{hp} - T_m\right)\left(\cosh(\xi x) - \tanh(\xi l)\sinh(\xi x)\right) \qquad \text{(A.7)}$$

$$\eta = \frac{T(x) - T_m}{T_w - T_m} = \left(\cosh(\xi x) - \tanh(\xi l)\sinh(\xi x)\right) \qquad \text{(A.8)}$$

where L is the melting front distance away from the fin. The heat transfer coefficient at the PCM side is assumed to be the conductivity of the PCM divided by the melting front distance, $h = k_{pcm}/L$.

Chapter 3

Efficient optimization of a longitudinal finned heat pipe structure for a latent thermal energy storage system

(Pan C., Vermaak N., Romero C. Neti S., et al. Efficient optimization of a longitudinal finned heat pipe structure for a latent thermal energy storage system, *Energy Conversion and Management* 2017, (153): 93-105.)

Efficient optimization of a longitudinal finned heat pipe structure for a latent thermal energy storage system

Chunjian Pan[1], Natasha Vermaak[1], Carlos Romero[1], Sudhakar Neti[1], Sean Hoenig [2], Chien-Hua Chen[2]

[1]Lehigh University, Bethlehem, PA 18015, USA

[2]Advanced Cooling Technologies, Inc., Lancaster, PA 17601, USA

Abstract

Phase Change Materials (PCMs) are gaining importance in energy storage applications. However, many PCMs are poor thermal conductors and thus can benefit from the optimal use of appropriate fins. This work introduces a PCM-fin structure optimization framework. Typically, the non-linear solidification process increases the complexity associated with solving the mathematical equations for the PCM-fin structure optimization problem, making it computationally expensive. In this paper a modeling approach called Layered Thermal Resistance (LTR) model is extended and developed in 2D cylindrical geometry in order to enable efficient PCM-fin structure optimization. The finned LTR model represents the nonlinear transient solidification process by analytic equations. This significantly reduces the computational cost associated with optimization. A finned heat pipe structure modeled by the finned LTR approach is optimized based on minimizing cost while meeting operational requirements. The optimal results imply that thinner fins result in lower system cost and that there is a thickness limit for the fins to be economically welded on a heat pipe. The finned LTR model also gives the optimal cost of material usage for a large scale latent thermal energy storage system in terms of dollars per kilowatt and it was found that the system cost is slightly lower by using carbon-steel as the construction material for the heat pipes and fins than by using Al 6061.

Key words: Latent energy storage, efficient PCM simulation, heat pipe embedded PCM, finned heat pipe, optimal design

Nomenclature

T_{hp}	Heating temperature at the boundary
T_m	PCM melting temperature
S_1, S_2	Heat transfer area (Shrinking liquid-solid interface)
$q(i)$	Heat flux
R_1, R_2	Thermal resistances for different heat paths
R_1^*	Thermal resistance includes both the fin and PCM domains
R_t	Total thermal resistance of a system
R_f	Fin thermal resistance
η	Fin efficiency
ξ	Parameter for fin efficiency calculation
L_m	Latent energy of PCM
Cp_{pcm}	Heat capacity of PCM
k_{pcm}	Conductivity of PCM
k_{fin}	Conductivity of fin
ρ_{pcm}	Density of PCM
ρ_{hp}	Density of heat pipe material
ρ_f	Density of fin material
$t(i)$	Discrete solidification time for PCM layers
t_s	Total solidification time
$D_r(i), L(i)$	Locations of solid fronts
c	Fin and PCM thickness
$dV(i)$	Layered PCM volumes
θ	Half spacing angle of a cell between two longitudinal fins
f	Resistance tuning surface in 2D
α	Resistance tuning value
t_{LTR}	PCM solidification time estimated by LTR model
t_{CFD}	PCM solidification time estimated by CFD model
t_{op}	Discharging time requirement
ε	Prediction discrepancy

T_{cell}	Temperature of a discrete element
T_{upper}	Upper PCM melting temperature
T_{lower}	Lower PCM melting temperature
$\psi(0)$	Dimensionless superheating parameter
T_{ini}	Initial temperature of the PCM domain
γ	PCM liquid fraction
h	Heat transfer coefficient on the PCM side
G	Cooling load target
C_{pcm}	Cost of PCM
C_{hp}	Cost of heat pipe
C_f	Cost of the fin
M_{pcm}	The amount of PCM to be used
M_{hp}	The amount of heat pipe material to be used
M_{fin}	The amount of fin material to be used
V_{pcm}	Total PCM volume
H_p	Height of each heat pipe
N_p	Total number of heat pipes
w_{hp}	Wall thickness of the heat pipe
r_0	Inner radius of the heat pipe
N_f	Total number of fins welded to a heat pipe
$r_1 = r_0 + w_{hp}$	Outer radius of the heat pipe
r_2	Radius of the longitudinal fin welded on the heat pipe
w	Thickness of the longitudinal fin
g	Cost equation

1 Introduction

Increasing research is focused on thermal energy storage systems due to their important role in clean energy technologies and the need to match renewable energy to load patterns. For example, thermal energy storage systems are needed to address the mismatch between the supply and demand of solar energy. Providing "cold storage" produced at lower costs during off peak hours of the day, is a practical way to reduce utilities' burden to produce enough electricity during high demand hours [1-2].

Many mature and industrial applications of thermal energy storage systems use sensible energy. Phase Change Materials (PCMs) are receiving more attention due to their high-energy densities. PCM can store or release energy at near isothermal conditions that are thermodynamically superior. However, the low conductivity of PCM materials is a barrier for many practical applications, especially for large scale systems. Researchers are eager to resolve this issue by employing different heat transfer enhancement techniques, i.e., including high conductivity foams or metal matrices into the PCM [3], dispersing high conductivity particles in the PCM [4], or using microencapsulation of the PCM [5]. Extensive research has been conducted to study the shell and tube systems with fins in the PCM since they can be simple and compact. [6-12].

Embedding Heat Pipes (HPs) between the PCM and the Heat Transfer Fluid (HTF) is also an approach that attracts a lot of research. Faghri [13, 14] patented methods to embed HPs into PCM to enhance the performance of thermal energy storage systems and heat exchangers. Horbaniuc et al. [15] analytically modeled the solidification of PCM within a longitudinally finned HP storage system. Liu et al. [16] experimentally studied a circumferentially-finned HP heat exchanger with latent heat storage similar to that of Horbaniuc et al. Shabgard et al. [17] developed a thermal network model for a HP

embedded latent thermal energy storage (LTES) unit. The same authors also used a thermal network model to analyze a LTES system with embedded HPs and cascading PCMs [18]. Christopher et al. [19] defined the HP effectiveness and experimentally investigated a LTES system utilizing HPs or fins. Nithyanandam [20] developed a thermal resistance network model of a shell and tube LTES with embedded HPs and parametric studies of the influence of the heat pipe. The same authors [21] also created a transient three-dimensional computational model for the system to guide design efforts. Nithyanandam [22] also provided numerical simulations to illustrate their methodology for design and optimization of the shell and tube LTES with embedded HPs for required storage costs. Sharifi [23] considered three operational modes (charging, discharging and simultaneous charging and discharging) of a vertical cylindrical enclosure PCM unit with concentric HPs at its center. Naghavi [24] experimentally investigated a solar water heater system with a latent heat storage tank embedded with HPs. Tiari [25-27] numerically studied the finned HP-assisted LTES unit in 2D and 3D. Almsater [28] used finned heat pipes to enhance heat transfer performance in concentrating solar thermal power applications.

Although a lot of researchers have numerically and experimentally studied finned HP-assisted LTES systems, limited research has been focused on the optimization of a finned HP, i.e. optimizing the length and number of fins. In terms of optimization methods, Veelken [29] used combined numerical modeling and a genetic algorithm to find optimal fin positions on a contact surface with non-uniform heat loads. Pizzolato[30] employed a topology optimization framework to find the optimal spatial layout of high conductivity material within PCMs. Lohrasbi [31-32] proposed to use a response surface

method (RSM) which requires establishing a relationship between the design variables of interest and the objective function. By estimating the effects of each parameter on the objective function, it provides a more efficient approach for parametric studies. RSM has also been applied to optimize a microchannel heat sink [52]. The use of central composite design (CCD) in microchannel heat sink optimization is also studied in [53]. In many cases, optimizations have often been based on parametric studies through simulations [33-37]. Multiple simulations need to be carried out for variations of the design parameters of interest. Due to the transient nonlinear behavior of PCM solidification or melting, the process is computationally expensive and can only guarantee near-optimal solutions. In this paper, an analytical Layered Thermal Resistance (LTR) model [38] is extended for the first time, to a 2D cylindrical geometry to support the efficient optimization of PCM-fin energy storage structures. The LTR model describes the nonlinear transient solidification process with algebraic equations, thus significantly reducing the computational complexity of the optimization problem. Moreover, most of the previous optimization analyses of the fin-PCM structure [31-37] are based on improving heat flux and increasing fin efficiency. In this paper, the focus is instead on directly optimizing system cost while the role of heat flux is indirectly addressed by setting the discharging time requirement. The LTR model can be used to easily incorporate this objective function and constraint in the optimization framework. With this framework, a more relevant engineering comparison among different fin configurations becomes possible. This novel modeling approach has wide applications for the optimal design of latent energy storage systems with fins. In this paper, the LTR mode is used for the first time to find the optimal dimensions of a finned heat pipe.

The content of this paper is organized as follows. In section 2, the LTR model for a 2D cylindrical geometry is developed. Section 3 introduces coupling fins to the LTR model. In section 4, the finned LTR model is employed to solve the finned HP optimization problem followed by a discussion of the results. Section 6 presents the conclusions.

2 Layered Thermal Resistance model in 2-D cylindrical coordinates

The Layered Thermal Resistance (LTR) model was first proposed in [38] for rectangular and cuboidal geometries; it is based on a thermal resistance network analysis [17, 20, 22]. In this section a new extension to PCM solidification with constant cooling temperatures at the boundaries in a cylindrical coordinate system is developed in order to represent tube-shell configurations. Figure 3.1 shows the geometry of interest, which is cooled at the two sides with constant temperature boundary conditions and has zero heat flux at the remaining two sides. The key component of the LTR model is the assumption that the liquid PCM is solidified in a layer by layer manner and that the final solidification time is estimated by adding together the solidification times of all of the discrete layers. In Figure 1, the dotted lines schematically represent successive solid front layers. Each discrete layer represents a new annulus section, which has the same angle θ and radial ratio $\frac{r_1}{r_2}$ as the original PCM shape, but in a shrinking manner to represent the solidification behavior. The modeling approach is given in Eqns. (2.1-2.6). Variables $L(i)$ and $D_r(i)$ designate the evolving location of the solidification front. A detailed calculation of $L(i)$ and $D_r(i)$ can be found in Appendix A. A small depth (5mm

into the page) of the 2D PCM domain is used to calculate the heat transfer areas $S_1(i)$ and $S_2(i)$, and at the same time a 2D geometry is used for analysis. There are two heat paths to the solidification front, represented by two thermal resistances, R_1 and R_2. An average temperature difference $0.5(T_{hp} - T_{m)}$ is used to account for the sensible energy, where T_{hp} is the cooling temperature and T_m is the melting temperature of the PCM.

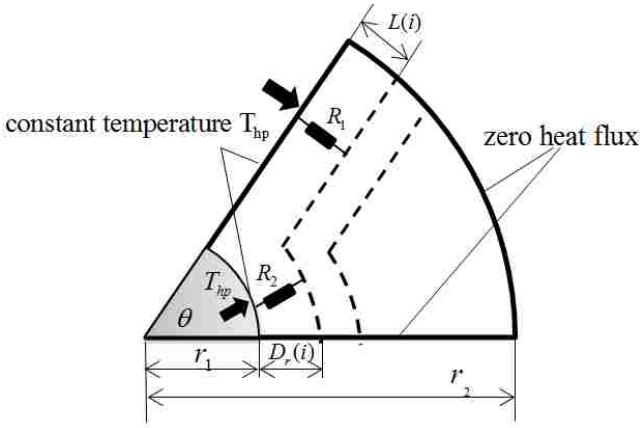

Figure 3.1 Geometry

$$R_1(i) = \frac{L(i)}{S_1(i)k_{pcm}}, \quad (2.1) \qquad R_2(i) = \frac{D_r(i)}{S_2(i)k_{pcm}}, \quad (2.2)$$

$$R_t(i) = \frac{R_1(i)R_2(i)}{R_1(i)+R_2(i)}, \quad (2.3) \qquad \mathrm{q}(i) = \frac{T_{hp}-T_m}{R_t(i)}, \quad (2.4)$$

$$\mathrm{t}(i) = \frac{dV(i)\rho_{pcm}[L_{pcm}+0.5C_p(T_{hp}-T_m)]}{q(i)}, \quad (2.5) \qquad t_s = \sum_{i=1}^{N-1} t(i). \quad (2.6)$$

Table 3.1 Annulus sector with different radii and angle

	r_1 (cm)	2.54	2.54	2.54	2.54	2.54	2.54	0.254
	r_2 (cm)	5.08	6.35	7.62	10.16	12.7	17.78	2.286
θ(°)	10	A11	A12	A13	A14	A15	A16	A17
	30	A21	A22	A23	A24	A25	A26	A27
	45	A31	A32	A33	A34	A35	A36	A37
	60	A41-	A42	A43	A44	A45	A46	A47
	90	A51	A52	A53	A54	A55	A56	A57

('Aij', i = 1: 5, j = 1: 7 represents a case number)

Thirty-five different testing cases are given in Table 3.1 of the annulus sector PCM domain. The cases have 5 different angles θ and 7 radial ratios $\frac{r_2}{r_1}$. The angle θ covers a range from 10° to 90°. The ratio $\frac{r_2}{r_1}$ ranges from 2.0 to 9.0; a ratio of 2.0 represents a case where a minimal compactness factor (CF) of 75% is set for the heat pipe PCM system with no fins. The CF of a PCM storage system is defined as the ratio of the volume of PCM to the volume of the whole system. The traditional PCM encapsulated in spheres can reduce the storage density by 50% [39], while tubes in PCM tank arrangements can achieve CFs of over 90% [40].

The Solidification & Melting Model in Fluent (commercial computational fluid dynamics (CFD) software) [41], which is based on the enthalpy-porosity method [42], is used to obtain the numerical solutions to verify the LTR model. For the enthalpy-porosity method, three regions, solid, liquid, and mushy zones, are defined in the computational domain. Given a PCM's melting range (T_{lower}, T_{upper}) and a cell temperature T_{cell}, a liquid fraction ranging from 0 to 1 is defined by eqn. (2-7) and is used to identify the three regions. The exact melting temperature used in the LTR model is defined as $T_m = \frac{1}{2}(T_{lower} + T_{upper})$. As the solidification process is conduction dominated [43], the momentum equations were turned off in the Fluent setup. Thus energy balance (See Eqn.2-8) is the main governing equation.

$$\gamma = \begin{cases} 1, & T_{cell} > T_{upper} \\ \frac{T_{cell} - T_{lower}}{T_{upper} - T_{lower}}, & T_{lower} \le T_{cell} \le T_{upper} \\ 0, & T_{cell} > T_{upper} \end{cases} \tag{2-7}$$

$$\frac{\partial}{\partial t}(\rho_{pcm} H) = \nabla \cdot (k_{pcm} \nabla T), \tag{2-8}$$

where specific enthalpy H is formulated according to the enthalpy method [42],

$$H = H_{ref} + \int_{T_{ref}}^{T} Cp_{pcm} dT + \gamma L_m \tag{2-9}$$

Validation of the solidification phenomenon predicted by the method [42] compared to experimental data is available in Ismail's work [44]. Figure 3.2, reproduced from [44], shows good agreement in the comparison of solidification fronts between the numerical and experimental results. The $\psi(0)$ in the figure is a dimensionless superheating parameter defined as $\psi(0) = (T_{ini} - T_m)/(T_{ini} - T_w)$ to represent the system with different initial temperature, where T_{ini} is the initial temperature of the system.

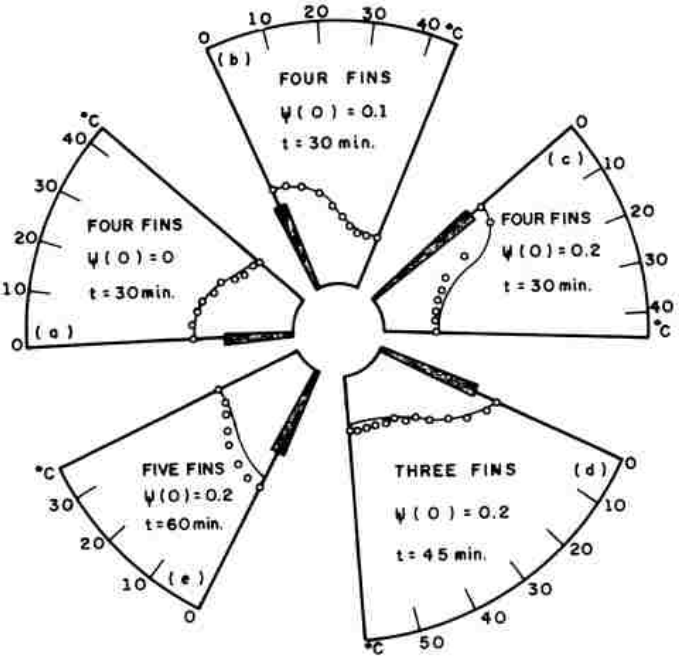

Figure 3.2 Comparison of numerical and experimental solidification fronts [44]

For the CFD simulations in the present study, the total number of elements used was 20,000-40,000 depending on the size of the geometry and the time step was around 3-6 s. Sensitivity studies were performed to confirm mesh and time-step independence of the results presented. The energy equation was discretized using the Second Order Upwind

scheme. A pressure based solver with double-precision was chosen. The convergence was checked at every 2 time steps with a scaled absolute residual of 10^{-9} that was used for the energy equation.

The CFD results are treated as a trusted reference to verify the LTR model. Figure 3.3 displays the solidification time estimates found by CFD (a) and the LTR model (b) for the ramp of θ and $\frac{r_2}{r_1}$ explored in the testing cases (Table 3.1). Figure 3.3 (c) shows a comparison of the solidification times t_{CFD}/t_{LTR}. It reveals that the LTR model significantly overestimates the solidification time but the two models share similar solidification-time surfaces (See Figure 3.3 (a) and 3.3 (b)). The solidification time ratio between the two models (Figure 3.3 (c)) actually indicates how much the thermal resistance is overestimated by the LTR model. It suggests that a resistance 'tuning surface' can be created based on the solidification time ratios of the two models. Thus an extra tuning factor is introduced in order to reliably use the LTR model. As the annulus sector has two geometric variables, the radial ratio $\frac{r_2}{r_1}$ and θ that define the shape and the resistance tuning factor will be defined by a surface $\alpha = f_2\left(\frac{r_2}{r_1}, \theta\right)$. A custom support vector regression (SVR) method [45] was used to establish the resistance tuning surface. Other interesting applications of regression models in engineering applications can be found in [51]. The 35 cases in Table 3.1 are used as the training samples for the SVR model. The solidification time ratio between the CFD model and the LTR model without tuning t_{CFD}/t_{LTR} is the output of the regression analysis. After a suitable model parameter is chosen for the SVR [45], the time-ratio surface of Figure 3.3 (c) is reconstructed in Figure 3.4. Once the regression tuning surface is identified, it is

employed to predict a tuning factor given a new pair of $\frac{r_2}{r_1}$ and θ, and to adjust the total resistance of the LTR model as shown in Eqns. (2.10-2.11)

$$\alpha = f_2\left(\frac{r_2}{r_1}, \theta\right), \qquad (2.10) \qquad R_t(i) = \alpha \frac{R_1(i)R_2(i)}{R_1(i)+R_2(i)} \qquad (2.11)$$

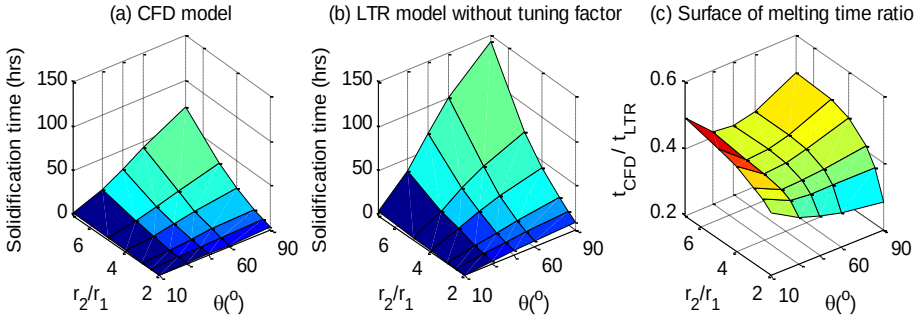

Figure 3.3 Solidification time estimated by CFD and LTR models without using tuning factors

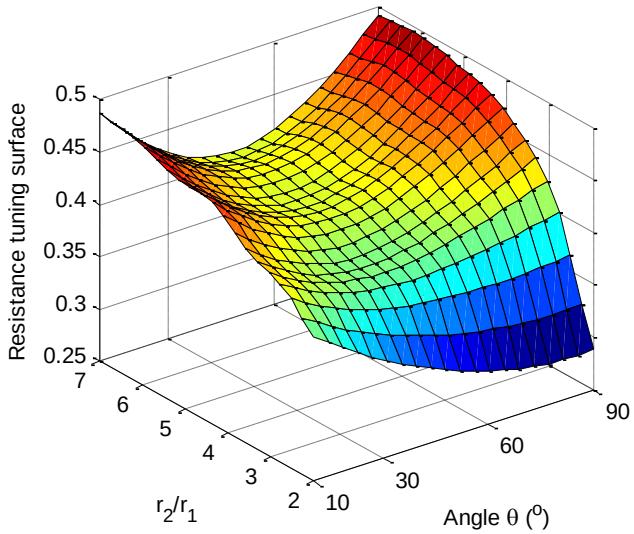

Figure 3.4 Resistance tuning surface by support vector regression (SVR)

Table 3.2 Twelve new testing cases for the LTR model modified with a tuning factor

Description	Same dT and k_{pcm} as the tuning surface varies			Smaller k_{pcm}; vary dT; vary dimensions;			Larger k_{pcm}; vary dT; vary dimensions;			Everything is the same as Cases 9-11 ; except k_{pcm}		
Cases	1	2	3	4	5	6	7	8	9	10	11	12
r_1 (cm)	1.27	5.08	5.08	3.81	3.81	3.81	3.81	3.81	3.81	3.81	3.81	3.81
r_2 (cm)	4.445	21.336	30.48	12.192	12.573	8.763	13.716	14.145	10.287	13.716	14.145	10.287
r_1/r_2	3.5	4.2	6.0	3.2	3.3	2.3	3.6	4.5	2.7	3.6	4.5	2.7
θ(°)	45	80	20	35	85	18	70	8	20	70	8	20
dT (℃)	10	10	10	15	30	8	15	8	5	15	8	5
k_{pcm} W /(mK)	1.0	1.0	1.0	0.5	0.5	0.5	2.0	2.0	2.0	1.0	1.0	1.0
α	0.3926	0.4528	0.4510	0.3917	0.4327	0.3856	0.4187	0.4701	0.4003	0.4187	0.4701	0.4003

Table 3.2 gives additional cases that are used to test the accuracy of the LTR model modified with the resistance tuning factor. The first 3 cases have different radial ratios $\frac{r_2}{r_1}$ and angles θ while keeping the same driving temperature and PCM conductivity as the cases in Table 3.1. (Cases in Table 3.1 are used for building the resistance tuning surface.) Cases 4-6 have different driving temperatures with a lower PCM conductivity. Cases 7-9 have different driving temperatures and a higher PCM conductivity. Cases 10-12 have exactly the same geometries and driving temperature differences as Cases 7-9, but they have a different PCM conductivity. It should be noted that the PCM conductivity is the only PCM material property varied because it not only affects heat transfer within the PCM domain, but it also is the only PCM property parameter that affects the fin efficiency calculation when coupling the fins to a PCM domain (See Eqn. B.3 in Appendix B). By considering different PCM conductivities, we are thus further verifying the method of coupling fins, which is important in terms of finding the optimal

configuration of a finned heat pipe. Once again we treat CFD simulation results as the trusted reference in comparison to the LTR model that is now modified with a resistance tuning factor. Estimation accuracy in terms of percent error is defined as,

$$\varepsilon = \frac{(t_{LTR} - t_{CFD})}{t_{CFD}} \times 100\%. \quad (2.12)$$

The performance of the LTR model is shown in Figure 3.5. Overall, the tuned LTR model accuracy is quite good, within 5.0% compared to the CFD results. Cases 7-9 and 10-12 have almost the same error pattern. The results suggest that the PCM conductivity has almost no effect on the performance of the tuned LTR model. Different driving temperatures also have negligible effect on the performance of the model. The tuning surface is almost only dependent on geometry. Consequently, once a resistance tuning surface is constructed based on a prescribed driving temperature and PCM conductivity, it can also be applied to cases with new driving temperature differences and PCM conductivities. Thus the resistance tuning surface provides flexibility for different applications.

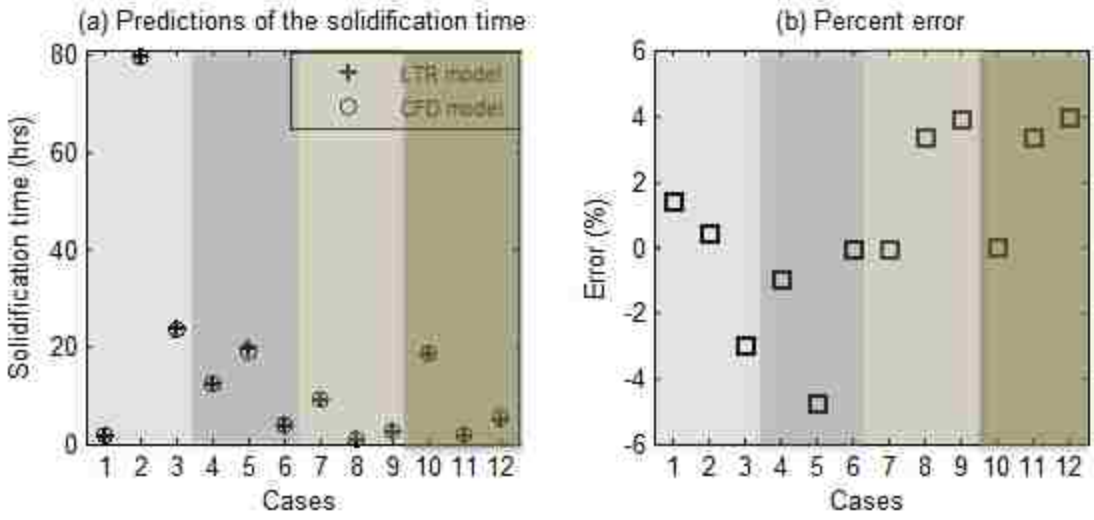

Figure 3.5 (a) Predictions of the 14 cases using LTR model with the tuning factor and (b) percent error between the CFD and LTR results

3 Coupled PCM Fin modeling based on tuned LTR Model

Many PCMs used for thermal energy storage are very poor thermal conductors, which is detrimental for energy transfer. This is particularly so during the energy retrieval (solidification) process which is conduction dominated [43]. Thus in this paper, the finned heat pipe structure shown in Figure 6 is studied to enhance the heat transfer performance within the PCM. In this section, a finned LTR model is constructed which is used for the optimal design of the dimensions of the finned heat pipe structure based on the solidification process. As the discharging process is conduction controlled [43], the fin-PCM structure optimization based on a conduction model is of interest. Given the costs of heat pipes and fins, the optimal dimensions (r_1, r_2, w, θ) are determined for an objective of minimum system cost while ensuring that the PCM meets a given solidification time requirement.

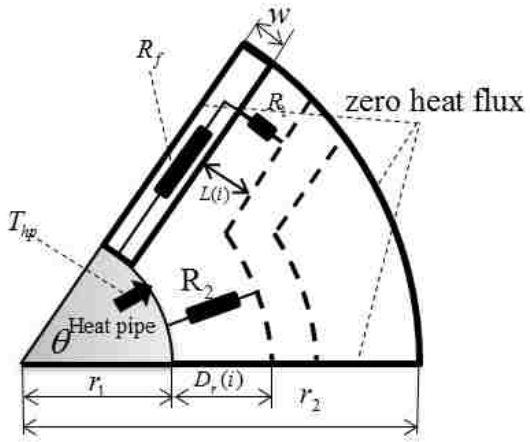

Figure 3.6 Finned annular sector

In the finned heat pipe structure (Figure 3.6), it is assumed that the heat pipe wall (r_1 is the outer radius of the heat pipe) maintains a constant temperature T_{hp} and the remaining boundaries have zero heat flux. There are two heat paths for cooling energy transfer to the PCM. One path is through the PCM with its thermal resistance R_2 and the other one is through the fin with thermal resistance R_f and the PCM with resistance R_1. Resistances R_1 and R_2 are the same as those defined in the LTR model with no fins in section 2 (Eqns. 2.1-2.2). R_f is defined as:

$$R_f = D_r(i)/cwk_{fin}\,, \tag{3.1}$$

where c is the depth of the fin and PCM, which is set as 5mm in all of the simulations in this paper; $D_r(i)$ is the distance to the solidification front in the radial direction. Besides the fin resistances to be incorporated into the tuned LTR model, fin efficiency is also a key factor that must be considered. The fin efficiency η eqn. (3.2) is derived by solving the energy balance equation of the fin (presented in Appendix B). More studies regarding fin efficiency analysis are available in [49, 50]. The thermal resistance passing through the fin will need to be increased by $1/\eta$ to account for the fin efficiency. Eqn. (3.3) is the

total resistance for the finned LTR model shown in Figure 3.6. The heat flux and solidification time calculations are the same as those listed in the first version of the LTR model with a tuning factor in section 2 Eqns. (2.4-2.6).

$$\eta = \frac{T(x)-T_m}{T_w-T_m} = cosh(\xi x) - tanh(\xi b)sinh(\xi x), \tag{3.2}$$

$$R_1^* = R_f + 1/\eta R_1 \tag{3.3}$$

$$R_t = \alpha(R_1^* R_2/R_1^* + R_2) \tag{3.4}$$

To test the prediction capabilities of the finned LTR model, 8 cases are considered in Table 3.3. The first 4 cases are repeated with a different PCM conductivity which is denoted by the asterisk symbol (i.e., case #1* is exactly the same as case #1 except the k_{pcm} is different). Three fin thicknesses (0.5mm, 1mm, 2.0mm) and two types of fin material (aluminum alloy 6061 and carbon steel) are also considered. The conductivity of the aluminum alloy fin is 170 $\mathrm{W/(mK)}$, and that of the carbon steel is 45 $\mathrm{W/(mK)}$.

Table 3.3 Additional test cases for the Finned LTR model with tuning factor.

	#1	#2	#3	#4	#1*	#2*	#3*	#4*
r_1 (cm)	2.54	2.54	2.54	2.54	2.54	2.54	2.54	2.54
r_2 (cm)	5.334	6.858	9.652	15.24	5.334	6.858	9.652	15.24
θ(°)	80	50	20	10	80	50	20	10
k_{pcm} W/(mK)	1.0	1.0	1.0	1.0	0.5	0.5	0.5	0.5
α tuning factor	0.3005	0.3783	0.4203	0.4801	0.3005	0.3783	0.4203	0.4801

(Cases 1-4 are repeated with different k_{pcm} denoted by the asterisk symbol)

Figure 3.7 shows the solidification time errors as defined in Section 2 Eqn. (2.12) for both the aluminum fins (Figure 3.7(a)) and the carbon-steel fins (Figure 3.7 (b)). The three points between the dotted vertical line dividers represent the three fin thicknesses (0.5mm, 1mm, 2.0mm) tried, respectively, for a single case in Table 3.3. For example

the first data point for case 1 corresponds to a 0.5mm fin thickness. For all of the aluminum fin cases with different thicknesses, the percent errors are within 10%. For the carbon-steel fins, larger percent error occurs when the fin thickness is 0.5mm. The reason is that when the fin efficiency drops to below a certain low value, the finned LTR model will tend to overestimate the solidification time. More detailed analysis of the limitations of the finned LTR model for rectangular and cuboidal systems is given in [38]. For the remaining cases, percent errors are close to 15%. The cases with lower PCM conductivity have relatively smaller percent errors. Figure 3.7 also shows the trend that larger fin thicknesses have smaller percent errors. Both lower PCM conductivity and larger fin thicknesses contribute to higher fin efficiency. Thus it can be concluded that the finned LTR model has better performance in cases where there is high fin efficiency. Discussion of how the solidification time errors will affect the optimal solutions will be given in the next section.

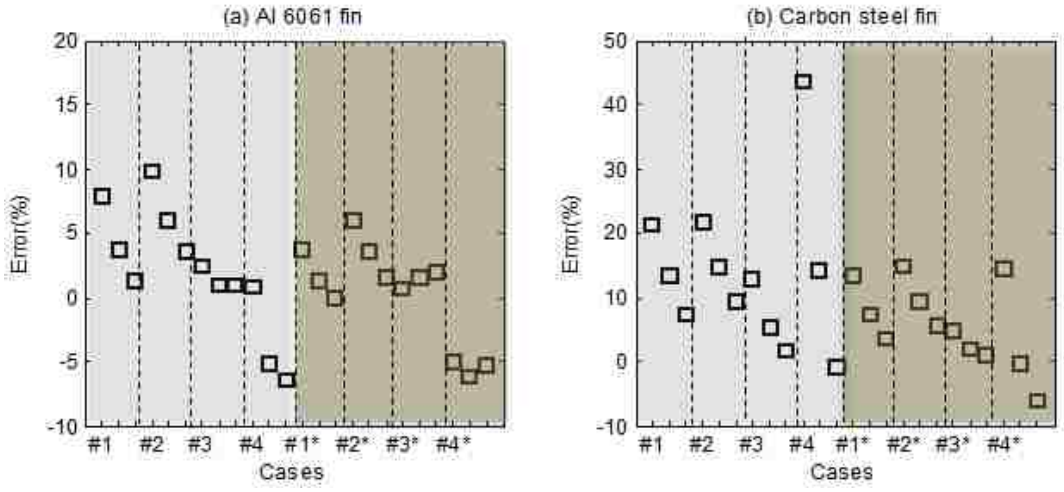

Figure 3.7 Percent errors between CFD and LTR solidification time predictions for all of the cases in Table 3.3. There are 3 data points for each case considered representing different fin thicknesses.

The heat flux during the solidification process is an important parameter to consider when evaluating the dynamic performance of a fin. Figure 3.8 shows the heat flux variation through the HP wall including both the PCM and fin face for two test cases. One case examined is #1 (Table 3.3) with a 2mm thick Al6061 fin and a 1.0 W/(mk) PCM conductivity, the other case is #4* (Table 3.3) with a 0.5 mm thick Al 6061 fin and 0.5 W/(m*k) PCM conductivity. The two cases represent a system with a short solidification time (#1) and a long solidification time (#4*) from Table 3.3. There is some discrepancy between the two heat flux curves predicted by the finned LTR and CFD models for both of the cases. However, the trend for the heat fluxes match well. This implies that the finned LTR model also has a good ability to represent the heat flux dynamics during the entire solidification process. Thus it is found that the performance of the finned LTR model is acceptable and ready to be used for finned PCM system design and optimization.

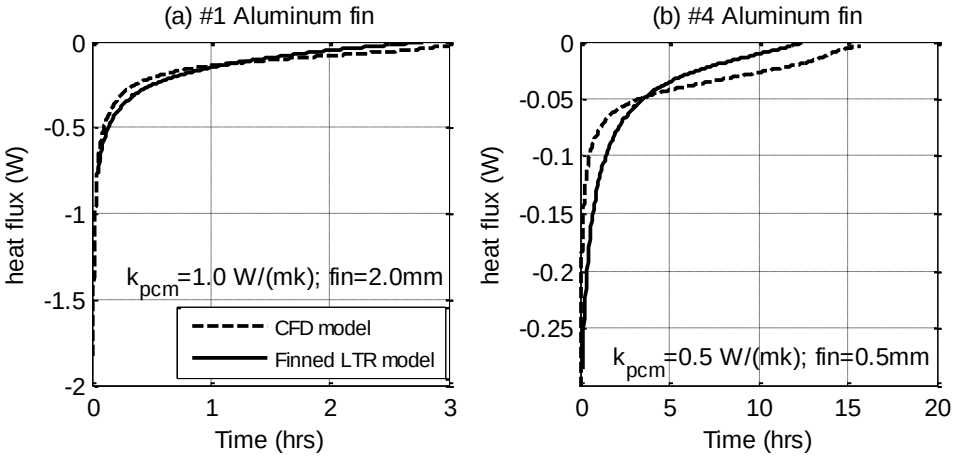

Figure 3.8 Heat flux comparisons between CFD and the finned LTR model

4 Optimal dimensions of a single unit of a HP-LTES system

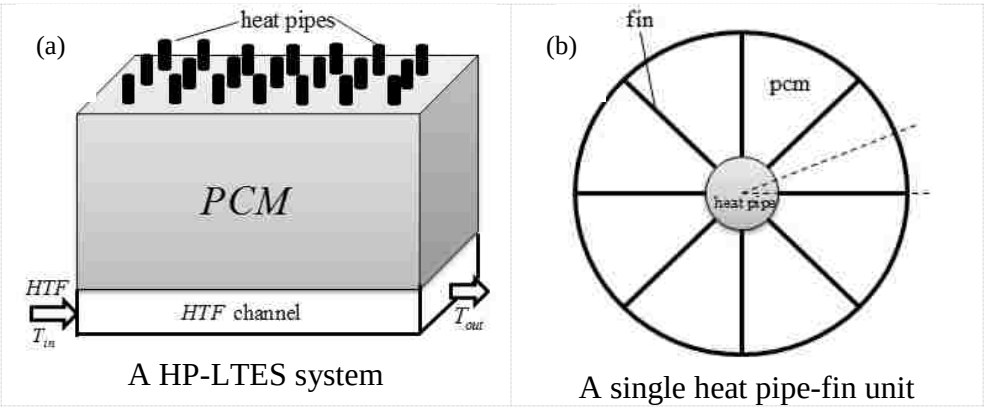

Figure 3.9 (a) Sketch of heat pipes embedded in a latent energy storage system and (b) representative analysis domain

For optimization purposes, we consider a latent thermal energy storage (HP-LTES) system with embedded heat pipes as shown in Figure 3.9 (a). Figure 3.9 (b) shows an idealization of a single HP unit with fins. Note that cylindrical analysis and radial symmetry is always chosen as a convenient analysis domain to reduce computational costs. In addition the shell-tube configuration is often a popular geometry for study. With the costs of manufacturing heat pipes (C_{hp}) and welding fins (C_{fin}) converted to dollars per kilogram ($/kg), the design problem of determining what proportions of heat pipe and fin material to use in the analysis domain is of interest. C_{hp}/C_{fin} is defined as the cost ratio. The objective is system cost minimization while ensuring that the system meets a given cooling time requirement. The detailed dimensions that need to be optimized are shown in Figure 3.6 in Section 2. Figure 3.6 represents a symmetrical sector cut in Figure 3.9 (b) denoted by the dotted lines.

The optimal design of a PCM-HP and fin structure is a typical PDE-constrained optimization problem. The PDEs describing the process need to be discretized in both time and space and thus the problem becomes a large scale optimization problem. In previous literature studies [33-37], optimization has often been based on parametric studies through simulations. Extensive simulation results are needed to find an optimal trend for the design parameters. The process is also computationally expensive and can only guarantee near-optimal solutions. The LTR model addresses these drawbacks by representing the nonlinear transient process with simple algebraic equations, thus reducing computational costs associated with the optimization problem. Formulation (4-1) is the optimal structure design problem where the finned LTR model is constrained to ensure the system will meet a given solidification time requirement. Note that the subscripts *PCM* and *fin* refer to material properties. The design variables are the same as those described in Figure 3.6 from Section 2.

$$\begin{aligned} \min_{r_1, r_2, w, \theta} \quad & g(r_1, r_2, w, \theta) \\ & t_{op} = f_{LTR}\left(r_1, r_2, w, \theta, \boldsymbol{PCM}, \boldsymbol{fin}\right) \\ & 2.0 \le \frac{r_2}{r_1} \le 9.0 \\ s.t. \quad & 1.27(\text{cm}) \le r_1 \le 5.08(\text{cm}) \\ & 10^{\circ} \le \theta \le 90^{\circ} \\ & 0.5(mm) \le w \le 3.0(mm) \end{aligned} \tag{4-1}$$

Given a certain cooling load and also the required time window $t_{op}$to solidify the PCM, the derivation of the cost equation, g, to minimize the equipment investment is presented in Appendix C. The variables $r_1, r_{2,} w, \theta$ specify the dimensions of a single HP-fin unit. The angle θ will determine the number of fins to be used. Formulation (4-1) is

a nonlinear constrained optimization problem and 'fmincon' (a gradient based method) and 'ga' (Genetic Algorithm (GA)) within the MATLAB optimization toolbox were employed to solve the problem [46, 47].

GA methods are supposed to find the global minimum, while Gradient Based Methods can only guarantee local minima. However, when applying these methods to the current problem, it was found that the gradient based method performed better than the GA approach as shown in Figure 3.10. Consequently, all of the following optimal solutions reported were founding by 'fmincon'. Table 3.4 shows the optimal dimensions that minimized system cost (g^*) while meeting the 8-hour solidification requirement. Each result was found for a given cost ratio C_{hp}/C_{fin}. In Table 3.4, g^* is the optimal value of the objective function g(x) whose derivation is presented in Appendix C. For a specific design case, after the optimal dimensions were obtained in Table 3.4, we further evaluated them by running CFD simulations in Fluent following the procedure outlined in Section 2. The predicted solidification times are shown in Figure 3.11. It can be seen that all the predicted solidification times are very close to 8 hours, which was set as the cooling time requirement in the optimization formulation. The error is within 0.5% in terms of the solidification fraction. The finned LTR model for the carbon-steel fin cases has errors that can reach more than 10% (see Figure 3.7) in terms of solidification time. This is mainly because of the "tailing" effect. The tailing effect refers to the situation when almost 70% of the PCM can be solidified within half of the total solidification time, and at the final stage, a small amount of PCM takes a relatively long time to solidify. Thus errors in terms of the solidification time are greatly diminished once it is represented by solid fraction. This phenomenon shows that despite the fact that the

finned LTR model can have solidification time errors around 20%, it still performs well for optimal PCM fin structure design applications.

Table 3.4 Optimal dimensions for different cost ratios

C_{hp}/C_{fin}	r_1(cm)	r_2(cm)	w (mm)	θ (°)	g*
0.7	1.27	5.3317	0.5	46.336	0.680
1.0	1.27	5.9406	0.5	33.909	0.814
2.0	1.27	6.9095	0.5	22.959	1.151
3.0	1.27	7.3218	0.5	18.281	1.430
4.0	1.27	7.7640	0.5	15.110	1.674

(Carbon-steel fin with k_{pcm} =0.5 W/(mK); t_{op}=8hrs)

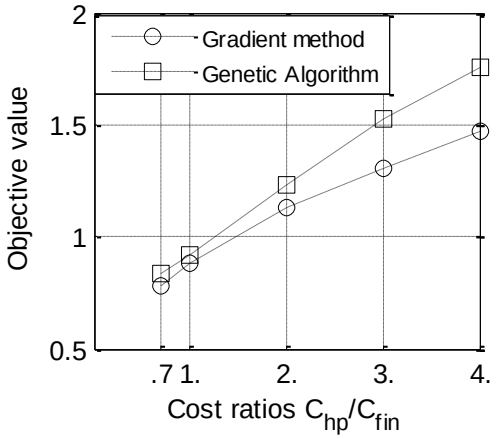

Figure 3.10 Optimal objective value

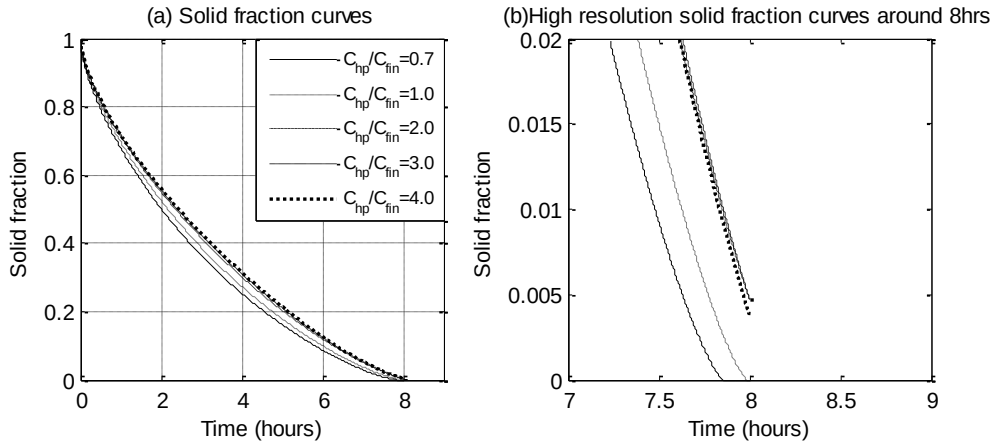

Figure 3.11 CFD verifications of the cases with optimal dimensions in Table 3.4

Figure 3.12 shows the optimal dimensions for 3 optimization cases with different discharging time (8/10hrs) and PCM conductivity (0.5 or 1.0 $\mathrm{W/mK}$). Results in Figure 3.12 (a) shows that when the system has 8-hours discharging time and the PCM conductivity is the lower 0.5 $\mathrm{W/(mK)}$ value, the system has the largest cost. Comparing the two cases with 10-hours discharging time but different PCM conductivities, it is seen that the lower PCM conductivity also increases cost. This follows intuition that the harder it is for the PCM to be solidified, the higher the cost of the system will be. Note that the optimal r_1 and w (Figure 3.12 (b) and (d)) are always at their lower bounds as specified in the constraints of the optimization formulation Eqns. (4.2). The optimal radius r_2 (Fig. 3.12 (b)) increases with increasing cost ratio and the optimal angle (Fig. 3.12 (c)) decreases with increasing cost ratio. This follows intuition that when manufacturing a heat pipe is more expensive than welding fins on it, then the distance between two heat pipes should be increased and more fins should be welded to achieve an optimal portion of HPs and fins to be used. Figure 3.13 shows the comparison between the aluminum-alloy HP-fin system and carbon-steel HP-fin system. When the cost ratio is less than 1.5, the system is made cheaper by using carbon steel. The aluminum fin system tends to have a larger radius for a single HP-fin unit. Figure 3.14 shows optimal results by setting different lower boundary values w_l for the thickness of the fin w in the constraint (Eqn.4-2). Figure 3.14 (a) shows that, overall, thinner fins will result in lower system cost. Figure 3.14 (d) shows the optimal fin thickness is always located at its lower limit. Figure 3.14 (c) shows that the optimal angle θ reaches 90° when the optimal fin thickness is 2mm and when the cost ratio is less than or equal to

1. Due to the symmetry of the geometry in Figure3.6, the number of fins welded on a heat pipe can be approximated by the angle θ,

$$N_f = \text{int}(\frac{360}{2\theta}), \tag{4-3}$$

where 'int' is used to get an integer number. Consequently 90° corresponds to an optimal fin number of 2. Moreover the constraint for angle θ in the optimization formulation (4-2) shows 90° is the limit of the angle θ. If the domain of the angle θ was extended, then the optimal angle could be larger than 90°. An angle larger than 90° may indicate no fins should be used. Thus when the fin thickness reaches a certain value (2mm for the current case study), a smaller number of fins or no fins should be used. The conclusion is that there is a thickness limit for the fins to be economically welded on a heat pipe and the economic value is reached when fins can be as thin as possible for the finned HP-PCM system.

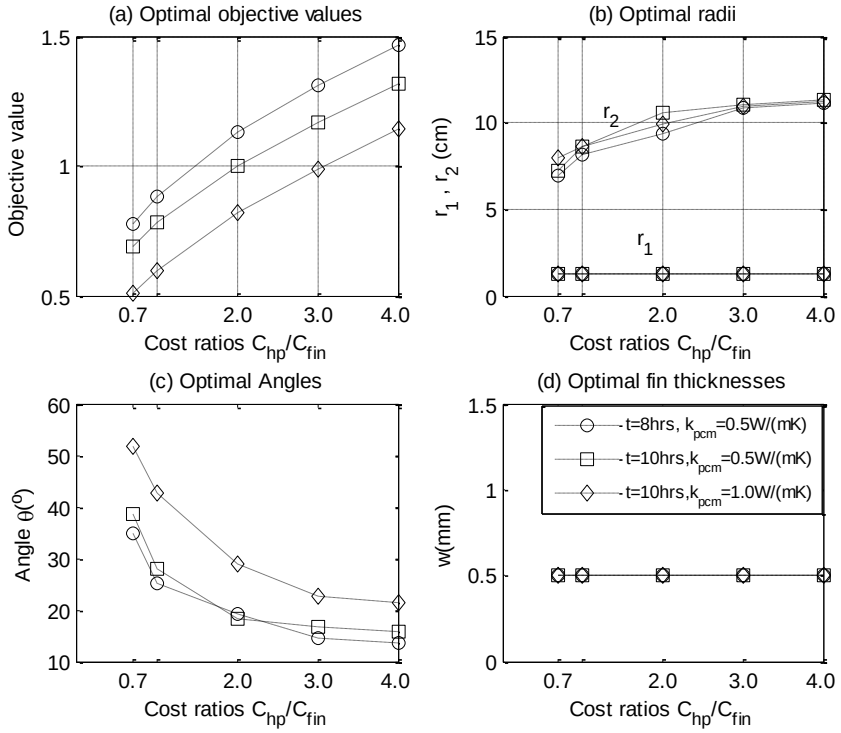

Figure 3.12 Optimal results for different operational times and PCM conductivities

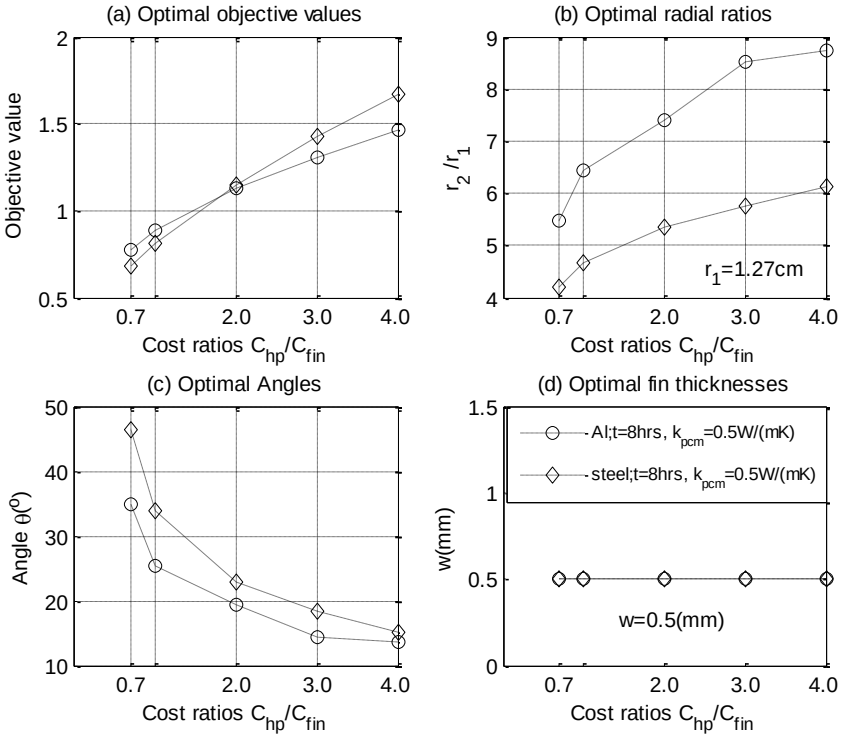

Figure 3.13 Optimal results comparison between Al 6061 fin and carbon-steel fin

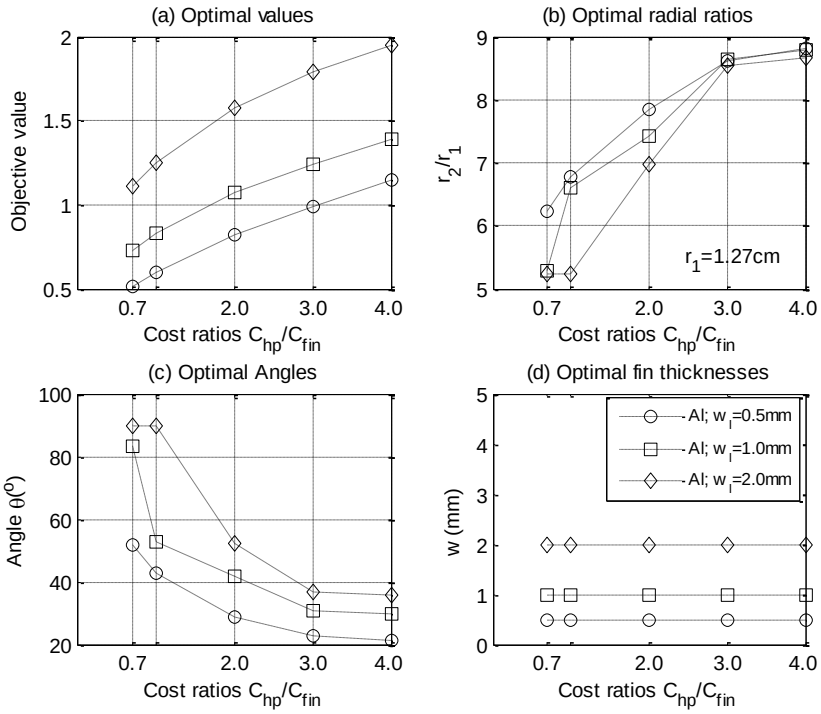

Figure 3.14 Effects of fin thickness on the optimal results

Assuming there is a 5 MW cooling load requirement for a system shown in Figure 3.9 and that the required discharging time is 8 hours, the dollars-per-kilowatt cost sensitivity with respect to the driving temperature difference is given in Figure 3.15. Each case presented in Figure 3.15 has a different driving temperature, and a unique optimal cost. The prices for the fins and PCM are listed in the figure and no additional manufacturing cost is considered, so the heat pipe and fin are assumed to have a cost ratio C_{hp}/C_{fin} equal to 1. It can be seen that by using carbon-steel as the construction material for the heat pipes and fins achieves slightly lower cost than by using Al 6061 for PCM with different conductivities and under different driving temperature differences. Thus corrosion behavior may finally determine the appropriate fin material to use. Corrosion between PCM ($CaCl_2 \cdot 6H_2O$) and fin containers was recently reported by Ren [48].

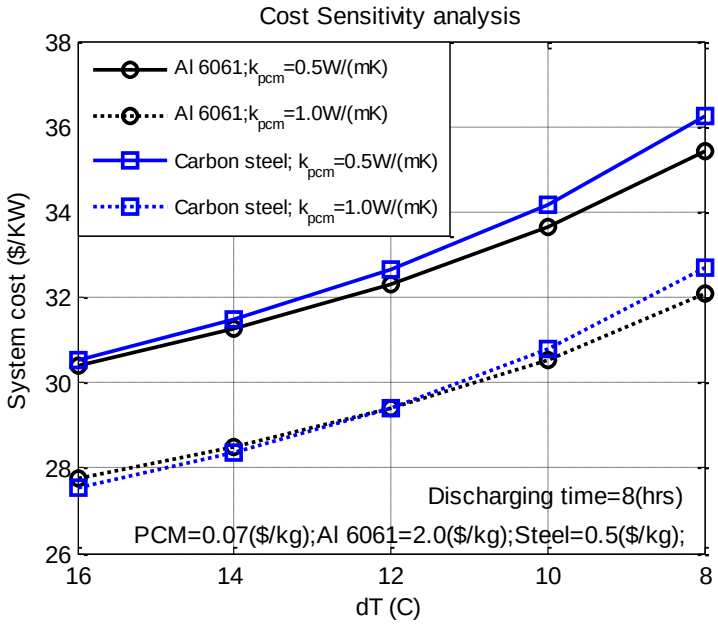

Figure 3.15 Cost sensitivity analyses with respect to driving temperature difference and fin materials

The following presents limitations and suggestions for further improvement of the models presented. The LTR models presented in sections 2 and 3 assume that there is no temperature drop in the heat pipe. When a temperature drop is considered, circular fins along the heat pipe can be introduced to account for the decreasing driving temperature difference. Thus the finned LTR model would have to be extended to 3D to allow for an optimal spacing of circular fins to be determined. When temperature rises are considered for the cooling HTF, the individual LTR modules can have different optimal dimensions along the flow direction of the cooling HTF channel. The finned LTR model could also be further developed to account for more complicated geometries, extending the applicability of the finned LTR model for optimal design.

5. Conclusions

An efficient Phase Change Material (PCM) solidification modeling approach for 2D cylindrical geometries is presented that accurately predicts the freezing time to solidify all the PCM in the domain. Based on verification with CFD analysis it is shown that this finned Layered Thermal Resistance (LTR) model also estimates heat flux quite accurately. Cost minimizations under operational requirement constraints are performed for optimal design determination. Using the finned LTR model, the optimal dimensions of a finned Heat Pipe (HP) unit structure of a Latent Thermal Energy Storage (LTES) can be efficiently determined. The optimal results imply that thinner fins result in lower system costs. In addition, there is a thickness limit for the fins to be economically welded on a heat pipe. In the current study, under the conditions that the manufacturing cost of the heat pipe is equal to or less than that of installing fins, the thickness limit of the fin is 2mm. Moreover, for a full scale HP-LTES system, under the assumptions that each HP has identical source temperature and there is no temperature drop along the length of the HP, the estimated system cost by using carbon-steel is slightly lower than by using Al 6061.

Acknowledgement

This research is sponsored by the ARPA-e ARID Program under Contract No. DE-AR0000582. Any opinions, findings, and conclusions or recommendations expressed in

this article are those of the authors and do not necessarily reflect the views of the Advanced Research Projects Agency-Energy.

References

[1] Rahdar, Mohammad Hoseini, Abolghasem Emamzadeh, and Abtin Ataei. A comparative study on PCM and ice thermal energy storage tank for air-conditioning systems in office buildings. Appl Therm Eng 2016; 96: 391-99.

[2] Ibrahim, Nasiru I., et al. Experimental testing of the performance of a solar absorption cooling system assisted with ice-storage for an office space. Energy Convers Manage 2017; 148: 1399-08.

[3] Fleming E, Wen S, Shi L, et al. Experimental and theoretical analysis of an aluminum foam enhanced phase change thermal storage unit. Int J Heat Mass Transfer 2015; 82: 273-81.

[4] Karaipekli A, Biçer A, Sarı A, et al. Thermal characteristics of expanded perlite/paraffin composite phase change material with enhanced thermal conductivity using carbon nanotubes. Energy Convers Manage 2017; 134: 373-81.

[5] Giro-Paloma J, Alkan C, Chimenos J M, et al. Comparison of Microencapsulated Phase Change Materials Prepared at Laboratory Containing the Same Core and Different Shell Material. Appl Sci 2017; 7(7): 723.

[6] Tehrani S S M, Taylor R A, Saberi P, et al. Design and feasibility of high temperature shell and tube latent heat thermal energy storage system for solar thermal power plants[J]. Renew Energy 2016; 96: 120-36.

[7] Riahi S, Saman W Y, Bruno F, et al. Comparative study of melting and solidification processes in different configurations of shell and tube high temperature latent heat storage system. Sol Energy 2017; 150: 363-74.

[8] Seddegh S, Wang X, Joybari M M, et al. Investigation of the effect of geometric and operating parameters on thermal behavior of vertical shell-and-tube latent heat energy storage systems. Energy 2017; 137: 69-82.

[9] Raud R, Cholette M E, Riahi S, et al. Design optimization method for tube and fin latent heat thermal energy storage systems. Energy 2017; 134:585-94.

[10] Lakhani S, Raul A, Saha S K. Dynamic Modelling of ORC-based Solar Thermal Power Plant Integrated with Multitube Shell and Tube Latent Heat Thermal Storage System[J]. Appl Therm Eng 2017; 123: 458-70.

[11] Gasia J, Diriken J, Bourke M, et al. Comparative study of the thermal performance of four different shell-and-tube heat exchangers used as latent heat thermal energy storage systems . Renew Energy 2017; 114: 934-44.

[12] Li Q, Tehrani S S M, Taylor R A. Techno-economic analysis of a concentrating solar collector with built-in shell and tube latent heat thermal energy storage. Energy 2017; 121: 220-37.

[13] A. Faghri, US Patent No. 4976308,1990.

[14] A. Faghri, US Patent No. 5000252,1991.

[15] B. Horbaniuc, G. Dumitrascu, A. Popescu. Mathematical models for the study of solidification within a longitudinally finned heat pipe latent thermal storage system. Energy Convers Manage 1999; 40: 1765-74.

[16] Z. Liu, Z. Wang, C. Ma. An experimental study on heat transfer characteristics of heat pipe heat exchanger with latent heat storage. Part I: charging only and discharging only modes. Energy Convers Manage 2006; 47: 944-66.

[17] H. Shabgard, T.L. Bergman, N. Sharifi, A. Faghri. High temperature latent heat thermal energy storage using heat pipes. Int J Heat Mass Transfer 2010; 53: 2979-88.

[18] Hamidreza Shabgard, Christopher W. Robak, Theodore L. Bergman, Amir Faghri. Heat transfer and exergy analysis of cascaded latent heat storage with gravity-assisted heat pipes for concentrating solar power applications. Sol Energy 2012; 86: 816-30.

[19] Christopher W. Robak, Theodore L. Bergman, Amir Faghri. Enhancement of latent heat energy storage using embedded heat pipes. Int J Heat Mass Transfer 2011; 54 :3476-84.

[20] K. Nithyanandam, R. Pitchumani. Analysis and optimization of a latent thermal energy storage system with embedded heat pipes. Int J Heat Mass Transfer 2011; 54: 4596-610.

[21] K. Nithyanandam, R. Pitchumani. Computational studies on a latent thermal energy storage system with integral heat pipes for concentrating solar power. Appl Energy 2013; 103: 400-15.

[22] K. Nithyanandam, R. Pitchumani. Design of a latent thermal energy storage system with embedded heat pipes. Appl Energy 2014; 126: 266-80.

[23] Nourouddin Sharifi, Amir Faghri, Theodore L. Bergman, Charles E. Andraka. Simulation of heat pipe-assisted latent heat thermal energy storage with simultaneous charging and discharging. Int J Heat Mass Transfer 2015; 80: 170-79.

[24] M.S. Naghavi, K.S. Ong, I.A. Badruddin, Mohammad Mehrali, H.S.C. Metselaar. Thermal performance of a compact design heat pipe solar collector with latent heat storage in charging/discharging modes. Energy 2017; 127:101-115.

[25] Saeed Tiari, Songgang Qiu, Mahboobe Mahdavi. Numerical study of finned heat pipe-assisted thermal energy storage system with high temperature phase change material. Energy Convers Manage 2015; 89: 833-42.

[26] Saeed Tiari, Songgang Qiu. Three-dimensional simulation of high temperature latent heat thermal energy storage system assisted by finned heat pipes. Energy Convers Manage 2015; 105: 260-71.

[27] Saeed Tiari, Songgang Qiu, Mahboobe Mahdavi. Discharging process of a finned heat pipe-assisted thermal energy storage system with high temperature phase change material. Energy Convers Manage 2016; 118: 426-37.

[28] Almsater S, Saman W, Bruno F. Performance enhancement of high temperature latent heat thermal storage systems using heat pipes with and without fins for concentrating solar thermal power plants. Renew Energy 2016; 89: 36-50.

[29] Veelken H, Schmitz G. Optimization of a composite latent heat storage (CLHS) with non-uniform heat fluxes using a genetic algorithm. Int J Heat Mass Transfer 2016; 101: 600-7.

[30] Pizzolato A, Sharma A, Maute K, et al. Topology optimization for heat transfer enhancement in Latent Heat Thermal Energy Storage. Int J Heat Mass Transfer 2017; 113: 875-88.

[31] Lohrasbi S, Gorji-Bandpy M, Ganji D D. Thermal penetration depth enhancement in latent heat thermal energy storage system in the presence of heat pipe based on both charging and discharging processes. Energy Convers Manage 2017; 148: 646-67.

[32] Sina Lohrasbi, Seyed Ziaedin Miry, Mofid Gorji-Bandpy. Performance enhancement of finned heat pipe assisted latent heat thermal energy storage system. Int J Hydrogen Energy 2017; 42: 6526-46.

[33] Xie J, Yuan C. Parametric study of ice thermal storage system with thin layer ring by Taguchi method. Appl Therm Eng 2016 ; 98: 246-55.

[34] Zhao R, Gu J, Liu J. Optimization of a phase change material based internal cooling system for cylindrical Li-ion battery pack and a hybrid cooling design. Energy 2017;135:811-822.

[35] Shinde A, Arpit S, Pramod K M, et al. Heat Transfer Characterization and Optimization of Latent Heat Thermal Storage System Using Fins for Medium Temperature Solar Applications. J Sol Energy Eng 2017; 139(3): 031003.

[36] Song H, Zhang W, Li Y, et al. Exergy analysis and parameter optimization of heat pipe receiver with integrated latent heat thermal energy storage for space station in charging process. Appl Therm Eng 2017; 119: 304-11.

[37] Saffari M, de Gracia A, Fernández C, et al. Simulation-based optimization of PCM melting temperature to improve the energy performance in buildings. Appl Energy 2017; 202: 420-34.

[38] Pan C, Hoenig S, Chen C H, et al. Efficient modeling of phase change material solidification with multidimensional fins. Int J Heat Mass Transfer 2017; 115: 897-909.

[39] Ismail KAR, Henriquez JR. Solidification of PCM inside a spherical capsule. Energy Convers Manage 2000; 41: 173-87.

[40] Helm M, Keil C, Hiebler S, Mehling H, Schweigler C. Solar heating and cooling system with absorption chiller and low temperature latent heat storage-energetic performance and operational experience. Int J Refrig 2009; 32:596-606.

[41] https://www.sharcnet.ca/Software/Fluent6/html/ug/node973.htm

[42] Brent AD. Voller VR, Reid KJ. Enthalpy-porosity technique for modeling convection-diffusion phase change: application to the melting of a pure metal. Num Heat Transfer Part B 1988; 13: 297-318.

[43] Jegadheeswaran S, Pohekar S D. Performance enhancement in latent heat thermal storage system: a review. Renew Sustain Energy Rev 2009; 13(9): 2225-44.

[44] Ismail KAR, Alves CLF, Modesto MS. Numerical and experimental study on the solidification of PCM around a vertical axially finned isothermal cylinder. Appl Therm Eng 2001; 21(1): 53-77.

[45] Smola, A.J., Schölkopf, B. A tutorial on support vector regression. Stat Comput 2004; 14: 199.

[46] https://www.mathworks.com/help/optim/ug/fmincon.html

[47] https://www.mathworks.com/help/gads/ga.html

[48] Ren S J, Charles J, Wang X C, et al. Corrosion testing of metals in contact with calcium chloride hexahydrate used for thermal energy storage. Mater Corros DOI: 10.1002/maco.201709432.

[49] Pirompugd W, Wongwises S. Partially wet fin efficiency for the longitudinal fins of rectangular, triangular, concave parabolic, and convex parabolic profiles. Journal of the Franklin Institute, 2013, 350(6): 1424-1442.

[50] Mosayebidorcheh S, Rahimi-Gorji M, Ganji D D, et al. Transient thermal behavior of radial fins of rectangular, triangular and hyperbolic profiles with temperature-dependent properties using DTM-FDM. Journal of Central South University, 2017, 24(3): 675-682.

[51] Rahimi-Gorji M, Ghajar M, Kakaee A H, et al. Modeling of the air conditions effects on the power and fuel consumption of the SI engine using neural networks and regression. Journal of the Brazilian Society of Mechanical Sciences and Engineering, 2017, 39(2): 375-384.

[52] Rahimi-Gorji M, Pourmehran O, Hatami M, et al. Statistical optimization of microchannel heat sink (MCHS) geometry cooled by different nanofluids using RSM analysis. The European Physical Journal Plus, 2015, 130(2): 22.

[53] Pourmehran O, Rahimi-Gorji M, Hatami M, et al. Numerical optimization of microchannel heat sink (MCHS) performance cooled by KKL based nanofluids in saturated porous medium. Journal of the Taiwan Institute of Chemical Engineers, 2015, 55: 49-68.

Appendix

A. Discretized $D_r(i)$ and L(i)

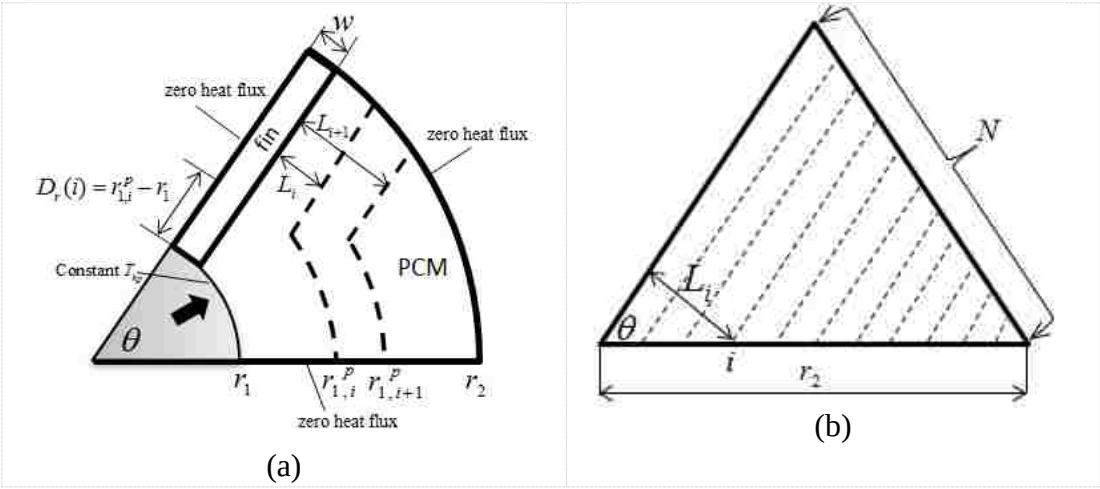

Figure 3.16 Schematic of annular sector for analysis domain

The discretization strategy is that each new unsolidified PCM area (the dotted line) maintains the same annulus sector as the original shape of the PCM. This strategy allows the PCM to solidify according to a shrinking behavior. So for each new annulus sector,$\theta = constant$, $r_{2i}/r_{1i} = constant$; and for all the shrinking annulus sectors, r_{2i} is always located at its original position while the location for each r_{1i} is $r_{1i}^p = r_2 - (r_{2i} - r_{1i})$. Thus the melting front distance r can be calculated as $D_r(i) = r_{1i}^p - r_1$. L is an arc length but is approximated here. As shown in Figure 3.16 (b), assuming there are N

shrinking annulus sectors (including the original one) simply represented by a series of triangles, then $L_i = Asin(\theta)\frac{ir_2}{N-1}$, where is a geometric factor to account for the use of a line segment to represent an arc. It is found that $A = \pi/2$ gives good agreement for the finned LTR model.

B. Fin efficiency calculation

The fin extended from the heat pipe is approximated by a 1D conduction bar. As shown in Figure 3.17, it has a constant temperature at one end and heat flux boundary condition on the PCM side; the other end and side have zero heat flux. Based on an energy balance of the bar, the fin efficiency is:

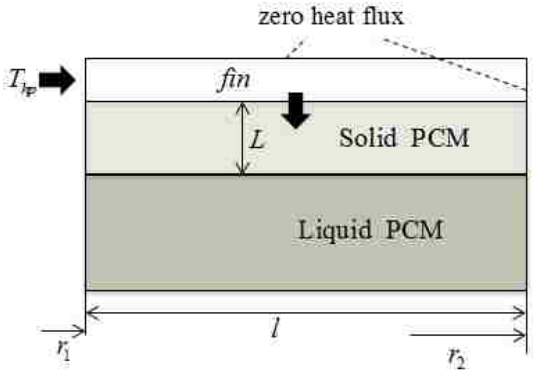

Figure 3.17 Geometry and boundary conditions for the 1D bar efficiency calculation

$$Q_x = Q_{x+\Delta x} + Q_c, \quad \Delta x \to 0 \Rightarrow Q_{x+\Delta x} = Q_x + \frac{dQ_x}{dx}\Delta x, \quad \frac{dQ_x}{dx}\Delta x + Q_c = 0 \qquad \text{(B.1)}$$

$$Q_x = -k_{fin} A \frac{dT}{dx}, \qquad Q_c = hS(T - T_{pcm}) \qquad \text{(B.2)}$$

$$A = cw, \qquad S = c\Delta x, \qquad h = \frac{k_{pcm}}{\boldsymbol{L}} \quad \text{(c: Thickness of the fin)} \qquad \text{(B.3)}$$

$$\frac{d}{dx}\left(-k_{fin} A \frac{dT}{dx}\right) + hS(T - T_{pcm}) = 0, \quad \text{assuming } \theta = T(x) - T_{pcm} \qquad \text{(B.4)}$$

$$\frac{d^2\theta}{dx^2} - \frac{k_{pcm}}{k_{fin} w d_m}\theta = 0, \qquad \theta\big|_{x=r_1} = T_{hp} - T_{pcm}, \qquad \left.\frac{\partial\theta}{\partial x}\right|_{x=r_2} = 0 \qquad \text{(B.5)}$$

$$\xi^2 = \frac{k_{pcm}}{k_{fin} w \boldsymbol{L}}, \quad l = r_2 - r_1 \qquad \text{(B.6)}$$

$$\theta = \left(T_{hp} - T_m\right)\left(\cosh(\xi x) - \tanh(\xi l)\sinh(\xi x)\right) \qquad \text{(B.7)}$$

$$\eta = \frac{T(x) - T_m}{T_w - T_m} = \left(\cosh(\xi x) - \tanh(\xi l)\sinh(\xi x)\right) \qquad \text{(B.8)}$$

where *L* is the melting front distance away from the fin calculated in Appendix A. The heat transfer coefficient at the PCM side is assumed to be the conductivity of the PCM divided by the melting front distance, h $= k_{pcm}/L$. As *L* will affect the fin efficiency, a reasonable layered discretization strategy to calculate *L* is important for the successful performance of the tuned LTR model coupled with fins. However for pure PCM domain modeling, *L* is not that important, because the tuning surface will correct for the effect of *L*.

C. Cost Function of a finned HP-LTES system

There are two main assumptions to derive the cost function of a full scale HP-LTES system shown in Figure 9(a). One is that there is negligible temperature drop along the length of a heat pipe, so that the system can be modeled by a 2D geometry. The other one

is that each heat pipe has the same temperature boundary conditions, so that all of the HP-fin units are identical.

$$V_{pcm} = \frac{Gt_{op}}{L_{pcm}\rho_{pcm}} \tag{C.1}$$

$$V_{unit\,pcm} = \pi(r_2^2 - r_1^2)H_p - N_f w_f (r_2 - r_1)H_p \tag{C.2}$$

$$N_p = \text{int}\left(\frac{V_{pcm}}{V_{unit\,pcm}}\right) \tag{C.3}$$

$$V_{hp} = N_p\left[\pi(r_1^2 - r_0^2)H_p\right] \tag{C.4}$$

$$V_{fin} = N_p N_f w(r_2 - r_1)H_p \tag{C.5}$$

$$C = C_{pcm}M_{pcm} + C_{hp}M_{hp} + C_f M_f$$

$$= C_{pcm}\frac{Gt_{op}}{L_{pcm}} + C_{hp}N_p\rho_{hp}\left[\pi(r_1^2 - r_0^2)H_p\right] + C_f N_p \rho_f N_f w(r_2 - r_1)H_p$$

$$= C_{pcm}\frac{Gt_{op}}{L_{pcm}} + \text{int}\left(\frac{\frac{Gt_{op}}{L_{pcm}\rho_{pcm}}}{\pi(r_2^2 - r_1^2)H_p - N_f w_f (r_2 - r_1)H_p}\right)\left\{C_{hp}\rho_{hp}\left[\pi(r_1^2 - r_0^2)H_p\right] + C_f \rho_f N_f w(r_2 - r_1)H_p\right\}$$

$$= C_{pcm}\frac{Gt_{op}}{L_{pcm}} + \text{int}\left(\frac{Gt_{op}}{L_{pcm}\rho_{pcm}[\pi(r_2^2 - r_1^2) - N_f w_f (r_2 - r_1)]}\right)\left\{C_{hp}\rho_{hp}\pi(r_1^2 - r_0^2) + C_f \rho_f N_f w(r_2 - r_1)\right\} \tag{C.6}$$

In Eqn. (C.6) the integer value by the operation int() is approximated by its real value:

$$\approx C_{pcm}\frac{Gt_{op}}{L_{pcm}} + \frac{Gt_{op}[C_{hp}\rho_{hp}\pi(r_1^2 - r_0^2) + C_f \rho_f N_f w(r_2 - r_1)]}{L_{pcm}\rho_{pcm}[\pi(r_2^2 - r_1^2) - N_f w(r_2 - r_1)]}$$

$$= \frac{C_{pcm}Gt_{op}}{L_{pcm}}\left(1 + \frac{C_{hp}\rho_{hp}\pi(r_1^2 - r_0^2) + C_f\rho_f N_f w(r_2 - r_1)}{C_{pcm}\rho_{pcm}[\pi(r_2^2 - r_1^2) - N_f w(r_2 - r_1)]}\right) \quad \text{(C.7)}$$

In Eqn. (C.7) $N_f = int\left(\frac{2\pi}{2\theta}\right)$, and it is approximated as $N_f \approx \frac{\pi}{\theta}$

$$\approx \frac{C_{pcm}Gt_{op}}{L_{pcm}}\left(1 + \frac{C_{hp}\rho_{hp}\pi(r_1^2 - r_0^2) + C_f\rho_f \frac{\pi}{\theta} w(r_2 - r_1)}{C_{pcm}\rho_{pcm}\left[\pi(r_2^2 - r_1^2) - \frac{\pi}{\theta} w(r_2 - r_1)\right]}\right)$$

$$= \frac{C_{pcm}Gt_{op}}{L_{pcm}}\left(1 + \frac{C_{hp}\rho_{hp}\theta(r_1^2 - r_0^2) + C_f\rho_f w(r_2 - r_1)}{C_{pcm}\rho_{pcm}[\theta(r_2^2 - r_1^2) - w(r_2 - r_1)]}\right) \quad \text{(C.8)}$$

$$\mathrm{g}(r_1, r_2, w, \theta) = \frac{C_{hp}\rho_{hp}\theta(r_1^2 - r_0^2) + C_f\rho_f w(r_2 - r_1)}{C_{pcm}\rho_{pcm}[\theta(r_2^2 - r_1^2) - w(r_2 - r_1)]} \quad \text{(C.9)}$$

In the derivation of the cost equation $\mathrm{g}(r_1, r_2, w, \theta)$, in Eqns. (C.7) and (C.8) an integer value is approximated by a real value in order to simplify the final objective expression. This simplification has little impact on the optimal solutions. In Eqn. (C.8), only the second term is dependent on the design variables(r_1, r_2, w, θ), so (C.9) becomes the final cost equation to be used in the optimization formulation, which is the cost ratio between the heat pipe with fin and PCM material. A smaller ratio value means smaller overall system cost.

Chapter 4

Cost estimation and sensitivity analysis of a latent thermal energy storage system for supplementary cooling of air cooled condensers

(Pan C., Vermaak N., Romero C., Neti S., et al. Cost estimation and sensitivity analysis of a latent thermal energy storage system for supplementary cooling of air cooled condensers. *Applied Energy*, 2018, (224): 52-68.)

Cost estimation and sensitivity analysis of a latent thermal energy storage system for supplementary cooling of air cooled condensers

Chunjian Pan[1], Natasha Vermaak[1], Carlos Romero[1], Sudhakar Neti[1]
Sean Hoenig [2], Chien-Hua Chen[2], Richard Bonner III[2]

[1]Energy Research Center, Lehigh University, Bethlehem, PA 18015, USA
[2]Advanced Cooling Technologies, Inc., Lancaster, PA 17601, USA

Abstract

As a booming economy drives the need for more electricity, demands on freshwater for thermoelectric power generation also grow. Facing the limited freshwater resources, alternative dry cooling technologies that reduce water consumption are becoming more prevalent. However, the performance of air cooled condensers (ACCs) is seriously deteriorated at ambient temperature. To address this challenge, a novel application of a Phase Change Material (PCM) based cooling system for supplementary cooling of ACCs is proposed. In order to evaluate the system cost, a solidification modeling approach called a Layered Thermal Resistance (LTR) model is extended to 3D in cylindrical coordinates for the first time. The LTR model efficiently estimates the behavior of a finned heat pipe module for the PCM-based cooling system. In the present work, a new nonlinear optimization problem is formulated, based on the LTR model, to estimate system cost and conduct sensitivity analysis. Overall, it is found that the material cost of the finned heat pipe-assisted PCM tank is around 30 $/kW for a 10-hour solidification time requirement, which is a promising cost for the system to be accepted in the market. Based on the sensitivity analyses, it is found that the latent energy of the PCM has first-order impact on the system cost.

Key words: Air cooled condensers, latent energy storage, efficient PCM simulation, finned heat pipe embedded PCM, cost optimal design

Nomenclature

A	Geometric factor
C	Cost of materials
C_p	Heat capacity of PCM
dT	Driving temperature difference
D, E, H	Locations of 3D discrete solid fronts
G	Cooling load target
h	Height of the longitudinal fin between two circular fins
HP	Height of a single heat pipe
k	Conductivity
K	Number of discrete layers
L	Latent energy
M	Material mass
N	Quantity
q	Heat flux
r_0	Inner radius of the heat pipe
r_1	Outer radius of the heat pipe
r_2	Radius of the longitudinal fin welded on the heat pipe
R	Thermal resistance
S	Heat transfer area (Shrinking liquid-solid interface)
t	Solidification time
T	Temperature
u	Heat transfer coefficient within the PCM
ΔV	Layered PCM volumes
V	Total material volume
w	Fin or heat pipe thickness
Greek symbols	
α	Resistance tuning parameter
θ	Half angle between two neighboring longitudinal fins
ρ	Density

ε	Prediction discrepancy
γ	PCM liquid fraction
η	Fin efficiency
σ	Thickness out of the paper
Subscript	
1,2,3	Three heat flow paths within a 3D bulk PCM
c	Circular fin
cell	A discrete element cell
CFD	Computational Fluid Dynamics model
f	Both longitudinal and circular fins
hp	Heat pipe
hp_pcm	PCM volume of a single heat pipe
l	Longitudinal fin
$lower$	Lower PCM melting temperature
LTR	Layered thermal resistance model
m	PCM melting temperature
op	Required solidification time
pcm	Phase change material
s	Bulk PCM solidification time
$total$	Total thermal resistance
$upper$	Upper PCM melting temperature
Superscript	
i	Discrete index
$*$	Thermal resistance incorporated with fin and fin efficiency

1 Introduction

Phase Change Materials (PCMs) have received increasing attention in the application of thermal energy storage systems due to their high-energy densities [1]. There are many research studies focused on using PCMs for cooling applications. Among them, popular applications include passive cooling for building envelopes using lower temperature PCMs [2-3]. A comprehensive review of PCM based cooling technologies that enhance the efficiency of photovoltaic power systems can be found in Chandel et. al [4]. Zhao [5] studied a PCM based internal cooling system for a cylindrical Li-ion battery pack. Arshad [6] investigated the thermal performance of PCM-based pin-finned heat sinks for electronic cooling. Ibrahim [7] experimentally tested a solar absorption cooling system assisted with ice storage. Ice storage for air conditioning in buildings has already been successfully implemented in several applications. In addition to electricity bill savings, cold energy produced and stored at lower costs during off-peak hours of the day can reduce the burden to produce enough electricity during high demand hours [8]. Researchers are continually working on further optimization of the ice storage-based air conditioning systems [9-10]. Luo [11] further reported that a large-scale ice-thermal storage system can be used as a smart load for fast voltage control and demand-side management in power systems with intermittent renewable power.

In this paper, an innovative application of a PCM-based cooling system (see Fig.4.1) for supplemental cooling/cool storage of air cooled condensers (ACCs) in power plants is proposed for the first time. The system does not involve the dissipation of water to the atmosphere and enables power plants to maintain their high efficiency even in hot seasons. As a booming economy drives the need for more electricity, demands on

freshwater for thermoelectric power generation also grow. However, freshwater is limited and is becoming more valuable for our growing global population. This constraint will affect future electricity generation. Thus, alternative dry-cooling technologies that reduce water consumption are needed. However, the performance of air-cooled condensers (ACC's) is very sensitive to wind conditions and is not optimal at ambient temperatures [12]. That is ACCs become less effective when ambient temperature is higher (see Fig. 4.2). Consequently, the existing ACCs may fail to condense all the steam (direct) or sufficiently cool the process coolant water (indirect).

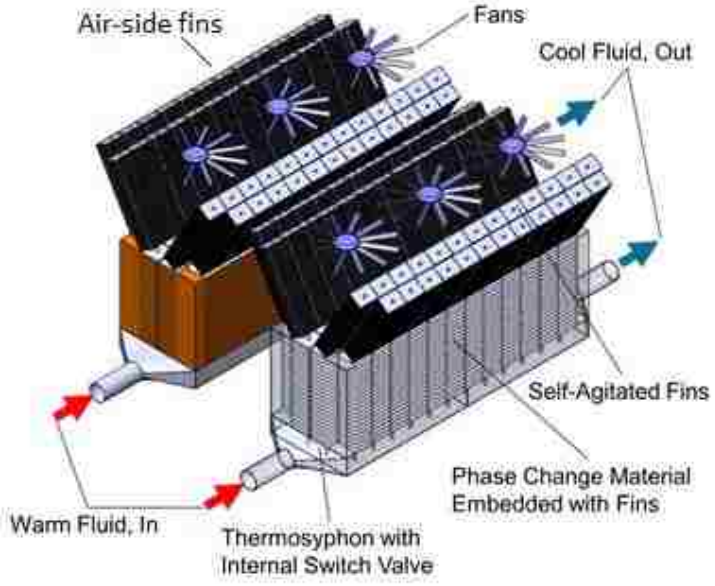

Figure 4.1 The concept design for the PCM cooling units

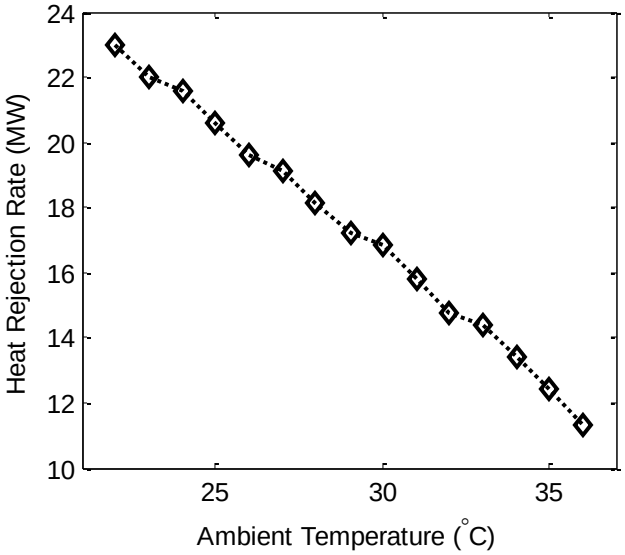

Figure 4.2 ACC heat rejection under fluctuations of ambient temperatures [12]

To address these challenges confronted by ACCs, a novel cooling concept by incorporating the use of PCMs is proposed in this paper for the purpose of supplementary cooling when the ACC's performance is deteriorated. The ACC's performance is most affected during hot summer daytimes. During the night, temperatures can be more than 10 ℃ lower than daytime, especially in relatively dry regions. Thus the idea is to turn the night-time lower temperature into cooling energy that can be used for cooling during daytime. The proposed approach is to use a PCM reservoir to store the cooling resource (freezing) during night-time and to provide cooling energy (melting) during the daytime. A suitable PCM candidate under investigation is $CaCl_2 \cdot 6H_2O$, which has a melting temperature that is relevant for the application of interest and also has a low cost. In addition $CaCl_2 \cdot 6H_2O$ is nonflammable and nontoxic. The long-term reversible phase change behavior of this PCM that can be achieved by small compositional changes was reported by Carlsson [13]. A primary corrosion study about this PCM with container and fin materials has been reported by Ren [14].

Fig.4.3 shows the schematic of incorporating the proposed PCM based supplementary cooling system in a power generation loop. The number of individual ACC cells required for a given size plant is a compromise between the capital cost and efficiency penalty. With effective cool storage and the shifting of energy rejection to more amenable lower ambient temperatures at night-time, the number of ACC cells required can be reduced without sacrificing the efficiency of a power plant. While the use of cool storage reduces the number of ACC cells required and their associated capital cost, the total system cost must not exceed the cost of the replaced ACC cells that provide equivalent cooling capacity. For typical conditions, the current ACC capital cost is approximated as 50 $/kW. However, on extremely hot days, the cooling capacity of each ACC cell is significantly reduced (i.e. from 12 MW to 4 MW). To accommodate the heat load with reduced cooling capacity, more ACC cells are required, resulting in a cost increase to about $150 /kW plus the significant increase in footprint and operational and maintenance costs. Thus, to be able to market this PCM-based cooling system, the overall design goal of the capital cost of the system is set to be less than 150 $/kW.

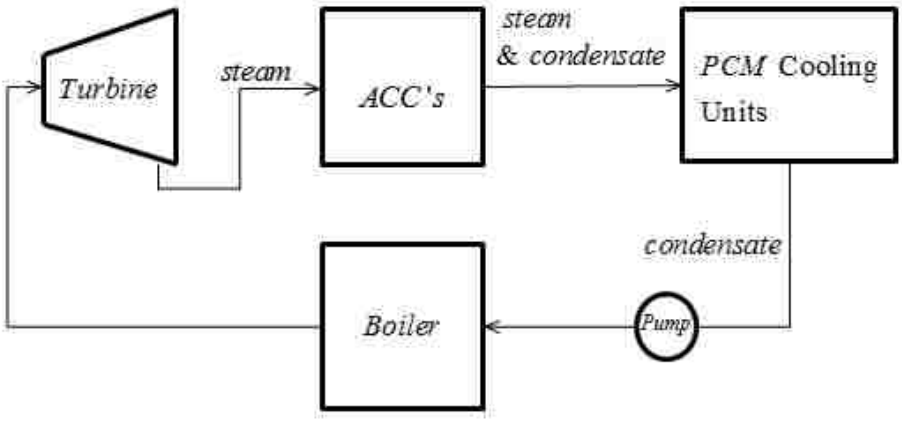

Figure 4.3 Schematic of the incorporation of the PCM based supplementary cooling system in the power generation loop

Fig.4.1 shows the concept design of the PCM based cooling units. A more detailed structure of the cooling unit is presented in the next section. Modeling plays an essential role in designing PCM cooling systems in the initial stages. To evaluate the economic feasibility of this solution, cost estimation is the first vital step. The low conductivity of PCM materials is a major barrier for many practical applications. In order to freeze the PCM during the night with limited available driving temperature differences, heat pipes and fin structures have to be employed. The fins and heat pipes are much more expensive than the PCM. The system cost is dictated by the optimal usage of these features.

There is limited literature presenting the cost analysis of a PCM-based thermal energy storage system. Most studies published are all within the field of the concentrating solar power (CSP) plant [15-19]. Robak [15] employed a thermal resistance network model to study a heat pipe assisted latent thermal energy storage system (LTESS) for CSP, which was reported to reduce the capital cost by 15% compared to that of a CSP with a sensible thermal storage system. The finned tube, which is an essential component of the latent heat storage module, was reported as an important evaluation parameter to minimize the investment cost in Hübner's study [17].

To estimate the cost of the proposed PCM-based cooling system, the optimal structure of the embedded finned heat pipes is the key determining factor. Due to the transient nonlinear nature of the PCM solidification process, the optimal design of the embedded finned heat pipes is a typical partial differential equation (PDE)-constrained nonlinear optimization problem. Previous optimizations of such systems have often been based on parametric studies [20-22], which are usually computationally expensive. Thus a novel modeling method called the Layered Thermal Resistance (LTR) model was

recently developed by Pan et al [23-24]. In this paper, the LTR model is extended, for the first time, to a 3D cylindrical geometry to support the efficient optimization of a finned heat pipe system. With a 3D model, both the circular fins and longitudinal fins attached to a heat pipe can be considered. The LTR model represents the nonlinear transient PCM solidification process with simple algebraic equations, thus reducing computational costs associated with the optimization problem. By employing the LTR modeling technique, sensitivity analyses of different parameters on the overall system cost can be efficiently evaluated, providing useful guidelines for design.

The content of this paper is organized as follows. In section 2, the nonlinear optimization formulation for optimal design and cost estimation is introduced. In section 3, the LTR model for a 3D cylindrical geometry is developed. Section 4 presents the optimal results and the sensitivity analyses of the parameters of interest. Section 5 summarizes the conclusions.

2. Cost minimization for a finned heat pipe assisted latent thermal energy storage system

This section presents the nonlinear programming formulation of cost minimization design for a finned heat pipe-assisted LTESS. The solidification process is more difficult to complete than the melting process, as it is conduction controlled [25]. For this reason, convection is not considered. Many researchers have proposed to use finned heat pipes to enhance the heat transfer performance of a LTESS [26-29]. In this paper, the finned heat pipe embedded LTESS under study is shown in Fig. 4.4. The air-side fins which

appear in Fig. 4.1 will be studied in future work. The focus of this paper is to solidify the PCM during the night, so an assumption being made is that the air side fins provide each heat pipe with the same temperature boundaries at the top of the heat pipe (Fig. 4.4). Also to allow PCM expansion during melting, there is a reserved air gap between the bottom of a plate fin and the PCM under the plate fin (Fig. 4.4). Due to the relatively very low conductivity of air, it is assumed that there is no heat transfer at the bottom of the plate fin. In order to employ radial symmetry to simplify the analysis and reduce computational cost, it is assumed that a single finned heat pipe shown in Fig. 4.5 (a) is the assembling unit for the whole LTESS. Thus the horizontal plate fins are represented by circular fins attached to a heat pipe. It is also assumed that there is negligible temperature drop along the length of the heat pipe so that the model domain can be further simplified to focus on a single circular fin (from a circular fin to the air gap). Typically there is a small temperature gradient along the length of a heat pipe and neglecting this small temperature gradient is appropriate for the overall optimal design and cost analysis. Also due to mirror symmetry, only half of the section between two neighboring longitudinal fins needs to be modeled. Thus Fig. 4.5 (b) shows the resulting model PCM domain of interest, which is defined at the extremities by longitudinal and circular fins and the air gap. More detailed dimensions of the modeling domain are shown in Fig. 4.6.

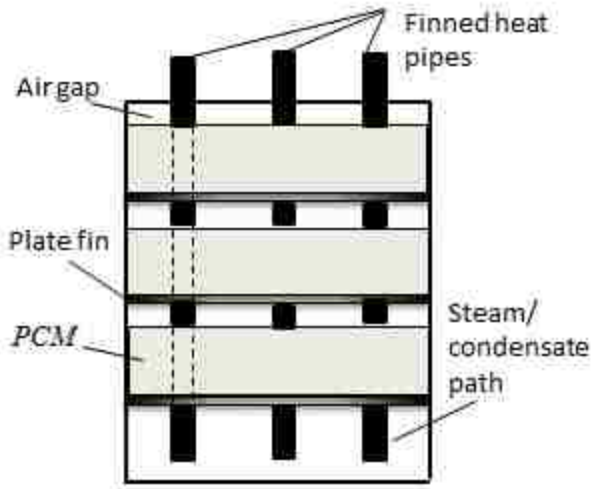

Figure 4.4 Schematic of a heat pipe-assisted LTESS (front view)

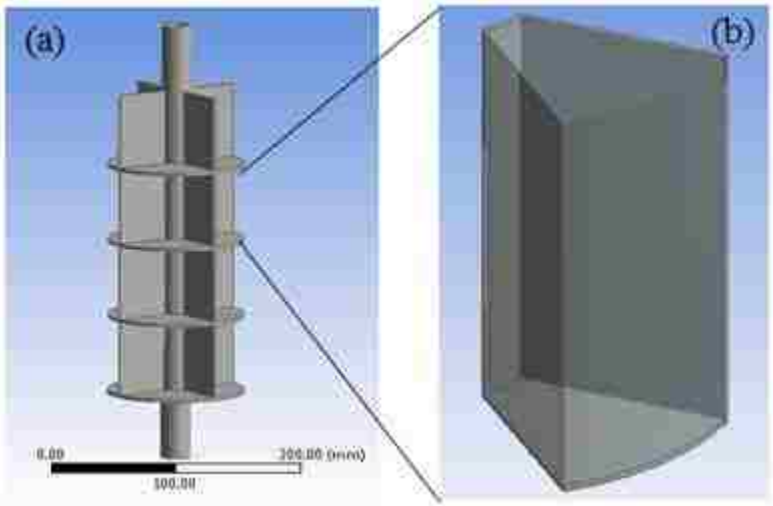

Figure 4.5 (a) Schematic of a 3D finned heat pipe; (b) A symmetry section of a PCM cell

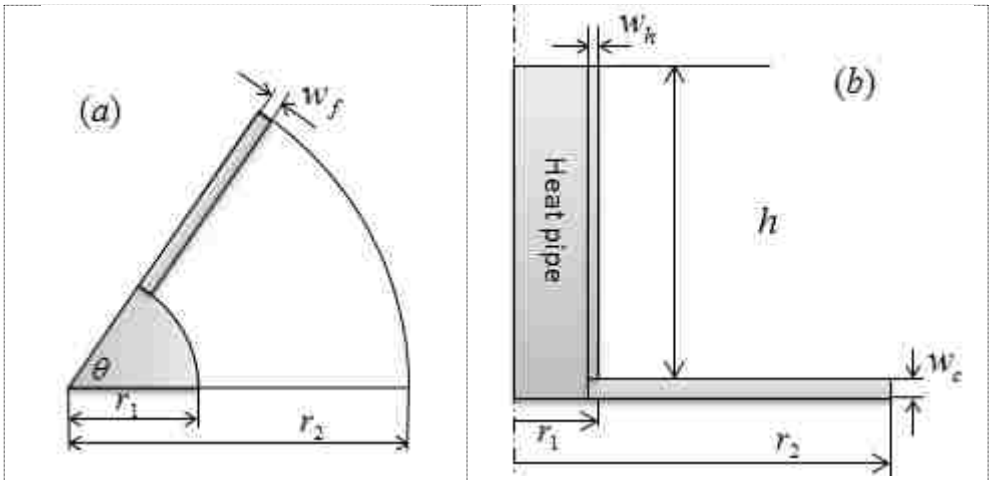

Top view (Mirror symmetry between two longitudinal fins)

Side view (From one circular fin to the air gap)

Figure 4.6 Detail dimensions of a symmetrical section of a half PCM cell

By incorporating heat pipes and fins into the PCM, the cost of the system in terms of dollars per kilowatt will inevitably be increased. A reliable estimation of system cost plays a very important role in evaluating the economic feasibility of any proposed system. In this paper, nonlinear programming is employed to find the optimal finned heat pipe geometries (Figs. 4.5 (a) & 4.6) that will result in minimum system cost. Eqn. (2.1) shows the constrained nonlinear optimization formulation of the design problem for finned heat pipe-assisted LTESS. As it is assumed that the whole LTESS system is composed of multiple identical finned heat pipes, the design variables are the dimensions of a single finned heat pipe, as shown in Fig. 4.6. The thickness of the heat pipe, w_{hp} is fixed and a typical value $w_{hp} = 1/16 \text{ inch} = 1.588 \text{ mm}$ is used.

$$\min_{r_1, r_2, h, \theta, w_{l,} w_c} \quad g\left(r_1, r_2, h, \theta, w_{l,} w_c\right)$$

$$\text{s.t.} \quad \begin{aligned} & t_{op} = f_{LTR}\left(r_1, r_2, h, \theta, w_{l,} w_c, PCM, fin\right) \\ & 0.5 \text{ cm} \le r_1 \le 4 \text{ cm} \\ & 2 \le \frac{r_2}{r_1} \le 20 \\ & 1 \le \frac{h}{r_2} \le 10 \\ & 10^{\circ} \le \theta \le 90^{\circ} \\ & 0.5 \text{ mm} \le w_l, w_c \le 3 \text{ mm} \end{aligned} \tag{2.1}$$

The variables $r_1, r_2, h, \theta, w_{l,} w_c$ specify the dimensions of the finned modeling domain. The angle θ determines the number of longitudinal fins to be used, $N_l = \text{int}(360/2\theta)$; where 'int' is used to get an integer number. Consequently 90° corresponds to an optimal longitudinal fin number of 2. As 90° is also the upper limit, it may also indicate that the optimizer suggests the use of no longitudinal fins. The constraints on the ratios $\frac{r_2}{r_1}$ and $\frac{h}{r_2}$ are determined by the f_{LTR} model set up. In the following, Section 3 introduces the construction and verification of the LTR model f_{LTR}. Section 4 presents the objective function and also optimal cost analysis. Derivation of the cost function $g\left(r_1, r_2, h, \theta, w_{l,} w_c\right)$ is given in Appendix A.

3 Layered Thermal Resistance model in 3D cylindrical coordinates

The Layered Thermal Resistance (LTR) model was first proposed in [23] for rectangular and cuboidal geometries and was also extended to 2D cylindrical coordinates in [24]. In this paper, the LTR model for PCM solidification is extended to 3D

cylindrical geometries to model a new PCM domain indicated in Fig. 4.6. The domain is bordered by circular and longitudinal fins and the heat pipe. Figs. 4.7(a) & 4.7(b) show the schematic application of the LTR model to the 3D cylindrical PCM domain. The key component of the LTR model is the assumption that the liquid PCM is solidified in a layer by layer manner and that the final solidification time is estimated by adding together the solidification times of all of the discrete layers. The dotted lines in Fig. 4.7(a) & 4.7(b) represent successive solid fronts. The discrete layer in Figs. 4.7(a) represents a new annulus section from the top view, which has the same angle θ and radial ratio $\frac{r_1}{r_2}$ as the original PCM shape, but in a shrinking manner to represent the solidification behavior. The height of the liquid PCM is also shrinking, and is depicted in Fig. 4.7(b). Variables D^i, $E^i$and H^i designate the evolving location of the solidification front. A detailed calculation of these parameters can be found in Appendix B. The cylindrical PCM domain is cooled at three surfaces and while the liquid PCM domain is shrinking due to solidification, the heat transfer surface areas (for cooling energy going into the liquid PCM denoted as S_1^i, S_2^i, and S_3^i) are also shrinking. There are three heat paths to the solidification front, represented by three thermal resistances, R_1, R_2 and R_3. The modeling approach is given in Eqns. (3.1-3.7). An average temperature difference $0.5(T_{hp} - T_{m)}$ is used to account for the sensible energy, where T_{hp} is the cooling temperature and T_m is the melting temperature of the PCM.

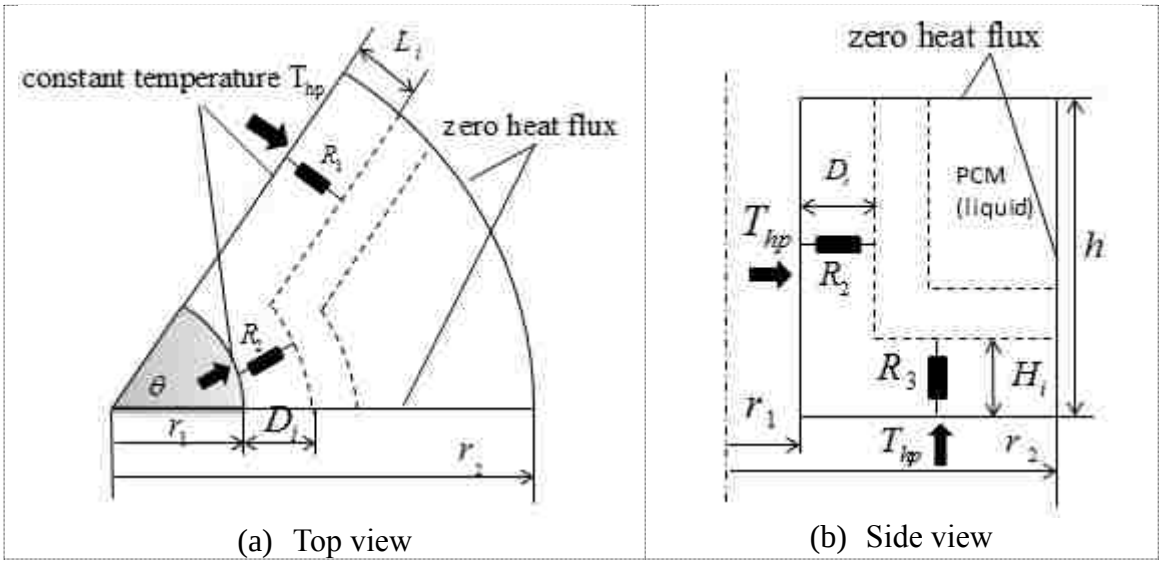

(a) Top view (b) Side view

Figure 4.7 Sketch of the annular geometry with dimensions and boundary conditions

$$R_1^i = \frac{E^i}{S_1^i k_{pcm}}, \quad (3.1) \qquad R_2^i = \frac{D^i}{S_2^i k_{pcm}}, \quad (3.2) \qquad R_3^i = \frac{H^i}{S_3^i k_{pcm}} \quad (3.3)$$

$$R_{total}^i = \frac{R_1^i R_2^i R_3^i}{R_1^i R_2^i + R_1^i R_3^i + R_2^i R_3^i}, \quad (3.4) \qquad q^i = \frac{T_{hp} - T_m}{R_{total}^i}, \quad (3.5)$$

$$t^i = \frac{\Delta V^i \rho_{pcm} [L_{pcm} + 0.5 C_p (T_{hp} - T_m)]}{q^i}, \quad (3.6) \qquad t_s = \sum_{i=1}^{K-1} t^i. \quad (3.7)$$

Table 4.1 Annulus sector with different radii, angles and heights

r_1 (cm)	1.0	1.0	1.0	1.0	1.0	0.5	0.1
r_2 (cm)	2.0	3.0	4.0	6.0	9.0	7.0	2.0
r_2/r_1	2.0	3.0	4.0	6.0	9.0	14.0	20.0
θ (°)	10	30	60	90	--	--	--
h/r_2	2.0	4.0	7.0	10.0	--	--	--

Table 4.2 PCM properties used in the simulations

PCM	ρ_{pcm}	k_{pcm}	C_p	L_{pcm}	T_m
$CaCl_2 \cdot 6H_2O$	1538 kg/m^3	1.09 W/(mK)	2145 J/(kgK)	170 kJ/kg	29.5 ℃

Table 4.1 shows 7 radial ratios $\frac{r_2}{r_1}$, 4 angles θ and 4 height-to-radius ratios $\frac{h}{r_2}$ for a 3D annulus sector PCM domain. With a combination ($7 \times 4 \times 4$) of the three variables $\frac{r_2}{r_1}$, θ, and h/r_2, there are a total of 112 cases. The angle θ covers a range from 10° to

90°. The h/r_2 includes a ratio range from 2.0 to 10.0. The ratio $\frac{r_2}{r_1}$ ranges from 2.0 to 20.0; where a ratio of 2.0 represents a case where a minimal compactness factor (CF) of 75% is set for the heat pipe PCM system with no fins. The CF of a PCM storage system is defined as the ratio of the volume of PCM to the volume of the whole system. The traditional PCM encapsulated in spheres can reduce the storage density by 50% [30], while tubes in PCM tank arrangements can achieve CFs of over 90% [31]. Table 4.2 shows the PCM properties used in the simulations.

The Solidification & Melting Model in Fluent (commercial computational fluid dynamics (CFD) software) [32], which is based on the enthalpy-porosity method [33], is used to obtain numerical solutions to verify the LTR model. For the enthalpy-porosity method, three regions, solid, liquid, and mushy zones, are defined in the computational domain. Given a PCM's melting range $\left(T_{lower}, T_{upper}\right)$ and a cell temperature T_{cell}, a liquid fraction ranging from 0 to 1 is defined by Eqn. (3.8) and is used to identify the three regions. The exact melting temperature used in the LTR model is defined as $T_m = \frac{1}{2}\left(T_{lower} + T_{upper}\right)$. As the solidification process is conduction dominated [25], the continuity and momentum equations were turned off in the Fluent setup. Validation of the solidification phenomenon predicted by the enthalpy-porosity method [32] compared to experimental data is available in Ismail's work [33].

$$\gamma = \begin{cases} 1, & T_{cell} > T_{upper} \\ \frac{T_{cell} - T_{lower}}{T_{upper} - T_{lower}}, & T_{lower} \leq T_{cell} \leq T_{upper} \\ 0, & T_{cell} > T_{upper} \end{cases} \tag{3.8}$$

For the CFD simulations corresponding to the cases in Table 4.1, the total number of elements used was 10,000-100,000 and the time step was 3-6 s, depending on the size of

the geometry. Sensitivity studies were performed to confirm mesh and time-step independence of the results presented. The energy equation was discretized using the Second Order Upwind scheme. A pressure based solver with double-precision was chosen. The convergence was checked at every 1 time steps with a scaled absolute residual of 10^{-9} that was used for the energy equation.

The CFD results are treated as a trusted reference to verify the LTR model. Fig.8 displays the solidification time ratio t_{CFD}/t_{LTR} surfaces found by comparison of the CFD and the LTR models for the variations of θ and $\frac{r_2}{r_1}$ at 4 different $\frac{h}{r_2}$ ratios (Table 4.1). The solidification time ratio between the two models (Fig. 4.8) actually indicates how much the thermal resistance is overestimated by the LTR model. Thus a geometrically-dependent ratio is introduced as a 'tuning factor' for the LTR model, which is used to adjust the total thermal resistance as shown in Eqn. (3.9). The tuning factor is dependent on three geometric variables: the radial ratio $\frac{\mathrm{r}_2}{\mathrm{r}_1}$, θ, and $\frac{h}{r_2}$. Thus a correlation between the tuning factor and the three geometric variables needs to be built, as shown in Eqn. (3.10). A custom support vector regression (SVR) method [35] was used to establish the correlation. The 112 cases in Table 4.1 are used as the database to build the SVR model. Fig. 4.9 shows the tuning factor at $\frac{h}{r_2} = 5$ for varying $\frac{\mathrm{r}_2}{\mathrm{r}_1}$ and θ, determined through the SVR model. The SVR model is also employed to predict a tuning factor given a new set of geometries, $\frac{r_2}{r_1}$, θ, and $\frac{h}{r_2}$ and it is used to adjust the total resistance of the LTR model as shown in Eqn. (3.9). It should be noted that in the following sections, whenever the LTR model is mentioned, it refers to the LTR model with a tuning factor.

$$R^i_{total} = \alpha \frac{R^i_1 R^i_2 R^i_3}{R^i_1 R^i_2 + R^i_1 R^i_3 + R^i_2 R^i_3} \qquad (3.9)$$

$$\alpha = f\left(\frac{r_2}{r_1}, \theta, \frac{h}{r_2}\right) \qquad (3.10)$$

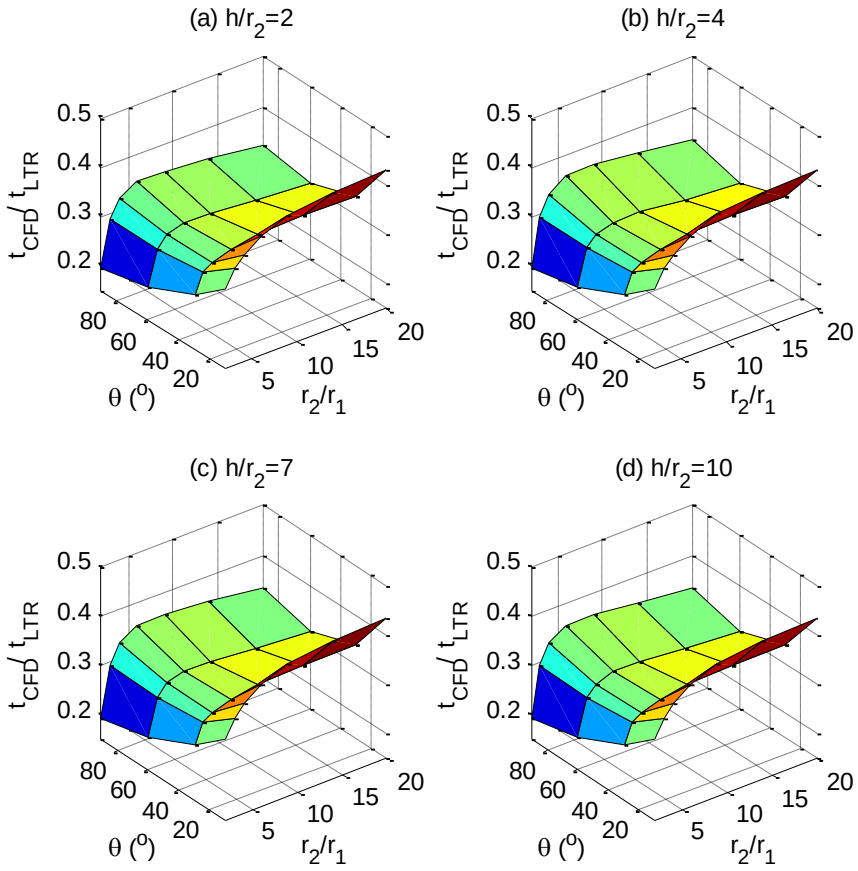

Figure 4.8 Solidification time ratio surfaces determined by CFD and LTR models without using tuning factors

Table 4.3 Testing cases for the LTR model

Cases	#1	#2	#3	#4	#5	#6	#7	#8
r_1 (cm)	2.	2.	2.	2.5	2.5	1.5	0.3	0.4
r_2(cm)	5.	10.	14.	20.	12.5	15	4.5	7.2
h (cm)	10.	30	126	100.	100.	90.	18	36
θ (°)	80.	40	20	50	70	15	45	85
dT (°C)	10.	10.	10.	20.	7.	15.	20.	30.
k_{pcm} (W/mK)	1.09	1.09	1.09	2.0	2.0	0.5	0.5	2.0
L_{pcm} (kJ/kg)	170	140	200	170	170	140	120	200
$\alpha = f\left(\frac{r_2}{r_1}, \theta, \frac{h}{r_2}\right)$	0.29	0.36	0.44	0.37	0.37	0.47	0.34	0.38

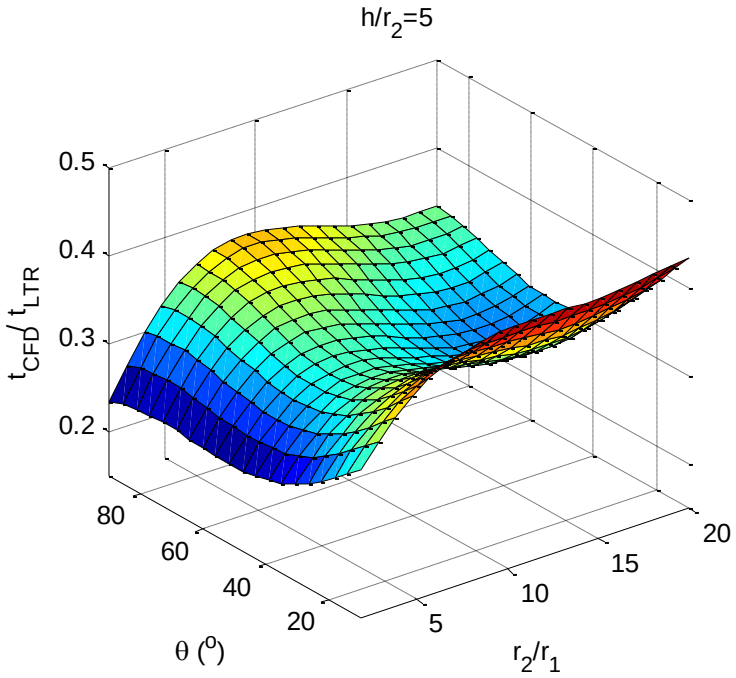

Figure 4.9 Resistance tuning surface by support vector regression (SVR)

Table 4.3 gives additional cases that are used to test the accuracy of the LTR model. All of the testing cases in Table 4.3 have new dimensions compared to Table 4.1. Except for Case 1, the other cases also have different driving temperatures, PCM conductivity and latent energies compared to those of the original cases in Table 4.1, which were used to construct the tuning factor. Once again we treat CFD simulation results as the trusted reference in comparison to the LTR model. Estimation accuracy in terms of percent error is defined as:

$$\varepsilon = \frac{(t_{LTR} - t_{CFD})}{t_{CFD}} \times 100\%. \qquad (3.11)$$

The performance of the LTR model is shown in Fig. 4.10. Overall, the tuned LTR model accuracy is quite good, within 10% compared to the CFD results. The results suggest that modifications of the PCM properties and driving temperature differences have almost no effect on the performance of the LTR model. The tuning factor is almost

only dependent on the geometry. It should be noted that the effect of the PCM density and heat capacity on the LTR model is not explicitly considered. However, the PCM conductivity can indirectly represent the effects of density and heat capacity. Together the three parameters define the thermal diffusivity $\frac{k_{pcm}}{\rho_{pcm}C_p}$, which is a dimensionless number that controls the behavior of the heat transfer process. Consequently, once a tuning factor is identified based on a prescribed driving temperature and a certain kind of PCM, it can also be applied to cases with new driving temperature differences and new PCMs. In this way the resistance tuning factor allows for flexibility for different applications.

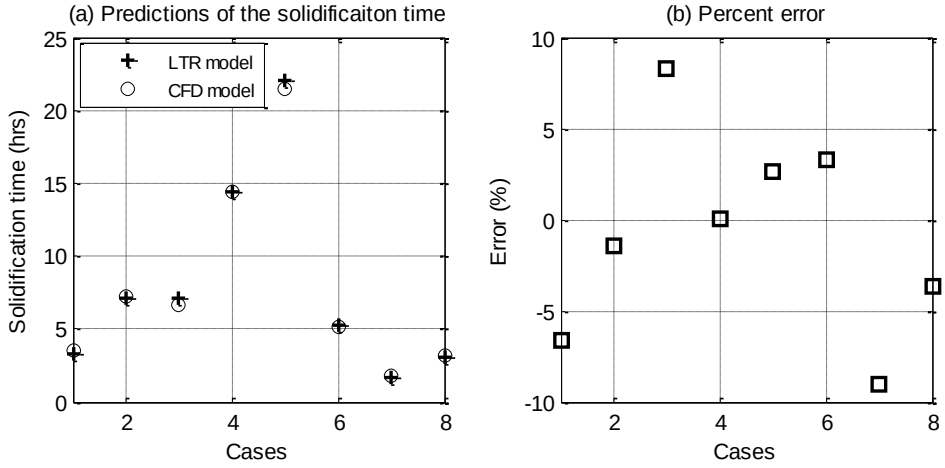

Figure 4.10 (a) Predictions of the 8 testing cases by the LTR model and (b) Percent error between the CFD and LTR results

In this section, the model developed above is modified by attaching fins to the 3D cylindrical PCM domain. In this way, a 3D finned LTR model is developed that is capable of modeling the finned PCM structure shown in Fig. 4.5. The finned LTR model can then be efficiently used in the optimal design problem (Eqn. 2.1). The longitudinal and circular fins attached to the PCM domain shown in Fig. 4.5 are also shown in Fig. 4.6. It is assumed that the heat pipe wall (r_1 is the outer radius of the heat pipe) maintains

a constant temperature T_{hp} and the remaining boundaries have zero heat flux.

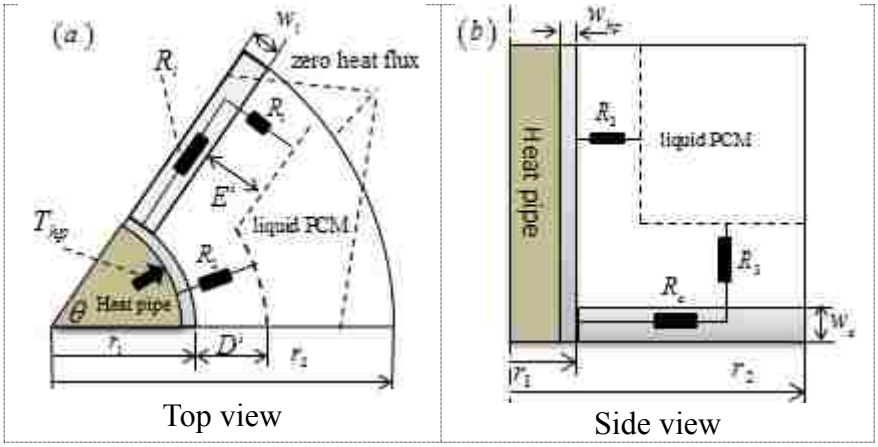

Figure 4.11 Sketch of the finned annular sector

Conceptually it is assumed that there are three heat paths for cooling energy transfer to the PCM. One is through the heat pipe wall, one is through the longitudinal fin and the last is through the circular fin. The resistance of the heat pipe wall can be neglected. It is assumed that the heat transfer within both the longitudinal and circular fins happens along one direction. In addition, it is assumed that the lengths of the fins that are used to calculate the thermal resistances are varying parameters, which are the distances of the solidification front to the heat pipe wall (Eqns. 3.12 & 3.13):

$$R_l^i = \frac{E^i}{w_l(h-H^i)k_f}, \qquad (3.12) \qquad R_c^i = \frac{ln(D^i/r_1)}{2\pi w_c k_f} \qquad (3.13)$$

Resistances R_1, R_2 R_3 within the solid PCM (representing the paths that the cooling energy can take to reach the solidification front) are the same as those defined in the LTR model with no fins (Eqns. 3.1-3.3).

Besides the fin resistances, the fin efficiency is also a key factor that must be considered when coupling fins to the PCM domain. The derivations of fin efficiencies η_l, η_c for the longitudinal and circular fins, are respectively presented in Appendix C. The

entire length of the fin is used for the fin efficiency calculation; the exact efficiencies η_l, η_c to be used for the coupling are obtained at the locations of the solidification fronts. The thermal resistance passing through these fins needs to be increased by $\frac{1}{\eta_l}$ and $\frac{1}{\eta_c}$, respectively, to account for the fin efficiency. Eqn. (3.14) is the thermal resistance for the heat passing through the longitudinal fin to the solidification front. Eqn. (3.15) is the thermal resistance for the heat passing through the circular fin to the solidification front. Eqn. (3.16) shows the total thermal resistance of the system shown in Fig. 4.11. The heat flux and solidification time calculations are the same as Eqns. (3.5-3.7).

$$R_1^* = R_l + \frac{1}{\eta_l} R_1 \qquad (3.14) \qquad R_3^* = R_c + \frac{1}{\eta_c} R_3 \qquad (3.15)$$

$$R_{total} = \alpha \frac{R_1^* R_2 R_3^*}{R_1^* R_2 + R_2 R_3^* + R_1^* R_3^*} \qquad (3.16)$$

To test the prediction capabilities of the finned LTR model, 2 geometries with different PCM properties are considered in Table 4.4. For each of the geometries, three fin thicknesses (0.5 mm, 1.0 mm, 2.0 mm) and two types of fin material, aluminum alloy 6061 (Al-6061) and carbon steel (CS) are also considered. The conductivity of the aluminum alloy fin is 170 $\mathrm{W/(mK)}$, and that of the carbon steel is 50 $\mathrm{W/(mK)}$.

Table 4.4 Additional test cases for the Finned LTR model with tuning factor

Cases	#1	#2
r_1 (cm)	4	0.5
r_2 (cm)	12	8
h (cm)	96	40
θ (°)	15	35
L_{pcm} (kJ/kg)	150	180
k_{pcm} (W/mK)	1.0	1.5
dT (°C)	10	20
α (tuning factor)	0.33	0.31

Figure 4.12 shows the solidification times and percentage errors (Eqn. (3.11)) for all

the cases. Most of the cases have a percentage error within 15%, except for Case #1*, with a carbon-steel material and 0.5mm fin thickness. Note that the'*' denotes all same parameters as #1 and #2, except the fin material is CS. The reason is that when the fin efficiency drops to below a certain low value, the finned LTR model will tend to overestimate the solidification time. More detailed analysis of the limitations of the finned LTR model can be found in [23]. It can also be seen that the aluminum alloy fins perform better than the carbon-steel fins. Overall the accuracy is acceptable and further discussion of how the solidification time errors will affect the optimal solutions will be given in the next section.

('#1, #2 denotes Al-6061 fins and #1*, #2* denotes CS fins; Every three consecutive points represent three different fin thicknesses, 0.5 mm, 1. mm, 2. mm.)

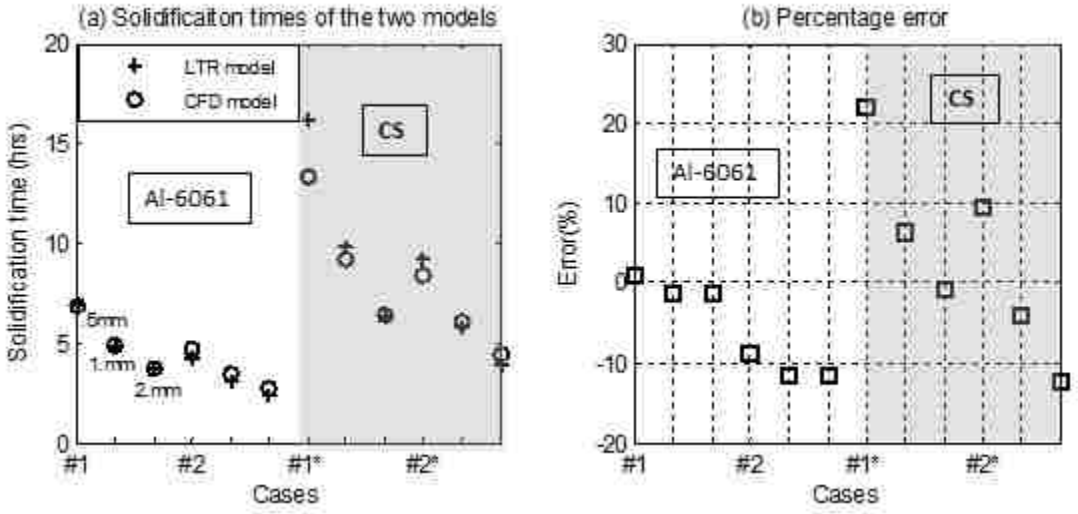

Figure 4.12 Solidification times and percent errors by the CFD and finned LTR models.

4 Sensitivity analyses of system parameters on the minimal cost of the finned HP-LTES system

This section introduces the cost function, the optimal dimensions of the HP-LTES

system (See Fig. 4.4), and cost sensitivity analysis for a set of variables (See Table 4.5). For the sensitivity analysis, when one variable is altered, the others take the base values. Material and manufacturing cost compose the main investment cost of the HP-LTES system. As the manufacturing cost is an uncertain variable, it is assumed that the system cost is based on the material cost times a manufacturing factor, i.e. 2.0. Thus the cost function in the optimal design analysis depends only on material usage. The detailed derivation of the cost function is presented in Appendix A.

Table 4.5 Parameters for Sensitivity Analysis

Parameters	Base case values
Driving temperature difference, dT	10 (℃)
Required solidification time, t_{op}	10 (hrs)
PCM conductivity, k_{pcm}	1.0 (W/mK)
PCM latent energy, L_{pcm}	170 (kJ/kg)
Heat pipe radius, r_1	1.0 (cm)
Minimal fin thickness, $w_{f_{min}}$	0.5 (mm)

The optimal design goal is to use the least amount of heat pipes and fins to freeze a given amount of PCM within the required solidification time t_{op}. This is formulated as a nonlinear programming problem in Section 2, Eqn. (2.1). With the LTR model (f_{LTR}) as the system constraint, and the cost function presented in Appendix A, the optimal design variables $r_1, r_2, h, \theta, w_l, w_c$ can be found by solving Eqn. (2.1). As it is a nonlinear constrained optimization problem, 'fmincon' (a gradient based method) within the MATLAB optimization toolbox was employed to solve the problem [36].

Table 4. 6 Optimal dimensions for different solidification times

t_{op} (hrs)	r_1 (cm)	r_2 (cm)	h (cm)	θ (°)	w_l (mm)	w_c (mm)
5	1.0	6.01	60.06	38.60	0.5	0.5
6	1.0	6.31	63.05	40.76	0.5	0.5
8	1.0	6.84	68.38	43.98	0.5	0.5
10	1.0	7.31	73.07	46.30	0.5	0.5
$fin: Al\ 6061$; $k_{pcm} = 1.0$ W/mK; $L_{pcm} = 170$ kJ/kg;						

Table 4.6 shows optimal dimensions under 4 different required solidification times t_{op} . To further verify the optimal results, the set of optimal dimensions $(r_1, r_2, h, \theta, w_{l,} w_c)$ in Table 4.6 were evaluated by running CFD simulations in Fluent following the procedure outlined in Section 3. The predicted solidification curves of the 4 cases are shown in Fig. 4.13. It can be seen that all of the CFD solidification times are almost equal to the t_{op} specified by the optimization formulation, Eqn. (2.1). The finned LTR model for the Al-6061 fin cases has errors that can reach more than 10% (see Fig. 4.12) in terms of solidification time. However, if the errors are instead calculated in terms of solid fraction under a specified t_{op} , the error almost diminishes to an insignificant value (<0.5%). This is mainly because of the "tailing" effect. The tailing effect refers to the situation when almost 70% of the PCM can be solidified within half of the total solidification time, and at the final stage, a small amount of PCM takes a relatively long time to solidify. Thus, error in terms of the solid fraction is greatly diminished. This phenomenon verifies the reliability of the finned LTR model for optimal PCM fin structure design applications.

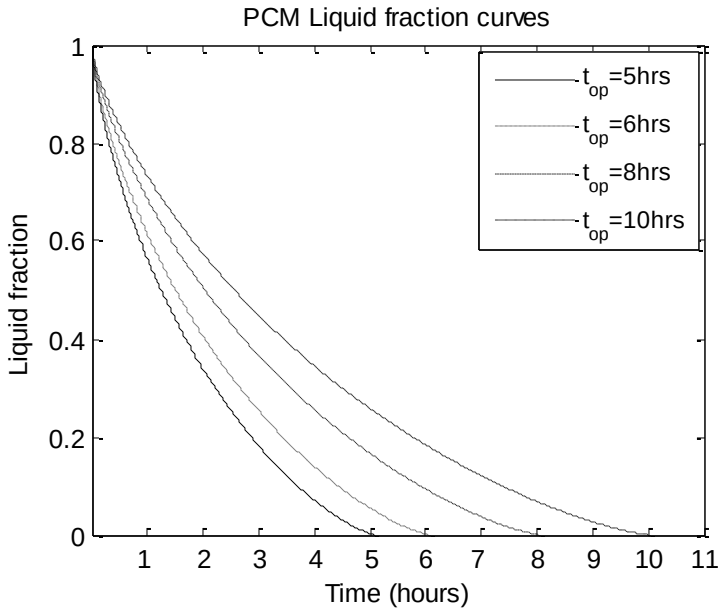

Figure 4.13 CFD verifications of the cases with optimal dimensions in Table 4.6

It should be noted that the heat pipe radius r_1 was treated as a parameter for sensitivity analysis because the optimal r_1 is always at the lower boundary of the constraint specified on r_1 in Eqn. (2.1). By varying the lower boundary of r_1, it becomes a sensitivity parameter for the analysis. The same situation occurs for the thicknesses of both the longitudinal and circular fins. Their optimal values are always equal to their lower prescribed bounds. Thus, the lower bound thickness $w_{f_{min}}$ for both of the two fins was treated as a sensitivity parameter for analysis.

The minimal cost and optimal dimensions under the varying parameters (See Table 4.5) are shown in Figs. 4.14-4.19. Subfigure (a) in those figures shows the minimized cost under the varying parameter of interest; subfigures (b), (c) and (d) in Fig. 4.14-4.19 show the corresponding optimal r_2/r_1, h/r_2 and θ. In Fig. 4.20, the x-axis represents the varying range of the parameters in Table 4.6 divided by their respective base values; and the y-axis represents all of the minimized costs using the varying parameters divided by the minimized cost under the base parameter values. Fig. 4.20 clearly shows that the

latent energy of the PCM (L_{pcm}) has the first-order sensitive effect on the system cost; the driving temperature difference (dT), the required solidification time (t_{op}), the PCM conductivity (k_{pcm}) and the thickness of the fins ($w_{f_{min}}$) have second-order sensitivity effect; the radius of the heat pipe (r_1) has the smallest sensitivity effect. The sensitivity results of the fin thickness also suggest that the fins attached to a heat pipe should be as thin as possible in order to lower the system cost. When the fin thickness is equal to or larger than 1.5 mm, the optimal θ reaches the upper boundary 90°, which implies that at most 2 longitudinal fins should be used to achieve optimal cost (or no longitudinal fins). As a result, it can be concluded that there is a thickness limit for the fins to be economically welded on a heat pipe.

All of the optimal h/r_2 shown in subfigures (c) of Figs. 4.14-4.19 reach the upper limit set as 10:1 in the optimization formulation Eqn. (2.1), except for the case of varying heat pipe radius (Fig .4.18c). For the optimal h/r_2 ratio points that are less than 10, their r_2/r_1 values are smaller, i.e. less than 5 (Fig. 4.18b). Thus, it appears that when r_2/r_1 is larger than a certain value, i.e. 5, the longitudinal fin is more economical than the circular fin. To further confirm this result, comparison to a previously reported 2D model with only longitudinal fins [24] is made. The boundary conditions and material properties for the two models are all the same as the base values in Table 4.6. Fig. 4.21 shows the cost comparison between attaching only longitudinal (2D) fins on a heat pipe and attaching both circular and longitudinal (3D) fins. The results show that at larger heat pipe radii, which also means smaller r_2/r_1 ratio (see Fig.4.18 (b), (c)), the combination of circular and longitudinal fins can achieve some economic benefit over using only longitudinal fins. However, the benefit is small. The overall conclusion is that the longitudinal fins

are not better for cost-effective performance than the circular fins. Moreover, for a vertically arranged annular pipe with circular fins, it has been elsewhere reported that, due to the solid sinking phenomenon, circular fins can be very efficient in promoting the melting process [37].

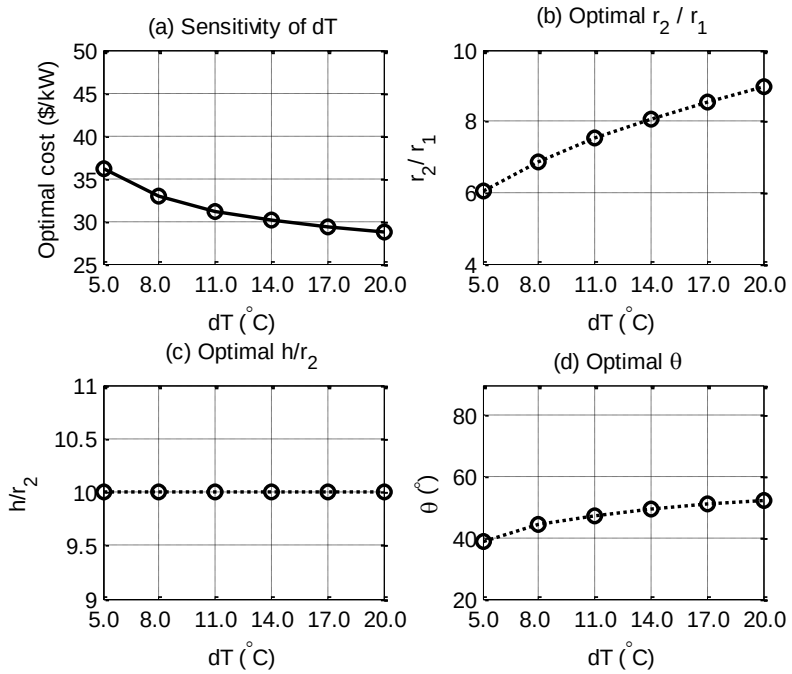

Figure 4.14 Sensitivity analysis of driving temperature difference and optimal dimensions

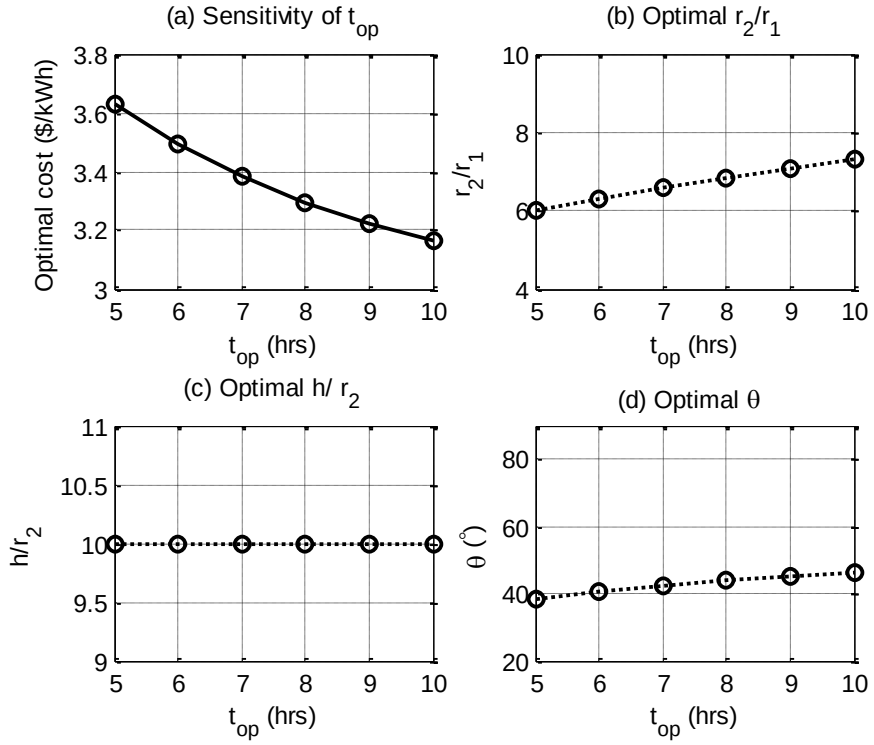

Figure 4.15 Sensitivity analysis of the solidification time and optimal dimensions

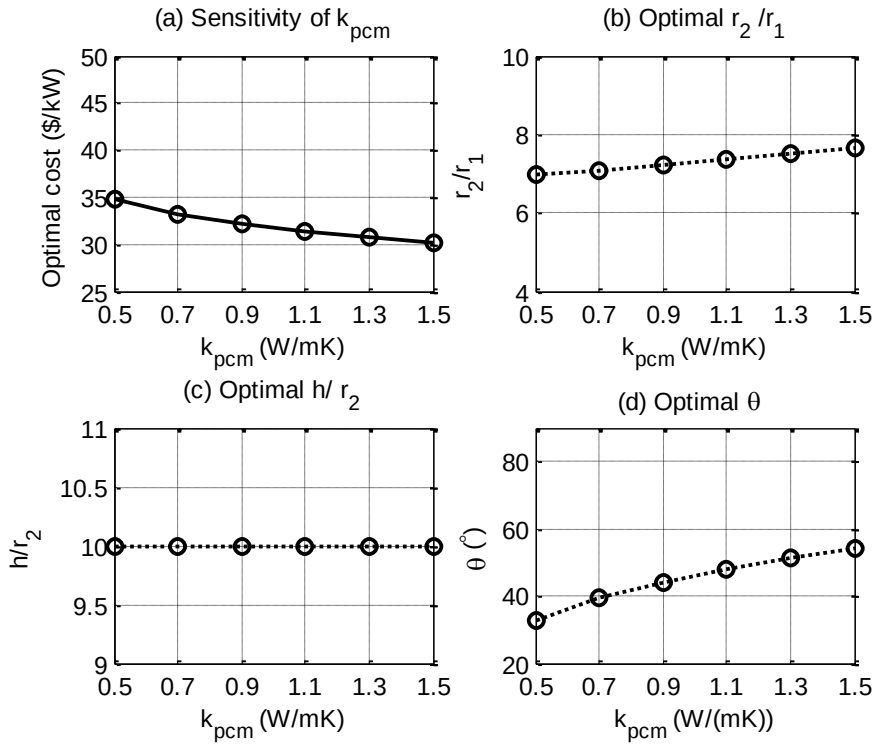

Figure 4.16 Sensitivity analysis of PCM conductivity and optimal dimensions

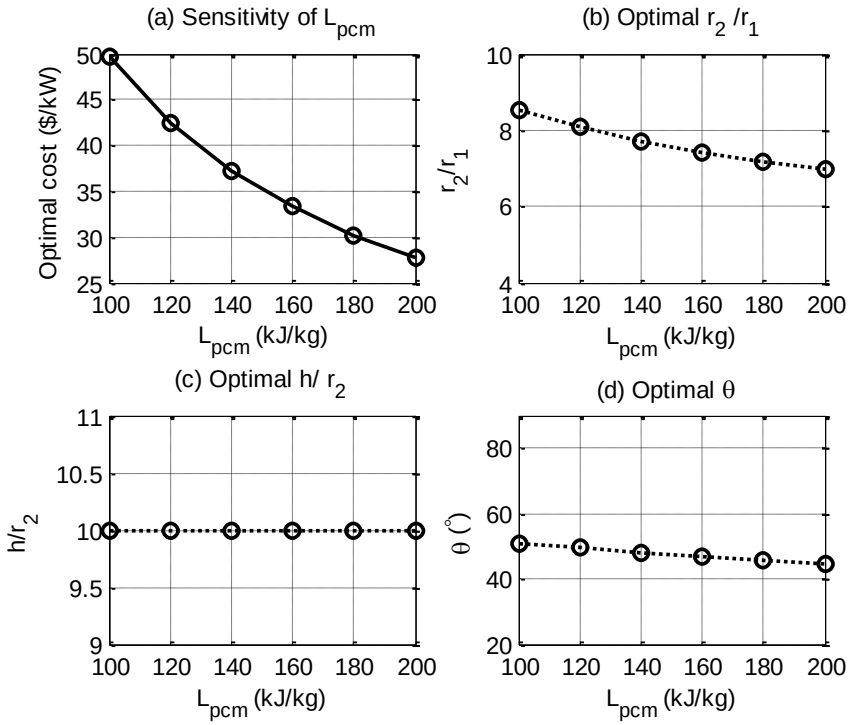

Figure 4.17 Sensitivity analysis of PCM latent energy and optimal dimensions

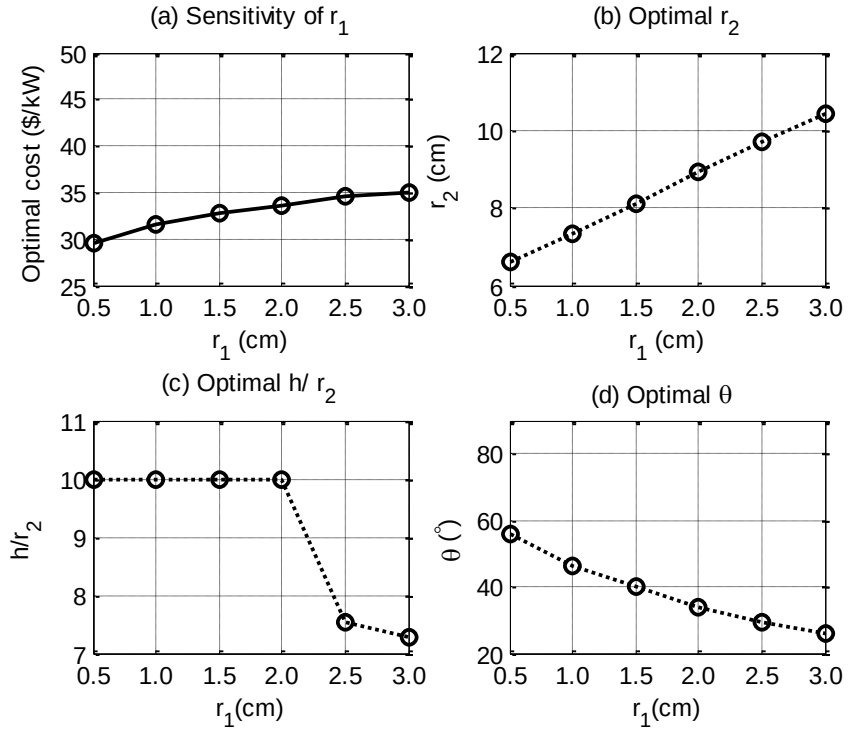

Figure 4.18 Sensitivity analysis of heat pipe radius and optimal dimensions

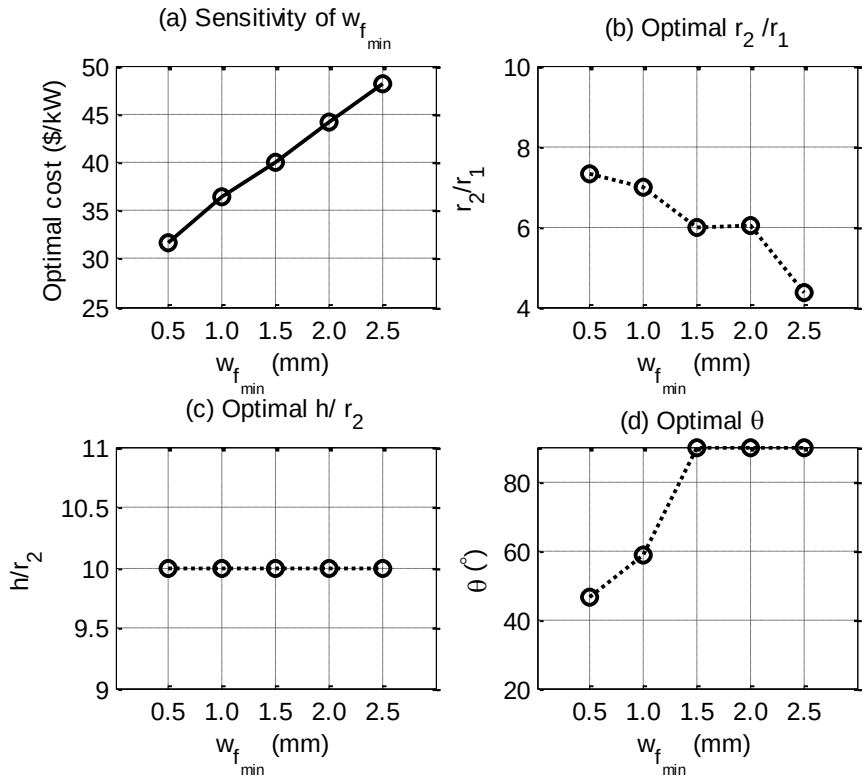

Figure 4.19 Sensitivity analysis of minimum fin thickness and optimal dimensions

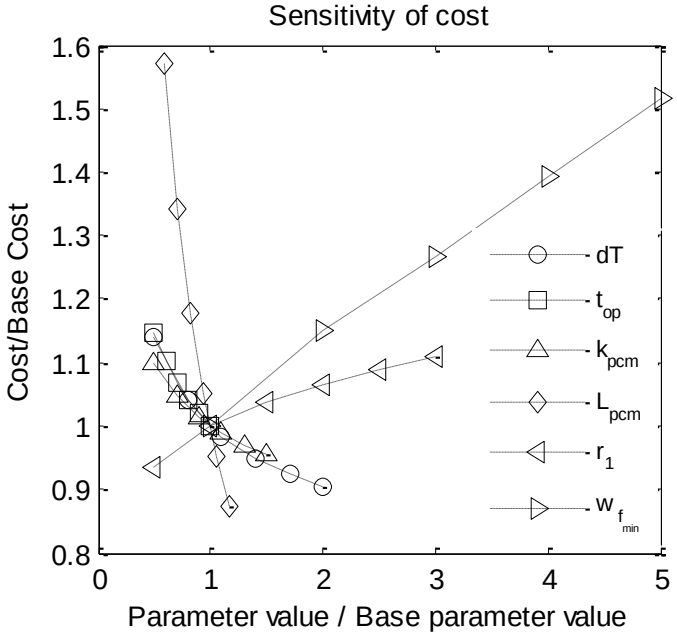

Figure 4.20 Cost sensitivity comparison of the 6 parameters in Table 4.6

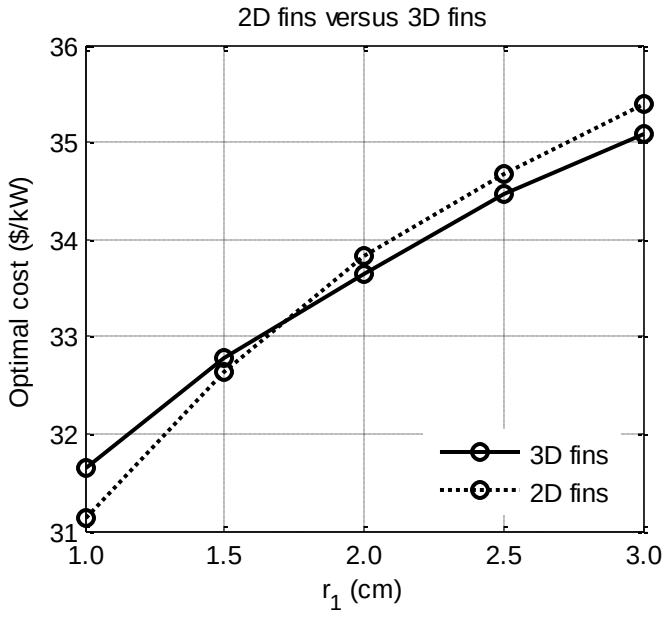

Figure 4.21 Cost comparison between using only longitudinal (2D) fins and using combined longitudinal and circular (3D) fins

5. Conclusions

A novel application of a Phase Change Material (PCM) based cooling system has been proposed for the supplementary cooling of air cooled condensers (ACCs). In order to evaluate the system cost, a solidification modeling approach called a Layered Thermal Resistance (LTR) model has been extended to 3D analysis for the first time to efficiently model the finned heat pipe module for a PCM-based supplementary cooling system. By employing the efficient LTR model, a nonlinear optimization problem was formulated to estimate the system cost and conduct sensitivity analyses on several important system parameters. Overall, the material cost of the finned heat pipe-assisted PCM tank is about 30 $/kW, which meets a 10-hour solidification time requirement. This is a promising cost for the system to be accepted in the market. Based on the sensitivity analysis performed, it can be concluded that the latent energy of the PCM has a first-order sensitive effect on

the system cost; the driving temperature difference, the PCM conductivity, the required solidification time and the fin thickness all have second-order impact on the system cost. The sensitivity analysis suggests that the fins attached to a heat pipe should be as thin as possible in order to lower system cost. Based on the optimal dimensions of the attached circular and longitudinal fins, it can also be concluded that the longitudinal and circular fins attached to a heat pipe have similar performance in terms of cost effectiveness. Thus the final decision on which type of fins should be attached to a heat pipe may be better decided based on their associated manufacturing costs, which is not explicitly accounted for in this paper.

Acknowledgement

This research is sponsored by the ARPA-e ARID Program under Contract No. DE-AR0000582. Any opinions, findings, and conclusions or recommendations expressed in this article are those of the authors and do not necessarily reflect the views of the Advanced Research Projects Agency-Energy.

References

[1] A. Sharma, V.V. Tyagi, C.R. Chen, D. Buddhi. Review on thermal energy storage with phase change materials and applications. Renew Sustain Energy Rev 2009; 13 (2): 318-345.

[2] H. Akeiber, P. Nejat, M. Majid, M. Wahid, F. Jomehzadeh, I. Z. Famileh, J. Calautit, B. Hughes, S. Zaki. A review on phase change material (PCM) for sustainable passive cooling in building envelopes. Renew Sustain Energy Rev 2016; 60: 1470-

1497.

[3] R. Ye, W. Lin, K. Yuan, X. Fang, Z. Zhang. Experimental and numerical investigations on the thermal performance of building plane containing CaCl2·6H2O/expanded graphite composite phase change material. Appl Energy 2017; 193: 325-335.

[4] S.S. Chandel, T. Agarwal. Review of cooling techniques using phase change materials for enhancing efficiency of photovoltaic power systems. Renew Sust Energ Rev 2017;73: 1342-1351.

[5] R. Zhao, J. Gu, J. Liu. Optimization of a phase change material based internal cooling system for cylindrical Li-ion battery pack and a hybrid cooling design. Energy 2017;135:811-822.

[6] A. Arshad, H. M. Ali, M. Ali, S. Manzoor. Thermal performance of phase change material (PCM) based pin-finned heat sinks for electronics devices: Effect of pin thickness and PCM volume fraction. Appl Therm Eng 2017; 112: 143-155.

[7] N. I. Ibrahim, M. M. A. Khan, I. M. Mahbubul, R. Saidur, F. A. Al-Sulaiman. Experimental testing of the performance of a solar absorption cooling system assisted with ice-storage for an office space. Energy Convers Manage 2017; 148: 1399-08.

[8] M. H. Rahdar, A. Emamzadeh, and A. Ataei. A comparative study on PCM and ice thermal energy storage tank for air-conditioning systems in office buildings. Appl Therm Eng 2016; 96: 391-99.

[9] Y. Ruan, Q. Liu, Z. Li, J. Wu. Optimization and analysis of Building Combined Cooling, Heating and Power (BCHP) plants with chilled ice thermal storage system. Appl Energy 2016:179: 738-754.

[10] N. Luo, T. Hong, H. Li, R. Jia, W. Weng. Data analytics and optimization of an ice-based energy storage system for commercial buildings. Appl Energy 2017; 204: 459-475.

[11] X. Luo, C. K. Lee, W.M. Ng, Y. Shuo, B.Chaudhuri, S.Y. R. Hui. Use of adaptive thermal storage system as smart load for voltage control and demand Response. IEEE Transactions on Smart Grid 2017; 8(3): 1231-1240.

[12] http://nuicone.org/site/common/proceedings/Mechamical/oral/ME-15.pdf

[13] B. Carlsson. Phase change behavior of some latent heat storage media based on

calcium chloride hexahydrate. Sol Energy 2009; 83(4): 485-500.

[14] S. J. Ren, J. Charles, X.C. Wang, F.X. Nie, C. Romero, S. Neti, Y. zheng, S. Hoenig, C. Chen, F. Cao, R. Bonner, H. Pearlman. Corrosion testing of metals in contact with calcium chloride hexahydrate used for thermal energy storage. Mater Corros DOI: 10.1002/maco.201709432.

[15] C. W. Robak, T. L. Bergman, A. Faghri. Economic evaluation of latent heat thermal energy storage using embedded thermosyphons for concentrating solar power applications. Sol Energy 2011; 85(10) :2461-2473.

[16] K. Nithyanandam, R. Pitchumani, Cost and performance analysis of concentrating solar power systems with integrated latent thermal energy storage. Energy 2014; 64:793-810.

[17] S. Hübner, M. Eck, C. Stiller, M. Seitz. Techno-economic heat transfer optimization of large scale latent heat energy storage systems in solar thermal power plants. Appl Therm Eng 2016; 98: 483-491.

[18] B. Zhao, M. Cheng, C. Liu, Z. Dai. Thermal performance and cost analysis of a multi-layered solid-PCM thermocline thermal energy storage for CSP tower plants. Appl Energy 2016; 178: 784-799.

[19] M. Seitz, M. Johnson, S. Hübner. Economic impact of latent heat thermal energy storage systems within direct steam generating solar thermal power plants with parabolic troughs. Energy Convers Manage 2017; 143: 286-294.

[20] J, Xie, C. Yuan. Parametric study of ice thermal storage system with thin layer ring by Taguchi method. Appl Therm Eng 2016 ; 98: 246-55.

[21] H. Song, W. Zhang, Y. Li, Z. Yang, A. Ming. Exergy analysis and parameter optimization of heat pipe receiver with integrated latent heat thermal energy storage for space station in charging process. Appl Therm Eng 2017; 119: 304-11.

[22] M. Saffari, A. Gracia, C. Fernández, L. F. Cabeza. Simulation-based optimization of PCM melting temperature to improve the energy performance in buildings. Appl Energy 2017; 202: 420-34.

[23] C. Pan, S. Hoenig, C. Chen, S. Neti, C. Romero, N. Vermaak. Efficient modeling of phase change material solidification with multidimensional fins. Int. J. Heat mass Trans. 2017; 115:897-909.

[24] C. Pan, N. Vermaak, C. Romero, S. Neti, S. Hoenig, C. Chen. Efficient optimization of a longitudinal finned heat pipe structure for a latent thermal energy storage system. Energy Convers Manage 2017; 153:93-105.

[25] S. Jegadheeswaran, S. D. Pohekar. Performance enhancement in latent heat thermal storage system: a review. Renew Sustain Energy Rev 2009; 13(9): 2225-44.

[26] K. Nithyanandam, R. Pitchumani. Design of a latent thermal energy storage system with embedded heat pipes. Appl Energy 2014; 126: 266-80.

[27] N. Sharifi, A. Faghri, T. L. Bergman, C. E. Andraka. Simulation of heat pipe-assisted latent heat thermal energy storage with simultaneous charging and discharging. Int J Heat Mass Transfer 2015; 80: 170-79.

[28] S. Tiari, S. Qiu, M. Mahdavi. Discharging process of a finned heat pipe-assisted thermal energy storage system with high temperature phase change material. Energy Convers Manage 2016; 118: 426-37.

[29] S. Almsater, W. Saman, F. Bruno. Performance enhancement of high temperature latent heat thermal storage systems using heat pipes with and without fins for concentrating solar thermal power plants. Renew Energy 2016; 89: 36-50.

[30] K.A.R. Ismail, J.R. Henriquez. Solidification of PCM inside a spherical capsule. Energy Convers Manage 2000; 41:173-87.

[31] M. Helm, C. Keil, S. Hiebler, H. Mehling, C. Schweigler. Solar heating and cooling system with absorption chiller and low temperature latent heat storage-energetic performance and operational experience. Int J Refrig 2009; 32:596-606.

[32] https://www.sharcnet.ca/Software/Fluent6/html/ug/node973.htm

[33] A.D. Brent, V.R. Voller, K.J. Reid. Enthalpy-porosity technique for modeling convection-diffusion phase change: application to the melting of a pure metal. Num Heat Transfer Part B 1988; 13: 297-318.

[34] K.A.R. Ismail, C.L.F. Alves, M.S. Modesto. Numerical and experimental study on the solidification of PCM around a vertical axially finned isothermal cylinder. Appl Therm Eng 2001; 21(1): 53-77.

[35] A.J. Smola, B. Schölkopf. A tutorial on support vector regression. Stat Comput 2004; 14: 199.

[36] https://www.mathworks.com/help/optim/ug/fmincon.html

[37] Y. Kozak, T. Rozenfeld, G. Ziskind. Close-contact melting in vertical annular enclosures with a non-isothermal base: Theoretical modeling and application to thermal storage. Int J Heat Mass Transfer 2014; 72:114-127.

Appendix

A. Cost Function of a finned heat pipe assisted LTESS

There are two main assumptions to derive the cost function of a full scale heat finned heat pipe assisted LTESS shown in Figs. 5(a) & 6. One is that there is negligible temperature drop along the length of a heat pipe, so that each unit has same boundary conditions. The other one is that each heat pipe has the same temperature boundary conditions at the air side fins, so that all of the finned heat pipe units are identical.

$$V_{pcm} = \frac{Gt_{op}}{L_{pcm}\rho_{pcm}} \tag{A.1}$$

$$N_c = int\left(\frac{HP}{h+w_c}\right) \tag{A.2}$$

$$V_{hp\_pcm} = N_c(\pi(r_2^2 - r_1^2)h - N_l w_l(r_2 - r_1)h) \tag{A.3}$$

$$N_{hp} = \text{int}\left(\frac{V_{pcm}}{V_{hp\_pcm}}\right) \tag{A.4}$$

$$V_{hp} = N_{hp}[\pi(r_1^2 - r_0^2)HP] \tag{A.5}$$

$$V_f = N_{hp}N_c(N_l w_l(r_2 - r_1)h + \pi(r_2^2 - r_1^2)w_c) \tag{A.6}$$

$$\begin{aligned} C &= C_{pcm}M_{pcm} + C_{hp}M_{hp} + C_f M_f \\ &= C_{pcm}\frac{Gt_{op}}{L_{pcm}} + C_{hp}N_{hp}\rho_{hp}[\pi(r_1^2 - r_0^2)HP] + \\ &\quad C_f\rho_f N_{hp}N_c(N_l w_l(r_2 - r_1)h + \pi(r_2^2 - r_1^2)w_c) \end{aligned} \tag{A.7}$$

$$\begin{aligned} C = C_{pcm}\frac{Gt_{op}}{L_{pcm}} + \text{int}\left(\frac{\frac{Gt_{op}}{\rho_{pcm}L_{pcm}}}{N_c(\pi(r_2^2 - r_1^2)h - N_l w_l(r_2 - r_1)h)}\right)\{C_{hp}\rho_{hp}[\pi(r_1^2 - r_0^2)HP] + \\ C_f\rho_f N_c(N_l w_l(r_2 - r_1)h + \pi(r_2^2 - r_1^2)w_c)\} \end{aligned} \tag{A.8}$$

$$C = C_{pcm}\frac{Gt_{op}}{L_{pcm}} + \frac{Gt_{op}\{C_{hp}\rho_{hp}\pi(r_1^2-r_0^2)(h+w_c)+C_f\rho_f(N_l w_l(r_2-r_1)h+\pi(r_2^2-r_1^2)w_c)\}}{L_{pcm}\rho_{pcm}(\pi(r_2^2-r_1^2)h-N_l w_l(r_2-r_1)h)} \quad \text{(A.9)}$$

To derive Eqn.A.9, the integer value obtained by the operation int () in Eqn. A.8 is approximated by its real value.

$$C = \frac{C_{pcm}Gt_{op}}{L_{pcm}}\left(1+\frac{C_{hp}\rho_{hp}\pi(r_1^2-r_0^2)(h+w_c)+C_f\rho_f(N_l w_l(r_2-r_1)h+\pi(r_2^2-r_1^2)w_c)}{C_{pcm}\rho_{pcm}(\pi(r_2^2-r_1^2)h-N_l w_l(r_2-r_1)h)}\right) \quad \text{(A.10)}$$

In Eqn. (A.8), $N_l = int\left(\frac{2\pi}{2\theta}\right)$, and it is approximated as $N_l \approx \frac{\pi}{\theta}$. Thus

$$C \approx \frac{C_{pcm}Gt_{op}}{L_{pcm}}\left(1+\frac{C_{hp}\rho_{hp}\pi(r_1^2-r_0^2)(h+w_c)+C_f\rho_f\left(\frac{\pi}{\theta}w_l(r_2-r_1)h+\pi(r_2^2-r_1^2)w_c\right)}{C_{pcm}\rho_{pcm}\left(\pi(r_2^2-r_1^2)h-\frac{\pi}{\theta}w_l(r_2-r_1)h\right)}\right)$$

$$= \frac{C_{pcm}Gt_{op}}{L_{pcm}}\left(1+\frac{C_{hp}\rho_{hp}\theta(r_1^2-r_0^2)(h+w_c)+C_f\rho_f(w_l(r_2-r_1)h+\theta(r_2^2-r_1^2)w_c)}{C_{pcm}\rho_{pcm}(\theta(r_2^2-r_1^2)h-w_l(r_2-r_1)h)}\right) \quad \text{(A.11)}$$

$$\mathrm{g}(h,r_1,r_2,w_l,w_c,\theta) = \frac{C_{hp}\rho_{hp}\theta(r_1^2-r_0^2)(h+w_c)+C_f\rho_f(w_l(r_2-r_1)h+\theta(r_2^2-r_1^2)w_c)}{C_{pcm}\rho_{pcm}(\theta(r_2^2-r_1^2)h-w_l(r_2-r_1)h)} \quad \text{(A.12)}$$

During the derivation of the cost equation $\mathrm{g}(h,r_1,r_2,w_l,w_c,\theta)$ in Eqns. A.8, A.9 and A.10, an integer value is approximated by a real value in order to simplify the final objective expression. This simplification has little impact on the optimal solutions. In Eqn. A.11, only the second term is dependent on the design variables$(h,r_1,r_2,w_l,w_c,\theta)$, so Eqn. A.12 becomes the final cost equation to be used in the optimization formulation, which is the cost ratio between the heat pipe with fins and the PCM material. A smaller ratio value indicates smaller overall system cost. The prices of the PCM and the fin and heat pipe materials used in the optimization are shown in Table 4.7.

Table 4.7 Cost of materials

Materials	PCM ($CaCl_2 \cdot 6H_2O$)	Al-6061	Carbon-steel
Cost (\$/kg)	0.1	2.0	0.5

B. Discretized D^i, $L^i$and H^i

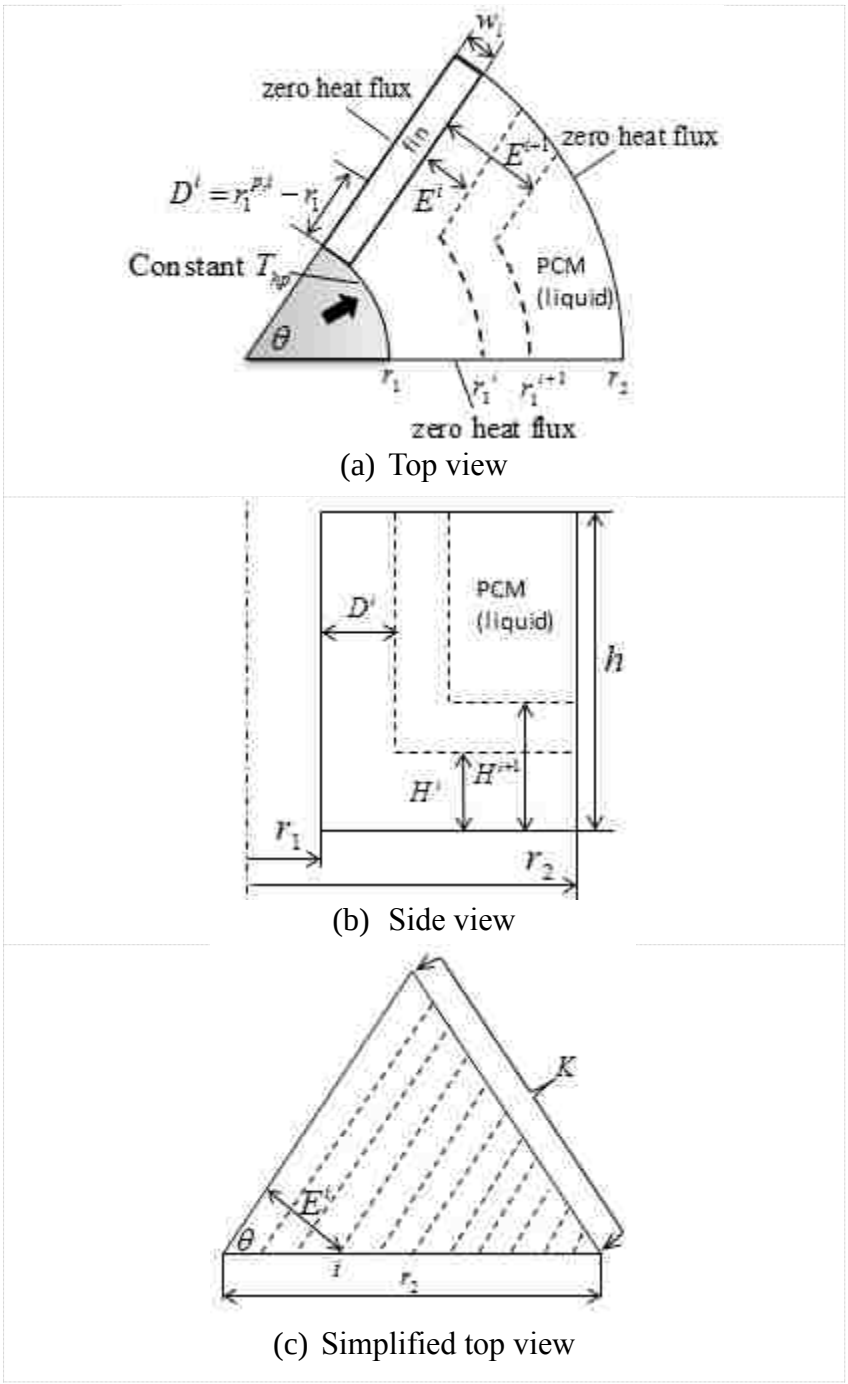

(a) Top view

(b) Side view

(c) Simplified top view

Figure 4.22 Schematic discretization of a 3D annular sector domain

The discretization strategy is that each new unsolidified PCM area (the dotted line) maintains the same annulus sector shape as the original shape of the PCM. This strategy allows for the PCM to solidify in a self-similar shrinking manner. It is assumed that there

are K shrinking annulus sectors (including the original one). So for each new annulus sector,$\theta = constant$, $r_2^i/r_1^i = constant$; and for all the shrinking annulus sectors, r_2^i is always located at its original position r_2 while the location for each r_1^i is $r_1^{p,i}$ =$r_2 - (r_2^i - r_1^i)$. Thus the solidification front distance D^i can be calculated as $D^i = r_1^{p,i} - r_1$ (Figure 4.22 (a)). The discretized solidification front along the height is $H^i = \frac{h}{K-1} i$ (Figure 4.22 (b)). E^i is an arc length but is approximated here. As shown in Figure 4.22 (c), the N shrinking annulus sectors are simply represented by a series of triangles, then $E^i = Asin(\theta)\frac{ir_2}{K-1}$, where A is a geometric factor to account for the use of a line segment to represent an arc. It is found that $A = \sqrt{\frac{\pi}{2}}$ gives good agreement for the finned LTR model.

C. Fin efficiency calculation

(a) Longitudinal fin

The fin extended from the heat pipe is approximated by a 1D conduction bar. As shown in Figure 4.23, it has a constant temperature at one end and a heat flux boundary condition on the PCM side; the other end and side have zero heat flux. Based on an energy balance of the bar, following is the fin efficiency calculation:

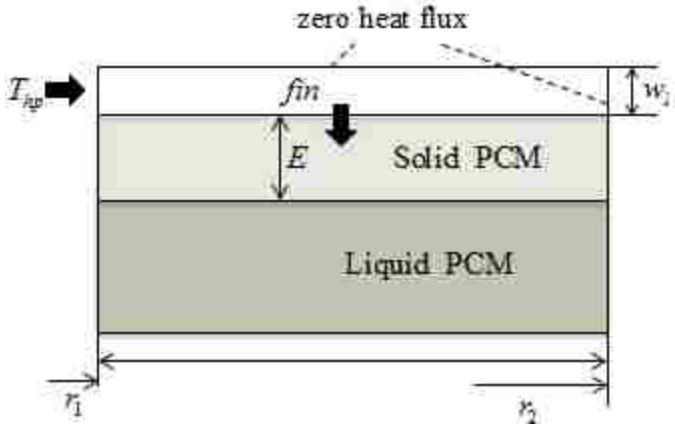

Figure 4.23 Geometry and boundary conditions for the 1D bar efficiency calculation

Energy balance on a small discrete element (Δx):

$$Q_c + \frac{dQ_x}{dx}\Delta x = 0, \qquad \text{C. a1}$$

where $Q_x = -k_f A\frac{dT}{dx}$, $Q_c = u_{pcm}S(T - T_{pcm})$, $A = \sigma w_l$, $S = \sigma\Delta x$, $u_{pcm} = k_{pcm}/E$. So,

$$\frac{d}{dx}\left(-k_f A\frac{dT}{dx}\right) + u_{pcm}S(T - T_{pcm}) = 0. \qquad \text{C. a2}$$

Assuming $\theta = T(x) - T_{pcm}$,

$$\frac{d^2\theta}{dx^2} - \frac{k_{pcm}}{k_f w_l E}\theta = 0. \qquad \text{C. a3}$$

With the boundary conditions, $\theta|_{x=0} = T_{hp} - T_{pcm}$, $\left.\frac{\partial\theta}{\partial x}\right|_{x=r_2-r_1} = 0$, and $\xi^2 = \frac{k_{pcm}}{k_f w_l E}$, the solution can be obtained as:

$$\theta = (T_{hp} - T_m)(cosh(\xi x) - tanh(\xi x)sinh(\xi x)). \qquad \text{C. a4}$$

Then the fin efficiency is:

$$\eta = \frac{T(x) - T_{pcm}}{T_{hp} - T_m} = cosh(\xi x) - tanh(\xi x)sinh(\xi x), \qquad \text{C. a5}$$

where E is the melting front distance away from the fin calculated in Appendix A. The heat transfer coefficient at the PCM side is assumed to be the conductivity of the PCM divided by the melting front distance, $u_{pcm} = k_{pcm}/E$. As E will affect the fin

efficiency, a reasonable layered discretization strategy to calculate E is important for the successful performance of the tuned LTR model coupled with fins. However for pure PCM domain modeling, E is not that important, because the tuning surface will correct for the effect of E.

(b) Circular fin

The fin extended from the heat pipe is approximated by a 1D conduction bar. As shown in Figure 4.24, it has a constant temperature at one end and heat flux boundary condition on the PCM side; the other end and side have zero heat flux. Based on an energy balance of the bar, the fin efficiency is:

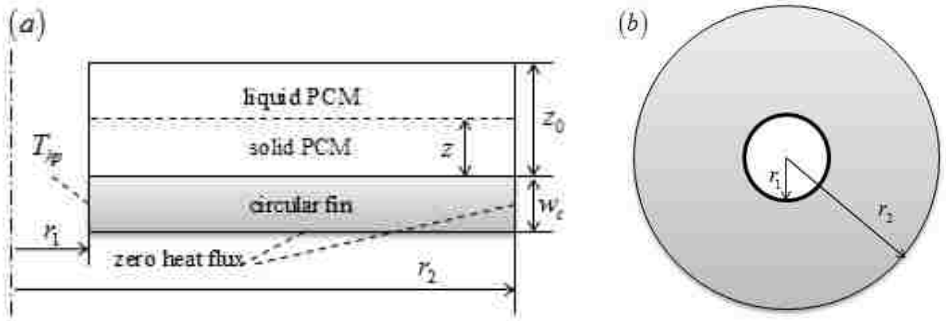

(a) Side view (b) Top view

Figure 4.24 Circular fin

$$Q_r = Q_{r+\Delta r} + Q_c \quad \text{C. b1}$$

$$Q_{r+\Delta r} = Q_r + \frac{dQ_r}{dr}\Delta r \quad \text{C. b2}$$

$$\frac{dQ_r}{dr}\Delta r + Q_c = 0 \quad \text{C. b3}$$

$$Q_r = -k_f 2\pi r w_c \frac{\mathrm{dT}}{dr} \quad \text{C. b4}$$

$$Q_c = u_{pcm} 2\pi r \Delta r (T - T_m) \quad \text{C. b5}$$

$$\frac{d}{dr}\left(-k_f 2\pi r w_c \frac{\mathrm{dT}}{dr}\right)\Delta r + u_{pcm} 2\pi r \Delta r (T - T_m) = 0 \quad \text{C. b6}$$

Introduce $\theta = (T - T_m)$, then Eqn. C.b6 becomes:

$$r\frac{d^2\theta}{dr^2} + \frac{d\theta}{dr} - \frac{u_{pcm}}{k_f w_c} r\theta = 0 \qquad \text{C. b7}$$

Set $s = \sqrt{\frac{u_{pcm}}{k_f w_c}} r$, then Eqn. C. b7 converts to,

$$s^2\frac{d^2\theta}{ds^2} + s\frac{d\theta}{ds} - s^2\theta = 0 \qquad \text{C. b8}$$

C.b8 is Modified Bessel's equation of zero order; its solution is given by

$$\theta = C_1 I_v(s) + C_2 K_v. \qquad \text{C. b9}$$

$$T(r) - T_{pcm} = C_1 I_v\left(\sqrt{\frac{u_{pcm}}{k_f w_c}} r\right) + C_2 K_v\left(\sqrt{\frac{u_{pcm}}{k_f w_c}} r\right), \qquad \text{C.b10}$$

where $I_v(s)$ is the modified Bessel function of the first kind; $K_v(s)$ is the modified Bessel function of the second kind. C_1 and C_2 are determined by the boundary conditions, $T|_{r=r_1} = T_{hp}$ and $\frac{\partial T}{\partial r}|_{r=r_2} = 0$

Chapter 5

Cost optimal design and sensitivity analysis of a shell and tube latent thermal energy storage system constrained by operational requirements

(Pan C., Vermaak N., Romero C., Neti S., et al. Cost optimal design and sensitivity analysis of a shell and tube latent thermal energy storage system constrained by operational requirements. *Applied Energy*, under review.)

Cost optimal design and sensitivity analysis of a shell and tube latent thermal energy storage system constrained by operational requirements

Chunjian Pan*[1], Natasha Vermaak[1], Carlos Romero[1], Sudhakar Neti[1],
Chien-Hua Chen[2], Richard Bonner III[2]
[1] Lehigh University, Bethlehem, PA 18015, USA
[2]Advanced Cooling Technologies, Inc., Lancaster, PA 17601, USA

Abstract

Shell and tube heat exchanger-based latent thermal energy storage (LTES) systems are promising configurations being considered for various thermal energy management applications. Due to their nonlinear and transient behavior, it is computationally expensive to optimize their design. LTES design optimizations are often based on parametric studies, which neglect the interaction between design variables in this complex system, resulting in unrealistic performance enhancements. In this paper, a general efficient modeling procedure for a shell and tube heat exchanger-based LTES unit is proposed. It is based on an explicit analytic solution for 1-D solidification in an annular geometry that is also developed in this paper. With this efficient computational procedure, a nonlinear programming formulation for cost optimization design of a shell and tube unit for the LTES system under operational constraints is presented. One of the main findings of the sensitivity analysis performed is that larger storage effectiveness is provided by smaller optimal heat transfer fluid (HTF) velocity in a single tube. The implication is that for a given heating/cooling load, more tubes are needed to handle a fixed amount of HTF mass flowrate, resulting in relatively higher storage capacity investment costs. This could indicate that the common practice of setting storage effectiveness as an optimization target is misleading. Other findings related to optimal PCM conductivity, HTF velocities, component geometry, and system costs are reported and discussed.

Key words: Shell and tube heat exchanger, Latent thermal energy storage, Analytic solidification solutions, Cost optimal design, Nonlinear programming

*: Corresponding author

Nomenclature

T_m	PCM melting temperature, ℃
T_w	Cooling temperature at the boundary, ℃
x	Moving solidification front, m
W	Length of 1-D PCM bar, m
Δx	Incremental length step, m
L_{pcm}	Latent energy of PCM, kJ/kg
k_{pcm}	PCM Conductivity, W/mK
C_{pm}	PCM specific heat, J/kgK
ρ_{pcm}	PCM density, kg/m^3
ε_r	Fraction factor for sensible energy for rectangular geometry
ε_c	Fraction factor for sensible energy for cylindrical geometry
$q_{1,2}$	Heat fluxes, W
A	Section surface area for the 1-D PCM bar, m^2
r_0	Inner radius of an annulus,m
r	Moving solidification front in annular geometry, m
r_w	Outer radius of the annular cylinder PCM, m
Δr	Incremental length step along the radial direction, m
Z	The axis length of the annular cylinder PCM, m
α	Ratio of solidification fronts between two coordinate systems
ρ_f	Density of the HTF, kg/m^3
C_{pf}	Heat capacity of the HTF, J/kgK
μ_f	Viscosity of the HTF, Pa · s
k_f	Conductivity of the HTF, W/mK
T^f	Temperature profile of the HTF in the tube, ℃
$T_i^{f,k}$	HTF tube temperature at a discrete point and time step, ℃
T^{pcm}	Temperature profile in the cylinder PCM, ℃
T_0	Interface temperature between the tube and the cylinder PCM, ℃
L	Total length of the tube, m
Δz	Incremental length step along the tube, m

T_{in}	Inlet temperature of the HTF, ℃
T_{out}	Output temperature of the HTF, ℃
u_f	HTF velocity of the HTF in the tube, $\mathrm{m/s}$
R_{pcm}^{i}	Thermal resistance within the cylinder PCM, $\mathrm{K/W}$
R_f	Thermal resistance within the HTF, $\mathrm{K/W}$
η	Latent energy storage effectiveness
Q_m	Mass flowrate of the HTF, $\mathrm{kg/s}$
Yrs	Total equipment lifetime, years
C_{op}	Operational cost, $\$/yr$
C_e	Price of electricity, $\$/\mathrm{kWhr}$
C_{tube}	Cost of tube material, $\$/kg$
C_{pcm}	Cost of PCM material, $\$/kg$
t_{op}	Hours of operation per day, hrs
ΔP	Pressure drop, Pa
Ω_p	Pump efficiency
P_s	Energy storage capacity cost, $\$/\mathrm{kWh}$

1. Introduction

Phase change materials (PCM) are receiving greater research attention as their high energy density during phase changes is a desired property for many thermal energy storage applications [1-3]. A shell and tube latent thermal energy storage (LTES) unit is one of the most popular configurations for study and application [4-13], as it is simple, compact and commercially available. Gasia et al. [8] experimentally tested the influence of the addition of fins and the use of two different heat transfer fluids in four different shell and tube heat exchanger-based LTES systems. Riahi et al. [9] numerically

investigated the performance of parallel and counter flow configurations of a shell and tube heat exchanger-based LTES system both in vertical and horizontal orientations. Kousha et al. [10] experimentally studied the performance of a shell and tube based LTES system subjected to inclination angle variations. Parsazadeh et al. [11] presented a numerical and statistical study of the heat transfer and energy storage performance of a vertical shell and tube LTES unit with CuO-water nanofluid in the tube and CuO nanoparticle enhanced PCM in the shell. Seddegh et al. [12] experimentally compared the heat transfer performance between cylindrical and conical vertical shell and tube based LTES systems. Riahi et al. [13] numerically studied characteristics and behaviors of LTES systems with plate fins multiple shell and tube configurations, including counter flow and parallel flow in vertical and horizontal orientations. The capital cost of shell and tube LTES for concentrating solar power applications was evaluated by Bai et al. [14].

Many studies have been conducted to improve the performance of a shell and tube LTES unit. Among them, the energy storage effectiveness is a popular parameter to be used to optimize the design of a LTES system to maximize the use of the thermal storage media [15-19]. Pirasaci and Goswami [19] employed the effective of the storage as the design criterion to study the influence of various parameters of a shell and tube model on direct steam generation power plants. Khan et al. [20] conducted parametric investigations to identify the enhancement in melting rate and thermal storage capacity of a novel geometrical configuration of a shell and tube LTES system through numerical study. Khan et al. [21] performed experiments to study the influence of operational conditions such as the inlet temperature and volume flowrate of heat transfer fluid (HTF)

on the thermal behavior of a LTES system. Niyas et al. [22] optimized the number of embedded tubes and fins on the tubes based on various performance parameters such as charging/discharging time, energy storage/discharge rate and melt fraction through numerical analysis. A group of optimal fin parameters was recommended by Yang et al. [23] by numerically investigating an annular finned shell and tube LTES unit. Tehrani et al. [24] optimized the geometric parameters of a shell and tube LTES system to achieve the highest amount of total stored/delivered energy with a minimum heat transfer surface area for a concentrated solar power plant application. In their study, a cost varying between 27 and 170 $/kWh was estimated for the optimized design. Often the optimizations to improve the performance of a shell and tube LTES are based on parametric studies [15-24], which neglect the interaction effects between design variables, making the findings suboptimal.

There are very limited research studies directly tackling the optimization of a shell and tube unit for minimal cost. Raud et al. [25] presented an optimal design approach for shell and tube or tube and fin containment vessels minimizing cost subject to geometric and performance constraints. Optimal results showed that a Na_2CO_3 based PCM that has 20% higher conductivity than that of the Na_2SO_3 based PCM can lower system costs even though Na_2CO_3 based PCMs are more than double the cost of Na_2SO_3 based ones. However, when relatively cheap aluminum fins were deployed, the thermal conductivity benefit of the Na_2CO_3 based PCM is reduced, and the cheaper priced Na_2SO_3 based PCM results in lower system cost.

Although direct optimal design approaches for minimal cost are rare in the literature for shell and tube LTES systems, there are many studies optimizing storage effectiveness,

charging/discharging time, or charging/discharging rate. However optimizing for these parameters will not necessary guarantee minimum system cost. For large scale LTES systems, it is of first priority to design the system to meet the operational requirements, i.e. total heating or cooling loads and targeted heating or cooling temperature, and system cost (including operational cost) must also be considered. Thus this paper proposes a nonlinear programming (NLP) formulation that directly finds the cost optimal configurations of a shell and tube unit and HTF flow rate simultaneously under given operational requirements.

One factor that complicates the mathematical optimization of a LTES system is its nonlinear and transient behaviors, which are typically computationally expensive to simulate. In order to facilitate NLP optimization of a shell and tube LTES system, first an efficient modelling method for a shell and tube unit is proposed in this paper. The advantage of the proposed simplified modeling method is that it does not involve solving systems of equations and therefore it has negligible computational cost. The modelling approach relies on a newly developed explicit analytic solution for solidification in 1-D annular geometries. To the best of the authors' knowledge, this is the first explicit solution of this kind available for annular geometries.

The content of this paper is organized as follows. In section 2, an explicit analytic solution for 1-D solidification in cylindrical coordinates is developed. Section 3 introduces the efficient modeling approach for a shell and tube LTES unit. Section 4 presents the NLP of a shell and tube LTES system and discussion of the results.

2. Explicit analytic solutions for 1-D solidification

The phase change phenomenon is a particular kind of moving boundary problem for a partial differential equation (PDE). By imposing the phase change temperature as the initial temperature, it was first solved analytically by Stefan [26]. The solution is in implicit form, as with a new boundary temperature, a nonlinear transcendental equation has to be solved. Neumann [27] extended Stefan's solution by considering an initial temperature that is not equal to the phase change temperature. However, these solutions cannot be directly/efficiently used as building module to construct a fast mathematical model for a shell and tube LTES, because the temperature input for the analytical solutions is a varying variable during the transient evolvement of the system, and thus at each time step a nonlinear equation is needed to be solved, which is computationally not trivial. To address this, an equivalent but explicit form of Stefan's solution is developed below.

2.1 Explicit analytic solution in rectangular coordinates

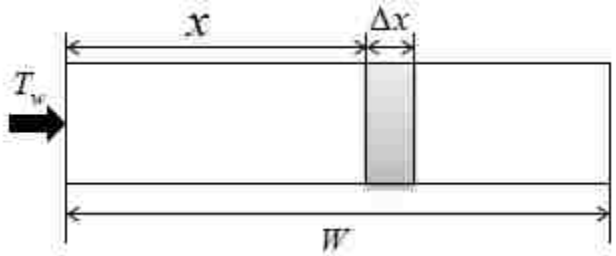

Figure 5.1 Sketch of 1-D PCM bar with constant temperature boundary

Fig. 5.1 shows a 1-D PCM bar with constant cooling temperature,T_w, at the left end while the right end is assumed to have zero heat flux. The proposed analytic solution is

obtained based on a physical description of the heat transfer process that the cooling energy flowing into the PCM bar through the boundary is equal to the energy change happening within it. The energy flow rate passing through the solid PCM to reach a small length of PCM Δx away from the cooling source with a distance x is determined by Fourier's Law (eqn. 2.1). At the same time, the energy going into the small portion of PCM,Δx, causes the PCM to be solidified. Eqn. 2.2 shows the rate of energy change within the small portion of the PCM. It includes the latent energy,L_{pcm}, and sensible energy,$\varepsilon_r C_{pm}(T_m - T_w)$; where ε_r is introduced to adjust the contribution of sensible energy as the temperature gradient is an unknown factor. ε_r would be equal to 1 if the temperature was equal to the boundary temperature everywhere within the solidified PCM section x. Later ε_r will be determined by an empirical study. Because the PCM bar is initialized at the exact phase change temperature T_m, there is no energy loss to the unsolidified PCM section. Thus $q_1 = q_2$, and the energy balance equation is established as eqn. (2.3).

$$q_1 = \mathrm{A}k_{pcm}\frac{T_{m-T_w}}{x}, \tag{2.1}$$

$$q_2 = \frac{\rho_{pcm}A\Delta x\left(L_{pcm}+\varepsilon_r C_{pm}\left(T_{m-T_w}\right)\right)}{\Delta t}, \tag{2.2}$$

$$\mathrm{A}k_{pcm}\frac{T_{m-T_w}}{x} = \frac{\rho_{pcm}A\Delta x\left(L_{pcm}+\varepsilon_r C_{pm}\left(T_{m-T_w}\right)\right)}{\Delta t}. \tag{2.3}$$

Evaluating eqn. (2.3) in the limit $\Delta x \to 0, \Delta t \to 0$ and after reorganizing, a differential equation is obtained:

$$\rho_{pcm}\left(L_{pcm} + \varepsilon_r C_p(T_m - T_w)\right)xdx = k_{pcm}(T_m - T_w)dt \tag{2.4}$$

With the initial condition $x(0) = 0$, an explicit expression of the moving solidification front is obtained by solving eqn. (2.4):

$$x = \sqrt{\frac{2k_{pcm}(T_m - T_w)t}{\rho_{pcm}\left(L_{pcm} + \varepsilon_r C_{pm}(T_m - T_w)\right)}} \tag{2.5}$$

Table 5.1 Representative thermal properties of PCM

Density ρ_{pcm}	Conductivity k_{pcm}	Heat Capacity C_{pm}	Latent Heat L_{pcm}
1600 kg/m^3	1.0 W/(mK)	2000 J/(kgK)	170 kJ/kg

2.2 Comparison of new explicit analytic solution with Stefan's solution

Given the representative PCM properties which are used throughout this paper (Table 5.1), the new explicit solution is compared to the classic Stefan's solution. It is found that the new analytic solutions proposed in this paper are equivalent to the classic solutions for Stefan's problem as it is assumed that the initial temperature in a finite bar uniformly equals the solidification temperature $T(x, 0) = T_m$. This assumption enables one to develop simplified analytic solutions for 1-D solidification in both rectangular and cylindrical coordinates with a finite length.

The driving temperature difference is defined as $\Delta T = T_m - T_w$. And the Stefan Number (St) is defined as:

$$\mathrm{St} = \frac{C_{pm}(T_m - T_w)}{L_{pcm}}. \tag{2.6}$$

Both Fig. 5.2 (a) and (b) show that $\varepsilon_r = 0.3$ gives a perfect match between the new analytic solution and the classic Stefan's solution. It can be concluded that $\varepsilon_r = 0.3$ is always applicable for the 1-D bar solidification problem with different St values. Thus

$\varepsilon_r = 0.3$ is used throughout the paper to account for the sensible energy during the solidification analysis for the 1-D PCM bar.

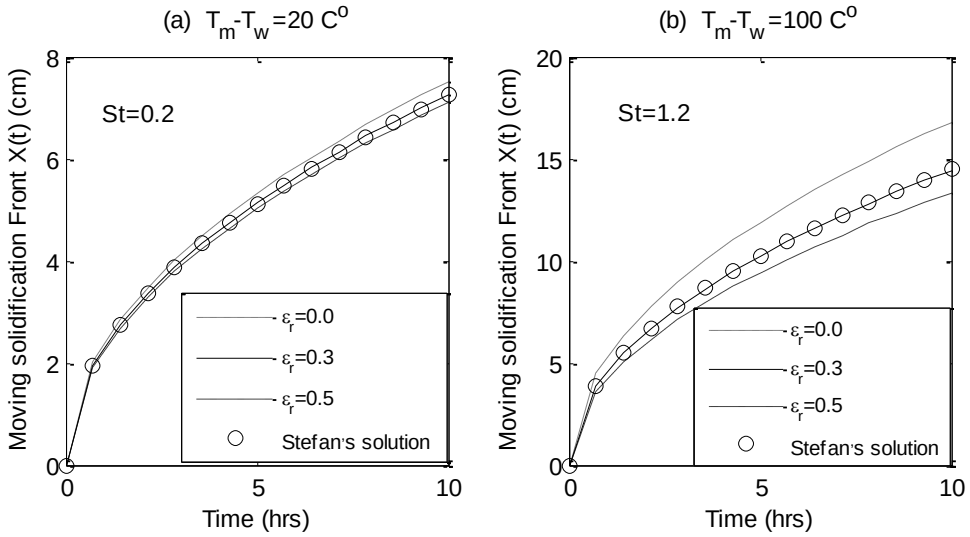

Figure 5.2 Comparison between the new explicit analytic solution and the classic Stefan's solution

2.2 Explicit analytic solution in cylindrical coordinates

To the best of the authors' knowledge, currently there are no explicit analytic solutions for annular solidification available in the literature. In this section, an analytic solution for 1-D PCM solidification for an annular shape is derived (Fig. 5.3), first in implicit and then explicit forms. The annular PCM is cooled at the inner radius with a constant temperature T_w and has zero heat flux at the outer radius. It is assumed that the initial temperature uniformly equals the solidification temperature $\mathrm{T}(x, 0) = T_m$.

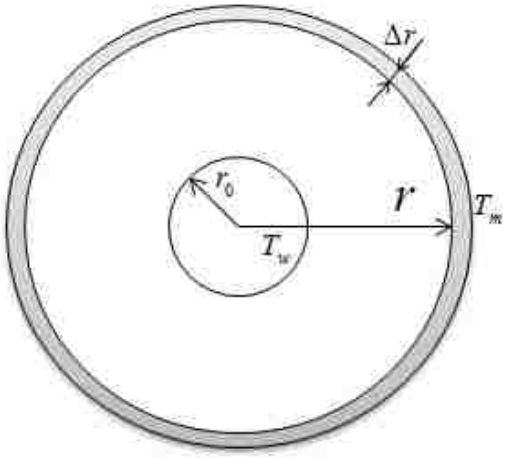

Figure 5.3 Sketch of 1-D annular PCM solidification

The derivation is the same as the 1-D bar case. Eqn. 2.7 shows that the energy flow rate passing through the solid PCM with a radial distance r equals the rate of energy change for the liquid PCM with a small annular distance Δr:

$$\frac{T_m - T_w}{\frac{ln(r/r_0)}{2\pi Z k_{pcm}}} = \frac{\rho_{pcm}\left(\pi(r+\Delta r)^2 - \pi r^2\right) Z\left(L_{pcm} + \varepsilon_c C_{pm}\left(T_{m-T_w}\right)\right)}{\Delta t}, \tag{2.7}$$

where Z is the axial length of the annulus; and an unknown factor ε_c is introduced to adjust the sensible energy $\varepsilon_c C_{pm}(T_m - T_w)$. Taking the limit $\Delta r \to 0, \Delta t \to 0$, eqn. 2.7 can be simplified:

$$r ln(r/r_0)\frac{dr}{dt} = \frac{k_{pcm}(T_m - T_w)}{\rho_l\left(L_{pcm} + \varepsilon_c C_{pm}(T_m - T_w)\right)}. \tag{2.8}$$

Integrating eqn. 2.8 with the initial condition $r(0) = r_0$, an implicit solution for the moving solid front r can be obtained:

$$\frac{1}{2} r^2 ln\left(\frac{r}{r_0}\right) - \frac{1}{4}(r^2 - r_0^2) = \frac{k_{pcm}(T_m - T_w)t}{\rho_{pcm}\left(L_{pcm} + \varepsilon_c C_{pm}(T_m - T_w)\right)}. \tag{2.9}$$

To verify the analytic solution and obtain a suitable value for ε_c, this problem was also solved numerically. The numerical solution is based on the enthalpy-porosity method [28]. Experimental validation of the simulation of the solidification phenomenon using the enthalpy method is available in Ismail's work [29].

Figs. 5.4-5.6 show comparisons of the analytic solutions and the numerical solutions with varying driving temperature differences, PCM conductivities and latent energy. For the current annular geometry, with $\varepsilon_c = 0.23$, there is a perfect match between the analytic solutions and the numerical ones. Here ε_c has a different value compared to ε_r for the 1-D bar case, because the different geometry results in a different temperature gradient for the sensible energy. Typically, a value in the range $[0.2,0.25]$ works equally well for the analytic solution. The factors ε_r and ε_c are quite robust for the analytic solution.

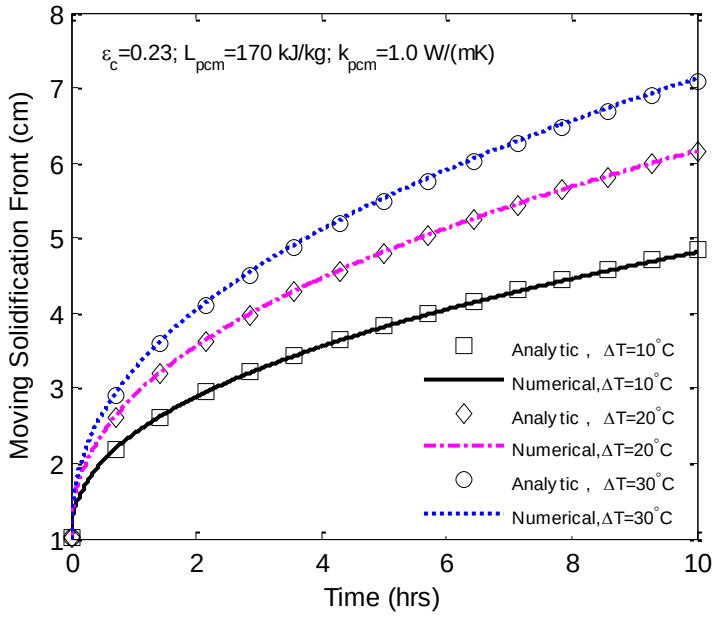

Figure 5.4 Moving solidification front under varying driving temperature differences

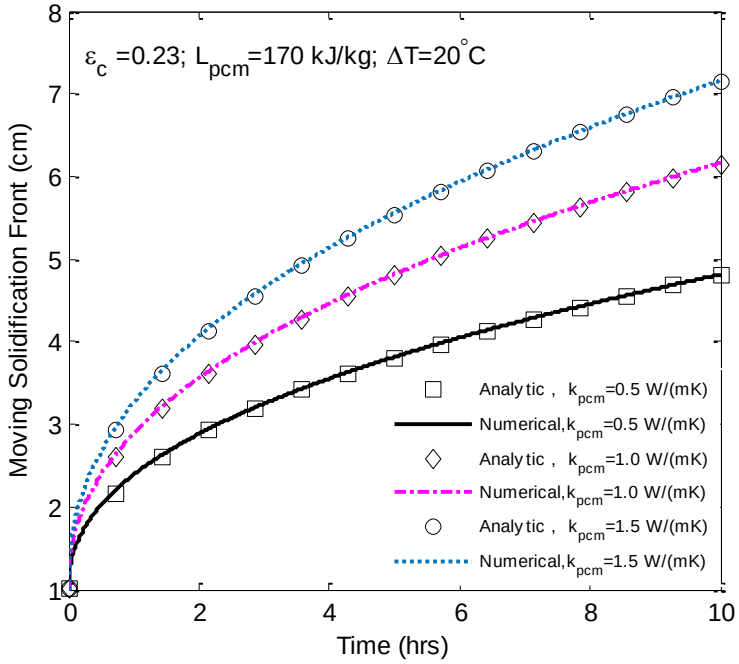

Figure 5.5 Moving solidification fronts with different PCM conductivities

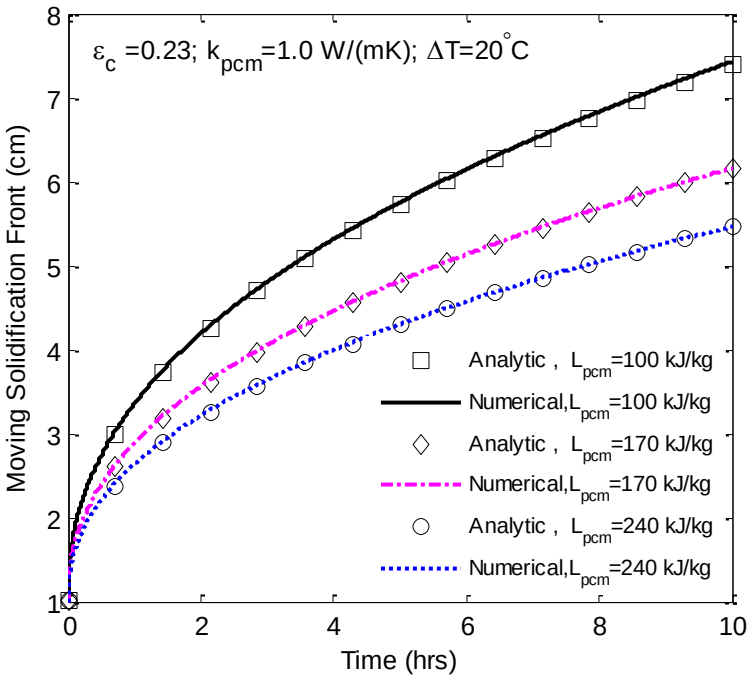

Figure 5.6 Moving solidification fronts with different PCM latent energy

Eqn. 2.9 gives an implicit expression for the moving solidification front of the 1-D annular shape. For application, often an explicit solution for the moving solidification front is desired, thus in this section, an explicit expression is developed. With the same material properties and boundary conditions, the different behaviors of the moving solidification front for the 1-D PCM bar and the 1-D annular PCM are essentially caused by geometrical effects. Thus the idea is to find a geometric factor to adjust the solidification behavior of the 1-D PCM bar, so that it can be used to represent the solidification behavior of the 1-D annular PCM.

To construct such a geometric factor, a geometric ratio between the moving solidification fronts of the 1-D PCM bar and annular PCM is introduced:

$$\alpha = \frac{r - r_0}{x}, \tag{2.10}$$

where r is the moving solidification front for the annular PCM (eqn.2.9), x is the moving solidification front for the 1-D PCM bar (see eqn. 2.5) and r_0 is the inner radius of the annulus. To investigate the behavior of the ratio α, variations of 4 parameters in Table 5.2 were considered. When one parameter varies within the given range, the other parameters are fixed at the baseline values. Fig. 5.7 shows the curves of the geometric factor α as a function of the moving solidification front of the 1-D PCM bar x. It is found that under the variations of the 4 different parameters, all of the curves almost overlap with each other for the same inner radius r_0. This confirms the assumption that the different behaviors of the moving solidification fronts in the two coordinate systems is only due to geometric effects. So it can be concluded that a correlation for the geometric factor $\alpha = \alpha(x, r_0)$ can be constructed based on the moving solidification front

of the 1-D PCM bar and inner radius of an annular cylinder. According to eqn. 2.10, an explicit expression for the moving solidification front can be obtained:

$$r(t) = \alpha(x(t), r_0)x(t) + r_0, \tag{2.11}$$

where $x(t)$ is calculated from eqn. 2.5.

Table 5.2 Parameters used to determine the geometric ratio α

Parameters	Solidification time t_s	Temperature difference $\Delta T = T_m - T_w$	PCM conductivity k_{pcm}	Latent energy L_{pcm}
Range	$(0.01 - 50)$ hrs	$(1 - 40)$ ℃	$(0.01 - 4.)\ \frac{\text{W}}{\text{mK}}$	$(60 - 300)\ \frac{\text{kJ}}{\text{kg}}$
Baseline value	10 hrs	20 ℃	$1.0\ \frac{\text{W}}{\text{mK}}$	$170\ \frac{\text{kJ}}{\text{kg}}$

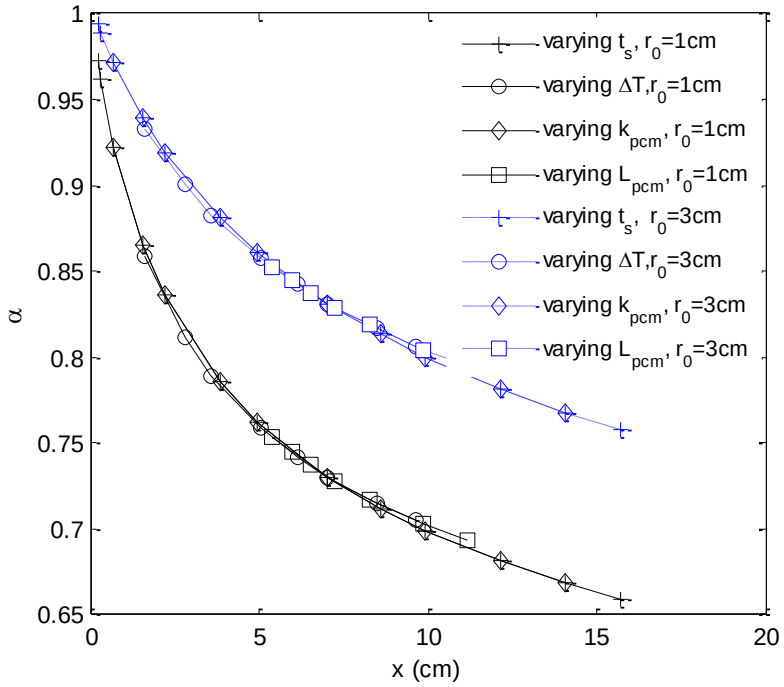

Figure 5.7 Moving solidification front ratios between 1-D bar PCM and annular PCM under varying parameter values

To construct the geometric factor α, a bivariate cubic tensor-product spline [30] was determined. The derivation and the resulting explicit expression for $\alpha = f_s(x, r_0)$ are presented in Appendix A. Table 5.3 shows 3 test cases for the explicit formulation, eqn.2.11. Fig. 5.8 shows excellent agreement between the explicit solution and the implicit solution. Thus an explicit analytic solution for the moving solidification front of an annular geometry is obtained.

Table 5.3 Test cases for the explicit annular moving solidification front solution

Case	r_0 (cm)	k_{pcm}(W/mk)	L_{pcm} (kJ/kg)	dT (°C)
#1	2.0	2.0	200	30
#2	3.0	1.5	150	15
#3	4.0	0.5	100	10

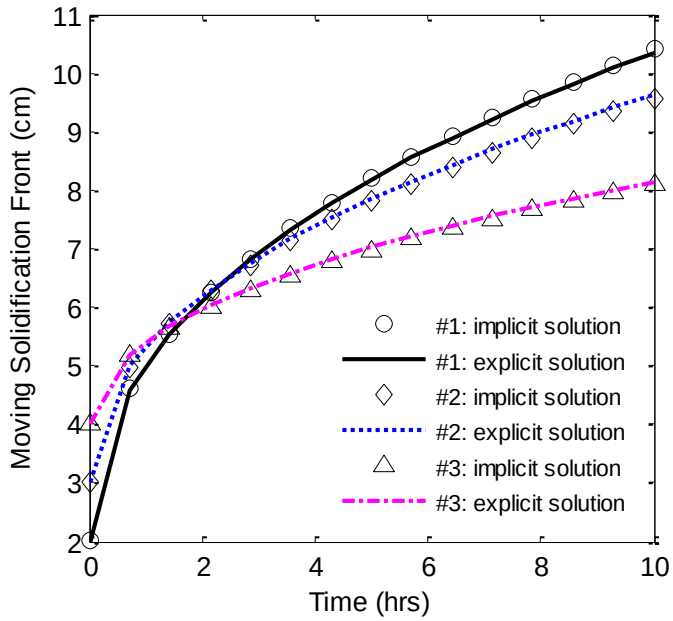

Figure 5.8 Comparison between the explicit and implicit solutions for the annular moving solidification front based on the 3 test cases in Table 5.3.

3. Efficient simulation procedure for a shell and tube LTES unit

The physical module of a shell and tube latent heat storage exchanger consists of a tube surrounded by a PCM cylinder (Fig. 5.9). A heat transfer fluid (HTF) flows through the inner tube and exchanges heat with the PCM. For a mathematical description of the process, the following assumptions are made: (1) the HTF is incompressible and viscous dissipation is negligible; (2) the HTF is radially uniform; (3) heat transfer in the PCM is conduction controlled; (4) the outer wall of the PCM is adiabatic; (5) PCM properties are constant; (6) the tube wall thickness is neglected, thus no thermal resistance of the wall is considered; (7) conduction in the HTF along the length of the tube is neglected.

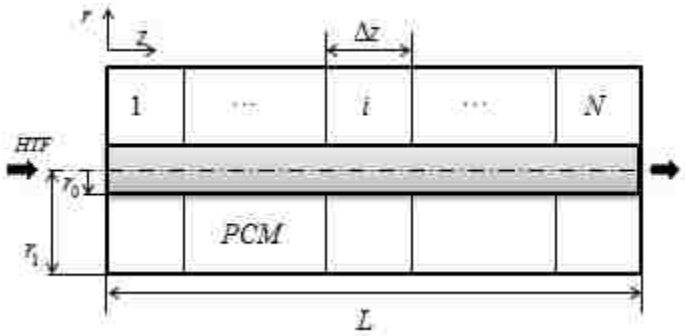

Figure 5.9 A shell and tube latent energy storage unit

Based on the above assumptions, the governing equation for energy transfer of the HTF in the tube is:

$$\rho_f C_{pf}\left(\frac{\partial T^f}{\partial t}+u\frac{\partial T^f}{\partial z}\right)=\frac{2h_f}{r_0}(T_0-T^f), \tag{3.1}$$

and the energy balance within the PCM is:

$$\rho_l\frac{\partial H}{\partial t}=\frac{1}{r}\frac{\partial}{\partial r}\left(k_s r\frac{\partial T^{pcm}}{\partial r}\right)+\frac{\partial}{z}\left(k_s\frac{\partial T^{pcm}}{\partial z}\right), \tag{3.2}$$

where the enthalpy H is defined in Eqn.2.23, and h_f is the heat transfer coefficient within the HTF. The calculation of h_f is available in many heat transfer text books [31]. The

tube wall temperature is $T_0 = T^{pcm}|_{r=r_0}$, which acts as the interface temperature boundary between the HTF in the tube and the PCM cylinder. The initial conditions are:

$$T^f(0,z) = T_m,\ T^{pcm}(0,r,z) = T_m,\ for\ r_0 \le r \le r_w, 0 \le z \le L, \tag{3.3}$$

and the boundary conditions are:

$$\left.\frac{\partial T^{pcm}}{\partial z}\right|_{z=0} = 0,\ \left.\frac{\partial T^{pcm}}{\partial z}\right|_{z=L} = 0, \quad for\ r_0 \le r \le r_1; \tag{3.4}$$

$$\left.\frac{\partial T^{pcm}}{\partial r}\right|_{r=r_1} = 0, \quad for\ 0 \le z \le L; \tag{3.5}$$

$$T^f\big|_{z=0} = T_{in},\ \left.\frac{\partial T^f}{\partial z}\right|_{z=L} = 0, \quad for\ 0 \le r \le r_0. \tag{3.6}$$

The interface condition between the HTF and the PCM cylinder is:

$$h_f\left(T^f - T^{pcm}|_{r=r_0}\right) = -k_{pcm}\left.\frac{\partial T^{pcm}}{\partial r}\right|_{r=r_0},\ for\ 0 \le z \le L. \tag{3.7}$$

The system can be solved by the finite element method. Due to the nonlinear behavior of the latent energy of the PCM, at each discretized time step, a nonlinear system of equations needs to be solved. In this section, by employing the explicit solution of the moving solidification front (Eqn. 2.11), an efficient numerical approach, which does not require the solution of any systems of equations for the modeling of a shell and tube LTES unit (Fig. 5.9), is proposed.

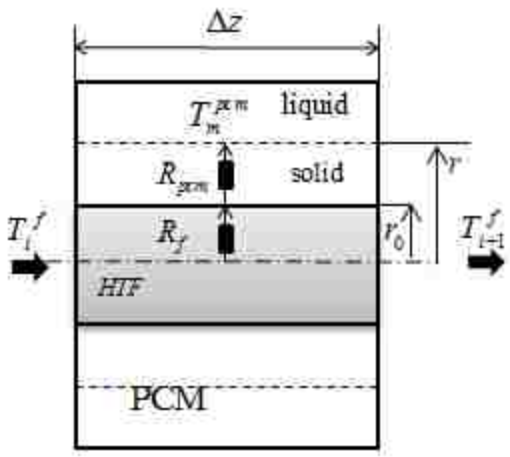

Figure 5.10 Thermal resistance scheme of element i based on Fig. 5.9

Fig. 5.10 shows a thermal resistance scheme of an element i from Fig. 5.9 for the development of an efficient modeling approach. It is assumed that the process is based on solidification, so that the explicit solution (eqn. 2.11) can be employed here (as the solidification is conduction controlled [32]). Thus the thermal resistance within the PCM for cooling energy from the tube to reach the solidification front,r, is:

$$R_{pcm}^{i}(t) = \frac{ln(r_i(t)/r_0)}{2\pi\Delta z k_s}. \tag{3.8}$$

A constraint should be set here that:

$$\text{when } r > r_1,\ R_{pcm}^{i}(t) = \infty \ and\ r(t) = r_1. \tag{3.9}$$

This can be implemented either by an 'if' condition statement, or by employing a logistic function to combine eqns. 3.8 and 3.9 in one expression:

$$R_{pcm}^{i}(t) = \frac{ln(r_i(t)/r_0)}{2\pi\Delta z k_s} + \frac{200}{1+e^{-500(r_i(t)-r_1)}}. \tag{3.10}$$

This expression is recommended for the optimization process. The thermal resistance within the HTF is:

$$R_f = \frac{1}{2\pi r_0 \Delta z h_f}. \tag{3.11}$$

With $N+1$ discrete points along the length of the tube, a finite discrete form of the energy balance equation for element i $(2 \le i \le N+1)$ (Fig. 5.10) is:

$$\frac{dT_i^f}{dt} + u\left(\frac{T_i^f - T_{i-1}^f}{\Delta z}\right) = \frac{2\pi r_0 h_f}{\rho_f C_{pf} \pi r_0^2}\left(T_0 - \frac{1}{2}\left(T_i^f + T_{i-1}^f\right)\right). \tag{3.12}$$

By applying the thermal resistance concept, the thermal resistance within the PCM can be directly incorporated into eqn. 3.12:

$$\Delta z \frac{dT_i^f}{dt} + u\left(T_i^f - T_{i-1}^f\right) = \frac{1}{\rho_f C_{pf} \pi r_0^2} \frac{\left(T_m - \frac{1}{2}\left(T_i^f + T_{i-1}^f\right)\right)}{R_f + R_{pcm}^{i-1}(t)}. \tag{3.13}$$

The thermal resistance within the PCM, $R_{pcm}^i(t) = f(r_i)$, is a function of the moving solidification front r, while $r = g(T_0, r_0, t)$ is a function of time and the boundary temperature condition (Eqn. 2.11). The interface temperature,T_0, is determined by the thermal resistance network, and it can be expressed as:

$$T_0^{i-1} = \frac{0.5\left(T_i^f + T_{i-1}^f\right)R_{pcm}^{i-1}(t) + R_f T_m}{R_{pcm}^{i-1}(t) + R_f}. \tag{3.14}$$

Implementing an implicit scheme for eqn. 3.11, it becomes:

$$\Delta z \frac{T_i^{f,k+1} - T_i^{f,k}}{\Delta t} + u\left(T_i^{f,k+1} - T_{i-1}^{f,k+1}\right) = \frac{1}{\rho_f C_{pf} \pi r_0^2} \frac{\left(T_m - 0.5\left(T_i^{f,k+1} + T_{i-1}^{f,k+1}\right)\right)}{R_f + R_{pcm}^{i-1}(t^k)}. \tag{3.15}$$

Setting $\Psi(t^k, i) = \frac{1}{\rho_f C_{pf} \pi r_0^2} \cdot \frac{1}{R_f + R_{pcm}^{i-1}(t^k)}$, and rearranging Eqn. 3.15, the overall calculation procedure is shown as follows, (which does not involve solving any systems of equations):

First, initialize the temperature profile in the tube

$T_i^{f,1} = T_{in},\ T_0^{i-1,1} = T_{in},\ 1 \le \mathrm{i} \ll \mathrm{N}+1;$

then $for \quad 1 \le \mathrm{k} \le \mathrm{K}$

$T_1^{f,k+1} = T_{in},$

$for\ 2 \le \mathrm{i} \le \mathrm{N}+1$

$r_{i-1}^k = g\left(T_0^{i-1,k}, r_0, t^k\right)$

$if \quad r_{i-1}^k > r_1$

$r_{i-1}^k = r_1;$

$R_{pcm}^{i-1}(t^k) = e^9;$

$else$

$R_{pcm}^{i-1}(t^k) = f\left(r_{i-1}(k)\right);$

end

$\Psi(t^k, i) = \frac{1}{\rho_f C_{pf} \pi r_0^2} \cdot \frac{1}{R_f + R_{pcm}^{i-1}(t^k)};$

$T_i^{f,k+1} = \frac{1}{\frac{\Delta z}{\Delta t} + u + \frac{1}{2}\Psi\left(t^k, i\right)} \left[\Psi(t^k, i) T_m + \frac{\Delta z}{\Delta t} T_i^{f,k} + \left(u - \frac{1}{2}\Psi(t^k, i)\right) T_{i-1}^{f,k+1}\right];$

$T_0^{i-1,k+1} = \frac{0.5\left(T_i^{f,k+1} + T_{i-1}^{f,k+1}\right) R_{pcm}^{i-1}\left(t^{k+1}\right) + R_f T_m}{R_{pcm}^{i-1}\left(t^{k+1}\right) + R_f};$

end

end

The above calculation procedure can be called a simplified shell and tube LTES unit model. In contrast, the finite element approach in [33] can be called a coupled finite element (FE) model. Verification of the simplified model presented here is achieved by comparing results to that of the coupled FE model previously described in [33]. It is assumed that water is used as the heat transfer fluid (HTF). The properties of water used are shown in Table 5.4. The PCM properties are available in Table 5.1. Two cases with varying inlet mass flow rates, temperatures and tube radii and lengths that are listed in

Table 5.5 were used to test the performance of the proposed simplified model. The other information needed for the simulations is also shown in Table 5.5.

Table 5.4 Properties of water

Density ρ_f	Conductivity k_f	Heat Capacity C_{pf}	Viscosity μ_f
988.2 $(\mathrm{kg/m^3})$	0.59846 (W/mK)	4184.1 (J/kgK)	1.0016e^{-3} (Pa · s)

Table 5.5 Test cases for the simplified shell and tube LTES unit model

Case	Inlet mass flowrate Q_m(kg/s)	Tube radius r_0 (cm)	Inlet HTF Temperature (℃)	Tube length L (m)
#1	0.001	1	10	1.0
#2	0.01	3	0	2.0
Outer radius of the cylinder PCM surrounding the tube $r_w = 10$ cm; Simulation time: 10 hrs.				

First, grid and time step independence studies were performed for the coupled FE model based on Case 1 in Table 5.5. The code for the coupled FE method is implemented in MATLAB. In Fig. 5.11, *N* is the number of grid elements along the length of the tube; *M* is the number of grid elements along the radial direction assigned to the cylinder PCM domain; *K* is the total number of time steps for the 10-hour simulation period. It can be seen that in order to capture the transient peak temperature well, a fine grid is needed along the radial direction for the cylinder PCM domain. It was found that a suitable total number of steps is around 3600. It costs about 1 hour to run a simulation with *N*=200, *M*=150 and *K*=3600 on a desktop with an Intel(R) Core™ i7-2600 processer (CPU: 3.4GHz). Depending on the size of the problem and also the efficiency of the coding, the computational cost typically ranges from minutes up to more than 1 hour.

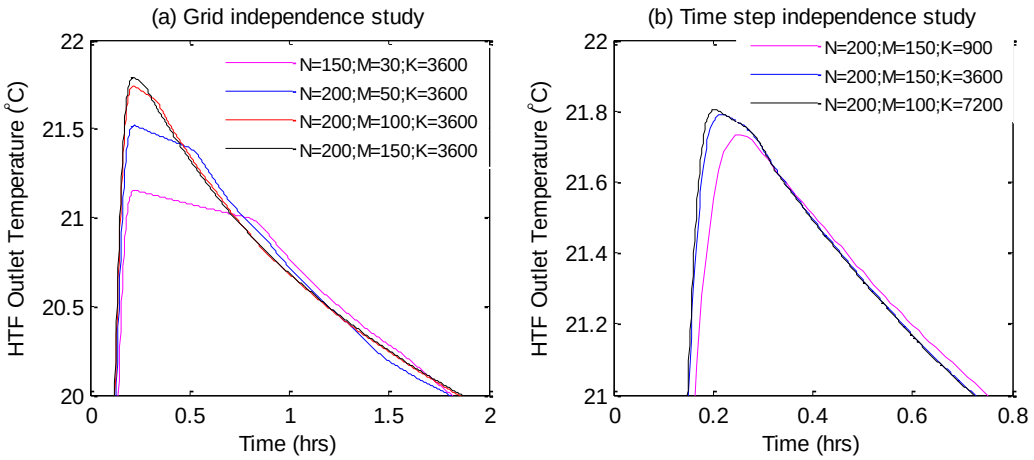

Figure 5.11 Grid and time step independence studies for the fully coupled shell and tube LTES unit model

A grid and time step independence study for the simplified model was also performed based on the same case. It can be seen from Fig. 5.12 that a suitable total number of grid elements along the length of the tube is N=50; and a suitable total number of time steps is K=3600. It costs less than 4 seconds to run a simulation with N=50 and K=3600 on the same computer used for the coupled studies.

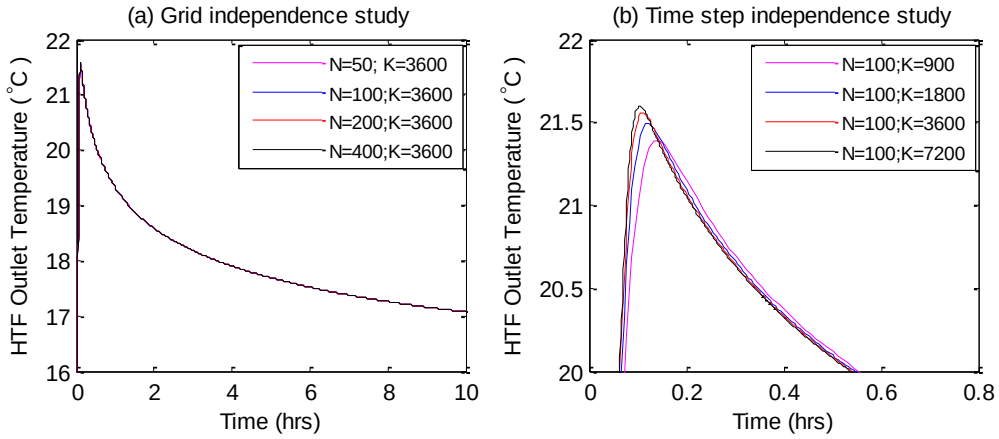

Figure 5.12 Grid and time step independence studies for the simplified shell and tube LTES unit model

Fig. 5.13 shows the outlet temperatures of the two cases for a 10-hour period simulation. It shows that the simplified model has overall a very good agreement with the coupled FE model, although there is a small deviation for both of the cases studied (less than around 7%). Fig. 5.14 indicates a possible source for the difference: it shows that the solidification fronts of the two cases with the two modeling approaches are also slightly different. One possible reason is that heat transfer happens in 2-D within the PCM domain for the coupled FE model while for the simplified model, heat transfer is assumed to occur in 1-D. Nevertheless, such small differences are acceptable for system level analysis. Considering the negligible simulation time, the proposed simplified modeling approach for a shell and tube LTES unit would be very useful for optimal design and operational research. From Fig. 5.14, it can be seen that the solidification front of Case 2 has a much smaller slope than that of Case 1. The implication is that the PCM in Case 2 is being used more effectively. Thus, optimal configurational design and operational research is needed to improve the performance of a LTES system, and at the same time to lower the system cost. Furthermore, the proposed modeling method may provide efficient modeling for a large scale LTES system. A complex large scale LTES system can be described as an assembly of identical modules, and the overall behavior of the system can be simulated in an interactive way. The key is to build an efficient characteristic model for a single module, i.e., the proposed analytic approach for the solidification front.

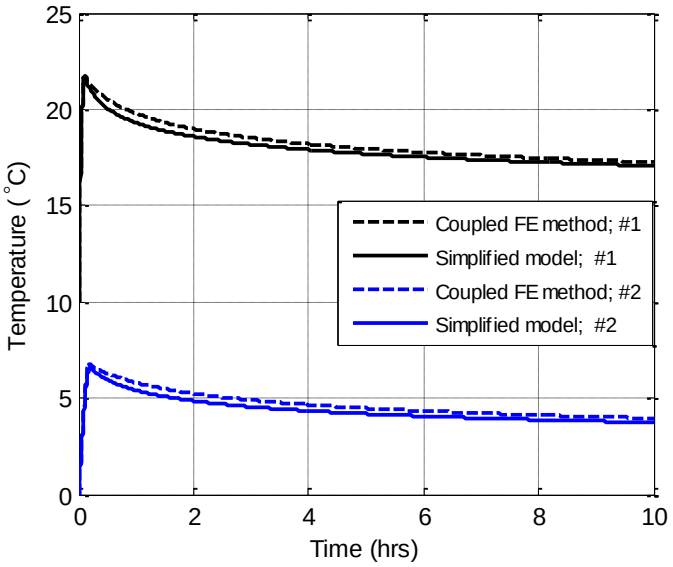

Figure 5.13 Performance of the simplified shell and tube LTES unit model

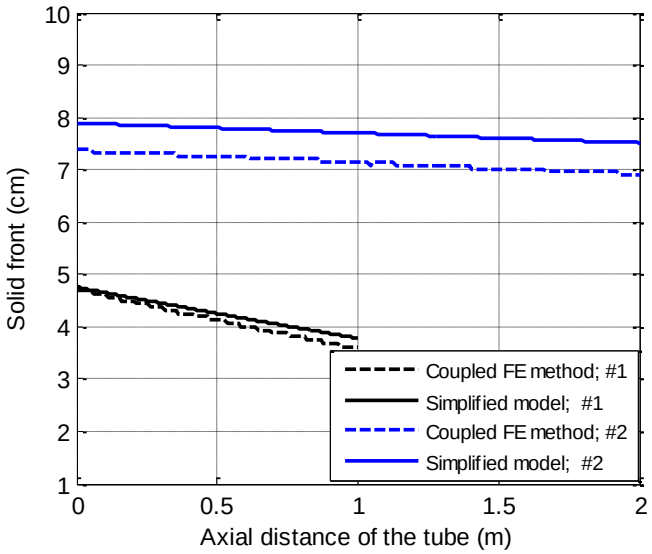

Figure 5.14 Solidification fronts in the radial direction along the tube after a 10-hour simulation

4. Optimal design and sensitivity analysis of a shell and tube LTES

In this section, given requirements for output temperature, operational time, and the storage capacity of a shell and tube LTES, an optimization formulation for minimal

material and operational cost is presented (Eqn. 4.1). There are four design variables: the tube radius r_0, the outer PCM radius r_1, the tube length L and the HTF velocity in the tube u_f. The operational parameter u_f plays an important role. It not only can affect the operational cost but also influence the investment. For example, for a given storage capacity, a small u_f requires more tubes to handle a fixed amount of HTF mass flowrate. The derivation of the cost function $C(\cdots)$ which includes the investment and operational costs is presented in Appendix B. The function $F(\cdots)$ represents the efficient computational approach presented in Section 3. The output $T_N^{f,K}$ of F is the HTF temperature of the last element in the tube at its final operation time t_{op}. During the whole operational time, it could be required by the application that the output temperature should always be larger than T_{out}. Thus, the output temperature of the LTES should meet this constraint at its final operation time, $T_N^{f,K} = T_{out}$. Some upper and lower limits of the design variables are also given in the formulation (Eqn. 4.1). As it is a nonlinear constrained optimization problem, 'fmincon' (a gradient based method) within the MATLAB optimization toolbox was employed to solve the problem [35]. The time cost of the optimization varies from several minutes to an hour (given the computing power outlined in SECTION 3). The problem has multiple local minima, thus it is recommended to test several initial conditions before choosing the final optimal one.

$$
\begin{aligned}
\underset{u_f, r_0, r_1, L,}{min} \quad & C\left(u_f, r_0, r_1, L, t_{op}, T_{in}, T_m\right) \\
& T_N^{f,K} = F\left(u_f, r_0, r_1, L, t_{op}, T_{in}, T_m\right) \\
& T_N^{f,K} = T_{out} \\
\text{s.t.} \quad & 1.0 \text{ cm} \le r_0 \le 3.0 \text{ cm} \\
& 5 \text{ cm} \le r_1 \le 8 \text{ cm} \\
& 0.5 \text{ m} \le L \le 3 \text{ m} \\
& 0.0001 \text{ m/s} \le u_f \le 0.01 \text{ m/s}
\end{aligned} \tag{4.1}
$$

A sensitivity analysis of the six system parameters on the optimal results is given in Table 5.6. When one variable is altered, the others are fixed at the baseline values. The PCM properties being used are shown in Table 5.1 and the properties of the HTF are available in Table 5.4. The optimal design trend under variation of the system variables is of interest in this paper.

Table 5.6 Parameters for Sensitivity Analysis

Parameters	Baseline case values
Total HTF mass flowrate, Q_m	5 (kg/s)
Required operational time, t_{op}	6 (hrs)
Effectiveness, ϵ	0.5
PCM conductivity, k_{pcm}	1.0 (W/mK)
PCM latent energy, L_{pcm}	170 (kJ/kg)
Lower bound of the tube radius, r_0^l	1.0 (cm)
Lower bound of the tube length, L^l	0.5 (m)

Effectiveness is defined as [15],

$$\eta = \frac{T_{out} - T_{in}}{T_{pcm} - T_{in}}. \tag{4.2}$$

Given the HTF inlet temperature T_{in} and a certain PCM, the effectiveness of the LTES can be specified by the output temperature of the HTF. In contrast to previous studies

[15-19], this parameter is not a design goal but is instead an important system parameter under investigation in this paper. It is preferred as a system parameter because the inlet and outlet temperatures are usually determined by the application, and the choice of a PCM from a group of suitable candidates will finally determine the effectiveness. Based on the optimal results, it is found that the optimal tube length is always located at its lower bound, thus the lower bound of the tube length is also considered as a system variable for the sensitivity analysis.

Figs. 5.15-5.20 show the optimal results under the variation of a system variable. In each figure, subplot (a) is the optimal u_f, (b) is the optimal radial ratio r_1/r_0 between the outer radius of the cylindrical PCM and the tube, (c) is the optimized yearly investment and operational cost C_{total} and (d) is the optimized energy storage capacity cost P_s, which is defined as

$$P_s = \frac{yearly\ cost}{yearly\ transfered\ energy} = \frac{C_{total}}{365 Q_m C_{pf} (T_{out} - T_{in}) t_{op}}. \tag{4.3}$$

The yearly cost C_{total} is presented in Appendix B. Q_m is the total HTF mass flowrate. It is assumed that the LTES operates once a day. The yearly cost may not be able to be used for fair comparison due to variation of the heating/cooling capacity, thus the energy storage capacity cost is introduced. Different heating/cooling capacities due to variation of a system variable are marked on subplots (c).

From Fig. 5.15, it can be seen that the yearly investment and operational cost of the LTES system scales up linearly with respect to the HTF mass flowrate. The energy storage capacity cost is independent of the HTF mass flowrate. Fig. 5.16 shows the sensitivity analyses of the effectiveness. The optimal HTF velocity is highly dependent

on the effectiveness. Higher effectiveness results in a smaller optimal velocity. Its effect on the optimal radii is relatively small. The energy storage capacity cost shows lower effectiveness is more economic than a system with a higher effectiveness. This also suggests that direct cost optimization is more appropriate than setting effectiveness as an optimization target as is done in references [15-19]. In terms of the competiveness of a LTES system, higher effectiveness is usually achieved at a lower HTF velocity, which means more tubes are required for a given heating or cooling load. Thus higher effectiveness could result in larger system volume and higher capacity cost. Fig. 5.17 shows the sensitivity results of the heating/cooling operational time. The operational time does not affect the optimal HTF velocity as much as its effect on the optimal radial ratio. Longer operational times require larger radial ratios and have lower energy storage capacity costs.

Figs. 5.18-5.20 have the same heating/cooling load. Either the yearly cost or the capacity cost can reveal the economic effect of the variable under consideration. Smaller PCM conductivity requires smaller HTF velocity and smaller radial ratio to achieve optimal cost. Smaller PCM latent energy requires larger optimal radial ratio while its effect on the optimal HTF velocity is small. The length of the tube almost has no influence at all on the system cost and optimal radial ratio. But a longer tube allows for larger HTF velocity.

Figs. 5.18-5.19 also show that both higher PCM conductivity and larger latent energy can result in lower system cost. The melting temperature of the PCM also influences the effectiveness, thus sensitivity comparisons of the three variables: PCM melting temperature, conductivity and latent energy on the sensitivity of energy storage

capacity cost is shown in Fig. 5.21. It can be seen that the effectiveness has a first-order sensitivity effect, followed by the latent energy and then conductivity. This finding could provide some guidance when selecting a PCM from a group of suitable candidates.

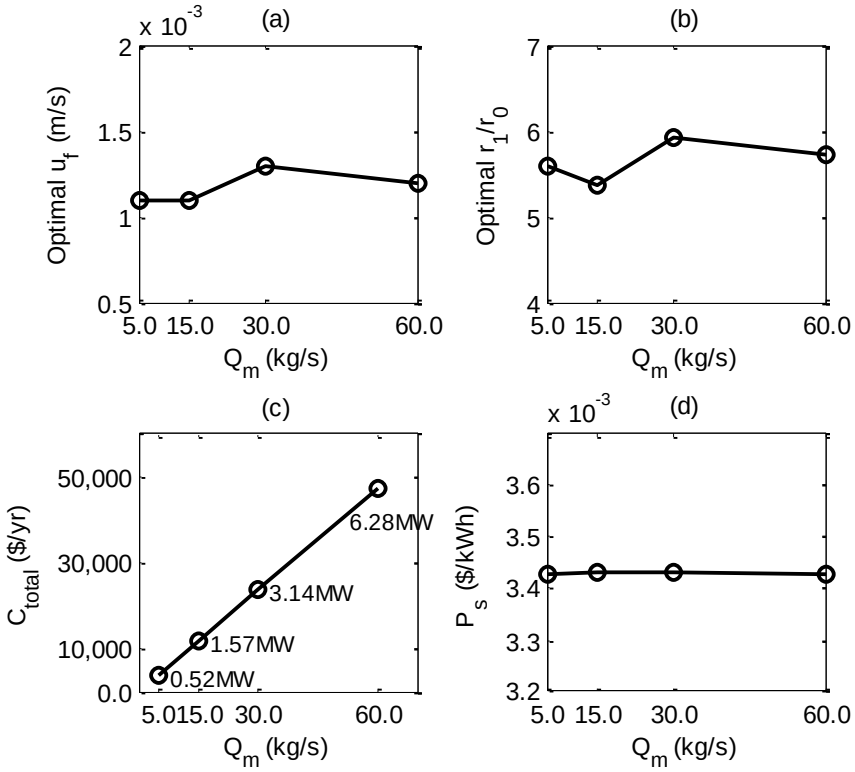

Figure 5.15 Optimal results under varying HTF mass flowrate

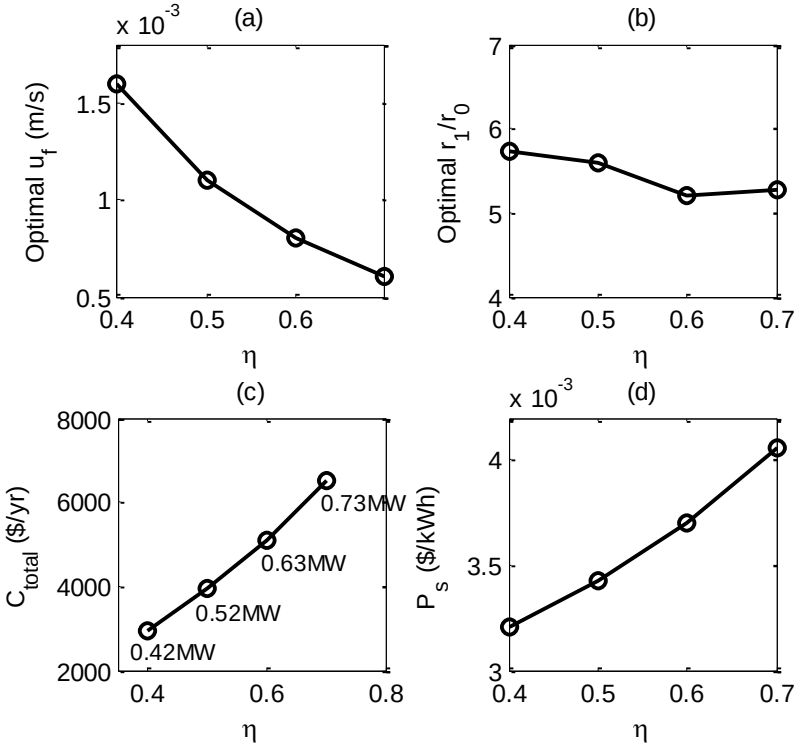

Figure 5.16 Optimal results under varying effectiveness

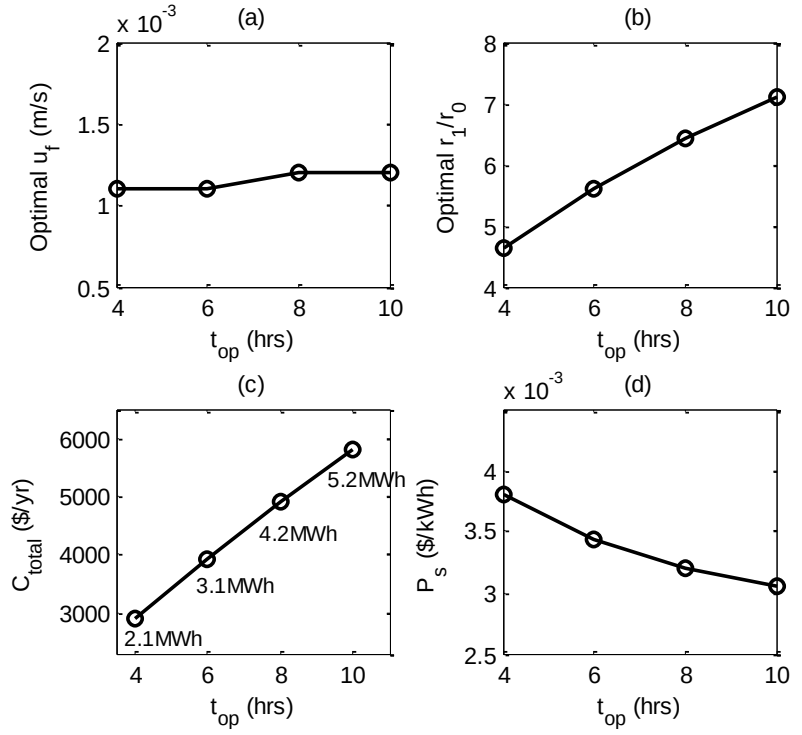

Figure 5.17 Optimal results under varying operational time

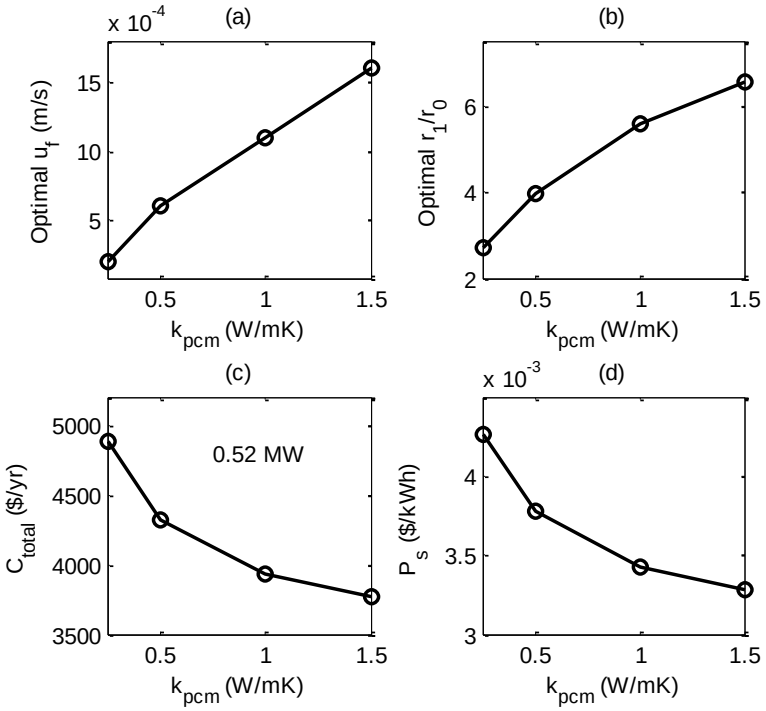

Figure 5.18 Optimal results under varying PCM conductivity

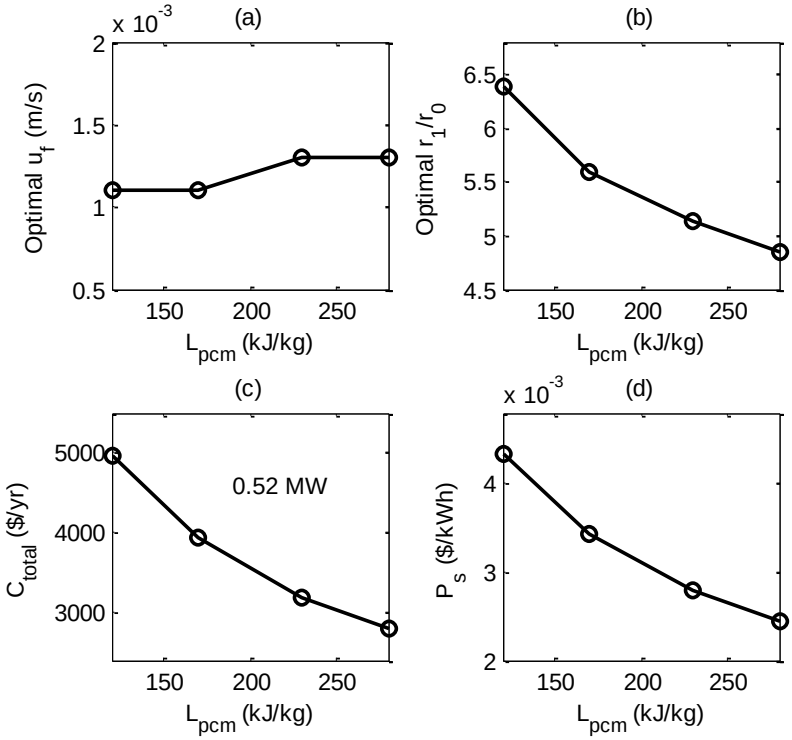

Figure 5.19 Optimal results under varying PCM latent energy

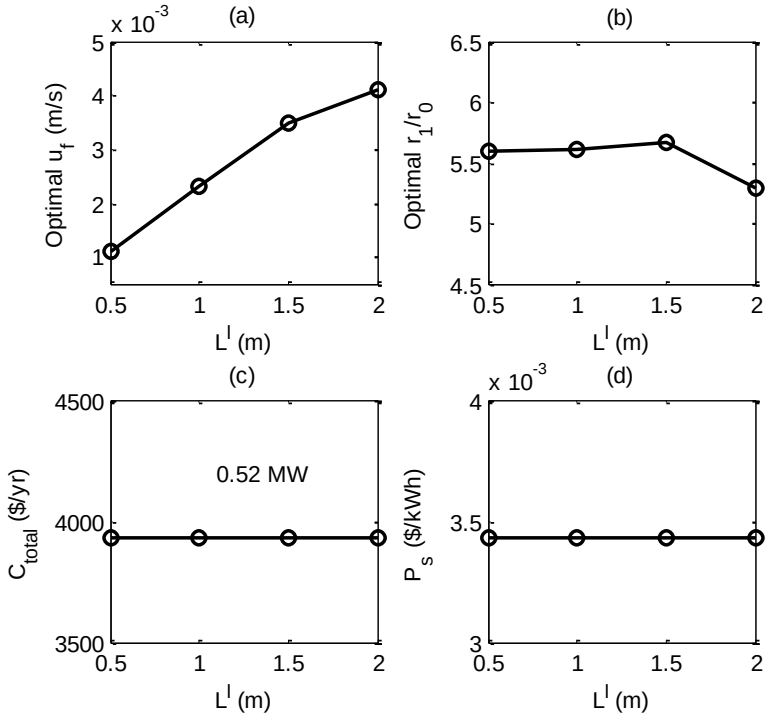

Figure 5.20 Optimal results under varying minimal tube length

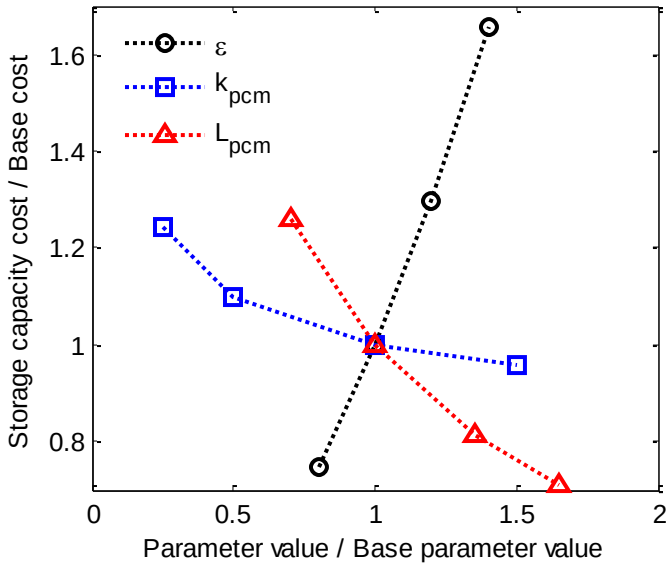

Figure 5.21 Sensitivity comparison of energy storage capacity cost

4. Conclusions

In this paper, new explicit analytic solutions for 1-D solidification in both rectangular and cylindrical coordinates are developed. To the best of the authors' knowledge, no explicit solutions of this kind for an annular geometry are currently available. These solutions are incorporated in an efficient simplified numerical procedure for a shell and tube heat exchanger based LTES unit model. The simplified model is shown to have good agreement with existing finite element (FE) approaches from the literature. The advantage of the proposed simplified approach is its computational efficiency and this is exploited in a new nonlinear programming formulation for the cost optimization design of a shell and tube unit for LTES systems under prescribed operational constraints. One of the main findings from the sensitivity analysis presented is that the effectiveness has a first-order sensitivity effect, followed by the latent energy and conductivity. The findings provide guidance for selecting a PCM and LTES optimal design.

Acknowledgement

This research is sponsored by the ARPA-e ARID Program under Contract No. DE-AR0000582. Any opinions, findings, and conclusions or recommendations expressed in this article are those of the authors and do not necessarily reflect the views of the Advanced Research Projects Agency-Energy.

References

[1] Manish K. Rathod, Jyotirmay Banerjee, Thermal stability of phase change materials used in latent heat energy storage systems: A review, Renew. Sustain. Energy Rev. 18 (2013) 246-258.

[2] Jose Pereira da Cunha, Philip Eames, Thermal energy storage for low and medium temperature applications using phase change materials – A review, Appl. Energy, 177 (2016) 227-238.

[3] Hussein Akeiber, Payam Nejat, et al, A review on phase change material (PCM) for sustainable passive cooling in building envelopes, Renew. Sustain. Energy Rev. 60 (2016) 1470-1497.

[4] Dongliang Zhao, Gang Tan, Numerical analysis of a shell-and-tube latent heat storage unit with fins for air-conditioning application, Applied Energy, 138,2015: 381-392.

[5] F. Fornarelli, S.M. Camporeale, B. Fortunato, M. Torresi, P. Oresta, L. Magliocchetti, A. Miliozzi, G. Santo, CFD analysis of melting process in a shell-and-tube latent heat storage for concentrated solar power plants, Applied Energy, 164,2016: 11-722.

[6] Y.B. Tao, V.P. Carey, Effects of PCM thermophysical properties on thermal storage performance of a shell-and-tube latent heat storage unit, Applied Energy, 179, 2016, 203-210.

[7] Qiyuan Li, S. Saeed Mostafavi Tehrani, Robert A. Taylor, Techno-economic analysis of a concentrating solar collector with built-in shell and tube latent heat thermal energy storage, Energy, 121 (2017) 220-237.

[8] Jaume Gasia, Jan Diriken, Malcolm Bourke, Johan Van Bael, Luisa F. Cabeza, Comparative study of the thermal performance of four different shell and tube heat exchangers used as latent heat thermal energy storage systems, Renew. Energy, 114, Part B, (2017) 934-944.

[9] Soheila Riahi, Wasim Y. Saman, Frank Bruno, Martin Belusko, N.H.S. Tay, Comparative study of melting and solidification processes in different configurations of shell and tube high temperature latent heat storage system, Solar Energy, 150 (2017) 363-374.

[10] N. Kousha, M.J. Hosseini, M.R. Aligoodarz, R. Pakrouh, R. Bahrampoury, Effect of inclination angle on the performance of a shell and tube heat storage unit – An experimental study, Appl. Therm. Eng. 112 (2017) 1497-1509.

[11] Mohammad Parsazadeh, Xili Duan, Numerical and statistical study on melting of nanoparticle enhanced phase change material in a shell and tube thermal energy storage system, Appl. Therm. Eng. 111 (2017) 950-960.

[12] Saeid Seddegh, S. Saeed Mostafavi Tehrani, Xiaolin Wang, Feng Cao, Robert A. Taylor, Comparison of heat transfer between cylindrical and conical vertical shell-and-tube latent heat thermal energy storage systems, Applied Thermal Engineering,130,2018, 1349-1362,

[13] Soheila Riahi, Wasim Y. Saman, Frank Bruno, Martin Belusko, N.H.S. Tay, Performance comparison of latent heat storage systems comprising plate fins with different shell and tube configurations, Applied Energy,212,2018, 1095-1106.

[14] F. Bai, Y. Wang, Z. Wang, Y. Sun, A. Beath, Economic Evaluation of Shell-and-tube Latent Heat Thermal Energy Storage for Concentrating Solar Power Applications, Energy Procedia, 69,2015,737-747.

[15] N.H.S. Tay, M. Belusko, F. Bruno, An effectiveness-NTU technique for characterising tube-in-tank phase change thermal energy storage systems, Applied Energy, Volume 91, Issue 1,2012, 309-319,

[16] N.A.M. Amin, M. Belusko, F. Bruno, M. Liu, Optimising PCM thermal storage systems for maximum energy storage effectiveness, Solar Energy, Volume 86, Issue 9,2012,Pages 2263-2272,

[17] N.H.S. Tay, M. Belusko, A. Castell, L.F. Cabeza, F. Bruno. An effectiveness-NTU technique for characterising a finned tubes PCM system using a CFD model, Applied Energy, Volume 131,2014,Pages 377-385.

[18] M. Belusko, N.H.S. Tay, M. Liu, F. Bruno. Effective tube-in-tank PCM thermal storage for CSP applications, Part 1: Impact of tube configuration on discharging effectiveness, Solar Energy, Volume 139,2016,Pages 733-743,

[19] Tolga Pirasaci, D. Yogi Goswami, Influence of design on performance of a latent heat storage system for a direct steam generation power plant, Applied Energy, 162,2016, 644-652,

[20] Zakir Khan, Zulfiqar Khan, Kamran Tabeshf, Parametric investigations to enhance thermal performance of paraffin through a novel geometrical configuration of shell and tube latent thermal storage system. Energy Conver. Manage.,127 (2016) 355-365.

[21] Zakir Khan, Zulfiqar Ahmad Khan, An experimental investigation of discharge/solidification cycle of paraffin in novel shell and tube with longitudinal fins based latent heat storage system, Energy Conver. Manage.,154 (2017) 157-167.

[22] Hakeem Niyas, Sunku Prasad, P. Muthukumar, Performance investigation of a lab–scale latent heat storage prototype – Numerical results, Energy Conversion and Management, 135,2017, 188-199.

[23] Xiaohu Yang, Zhao Lu, Qingsong Bai, Qunli Zhang, Liwen Jin, Jinyue Yan, Thermal performance of a shell-and-tube latent heat thermal energy storage unit: Role of annular fins, Applied Energy, 202, 2017,558-570.

[24] S. Saeed Mostafavi Tehrani, Robert A. Taylor, Pouya Saberi, Gonzalo Diarce, Design and feasibility of high temperature shell and tube latent heat thermal energy storage system for solar thermal power plants, Renew. Energy, 96, Part A, (2016) 120-136.

[25] Ralf Raud, Michael E. Cholette, Soheila Riahi, Frank Bruno, Wasim Saman, Geoffrey Will, Theodore A. Steinberg, Design optimization method for tube and fin latent heat thermal energy storage systems, Energy, 134 (2017) 585-594.

[26] Stefan J.. S B Wien Akad. Mat. Natur.98 (1889) 473-484,965-983.

[27] Neumann F., Die paruellen differentialgleichungen der mathematischen physik, vol 2, 1912 (Reimann-Weber) P 121.

[28] Brent AD. Voller VR, Reid KJ. Enthalpy-porosity technique for modeling convection-diffusion phase change: application to the solidifying of a pure metal. Num. Heat Tr. Part A (13) 1988 297-318.

[29] Ismail KAR, Alves CLF, Modesto MS. Numerical and experimental study on the solidification of PCM around a vertical axially finned isothermal cylinder. Appl. Therm. Eng. (21) 2001 53-77.

[30] https://www.mathworks.com/help/curvefit/multivariate-tensor-product-splines.html

[31] Frank P. Incropera, David P. DeWitt, Theodore L. Bergman, Adrienne S. Lavine. Fundamentals of Heat and Mass Transfer, 6th edition. John Wiley & Sons, 2007.

[32] Jegadheeswaran S, Pohekar S D. Performance enhancement in latent heat thermal storage system: a review. Renew. Sustainable Energy Rev. 13(9) (2009) 2225-2244.

[33] Zhen-Xiang Gong, Arun S. Mujumdar. Finite-element analysis of cyclic heat transfer in a shell and tube latent heat energy storage exchanger. Applied Thermal Engineering, 1997 (17): 583-591.

[34] https://www.mathworks.com/help/curvefit/spapi.html

[35] https://www.mathworks.com/help/optim/ug/fmincon.html

Appendix A

Explicit expression of the geometric factor

If g is a function of x, and h is a function of y, then their tensor-product is $f(x,y) = g(x)h(y)$. To express $g(x)h(y)$ in terms of polynomial spline functions, it is assumed $x \in (x_l, x_u)$, $y \in (y_l, y_u)$, and there are $J+1$ monotonically increasing sequence knots $x_1, \cdots x_{i,} \cdots x_{J+1}, i = 1{:}J+1$ in the space of x and $K+1$ monotonically increasing sequence knots $y_1, \cdots y_{j,} \cdots y_{J+1}$, $j = 1{:}K+1$ in the space of y (typically, $x_1 = x_l$, $x_{J+1} = x_u$, $y_1 = y_l$, $y_{K+1} = y_u$). These knots are called breaks.

For the variable x, the polynomial form basis functions of order M at the breaks x_i are:

$$\left[(x-x_i)^{M-1}, \cdots, (x-x_i)^{j-1}, \cdots, (x-x_i)^{1-1}\right], i = 1{:}J, j = 1{:}M, \qquad \text{A.1}$$

which can be represented as a vector $\boldsymbol{\varphi}_i(x)$ of length M. (It should be noted that here all the vectors mentioned are row vectors, and $\boldsymbol{\varphi}_i^T(x)$ indicates a column vector.)

For the variable y, the polynomial form basis functions of order N at the breaks y_i are,

$$\left[(y-y_i)^{N-1},\cdots,(y-y_i)^{j-1},\cdots,(y-y_i)^{1-1}\right], i=1{:}K, j=1{:}N, \quad \text{A.2}$$

which can be represented as a vector $\boldsymbol{\phi}_i(y)$ of length N. Within one block defined as $x_i \ll x < x_{i+1}, y_j \ll y < y_{j+1}, i=1{:}J, j=1{:}K$, the tensor product of $g(x)h(y)$ can be expressed as:

$$g(x)h(y) = \boldsymbol{\varphi}_i(x) C^{ij} \boldsymbol{\phi}_i^T(y), \quad \text{A.3}$$

where C^{ij} is a coefficient matrix of dimension $M \times N$. Thus for all the $J \times K$ blocks, the tensor-product spline of $g(x)h(y)$ can be expressed as:

$$g(x)h(y) = \boldsymbol{\Psi}(x)\boldsymbol{\Sigma}\boldsymbol{\Phi}(y), \quad \text{A.4}$$

where $\boldsymbol{\Psi}(x) = \left[\boldsymbol{\varphi}_1(x),\cdots,\boldsymbol{\varphi}_J(x)\right]$, $\boldsymbol{\Phi}(y) = [\boldsymbol{\phi}_1(y),\cdots,\boldsymbol{\phi}_K(y)]^T$, and

$$\boldsymbol{\Sigma} = \begin{bmatrix} \boldsymbol{C^{11}} & \cdots & \boldsymbol{C^{1K}} \\ \vdots & \ddots & \vdots \\ \boldsymbol{C^{J1}} & \cdots & \boldsymbol{C^{JK}} \end{bmatrix}.$$

The MATLAB toolbox provides multiple imbedded functions to work with multivariable tensor-product splines. Here, an explicit equation for the tensor-product spline of the current problem is given, which is not directly provided by the spline toolbox. The embedded function that can be used is 'spapi' [34]. By varying the solidification time, the moving solidification front *x* for a 1-D PCM bar, and the implicit moving solidification front *r* for an annular cylinder can be calculated by eqn. 2.5 and eqn. 2.9, respectively. Then the geometric factor α can be calculated using eqn. 2.10.

For different inner radii r_0 of an annular cylinder, different geometric factors can be obtained at the same location *x*. Table 5.7 shows the geometric factors under different *x* and r_0, which is the required input data for 'spapi'.

Table 5.7 Geometric factors under different combinations of (x, r_0)

α	*x*(1)=0cm	*x*(2)=1.5724cm	*x*(3)=3.8516cm	*x*(4)=8.613cm	*x*(5)=15.724cm
r_0=1cm	1.0	0.8653	0.7863	0.7120	0.6593
r_0=2cm	1.0	0.9156	0.8484	0.7760	0.7203
r_0=5cm	1.0	0.9624	0.9179	0.8587	0.8058

Assume $\alpha = f(x, r_0) = g(x)h(r_0)$. The order of the polynomial for the univariate splines $g(x)$ and $h(r_0)$ is 3. The breaks for x are [0, 0.02712, 0.062321, 0.157243] (with units of m) and for r_0 are [1, 5] (with units of cm). Thus there are 3 block coefficient matrices,

$$\boldsymbol{C}^{11} = \begin{bmatrix} 15.5390 & -97.4093 & 152.3088 \\ -0.7970 & 5.2868 & -10.9625 \\ 0 & 0 & 1.0 \end{bmatrix} \quad \text{A.5}$$

$$\boldsymbol{C}^{21} = \begin{bmatrix} -0.5682 & 0.5549 & 18.3427 \\ 0.0458 & 0.0033 & -2.7012 \\ -0.0102 & 0.0717 & 0.8147 \end{bmatrix} \quad \text{A.6}$$

$$\boldsymbol{C}^{31} = \begin{bmatrix} 0.0684 & -0.8329 & 5.6381 \\ 0.0058 & 0.0423 & -1.4098 \\ -0.0093 & 0.0725 & 0.7424 \end{bmatrix} \quad \text{A.7}$$

The basis functions for $g(x)$ are:

$$\boldsymbol{\varphi_1}(x) = [(x-0)^2, (x-0)^1, 1], \quad \text{A.8}$$

$$\boldsymbol{\varphi_2}(x) = [(x-0.02712)^2, (x-0.02712)^1, 1], \quad \text{A.9}$$

$$\boldsymbol{\varphi_3}(x) = [(x-0.062321)^2, (x-0.062321)^1, 1]. \quad \text{A.10}$$

The basis function for $h(r_0)$ is:

$$\boldsymbol{\phi_1}(r_0) = [(r_0 - 1)^2, (r_0 - 1)^1, 1]. \quad \text{A.11}$$

According to eqn. A4, the final form is:

$$\alpha = f(x, r_0) = \begin{cases} \boldsymbol{\varphi_1}(x)\boldsymbol{C}^{11}\boldsymbol{\phi}_1^T(r_0) & 0 \le x < 0.02712; \quad 1 \le r_0 \le 5 \\ \boldsymbol{\varphi_2}(x)\boldsymbol{C}^{21}\boldsymbol{\phi}_1^T(r_0) & 0.02712 \le x < 0.062321; \ 1 \le r_0 \le 5 \\ \boldsymbol{\varphi_3}(x)\boldsymbol{C}^{31}\boldsymbol{\phi}_1^T(r_0) & 0.062321 \le x \le 0.157243; \ 1 \le r_0 \le 5 \end{cases}. \quad \text{A.12}$$

Appendix B

Cost function of a shell and tube LTES

The total energy load requirement of a LTES can be expressed as:

$$\mathrm{G} = Q_m C_p (T_{out} - T_{in}), \quad \text{B.1}$$

where Q_m is the total HTF mass flowrate, T_{in} is the inlet HTF temperature and T_{out} is the outlet temperature, which could be specified by the application, i.e., minimal superheated steam temperature for efficient turbine power generation in a concentrated solar power plant [19]. Assume HTF flow velocity is uniform in each tube and equals u_f, thus the mass flow rate is, $q_m = \rho_f \pi r_0^2 u_f$. The total number of tubes needed is $N = \frac{Q_m}{q_m}$.

Assume the tubes, PCM and a large cylindrical container that encapsulates the tubes and PCM compose the main material cost of the shell and tube LTES. A factor $C_0 = 1.25$ is introduced to account for the manufacturing cost. Thus yearly investment cost C_{inv} of a shell and tube LTES is:

$$C_{inv} = \frac{1}{Yrs} C_0 \left[C_{tube}(Nm_{tube} + m_{container}) + C_{pcm} N m_{pcm} \right], \quad \text{B.2}$$

where Yrs is the operational years of life time of the equipment.

The radius of the container $r_{container}$ is approximated as the addition of all of the radii of the PCM solidification fronts r_1 around each tube, $r_{container} = Nr_1$. This approximation is often employed [19, 25] to study the optimal geometry of a shell and tube unit, which is representative of the whole LTES. Thus a more detailed expression of A.2 can be written:

$$C_{inv} = \frac{1}{Yrs} C_0 L \{ C_{tube} N \rho_{tube} \pi ((r_0 + w_t)^2 - r_0^2) + C_{tube} \rho_{tube} \pi [(Nr_1 + w_c)^2 - (Nr_1)^2] + C_{pcm} \rho_{pcm} N \pi (r_1^2 - r_0^2) \}, \quad \text{B. 3}$$

where w_t is the thickness of the tube and w_c is the thickness of the container.

The yearly pumping cost C_{op} can be calculated as:

$$C_{op} = 365 t_{op} C_e \frac{\Delta P N \pi r_0^2 u_f}{1000 \Omega_p}, \quad \text{B.4}$$

where C_e is the cost of the electricity, t_{op} is the operational hours each day, and Ω_p is the pump efficiency. Thus total yearly cost, which is the objective function for the NLP formulation for optimal design is:

$$C_{total} = C_{inv} + C_{op}. \quad \text{B. 5}$$

The parameter values needed are shown in Table 5.8.

Table 5.8 Parameter values used in the optimization cost function

C_0	1.25	Ω_p	0.75
C_e	0.2, \$/kWh	w_t	1/16, inch
C_{tube}	2.0, \$/kg	w_c	1/8, inch
C_{pcm}	0.75, \$/kg	Yrs	30, years

Chapter 6

A discrete time dynamical model for operational research involving a large scale latent thermal energy storage system

(Pan C., Vermaak N., Romero C., Neti S., et al. A discrete-time dynamical model for a large scale latent thermal energy storage system and its operational research. Submitted to *Energy Conversion and Management*.)

A discrete time dynamical model for operational research involving a large scale latent thermal energy storage system

Chunjian Pan[1], Natasha Vermaak[1], Carlos Romero[1], Sudhakar Neti[1],
Chien-Hua Chen[2]
[1] Lehigh University, Bethlehem, PA 18015, USA
[2]Advanced Cooling Technologies, Inc., Lancaster, PA 17601, USA

Abstract
One of the engineering challenges that prevents the commercial application of latent thermal energy storage (LTES) systems is the lack of computationally efficient methods to model the transient and nonlinear behavior of the system for design and operational research. In this paper, an efficient discrete time dynamical model for a large scale LTES system is proposed. Its application for operational research is successfully demonstrated by several examples. For example, given three identical LTES units, it is found that controlled variable distribution of the heat transfer fluid (HTF) to three parallel units is preferred to meet design requirements for output temperatures with longer operational time windows than operation in either series or parallel with equal distribution of the HTF into the three units.

Key words: Large-scale latent thermal energy storage system, dynamical modeling, operational research, phase change materials

Nomenclature

T_m	Phase change material (PCM) melting temperature
T_{hp}	Heat pipe inner temperature
T_w	Heat pipe wall temperature
T_{int}	Interface temperature heat transfer fluid (HTF) and the heat pipe
T	Temperature
r_1	Radius of heat pipe
r_2	Outer radius of the annular plate fin
h_0	PCM height on each circular plate
h_g	Air gap between the PCM and the circular fin
w_{fin}	Thickness of bottom circular fin
r	Melting front along radial direction
h	Melting front along the vertical direction
R	Thermal resistance
R_1	Thermal resistance within the PCM along the radial direction
R_2	Thermal resistance within the PCM along the vertical direction
R_t	Total thermal resistance
W	Width of the tank LTES system
H	Height of the tank LTES system
Y	Height of the HTF channel
Z	Length of the HTF channel or the tank LTES system
ρ	Density
C_p	Heat capacity
k_f	Conductivity of HTF
k_{pcm}	Conductivity of PCM
L	Latent energy
μ	Viscosity
h_f	Convective heat transfer coefficient in the HTF channel
h_{hp}	Effective convective heat transfer coefficient of a heat pipe
N_x	Number of heat pipes in a row perpendicular to the flow direction
N_y	Number of circular plate fins along the height of a heat pipe

N_z	Number of heat pipe rows along the flow direction
Δ	Incremental step change
V	PCM volume
q_f	Mass flow rate of the HTF
Q	Accumulated energy in the HTF
Superscripts	
i	Discrete location
k	Discrete time step
in	Inlet conditions of HTF
Subscripts	
pcm	Phase change material
f	Heat transfer fluid (HTF)
hp	Heat pipe
fin	Bottom circular fin

1. Introduction

Latent thermal energy storage (LTES) systems based on phase change materials (PCM) have two obvious advantages over sensible thermal energy storage. One is higher energy density, resulting in smaller equipment size and less investment cost. The other is that PCM-based LTES release or absorb heat isothermally, resulting in efficient temperature management. Despite these advantages, only a few commercial applications employ LTES due to several engineering challenges. One major problem is the lack of computationally efficient models for the transient and nonlinear behavior of a LTES system. The low conductivity of PCMs is another engineering challenge preventing

commercial applications of LTES systems. These and other challenges for LTES systems affect their ability to be integrated into applications like solar heating or heat pump systems. At present, LTES systems are mainly studied in the literature for optimal storage and performance design [1-5]. These studies are often based on computational fluid dynamics (CFD), which leads to time-consuming computationally expensive simulations. As application processes with energy storage are inherently transient [6], i.e., solar thermal systems, building heating ventilation and air condition (HVAC) systems, operational strategies for effective dynamic heat management are needed [7].

The inherent nonlinearity and transient charging or discharging of a LTES system further complicates the formulation of a control problem. A dynamical model for advanced control (such as model predictive control) or operational research is rare in the literature [8-12]. A control oriented dynamical model for a LTES unit coupled with a solar thermal collector and a backup electric heater was developed by Serale et al. [8] for space heating. A mixed logic-dynamical approach was introduced to regulate the system with intrinsic nonlinearities. With the aim to efficiently model the non-linear operational characteristics of a LTES system, Ghani et al. [9] built a dynamic model by using a Layered Digital Dynamical Neural type network which was trained with experimental data obtained from a latent heat exchanger. Luu et al. [10] proposed integrating a latent heat system into a domestic solar water heater to eliminate the traditional water tank. A dynamical model for process operation analysis was developed and validated against experimental data. To monitor safe operation of lithium-ion battery packs coupled with phase change composites for passive cooling, Salameh et al. [11] developed a state-space dynamical model to estimate the melt fraction of the stored latent cooling energy in the

system. Barz et al. [12] developed a nonlinear state observer based on a physical 2D dynamical model to reconstruct transient spatial temperature fields inside the storage and estimate the stored energy and the state of charge.

To offset the low conductivity of PCMs, heat pipes are often embedded in PCMs to increase the heat transfer performance for applications [13-19.] A heat pipe assisted LTES system is a convenient configuration for large scale applications, i.e., the concentrating solar power field [13, 14]. Most studies of a heat pipe assisted LTES system have been numerically or experimentally focused on a single pipe unit [15-19]. Limited literature is available on modeling and design at the level of a whole system for a large scale LTES system. A thermal network model was developed by Shabgard et al. [13] to predict the performance of a LTES system with cascaded PCMs based on exergy analysis. A dynamic numerical model based on a thermal resistance network was developed by Nithyanandam & Pitchumani [14] to study the influence of design and operating parameters on the charge and discharge performance of a large scale LTES system.

It is crucial to estimate how long the system can continue to supply or store latent energy at a given heat flow for a large scale LTES system. Moreover, optimal operational strategies could result in substantial investment savings for a large scale system. In order to use the modeling approaches currently available for large scale LTES systems to perform this kind of operational research, the thermal network models developed in [13, 14] require solving large coupled system of governing equations. As a result, the computational efficiency of these models is not sufficient for operational research purposes. That is why the studies outlined above [8-12] only involve small scale LTES

systems. Indeed dynamical models of large scale LTES systems for operational research have not been widely studied in the literature. To address this research need, in this paper, an efficient discrete time dynamical model for a heat pipe assisted large scale LTES system is developed. Its verification and successful application for operational studies is demonstrated by several examples.

The content of this paper is organized as follows. In section 2, a discrete time dynamical model for a single annular finned heat-pipe enhanced PCM module is constructed. In section 3, the module developed in Section 2 is employed to create a discrete time dynamical model for a full large scale LTES system. In section 4 the discrete time dynamical model is used for operational research. Section 5 summarizes the conclusions.

2. A discrete-time dynamical model for an annular finned PCM module

A heat pipe assisted large scale LTES system is shown in Fig. 6.1. Heat pipes are embedded in the PCM tank and connected to a heat transfer fluid (HTF) channel. A possible application of such a system is reported in [20]. Annular fins are attached to a single heat pipe as shown in Fig. 6.2. Finned heat pipe structures are necessary to enhance the heat transfer performance of the LTES system due to the low thermal conductivity of PCM. For a heat pipe, it is reasonable to assume that there is no temperature drop along its length [21], so the transient PCM behavior of a single annular fin extended from the tube (See Fig. 6.3) can be used to represent a whole tube.

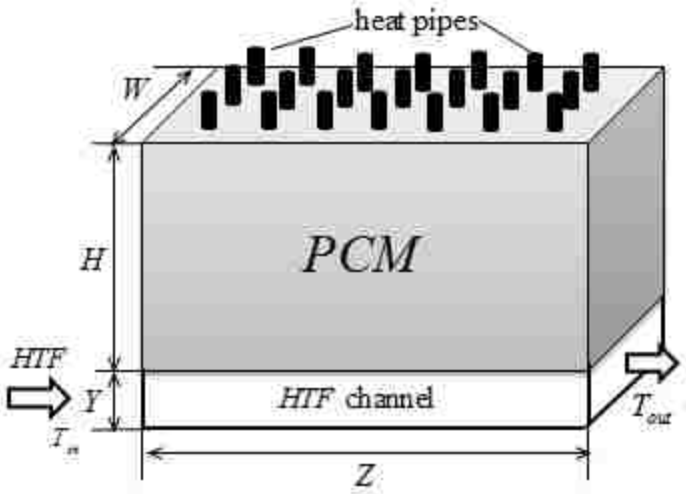

Figure 6.1 Sketch of a large scale LTES system with embedded heat pipes

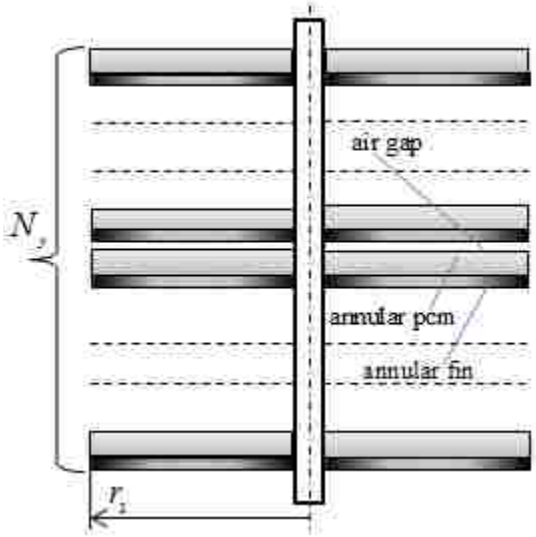

Figure 6.2 Cross-sectional schematic of a single heat pipe unit with annular fins

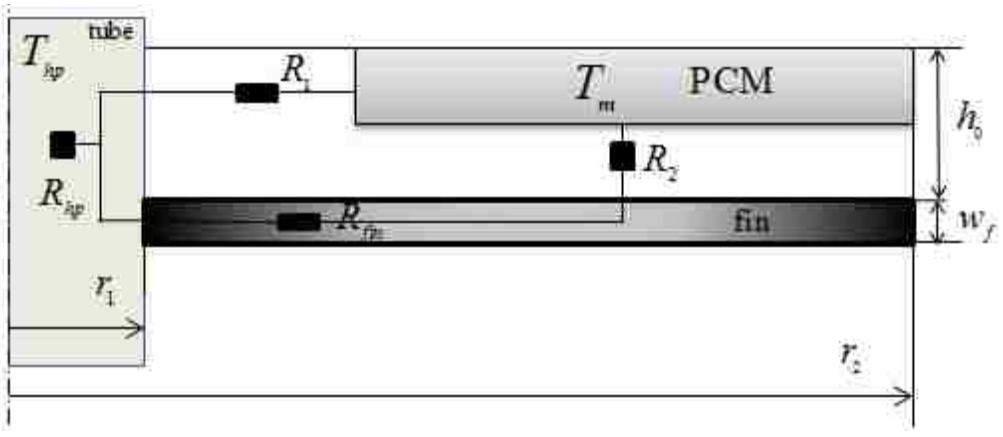

Figure 6.3 Sketch of annular finned PCM unit of a heat pipe

Although temperature drop in a heat pipe can be neglected, in the following description, a thermal resistance of a heat pipe (R_{hp}) is nevertheless introduced to generalize the mathematical model, so that it can be applied to the situation when the heat pipe is replaced by a tube with heat transfer fluid (HTF) going through it. Thus an inner heat pipe temperature T_{hp} and heat pipe wall temperature T_w are also introduced. Based on the concept of thermal resistance networks for heat flow, the heat coming from the heat pipe into the PCM can be written as:

$$\frac{T_{hp}-T_w}{R_{hp}} = \frac{T_w-T_m}{R_1} + \frac{T_w-T_m}{R_{fin}+R_2} \tag{2-1}$$

As a result, the wall temperature of the heat pipe is:

$$T_w = \frac{R_1(R_{fin}+R_2)T_{hp}+R_{hp}(R_{fin}+R_2)T_m+R_1R_{hp}T_m}{R_1(R_{fin}+R_2)+R_{tube}(R_{fin}+R_2)+R_1R_{hp}} \tag{2-2}$$

The total thermal resistance from the heat pipe to the moving fronts of the PCM can be written as:

$$R_t = R_{hp} + \frac{R_1+R_2+R_{fin}}{R_1(R_{fin}+R_2)}, \tag{2-3}$$

which, because this depends on the moving fronts of the PCM, it is a transient variable.

In the radial direction, the heat flow into the PCM within a small time window Δt is equal to the latent energy change happening in a small radial distance Δr, thus an energy balance equation can be written as:

$$\frac{T_w-T_m}{R_1} = \frac{\rho_{pcm}2\pi r^{k-1}\Delta r^k h^{k-1}L_{pcm}}{\Delta t^k}. \tag{2-4}$$

Consequently, the marching melt front at the time k is:

$$\Delta r^k = \frac{(T_w-T_m)\Delta t^k}{R_1\rho_{pcm}2\pi r^{k-1}h^{k-1}L_{pcm}} \tag{2-5}$$

The distance of the melting front away from the heat pipe wall along the *radial direction* is updated as:

$$r^k = r^{k-1} + \Delta r^k \tag{2-6}$$

Similarly, along the *vertical direction*, the energy balance equation is:

$$\frac{T_w - T_m}{R_{fin} + R_2} = \frac{\Delta m L_{pcm}}{\Delta t^k} = \frac{\rho_{pcm}\pi\left(r_2^2 - \left(r^k\right)^2\right)\Delta h^k L_{pcm}}{\Delta t^k}. \tag{2-7}$$

Thus, the incremental melt front along the vertical direction at the time k with the updated melt front r^k can be obtained as:

$$\Delta h^k = \frac{(T_w - T_m)\Delta t^k}{(R_{fin} + R_2)\rho_{pcm}\pi\left(r_2^2 - \left(r^k\right)^2\right)L_{pcm}}. \tag{2-8}$$

The distance of the melting front away from the annular fin along the vertical direction is updated as:

$$h^k = h^{k-1} + \Delta h^k \ . \tag{2-9}$$

Generally, this discrete time dynamical (DTD) model can be written as:

$$[h^k, r^k, R_t^k] = F\left(T_f^k, \Delta t^k\right). \tag{2-10}$$

The following lists the calculations of the thermal resistances. The thermal resistances within the PCM are updated according to the moving fronts h^k,r^k, and they can be expressed as:

$$R_1^k = \frac{log(r^k/r_1)}{2\pi(h_0 - h^k)} \tag{2-11}$$

$$R_2^k = \frac{h^k}{\pi\left[(r_2)^2 - \left(r^k\right)^2\right]k_{pcm}} \quad . \tag{2-12}$$

The thermal resistance of the fin is:

$$R_{fin} = \frac{log(r_2/r_1)}{2\pi w_{fin} k_f} \ . \tag{2-13}$$

The thermal resistance in the heat pipe includes the wall conduction resistance and effective convection heat transfer resistance:

$$R_{hp} = \frac{1}{2\pi r_1(w_f+h_0)h_{hp}} + \frac{log(r_1/(r_2-w_t))}{2\pi(w_f+h_0)k_f}, \quad (2\text{-}14)$$

where h_{hp} is the effective heat transfer coefficient of the heat pipe and w_t is the tube wall thickness.

For a set of 8 testing cases (Table 6.1), numerical computational fluid dynamics solutions were found using the Solidification & Melting Model within the commercially software FLUENT (Available in Ansys 16.0). A detailed Fluent model description, as well as mesh and time-step independence studies that are very close to the current numerical cases can be found in [20]. The numerical results of the testing cases (Table 6.1) are used to verify the applicability of the DTD model outlined in Section 2, which was coded in MATLAB.

Note that the first 4 test cases have different geometries but the same boundary conditions, while the last 4 cases have different boundary conditions, fin thicknesses and properties. Fig. 6.4 shows the comparison between the DTD model (noted as 'DTD.') and the numerical results by Fluent ('num.') for the 8 testing cases. Overall, the DTD model agrees very well with the transient freezing curve determined by the Fluent simulations (within 15 % for the worst case in terms of final freezing time).

For comparison of the testing cases, the ratio $\frac{h_0}{r_1}$ is a quantity that gives an indication of the dominant cooling mechanism. This is because when the ratio $\frac{h_0}{r_1}$ is large enough, the cooling from the inner tube wall dominates, while cooling effects from the bottom become negligible. The ratio $\frac{h_0}{r_1}$ of cases #2 and #3 is 12 and 20 which suggests high ratio

values. Based on the DTD model and fluent results Figure 6.4(a) shows that their corresponding liquid fraction curves are almost identical, this is expected because as the outer radius for # 2 & 3 is the same, the two cases have almost identical freezing behavior. In the testing cases, the minimum $\frac{h_0}{r_1}$ is 0.5 (cases # 1 & 4). Thus it can be concluded that the DTD model is applicable for conditions where the dimension $\frac{h_0}{r_1} \geq 0.5$. Also based on the testing cases, a confident working range for the ratio $\frac{r_2}{r_1}$ of the DTD model is $4 \leq \frac{r_2}{r_1} \leq 12$. The lower bound may not have to be specified, because when $\frac{r_2}{r_1}$ is small, heat transfer from the tube wall dominates, and under such conditions, it was shown by cases #2 & 3 that the DTD model has good performance. Cases # 5-8 have the same dimensions, but different boundary conditions, fin thicknesses and properties. Through the comparisons, it can be seen that the DTD model can also perform quite well under variations of those parameters (with only a maximum of 6% difference exhibited in terms of final freezing time). Thus besides its dynamical performance tracking, the DTD model can also be used for optimal dimensional design of LTES systems (Fig. 6.1) with embedded annular finned heat pipes.

Table 6.1 Test cases

Cases	r_1 (cm)	r_2 (cm)	h_0 (cm)	w_{fin} (mm)	h_{hp}	dT	Fin
#1	0.5	2.0	0.25	0.5	350	10	Steel
#2	0.5	2.0	6.0	0.5	350	10	Steel
#3	0.5	2.0	10.0	0.5	350	10	Steel
#4	0.5	6.0	0.25	0.5	350	10	Steel
#5	0.5	3.0	2.0	0.25	350	20	Steel
#6	0.5	3.0	2.0	1.0	150	10	Steel
#7	0.5	3.0	2.0	0.5	500	5	Steel
#8	0.5	3.0	2.0	0.25	350	10	Al

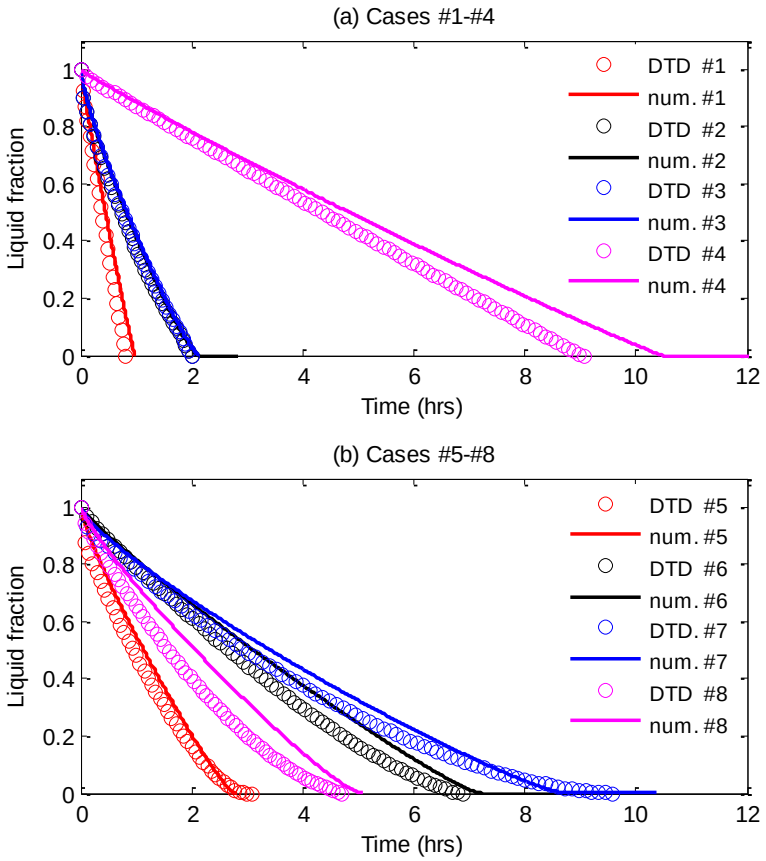

Figure 6.4 Testing cases used in verifying the DTD model against numerical Fluent simulations

3. Coupled model (PCM and HTF) of the large-scale LTES system

A heat transfer fluid (HTF) flows through the rectangular channel exchanging heat with the PCM. For a mathematical description of the process, the following assumptions are made: (1) the HTF is incompressible and viscous dissipation is negligible; (2) the HTF is uniform over the cross sectional area; (3) heat transfer along the HTF flow direction is negligible; (4) heat transfer in the PCM is conduction controlled; (5) the outer wall of the PCM is adiabatic; (6) PCM properties are constant; (7) the channel wall thickness is neglected, thus no thermal resistance of the wall is considered; (8) the heat

pipes pass through the PCM tank and almost reach the bottom of the HTF channel.

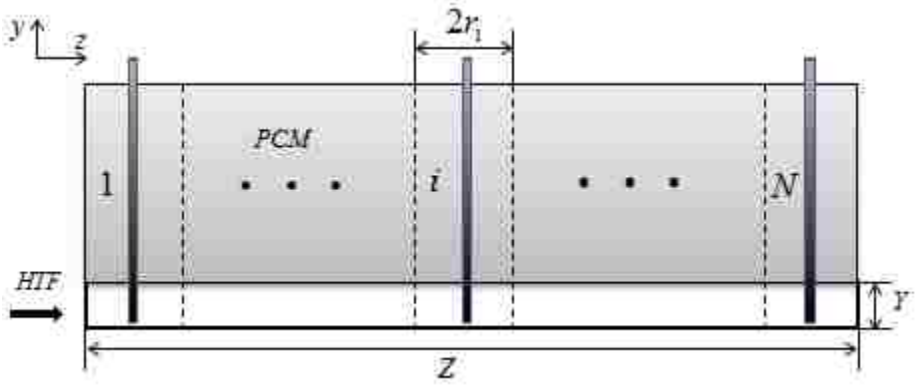

Figure 6.5 A shell and tube latent energy storage unit

Within the channel, heat transfer takes place not only between the HTF and the immersed section of the heat pipes in the channel, but also between the upper contact surface of the channel and the PCM tank. However, within a single annular finned module, there is an air gap between two neighboring modules; this gap is reserved for PCM expansion (See Fig. 6.2). This air gap also poses a large thermal barrier for heat transfer from a lower annular finned PCM to an upper unit through the bottom of the annular fin. Besides the very bottom annular finned PCM that can be heated by the upper channel surface, the remaining units are almost all heated by the heat pipes. Thus it is justified to assume that the HTF only transfers heat through the immersed section of the heat pipes within the channel. Based on the above assumptions, the governing equation for energy transfer of the HTF in the tube is:

$$\rho_f C_{pf} Y W \Delta Z \left(\frac{\partial T_f}{\partial t} + u\frac{\partial T_f}{\partial z}\right) = 2\pi r_1 Y N_x h_f \left(T_{int} - T_f\right), \quad (3\text{-}1)$$

where h_f is the heat transfer coefficient based on correlation equations for cross flow [22] ; N_x is the number of heat pipes in a row perpendicular to the flow direction; ΔZ is the discrete distance accounting for the number of rows of heat pipes. T_{int} acts as the interface temperature between the HTF in the channel and the heat pipe.

In the following, by employing the time-discrete dynamical (DTD) module developed in Section 2, an efficient numerical approach that does not require the solution of any systems of equations for the modeling of the large scale LTES system (Fig. 6.1), is proposed.

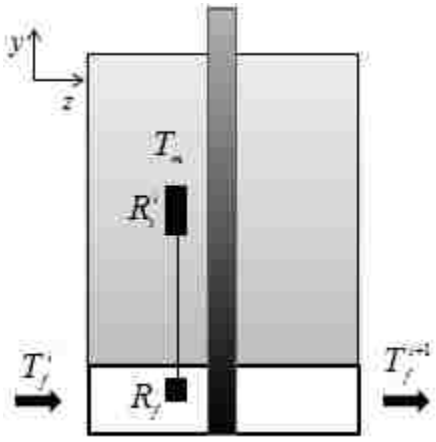

Figure 6.6 Thermal resistance scheme of element i based on Fig. 6.5

Fig. 6.6 shows a discrete unit composed of a single heat pipe. Multiple heat pipes along the flow direction can also be grouped as one discrete unit for the large scale LTES system shown in Fig. 6.1. The following analysis is based on a one-row heat pipe unit (which also applies to a discrete unit along the HTF flow direction composed of multiple rows of heat pipes). The thermal resistance of the i^{th} discrete unit depends on the moving freezing fronts of $r^{i,k}, h^{i,k}$ at time *k* and is written as:

$$\left[h^{i,k}, r^{i,k}, R_t^{i,k}\right] = F\left(T_{int}^{i,k}, \Delta t^k\right). \tag{3-2}$$

Between each time interval, the volume of PCM turning from liquid to solid can be calculated as:

$$V^{i,k} = \pi(r_2^2 - r_1^2)h^k + \pi\left(\left(r^{i,k}\right)^2 - r_1^2\right)(h_0 - h^k); \tag{3-3}$$

$$V^{i,k-1} = \pi(r_2^2 - r_1^2)h^{k-1} + \pi\left(\left(r^{i,k-1}\right)^2 - r_1^2\right)(h_0 - h^{k-1}); \tag{3-4}$$

$$\Delta V^{i,k} = V^{i,k} - V^{i,k-1}. \tag{3-5}$$

The latent energy transfer associated with this volume change transfers to the HTF channel; an energy balance equation for a discrete unit with one row of heat pipes perpendicular to the flow direction can be written as:

$$2\pi r_1 Y N_x h_f \left(T_{int}^{i,k+1} - T_f^{i,k+1}\right) = \frac{\rho_{pcm} L_{pcm} \Delta V^{i,k}}{\Delta t}. \tag{3-6}$$

Then the energy balance equation in the HTF channel can also be written as:

$$\rho_f C_{pf} Y W \Delta Z \left(\frac{\partial T_f}{\partial t} + u \frac{\partial T_f}{\partial z}\right) = \frac{\rho_{pcm} L_{pcm} \Delta V^{i,k}}{\Delta t}. \tag{3-7}$$

Assume N_y is the total number of annular plate fins along the height of a heat pipe. Implementing an implicit scheme and using a finite difference approach for the partial differential terms, eqn. (3-7) becomes:

$$\rho_f C_{pf} Y W \Delta Z \left(\frac{T_f^{i,k+1} - T_f^{i,k}}{\Delta t} + u \frac{T_f^{i,k+1} - T_f^{i-1,k+1}}{\Delta Z}\right) = N_x N_y \frac{\rho_{pcm} L_{pcm} \Delta V^{i,k}}{\Delta t}. \tag{3-8}$$

Setting $\Psi(t^k, i) = \frac{N_x N_y}{\rho_f C_{pf} Y W} \cdot \frac{\rho_{pcm} L_{pcm} \Delta V^{i,k}}{\Delta t}$, the temperature in the HTF can be updated as:

$$T_f^{i,k+1} = \frac{1}{\Delta z/\Delta t + u}\left(\Psi(t^k, i) + \frac{\Delta z}{\Delta t} T_f^{i,k} + u T_f^{i-1,k+1}\right). \tag{3-9}$$

The interface temperature can be updated based on eqn. (3-6), and it can be written as:

$$T_{int}^{i,k+1} = \frac{T_m + 2\pi r_1 Y h_f R_t^{i,k} T_f^{i,k+1}}{1 + 2\pi r_1 Y h_f R_t^{i,k}}. \tag{3-10}$$

Due to the sizing limitations of an annular finned unit, in the simulation when either $h^{i,k}$ or $r^{i,k}$ reaches the boundary first, a constraint is set as:

when $h^{i,k} \geq h_0$, *or* $r^{i,k} \geq r_2$ $R_t^{i,k} = \infty$. (3.11)

The overall calculation procedure is shown as following, (which it should be emphasized again that it does not involve solving any systems of equations):

First, initialize the temperature profile in the tube

$T_f^{i,1} = T_{in},\ T_{int}^{i,1} = T_m,\ 1 \le \mathrm{i} \le N_z$;

for $\mathrm{k} = 1{:}\,\mathrm{K}$

$\left[h^{i,k}, r^{i,k}, R_t^{i,k}\right] = F\left(T_{int}^{i,k}, \Delta t^k\right)$

$if \quad h^{i.k} \ge h_0$ or $r^{i.k} \ge r_2$

$R_t^{i,k} = e^{15}$;

end

$T_f^{1,k} = T_{in}$;

$\Psi(t^k, i) = \frac{N_x N_y}{\rho_f C_{pf} Y W} \cdot \frac{\rho_{pcm} L_{pcm} \Delta V^{i,k}}{\Delta t}$;

$T_f^{i,k+1} = \frac{1}{\Delta z/\Delta t + u}\left(\Psi(t^k, i) + \frac{\Delta z}{\Delta t}\, T_f^{i,k} + u T_f^{i-1,k+1}\right)$;

$T_{int}^{i,k+1} = \frac{T_m + 2\pi r_1 Y h_f R_t^{i,k} T_f^{i,k+1}}{1 + 2\pi r_1 Y h_f R_t^{i,k}}$

end

A first verification of this large scale LTES model can be performed via an energy balance between the HTF and the PCM in the tank. Testing cases with three different HTF channel length (Z) (Fig. 6.1) were considered. The detailed dimensions of the cases are listed in Table 6.2 and it is assumed that (i) the HTF is water (properties shown in Table 6.3) (ii) the HTF mass flowrate is 10 (kg/s) and (iii) the inlet temperature is 0 $(℃)$. The PCM properties used are shown in Table 6.4. Fig. 6.7 shows the output temperature profiles of the HTF going through three different channel lengths. Longer channels result in longer dwell time for the HTF, leading to higher output temperatures. The accumulated energy of the HTF is calculated as:

$$Q = \sum_{k=1}^{K} q_f Cp_f \left(T_f^{N,k} - T_f^{in}\right) \Delta t, \tag{3.12}$$

where q_f is HTF inlet mass flowrate and T_f^{in} is its inlet temperature. It can be seen from Fig. 6.8 that for the three cases, the total amount of latent energy within the PCM is balanced with the total amount of energy carried away by the HTF. Thus the modeling procedure for such a large-scale LTES system is a reliable approximation for preliminary operational design purposes. Moreover an exact similar modelling approach was applied to a shell and tube LTES unit that was verified by comparing the results to a finite difference based solution [22].

Table 6.2 Geometries for energy balance testing

$r_1(cm)$	$r_2(cm)$	$h_0(cm)$	$h_g(cm)$	$w_{fin}(mm)$	W(m)	H(m)	Y(m)	Z (m)
0.4	4	2	0.15	0.5	2	1.26	0.3	10,20,30

Table 6.3 Properties of water

Density ρ_f	Conductivity k_f	Heat Capacity C_{pf}	Viscosity μ_f
988.2 (kg/m^3)	0.59846 (W/mK)	4184.1 (J/kgK)	1.0016e^{-3} (Pa · s)

Table 6.4 Representative thermal properties of PCM

Density ρ_{pcm}	Conductivity k_{pcm}	Melting Temperature T_m	Latent Heat L_{pcm}
1538 (kg/m^3)	1.0 (W/mK)	45 (℃)	170 kJ/kg

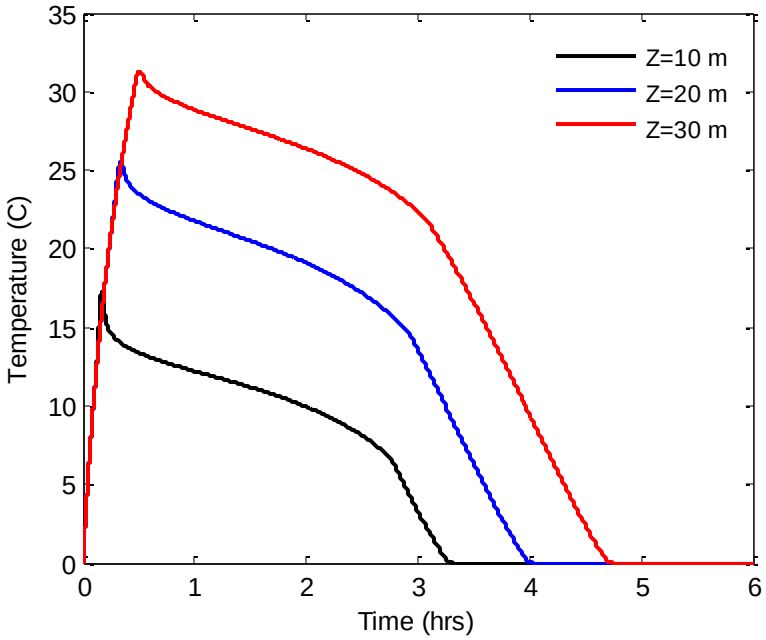

Figure 6.7 Outlet temperature of the HTF

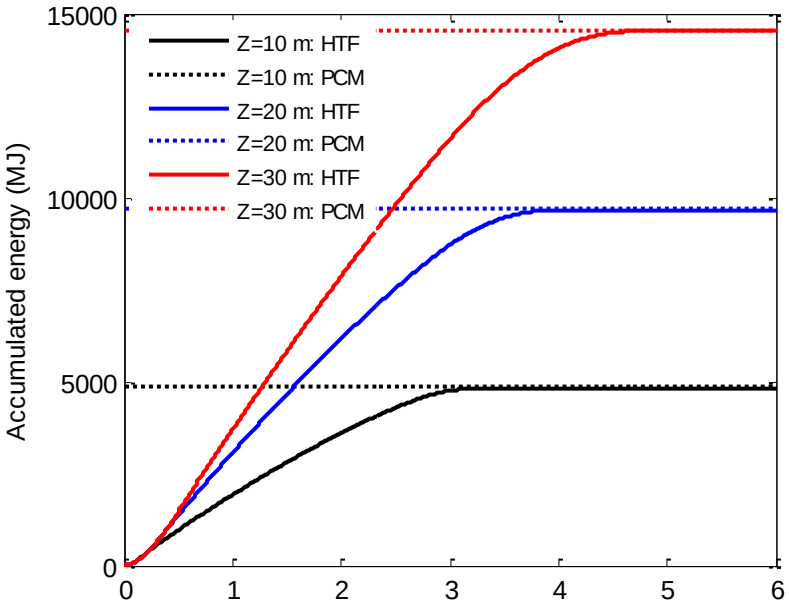

Figure 6.8 Accumulated energy within the HTF

4. Results and discussion for operational research of a large scale LTES

system

For a large scale LTES system, operational strategies could be vital for cost savings. Thus the dynamical model developed in Sections 2-3 is employed to explore possible operational strategies for more efficient use of the stored energy in a LTES system.

According to Section 3, a general DTD model for the large-scale LTES system (See Fig. 6.1) can be represented as:

$$T_f^{out}(t^k) = G\left(q_f(t^k), T_f^{in}\right), \tag{4.1}$$

where T_f^{out} is the output temperature of the HTF, q_f is the inlet HTF mass flowrate with a constant inlet temperature T_f^{in}. The specific geometries of a single circular finned heat pipe are listed in Table 6.2 (the length of the channel is assumed to be 10 m). The material properties of the HTF and the PCM are shown in Tables 6.3 and 6.4, respectively.

4.1 Study finding variable mass flow rate profiles under a temperature constraint

For a real application, the HTF is often required to be heated to a desired temperature. Based on Fig. 6.7, it can be seen that the length of the channel should be optimally determined so that a required operational temperature can be obtained. Fig. 6.7 also indicates that the output HTF temperature could decrease quickly and fail to meet the target temperature when there is not sufficient latent energy in the LTES system. Nevertheless, there still could be a substantial amount of unused stored latent energy in the large-scale system. To make more efficient use of this stored latent energy, one solution is to reduce the flowrate of the HTF, thus its dwell time in the LTES system can be prolonged and its output temperature may still reach the target temperature. Under

such conditions, the DTD model (eqn. 4.1) can conveniently be employed to find such a desired flowrate profile. The deviation of the output temperature of the HTF from the design point T_d should be as small as possible at each time step. A corresponding optimization problem can be formulated as (eqn.4.2):

$$\begin{aligned} &\min_{q_f(t^k)} \quad \left(T_f^{out}(t^k) - T_d\right)^2 \\ \text{s.t.} \quad &T_f^{out}(t^k) = G\left[q_f^{in}, T_f^{in}\right] \\ &0 \le q_f(t^k) \le 4 \end{aligned} \tag{4.2}$$

The design temperature is set at 20℃. Fig. 6.9 shows the controlled inlet HTF mass flowrate profile with its output temperature profile determined by the design algorithm. Initially the inlet HTF mass flowrate is set at $3kg/s$. After the output temperature increases to the maximum allowable temperature, a control strategy is implemented (red section of the curves in Fig. 6.9). At the beginning there is sufficient latent energy in the LTES system, so the inlet mass flowrate reaches its upper bound. When the remaining stored energy in the system cannot maintain the output temperature at the design point with the upper-bound mass flowrate, a decreasing mass flowrate is found at each discrete time window to satisfy the temperature constraint.

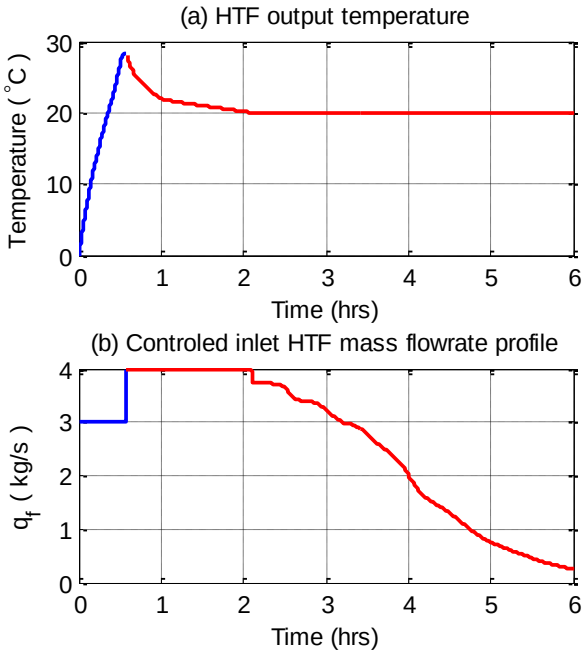

Figure 6.9 Profiles of the HTF output temperature and inlet mass flowrate

4.2 *Study of configuration effects on temperature profiles for prescribed HTF mass flowrate*

While the above results illustrate the utility of the approach for output temperature control of a LTES unit with greater flexibility, there are also many applications for which the mass flowrate of the HTF is fixed. In that case, a single controlled decreasing flowrate profile is impractical. Addressing this issue, the configuration of several parallel units of the LTES system (Fig. 6.1) is considered. Fig. 6.10 shows three units arranged in series and also in parallel. Assuming that there is a fixed HTF mass flowrate 9 kg/s with 0℃ inlet temperature going through the LTES system in series or equally distributed to the parallel units at 3 kg/s each. Fig. 6.11 shows the temperature profiles obtained in each of the two operational configurations. If the required operational temperature is 20℃, operation in parallel has obvious advantages over operation in series. That is, with the same amount of latent energy, operation in parallel has longer operational times,

which in turn means cost savings (by building a smaller LTES system to meet the operational time window requirement).

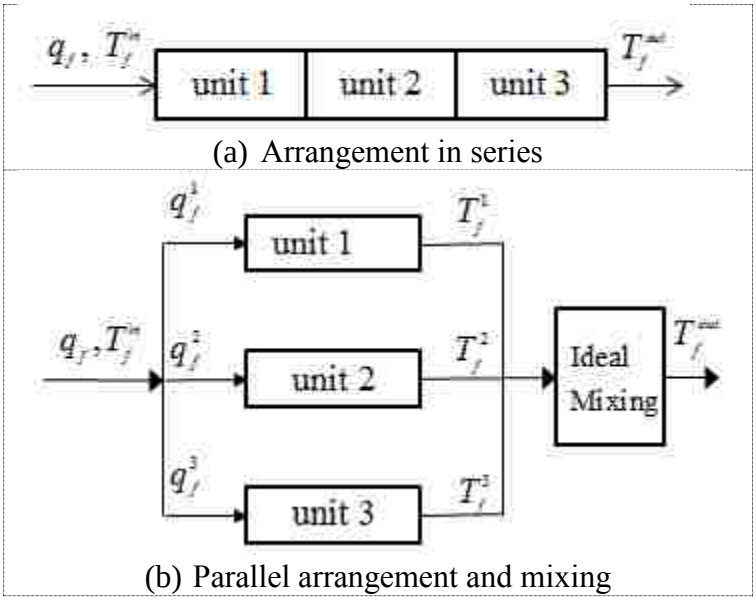

(a) Arrangement in series

(b) Parallel arrangement and mixing

Figure 6.10 Schematic of operational designs

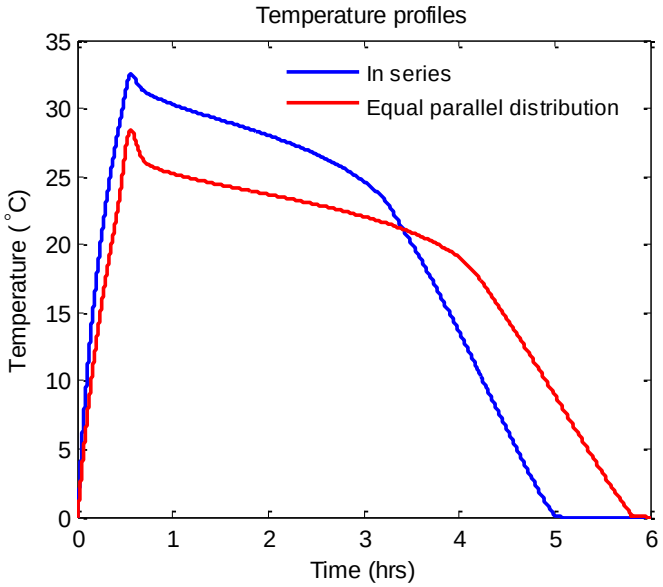

Figure 6.11 Temperature profiles of in series and parallel operational configurations for a prescribed heating load

In addition, the flowrate control problem (eqn. 4.2) indicates that there could be other efficient flowrate distribution strategies that could increase the operational time

window for the same LTES system. Thus a controlled distribution of a fixed mass flowrate HTF into three parallel LTES units is proposed as eqn. 4.3. The target function is the sum of the square of the mass flowrate going into each LTES unit. In the constraints, the design temperature is specified as the ideal mixing temperature of the flows coming from the three units. By assigning different weight values,C_1, C_2, C_3, the operational priority of each unit can be determined. In the following simulations, a set of values used for C_1, C_2, C_3, are 10, 500 and 1000, respectively. Such a set of weights ensures that, at the beginning, more mass flowrate will be distributed to the first unit and when there is not enough latent energy left in the first unit to meet the required design temperature, more mass flowrate is distributed to the second and then to the third. By such a means of controlled variable distribution, more latent energy in the first and second unit can be used.

$$
\begin{aligned}
\min_{q_f^1, q_f^2, q_f^3} \quad & C_1\left(q_f^1\right)^2 + C_2\left(q_f^2\right)^2 + C_3\left(q_f^3\right)^2 \\
& T_f^1(t^f) = G\left(q_f^1, T_f^{in}\right) \\
& T_f^2(t^f) = G\left(q_f^2, T_f^{in}\right) \\
& T_f^3(t^f) = G\left(q_f^3, T_f^{in}\right) \\
\text{s.t.} \quad & q_f = q_f^1 + q_f^2 + q_f^3 \\
& q_f^1 T_f^1(t^f) + q_f^2 T_f^2(t^f) + T_f^3(t^f) q_f^3 = q_f T_f^{out}(t^f) \\
& T_f^{out}(t^f) = T_d
\end{aligned}
\tag{4.3}
$$

Fig. 6.12 shows the output temperature profiles of each unit due to the controlled mass flowrate distribution and the temperature profile after assumed ideal mixing. After the initial period, the mixing temperature meets the design temperature requirement until there is no longer sufficient latent energy left in all of the three units. Figure 6.13 shows

a fixed mass flowrate HTF being distributed into three identical units. It can be seen that, at the beginning, more flowrate is distributed through the first unit which is forced by the weighting effect in the target function. As intended, when there is not enough latent energy remaining, the flowrates going through the 2nd and 3rd units increase.

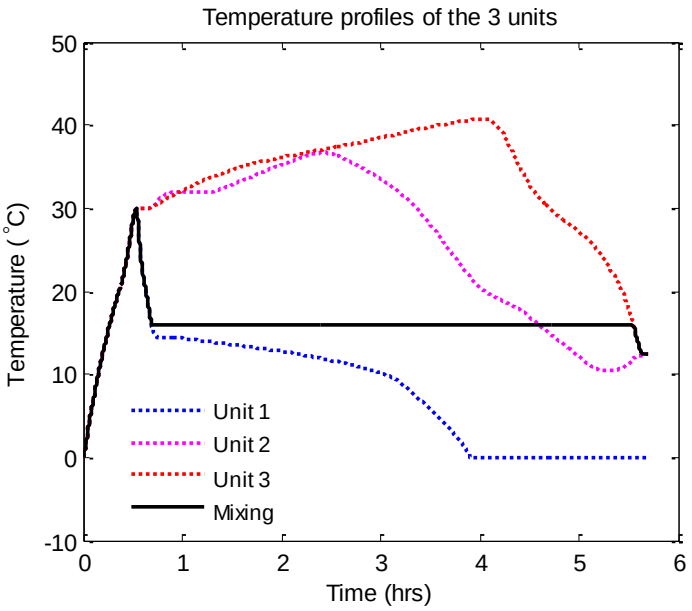

Figure 6.12 Output temperatue profiles of each unit due to the controlled distribution of the mass flowrate

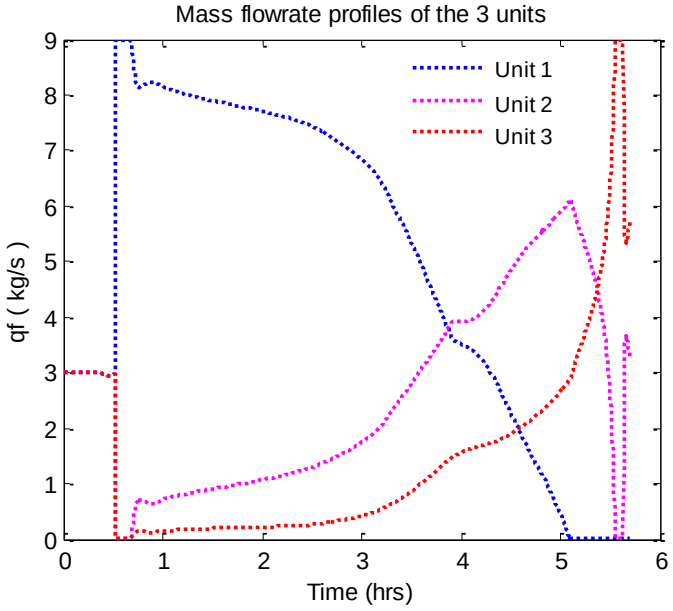

Figure 6.13 Controlled mass flowrate distribution through each unit

Fig. 6.14 shows the output temperature profiles corresponding to the three operational strategies. When the design temperature is 16 ℃, the operational time window determined by the controlled distribution scheme, can be extended much longer than the other two approaches for a LTES system with the same total stored latent energy. When the design temperature is 22 ℃, the advantage of the controlled operation decreases. This is because the output temperature is limited by the length of a LTES system (Fig. 6.1) for HTFs with a fixed mass flowrate. Here, the effectiveness of a LTES system is introduced which is defined as [24, 25]:

$$\varepsilon = \frac{T_f^{out} - T_f^{in}}{T_m - T_f^{in}}, \tag{4.4}$$

where T_m is the melting temperature of the PCM. Given a fixed length of a LTES system (Fig. 6.1), and the melting temperature of the PCM, the output temperature defines the effectiveness of a LTES system which is also influenced by the HTF mass flowrate. From Fig. 6.15(a) it can be seen that with small effectiveness, the operational time window can be increased by more than 26% compared to the parallel operational configuration. Similarly, the operational window can be increased by more than 46% compared to the in-series operational configuration. However, this advantage also decreases with the increase of the effectiveness. When the effectiveness is over 0.5, in series operation out-performs the other two options. This is because the length of a LTES has reached a prescribed limit to meet the design output temperature for a certain mass flowrate HTF. To increase the effectiveness, the mass flow rate of the HTF should be reduced. Fig. 6.15(b) shows the operational time windows in the higher effectiveness range due to reduced inlet mass flowrate of the HTF. It still shows that the controlled distribution has longer operational time windows for a given design temperature

compared to the other operational configurations for the same sized LTES system. However, the effectiveness is not the decisive factor in determining the performance of the controlled distribution operation. When the controlled distribution cannot compete with the series operation, the implication is that the design temperature reaches a limit under the current sized LTES system with a given HTF mass flow rate.

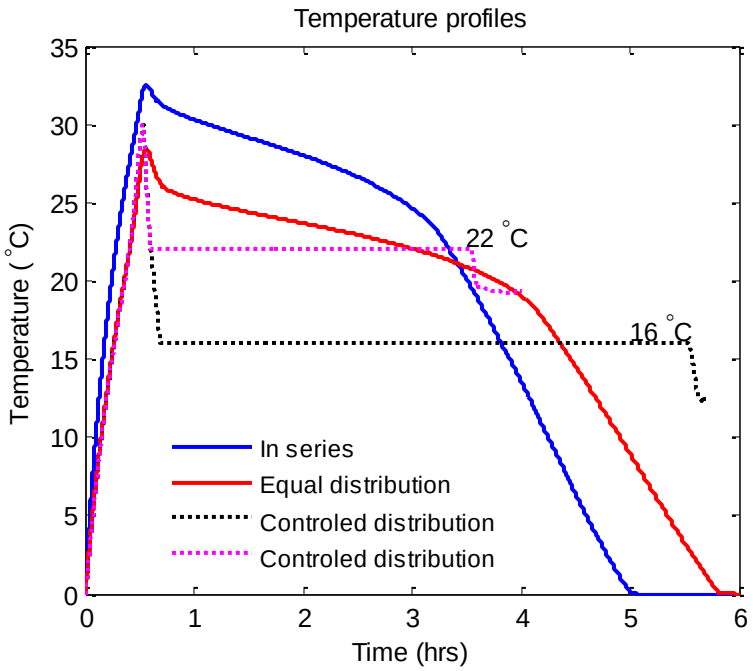

Figure 6.14 Comparison of output temperature profiles for different operational strategies

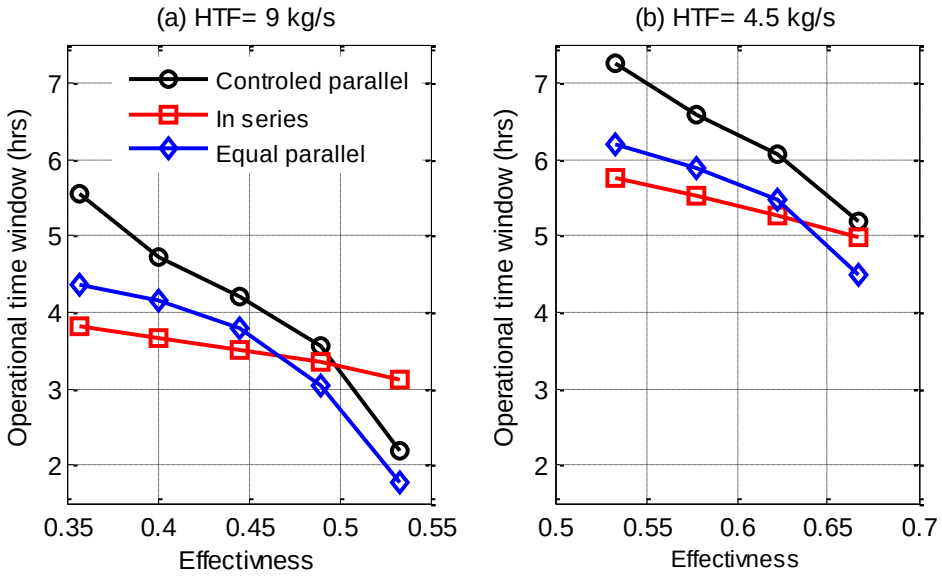

Figure 6.15 Operational time windows under varying effectiveness

4. Conclusions

In this paper, an efficient discrete time dynamical (DTD) model for a large scale LTES system is proposed. The LTES system is a bulky tank with embedded circular finned heat pipes to enhance the heat transfer performance. The dynamical model was employed for operational research studies to address important questions regarding the state of charging or discharging, optimal control of mass flow rate of the heat transfer fluid (HTF) and the configuration of multiple LTES units. For a prescribed heating load requirement, the effects of three different operational configurations were explored using the dynamical model. These included (i) equal distribution of the heat transfer fluid (HTF) into 3 parallel identical units (ii) operation in series of the three units and lastly, a controlled variable distribution of the HTF to three parallel LTES units. It was found that for a given size of a LTES system, controlled variable distribution of the HTF can operate under the required design temperature for a longer time window than the other two

operational configurations. Thus for a prescribed heating time window, smaller sized LTES systems can be used for investment savings.

Acknowledgement

This research is sponsored by the ARPA-e ARID Program under Contract No. DE-AR0000582. Any opinions, findings, and conclusions or recommendations expressed in this article are those of the authors and do not necessarily reflect the views of the Advanced Research Projects Agency-Energy.

References

[1] Ammar M. Abdulateef, Sohif Mat, Jasim Abdulateef, Kamaruzzaman Sopian, Abduljalil A. Al-Abidi. Geometric and design parameters of fins employed for enhancing thermal energy storage systems: a review. Renew a Sustain Energy Rev 2018; 82 (1): 1620-35.

[2] Mohammed Mumtaz A. Khan, Nasiru I. Ibrahim, I.M. Mahbubul, Hafiz Muhammad. Ali, R. Saidur, Fahad A. Al-Sulaiman. Evaluation of solar collector designs with integrated latent heat thermal energy storage: A review. Sol Energy 2018; 166: 334-50.

[3] S. Saeed Mostafavi Tehrani, Yashar Shoraka, Gonzalo Diarce, Robert A. Taylor. An improved, generalized effective thermal conductivity method for rapid design of high temperature shell-and-tube latent heat thermal energy storage systems. Renew Energy 2019; 132:694-708.

[4] G. Diarce, Á. Campos-Celador, J.M. Sala, A. Garc á-Romero. A novel correlation for the direct determination of the discharging time of plate-based latent heat thermal energy storage systems. Appl Therm Eng 2018; 129: 521-34.

[5] Stefan Hübner, Markus Eck, Christoph Stiller, Markus Seitz. Techno-economic heat transfer optimization of large scale latent heat energy storage systems in solar thermal power plants. Appl Therm Eng 2016; 98: 483-91.

[6] Edgar, T.F., Powell, K.M., Energy intensification using thermal storage. Current Opinion in Chemical Engineering 2015. 9: 83-8.

[7] Cole, W., Powell, K. & Edgar, T.. Optimization and advanced control of thermal energy storage systems 2012; 28(2-3): 81-99.

[8] Gianluca Serale, Massimo Fiorentini, Alfonso Capozzoli, Paul Cooper, Marco Perino. Formulation of a model predictive control algorithm to enhance the performance of a latent heat solar thermal system. Energy Convers Manage 2018; 173:438-49.

[9] F. Ghani, R. Waser, T.S. O'Donovan, P. Schuetz, M. Zaglio, J. Wortischek. Non-linear system identification of a latent heat thermal energy storage system. Appl Therm Eng 2018; 134: 585-93.

[10] Minh Tri Luu, Dia Milani, Mobin Nomvar, Ali Abbas. Dynamic modelling and analysis of a novel latent heat battery in tankless domestic solar water heating. Energ Buildings 2017; 152: 227-42.

[11] Mohamad Salameh, Stephen Wilke, Ben Schweitzer, Peter Sveum, Said Al-Hallaj and Mahesh Krishnamurthy. Thermal state of charge estimation in phase change composites for passively cooled lithium-ion battery packs. IEEE T Ind Appl 2018; 54(1): 426-36.

[12] Tilman Barz, Dominik Seliger, Klemens Marx, Andreas Sommer, Sebastian F. Walter, Hans Georg Bock, Stefan Körkel. State and state of charge estimation for a latent heat storage. Control Eng Pract 2018; 72: 151-66.

[13] Hamidreza Shabgard, Christopher W. Robak, Theodore L. Bergman, Amir Faghri. Heat transfer and exergy analysis of cascaded latent heat storage with gravity-assisted heat pipes for concentrating solar power applications. Sol Energy 2012; 86(3):816-30.

[14] K. Nithyanandam, R. Pitchumani. Design of a latent thermal energy storage system with embedded heat pipes. Appl Energy 2014; 126: 266-80.

[15] Christopher W. Robak, Theodore L. Bergman, Amir Faghri. Enhancement of

latent heat energy storage using embedded heat pipes. Int J Heat Mass Trans 2011; 54 (15–16):3476-84.

[16] Bo-wen Hu, Qian Wang, Zhen-Hua Liu. Fundamental research on the gravity assisted heat pipe thermal storage unit (GAHP-TSU) with porous phase change materials (PCMs) for medium temperature applications. Energy Convers Manage 2015; 89:376-86.

[17] Sina Lohrasbi, Seyed Ziaedin Miry, Mofid Gorji-Bandpy, Davood Domiri Ganji. Performance enhancement of finned heat pipe assisted latent heat thermal energy storage system in the presence of nano-enhanced H2O as phase change material. Int J Hydrog Energy 2017; 42(1): 6526-46.

[18] Nourouddin Sharifi, Amir Faghri, Theodore L. Bergman, Charles E. Andraka. Simulation of heat pipe-assisted latent heat thermal energy storage with simultaneous charging and discharging. Int J Heat Mass Trans 2015; 8: 170-79.

[19] Chunjian Pan, Natasha Vermaak, Carlos Romero, Sudhakar Neti, Sean Hoenig, Chien-Hua Chen. Efficient optimization of a longitudinal finned heat pipe structure for a latent thermal energy storage system. Energy Convers Manage 2017; (153): 93-105.

[20] Chunjian Pan, Natasha Vermaak, Carlos Romero, Sudhakar Neti, Sean Hoenig, Chien-Hua Chen, Richard Bonner. Cost estimation and sensitivity analysis of a latent thermal energy storage system for supplementary cooling of air cooled condensers. Appl Energy 2018; 224: 52-68.

[21] Zhongliang Liu, Zengyi Wang, Chongfang Ma. An experimental study on heat transfer characteristics of heat pipe heat exchanger with latent heat storage. Part I: Charging only and discharging only modes. Energy Convers Manage 2006; 47(7–8):944-66.

[22] Theodore L. Bergman, Adrienne S. Lavine, Frank P. Incropear, David P. DeWitt. Fundamentals of Heat and Mass Transfer, 7th edition , John Wiley & Sons 2011.

[23] Pan C., Vermaak N., Romero C., Neti S., Sean Hoenig, Chien-Hua Chen, Richard Bonner III. Cost optimal design and sensitivity analysis of a shell and tube latent thermal energy storage system constrained by operational requirements. Appl Energ, under review.

[24] N.A.M. Amin, M. Belusko, F. Bruno, M. Liu. Optimising PCM thermal storage systems for maximum energy storage effectiveness. Sol Energy 2012; 86 (9):2263-72.

[25] N.H.S. Tay, M. Belusko, F. Bruno. An effectiveness-NTU technique for characterising tube-in-tank phase change thermal energy storage systems. Appl Energy 2012; 91(1): 309-19.

Chapter 7

Experimental, numerical and analytic study of unconstrained melting in a vertical cylinder with a focus on mushy region effects

(Pan, C., Charles, J., Vermaak, N., Romero, C., Neti S., et al. Experimental, numerical and analytic study of unconstrained melting in a vertical cylinder with a focus on mushy region effects. *International Journal of Heat and Mass Transfer*, 124, p.1015-1024, 2018.)

Experimental, numerical and analytic study of unconstrained melting in a vertical cylinder with a focus on mushy region effects

Chunjian Pan*[1], Joshua Charles[1], Natasha Vermaak[1], Carlos Romero[1], Sudhakar Neti[1],
Ying Zheng[2] Chien-Hua Chen[2], Richard Bonner III[2]
[1]Energy Research Center, Lehigh University, Bethlehem, PA 18015, USA
[2]Advanced Cooling Technologies, Inc., Lancaster, PA 17601, USA

Abstract

The enthalpy-porosity method is widely used in solving solid-liquid phase change problems that involve convection in the melt; however the influence of the required mushy zone parameter on the melting process has been largely overlooked. In this paper, further investigation of the mushy zone parameter is presented. The enthalpy-porosity method is the default model in Fluent for melting simulations. A comprehensive discussion of previously reported mushy zone parameter values is presented with a comparison to numerical and experimental results. In this paper, based on experimental validations of melting times, it is found that mushy zone parameters can be optimized based on relevant driving temperature differences. And despite the fact that the model cannot capture bulk solid sinking behaviors, numerical solid sinking behaviors by Fluent are still widely reported in the literature. Explanations and supporting numerical analysis are given for this seeming contradiction. Finally, an analytic solution for unconstrained sinking with the incorporation of the mushy zone concept is developed. With the introduction of a tuning parameter to modify the viscosity of the mushy region in the bottom liquid layer, good agreement between the analytical model and experimental results is achieved. A linear correlation for the tuning parameter based on driving temperature differences is given.

Key words: enthalpy-porosity method, mushy zone constant, unconstrained melting

Nomenclature

S	A source term to modify the moment equation
C	Mushy zone parameter
$\vec{v}$	Velocity field, $\mathrm{m/s}$
D	Diameter of the cylinder, cm
w_s	Thickness of the cylinder bottle wall, mm
w_b	Thickness of the cylinder bottle bottom, mm
std	Standard deviation, s
dT	Driving temperature difference, ℃
H	Height, m
R	Radius of solid PCM for the analytic solution, m
h	Remaining height of solid PCM during analytic melting, m
r	Shrinking radius of the solid PCM, m
T	Temperature, ℃
$u(r)$	Flow velocity in the bottom liquid layer, $\mathrm{m/s}$
$P(r)$	Pressure distribution in the bottom liquid layer, Pa
z	Height variable, m
M	Tuning parameter for the viscosity in the mushy zone liquid layer
g	Acceleration due to gravity, $\mathrm{m/s^2}$
L_f	Latent thermal energy of PCM, J/kg
L_e	Virtual latent thermal energy of PCM, J/kg
Cp	Heat capacity of PCM, J/kgK
k	Conductivity of PCM, W/mK
X	Liquid fraction of PCM
V	Volume, $\mathrm{m^3}$
t	Time, min
x	Width of a drawn vector box, cm
y	Height of a drawn vector box, cm
Greek letters	
$\in$	A small number to prevent division by zero

ρ	Density of PCM, kg/m^3
μ	Viscosity, $Pa \cdot s$
δ	Bottom liquid thickness, m
α	Liquid volume fraction of PCM
Subscripts	
l	Liquid state
s	Solid state
i	Initial
m	Melting
w	Wall
c	Cylinder
pcm	Phase change material

1. Introduction

The enthalpy-porosity method [1], which is based on fixed grids, is the most popular modeling method for solid-liquid phase change problems that involve convection in the melt. It is the default method employed in the commercial computational fluid dynamics (CFD) code ANSYS Fluent. The enthalpy-porosity technique treats the mushy region (partially solidified region) as a porous medium. The porosity is set equal to the liquid fraction of the region. The fully solidified region has zero porosity and the phase change material (PCM) velocity approaches zero. To capture the mushy zone behavior, a source term is used to modify the momentum equation in the mushy region. The source term has the form [2]:

$$S = C\frac{(1-\alpha)^2}{(\alpha^3+\epsilon)}\vec{v}, \tag{1.1}$$

where ϵ is a small number (0.001) to prevent division by zero, α is the PCM liquid

volume fraction, $\vec{v}$ is velocity field and C is the mushy zone parameter. In the liquid region ($\alpha = 1$), the source term has a zero value and the momentum equation describes the actual fluid velocities. In the mushy zone region, the moment equation approximates the Darcy law. A small C allows for significant flow and a large value suppresses the fluid velocities. In the solid region ($\alpha = 0$), the parameter C effectively forces the velocities to zero. However, when C is too small, i.e. $C = 10^2$, the solid PCM is treated like a highly viscous fluid. When C is too large, i.e. $C = 10^8$, the solid remains suspended in the liquid contrary to experimental findings that demonstrate the sinking of the solid PCM [3]. It is clear that the default enthalpy-porosity method within ANSYS Fluent [2] is incapable of modeling the bulk solid sinking behavior.

The influence and treatment of the mushy zone parameter on melting processes within the enthalpy-porosity method has been largely overlooked, despite the fact that the method is widely employed. Kumar and Krishna [4] numerically studied melting in a 2-D rectangular cavity by using the CFD code ANSYS Fluent 16.0. It was observed that the mushy zone constant had significant influence on the thermohydraulics of the melt PCM. As a result, the melt fraction curve depends sensitively on the mushy zone parameter.

Assis et al. [5] studied melting in a spherical shell both experimentally and numerically. It was found that $C = 10^5$ showed solid sinking behavior in the simulations and fitted well to the experimental results. A commercial PCM, RT27, was used in his study and its viscosity is around 0.0035 $\mathrm{Pa \cdot s}$ [6]. Hosseinizadeh et al. [7] also studied unconstrained melting in a spherical shell using n-octadecane, whose viscosity is 0.0039 $\mathrm{Pa \cdot s}$. It was also confirmed that $C = 10^5$ gave good agreement between the numerical

and experimental results. Dari et al. [8] numerically studied unconstrained melting in a rectangular enclosure. With the mushy zone parameter C set at $C = 10^5$, solid sinking behaviors were observed. After Assis's work [5], many researchers [8-13] mentioned using a value of $C = 10^5$ for the mushy zone parameter when modeling PCM melting processes by the enthalpy-porosity method [1].

Mushy zone constants with some other values have also been reported in the literature. Tiari et al. [14] reported that with a mushy zone value $C = 2.5 \times 10^6$ the numerical results showed good agreement with previous experimental works. The PCM used in Tiari's work [14] is KNO_3, whose viscosity is 0.00259 $\mathrm{Pa \cdot s}$. Elbahjaoui and Qarnia [15] numerically studied melting of a paraffin wax (P116) dispersed with Al_2O_3 nanoparticles in a rectangular storage unit. The viscosity of P116 is 0.0013 $\mathrm{Pa \cdot s}$. A mushy zone value $C = 1.6 \times 10^6$ was used, which was reported to have good agreement with experimental results in the literature.

However, with these parameter values, disagreement between numerical and experimental results was also reported in the literature. Shmueli et al. [16] simulated PCM (RT27) melting in a vertical cylindrical tube, which was insulated at the bottom and exposed to air at the top and heated at the tube wall. The effect of the mushy zone parameter C on the simulation results was investigated. It was found that with $C = 10^5$, the resulting melting time by the simulation was about 2.5 times shorter than the experimentally measured time under the same conditions. A concern should be raised because the discrepancy could not be overcome by any changes of the mushy zone parameter and also material properties (such as the density and viscosity of the liquid phase) [16]. What's more disturbing is that in Assis's work looking at the spherical

geometry [5], with the same PCM (RT27), good agreement between the numerical and experimental results was reported.

Thus a further look into the two cases is necessary. The most obvious differences between the cases are the geometry and the boundary conditions. For both of the cases, the PCM would sink towards the bottom of the container during the experiments, which will effectively reduce the thermal resistance between the solid PCM and the bottoms of the containers. However, for the vertical cylinder case [16], the bottom was insulated, so the solid sinking phenomenon would have small contribution to heat transfer enhancement. While for the sphere case [5], it was heated around the spherical shell, so the solid sinking phenomenon accelerated the melting process as demonstrated by the experimental melting patterns [5]. It can be argued that with the mushy zone parameter set to $C = 10^5$, the source term (Eqn. 1.1) generates suitable level of convection enhanced heat transfer in the liquid PCM, which agrees with the experiment. However, for the vertical cylinder case [16], one presumed conclusion is that the source term---with any value of the mushy zone parameter--- always creates more convection in the liquid PCM than the real experimental situation when the solid sinking has a small role in enhancing the heat transfer.

Moreover, it is mentioned that the melting model in Fluent does not have the mechanism to model solid sinking. Ghasemi and Molki [17] numerically studied unconstrained melting in square cavities by a fixed-grid enthalpy formulation. In their work, to account for solid sinking, besides the natural convection source term in the momentum equation, the bulk solid sinking induced convection was expressed as a separate source term, which captures the sinking of the solid phase. It was found that

when the sinking source term was set to zero, natural convection can also cause the solid to sink as the convection in the liquid phase can exert a downward shearing force on the solid. The two sources terms can achieve similar PCM melting patterns. However, studies [5, 7, 8] without such a source term also demonstrated that with a suitable mushy zone parameter value, solid sinking patterns were observed by numerical analysis. Thus a suitable mushy zone parameter value is needed to match the numerical results by Fluent with the experimental ones [5, 7]. This further concludes that the mushy zone parameter plays a vital role in modeling PCM melting by the enthalpy-porosity method [1]. It needs to be calibrated by experimental results for reliable numerical analysis.

From above discussions, further study on the mushy zone parameter is needed. In this paper, an experimental study of PCM melting in a vertical cylinder that is heated in a water bath is carried out. The PCM used in this paper is Calcium Chloride hexahydrate ($CaCl_2 \cdot 6H_2O$), whose viscosity is 0.01 Pa · s, which is much larger than that of paraffin. Then numerical simulations with different values of the mushy zone parameter are compared to the experimental results. On the one hand, this study is used to confirm whether the numerical solution can match the experimental results when heat transfer is enhanced by the solid sinking behavior. On the other hand, it is desired to find a suitable mushy zone parameter value, which can be applied to PCM melting in a vertical cylindrical geometry with solid sinking phenomenon, as in the previous studies [5, 7] that were based on a spherical geometry. Furthermore, whether the numerical model can capture the sinking phenomenon is discussed by comparing the numerical results with the experimental ones.

Finally, as the numerical method is incapable of modeling the sinking phenomenon,

a modified analytic solution based on the bulk solid sinking phenomenon was developed. During earlier works, Moore and Bayazitoglu [20] studied contact melting of a PCM within a spherical enclosure. Their mathematical model was confirmed by experimental evidence. The contact melting process of solid materials on circular and rectangular heated plates was analyzed by Webb and Viskanta [21]. Chen et al. [22] developed an analytic solution for close-contact melting in a vertical tube with isothermal heating both at the side wall and the bottom. Close-contact melting of a PCM inside a heated rectangular capsule was also analytically studied by Chen. et al [23]. Yoo [24] analytically studied unsteady close-contact melting on a plate and showed that initially the melt height is far from constant. Kozak, et al. [25] studied close-contact melting in vertical annular enclosures both numerically and analytically. Rozenfeld et al. [26] studied close-contact melting in a horizontal cylindrical enclosure with longitudinal plate fins. More recently, Zhao et al. [27] theoretically and experimentally studied close-contact melting in a rectangular cavity at different tilt angles. In this paper, considering the analytic model by Chen et al. [22] tends to under predict the melting time, a tuning parameter that can effectively controls the thickness of the bottom liquid layer is introduced in the development of the solution. With this tuning parameter, the analytical solution achieves good agreement with the experimental results.

The content of this paper is organized as follows. In section 2, the experimental setup is introduced. In section 3, numerical studies by Fluent are performed along with the determination of the mushy zone parameters to match the experimental results. Section 4 presents a new analytic solution. Section 5 summarizes the conclusions.

2. Experimental setup and results

In this paper, Calcium Chloride hexahydrate ($CaCl_2 \cdot 6H_2O$) was used for the experimental study of unconstrained melting. The properties of $CaCl_2 \cdot 6H_2O$ are given in Table 7.1. Figure 7.1 shows the schematic of the experimental setup. It primarily consists of a controllable water bath, a GoPro camera, a light and a glass tube containing the PCM. During the experiment, the PCM tube is vertically suspended in the water bath. The GoPro is set to acquire a photo every 10 seconds, which allows the final melting time of one sample to be recorded. Before the experiment, the sample was immersed in a separate water bath overnight with its temperature held at 24℃. This temperature will be the initial temperature to be used in the numerical analyses.

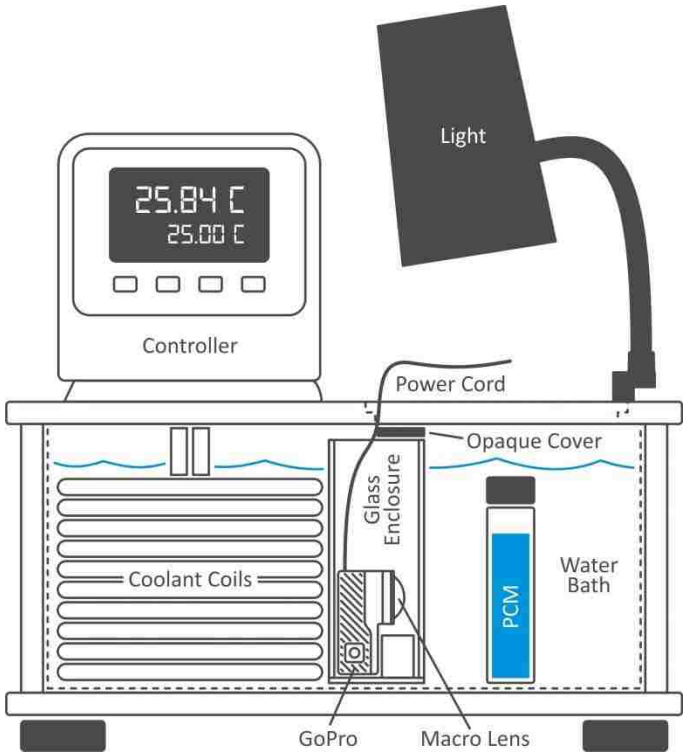

Figure 7.1 Schematic diagram of the experimental setup

Two samples (10g & 20g) were used to record the melting time. The height values in Table 7.1 are calculated based on the two weights and inner tube diameter. Multiple samples were prepared with the same weight. In addition, melting tests of these samples were repeated under three different driving temperature differences (10℃, 15℃ and 20℃). Table 7.4 shows the melting times, along with mean values and standard deviations (std) of the two sample weights under the three temperature differences. Figure 7.3 shows the melting patterns of one case at different times. It can be seen that the solid shrinking happened much faster along the height than in the radial direction, which clearly demonstrate solid sinking can efficiently promote melting. Figure 7.4 summarizes the experimental results.

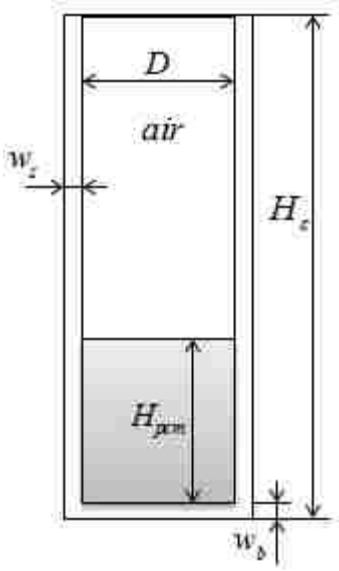

Figure 7.2 Computational domain of the tube

Table 7.1 Samples

Cases	H_{pcm} (cm)
#1 (10g)	1.6237
#2 (20g)	3.2474

Table 7.2 Tube dimensions

H_c	9.5 (cm)
D	2.258(cm)
w_s	1.08 (mm)
w_b	1.0 (mm)

Table 7.3 Tube properties

Density	$2235(kg/m^3)$
Thermal conductivity	1.1 (W/mK)
Specific heat	800 (J/kgK)

Table 7.4 Melting time for multiple samples under different temperature differences

Cases	dT(℃)	Melting times (s)							
		1	2	3	4	5	6	mean	*std*
#1	10.0	680	700	710	680	610	660	673.33	35.59
#2		1140	1080	1080	1030	990	1000	1053.33	57.15
#1	15.0	440	450	480	500	510	520	483.33	32.65
#2		690	700	720	730	740	780	726.67	32.04
#1	20.0	360	360	330	320	330	350	341.67	17.22
#2		510	550	530	550	560	490	531.67	27.14

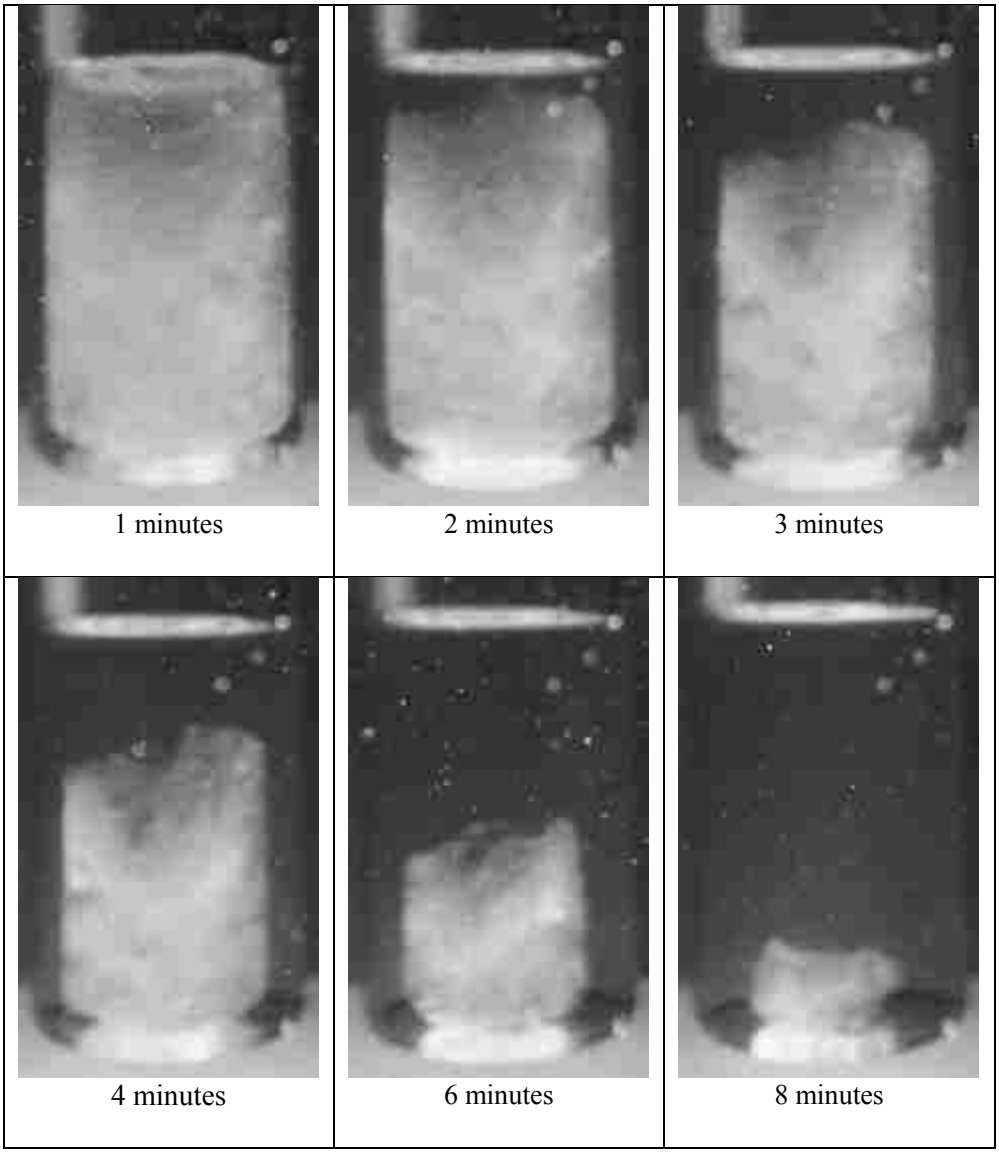

Figure 7.3 Melting patterns under 20℃ temperature differences for Case # 2

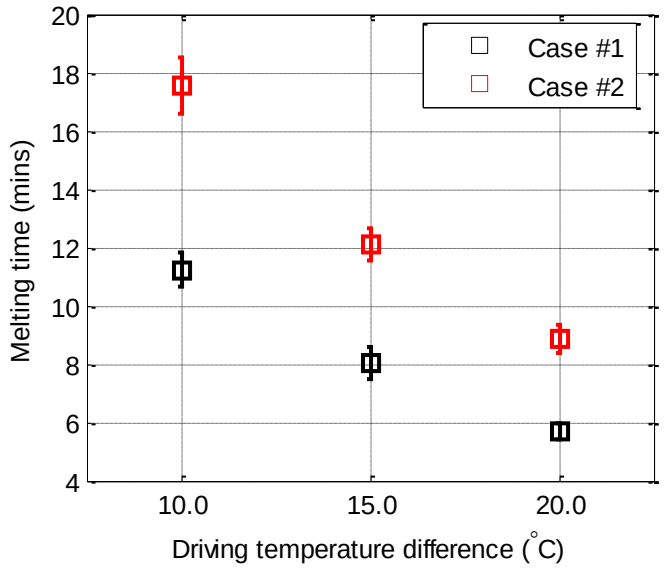

Figure 7.4 Mean melting times & standard deviations of two sample weights under three temperature differences.

3. Numerical study and discussions

Numerical studies were carried out using the commercial software ANSYS 16.0\Fluent. The computational domain of the model is shown in Figure 2, along with its dimensions in Tables 7.1 & 7.2. The 'volume-of-fluid' (VOF) model is used to describe the PCM-air system in the Fluent software. The VOF model treats two or more fluids as non-interpenetrating phases. To simulate the melting process, Fluent uses an enthalpy-porosity formulation by Voller et al. [2, 18]. Extensive descriptions of the numerical models can be found in the literature [5, 20]. Thus mathematical description is omitted in this paper.

Figure 7.2 in Section 2 shows the computational domain to be simulated in Fluent. Constant temperature was applied to both the bottom and the side wall of the cylinder. The top of the cylinder is closed and is adiabatic. Properties of $CaCl_2 \cdot 6H_2O$ used in the

simulations are shown in Table 7.5. The melting temperature range is $(301\ \mathrm{K} - 303\ \mathrm{K})$. In the numerical simulations, as the difference of the specific heats of the solid and liquid phases is small, an average value $2145\ \mathrm{J/kgK}$ is used, which makes it easier to be implemented in the analytic solution. Piecewise linear functions were used for both the density and thermal conductivity (Table 7.6).

Table 7.5 Thermophysical properties of $CaCl_2 \cdot 6H_2O$

Properties	Values
Melting temperature	29 (℃)
Density (solid/liquid)	1706/1538 ($\mathrm{kg/m^3}$)
Thermal Conductivity (solid/liquid)	1.09/0.546 ($\mathrm{W/mK}$)
Specific heat (solid/liquid)	2060/2230 ($\mathrm{J/kgK}$)
Latent heat	170 ($\mathrm{kJ/kg}$)
Dynamic viscosity	0.01 $\mathrm{Pa \cdot s}$
Coefficient of thermal expansion	0.0005 $\mathrm{K^{-1}}$

Table 7.6 Properties used in the simulations

Temperature (K)	301	302	303
Density (kg/m^3)	1706	1622	1538
Conductivity (W/mK)	1.09	0.818	0.546

In the setting of the numerical model in Fluent, an explicit scheme was chosen for the volume fractions of air and PCM and a sharp interface between them was selected; the cutoff criterion is 1×10^{-7} and the Courant number is set to 0.25. The SIMPLE algorithm was used and second order upwind spatial discretization was chosen for both the momentum and energy equations. A quadrilateral grid structure was used for the mesh. According to the mesh and time step independence study shown in Figure 7.5, an element size 0.2mm and a time step of 0.01s were chosen for all the following numerical simulations.

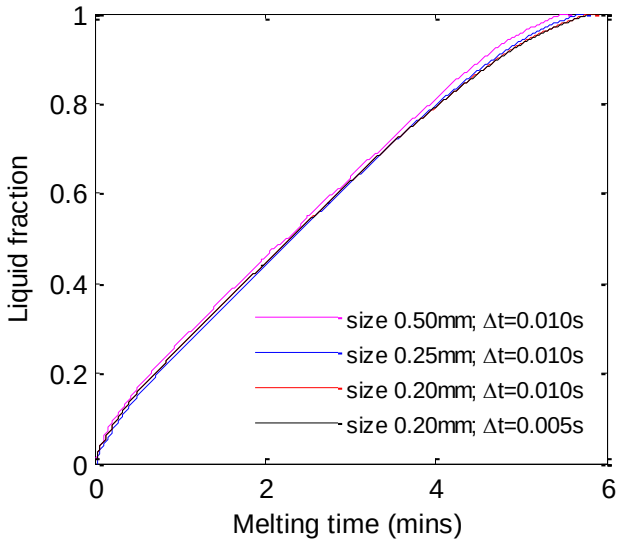

Figure 7.5 Mesh and time step independence study

To estimate the melt fraction throughout the melting process, images from the GoPro were imported into CorelDraw. CorelDraw is a vector-based design software package. Since the frames were taken at 10 second intervals, the time for each frame could be easily determined. After importing the images into CorelDraw, the images were scaled to the correct dimensions using the outside diameter of the bottle. Once scaled, a vector box was drawn over the solid portion of the PCM. The volume of this solid portion was calculated as $V_s = \left(\frac{x}{2}\right)^2 \pi y$, where x is the width of the drawn box and y is the height of the same box. At t = 0, V_s is assumed to be equal to 1. All V_s values for t > 0 are referenced to V_s (t=0). Three repeated experimental data sets were used to estimate the liquid fraction during the melting for each case as shown in Figures 7.6 & 7.7. The consistency of the liquid fractions for the same case by this method is acceptable.

Figures 7.6 & 7.7 show liquid fraction curves of Case #1 with different values of the mushy zone constant under 10℃ and 20℃ driving temperature differences, respectively. It was found that for $dT = 10℃$ a mushy zone constant $\mathrm{C} = 38 \times 10^5$

gives the best agreement with the experimental points. For $dT = 20℃$, an optimal mushy zone constant is $\mathrm{C} = 7.5 \times 10^5$. It seems that for different driving temperature differences, a different mushy zone constant is needed to match the numerical melting time with the experiment. This situation is further confirmed in Figure 7.8. For $dT = 15℃$, an optimal mushy zone constant is $\mathrm{C} = 18 \times 10^5$. It can be seen that under the same driving temperature difference, with the same mushy zone constant, the numerical melting time for Case #2, which has a different mass of PCM and a different height-to-radius ratio than Case #1, shows good agreement with the experiments. Thus, it can be concluded that an optimal mushy zone constant is needed based on driving temperature difference when using Fluent to simulate melting. However, as indicated by Figure 7.9, there is no strong linear relationship between the driving temperature difference and the mushy zone constant that is suggested by the experiments. A possible reason for this is that the differences in temperature gradients results in different magnitudes of natural convection, which affects the heat transfer performance in the liquid phase. Calibration with experiment is necessary to find a suitable mushy zone parameter value.

As a reminder, Shmueli [16] who also studied melting in a vertical cylindrical tube reported that no match can be found between the experimental and the numerical results for any value of the mushy zone parameter. The main difference is that with no bottom surface heating in Shmueli's [16] experiment, no heat transfer was promoted by the solid sinking phenomenon. Because of this, melting in the experiment happened much slower than the melting model in Fluent can predicted. When solid sinking promotes melting in the experiment, a match between the experiment and the numerical model

was found with the optimal value of the mushy zone constant reported in [5, 7].

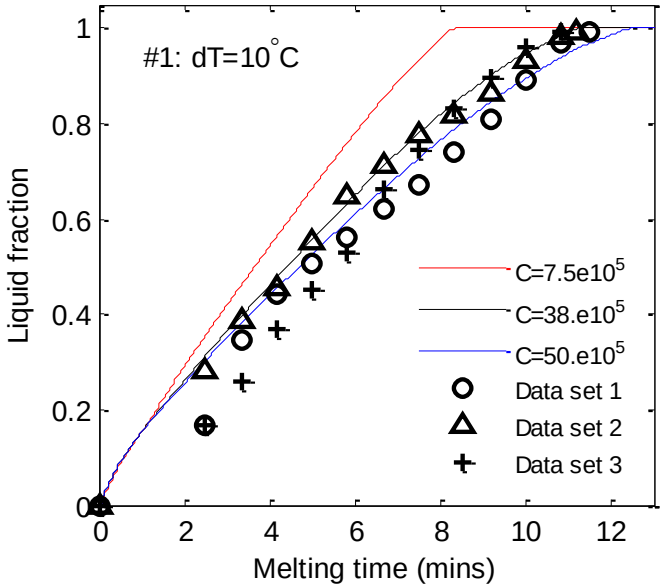

Figure 7.6 Mushy zone constant study for Case 1 with 10℃ driving temperature difference

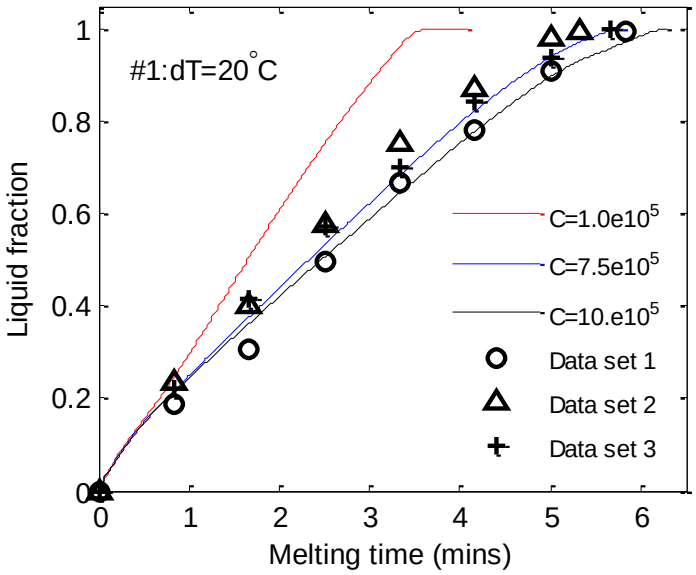

Figure 7.7 Mushy zone constant study for Case 1 with 20℃ driving temperature difference

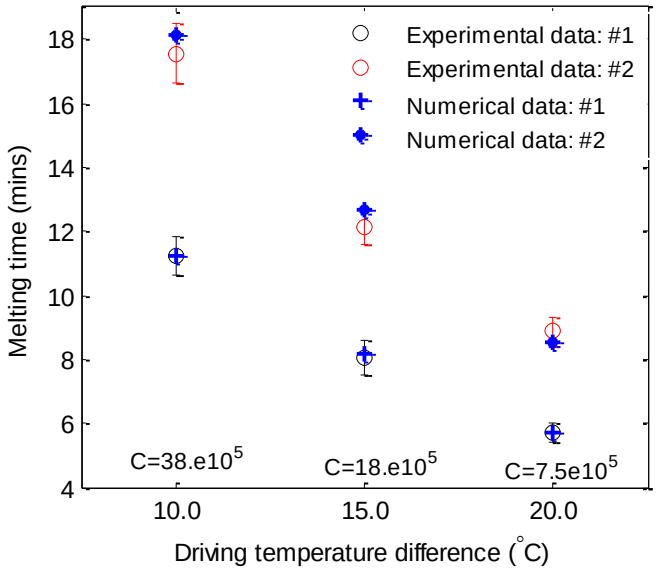

Figure 7.8 Numerical and experimental melting times comparisons

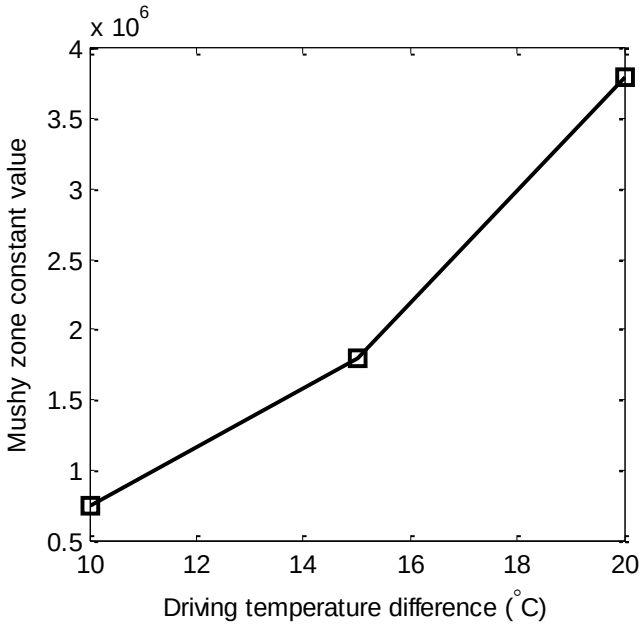

Figure 7.9 Relationship between the driving temperature difference and verified mushy constant value

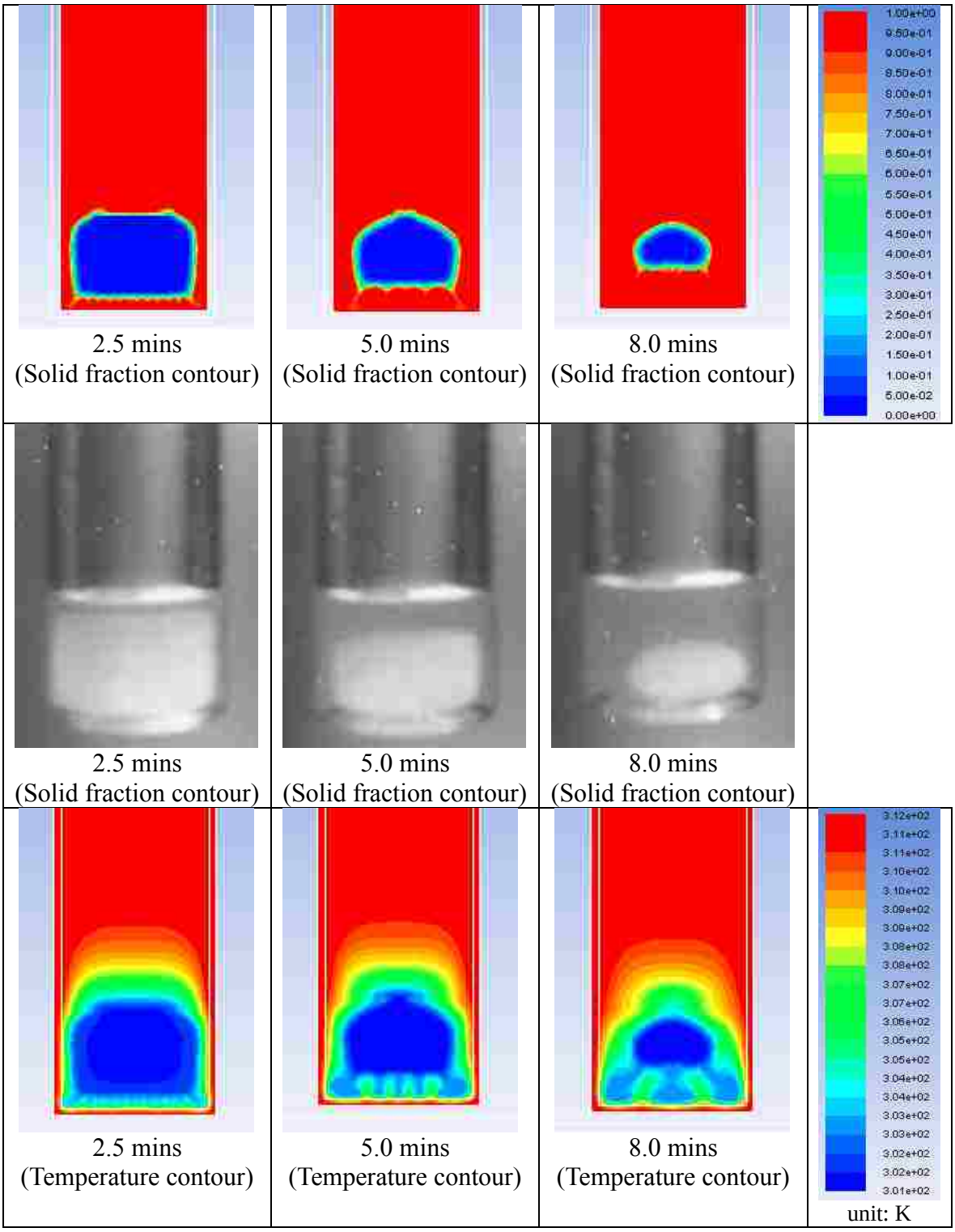

Figure 7.10 Numerical and experimental melting patterns comparisons

Figure 7.10 shows the numerical and experimental melting patterns. In terms of the

solid fraction, the numerical and the experimental results show the same trend with time. No bulk solid sinking phenomenon is shown in the numerical fraction contours. However, the temperature contours seem to exhibit some sinking phenomenon. It is clear that the melting model in Fluent does not have the mechanism to capture the bulk solid downward movement. Nevertheless, in the mushy zone, due to the density difference, natural convection drives the heavier mushy components (partial solid) downward. Thus, relatively lower temperature at the bottom of the tube (blue 'tailing' temperature contour) is observed through the melting process. This behavior to some degree mimics the contact melting phenomenon, as the incompletely melted solids fall down to the bottom, although there is no differentiation between the solid and the liquid in the numerical approach. This may also explain the numerical sinking phenomenon reported in the literature [5, 7, 8] when using Fluent.

Furthermore, as the mushy zone parameter C controls the intensity of convection, especially in the mushy zone, C can affect the 'sinking' of the mushy components through natural convection, when the bottom surface is heated. This can be the reason that for each driving temperature difference, an optimal C is needed so that the numerical melting rate will be comparable to the experiment. However, when the bottom surface is insulated (no solid sinking to promote melting), the tuning of C is of no use due to the much slower melting process in the experiment [16]. When the bottom is heated, a good match can be achieved with a proper C value [5, 7]. There are two probable reasons for the C values reported in this paper to be different from those in the literature [5, 7]: one is the different viscosity, the other may be the differences in the bottom shape (flat versus curved). With a spherical bottom, heat transfer enhancement by solid sinking is more

effective than the cylindrical shape in the current paper, resulting in a smaller mushy zone parameter ($C = 10^5$) for the numerical model to match the experiment.

4. A modified analytic solution for unconstrained melting in a tube

The analytic solution proposed here for melting in a tube is based on contact melting analysis [20-24]. When PCM melts, a thin fluid layer with thickness δ is formed between the solid PCM and the bottom heating surface (Figure 7.11). The heavier solid PCM tends to squeeze out the liquid and so δ remains thin. It is assumed that the process is quasi-steady, which means at every moment the weight of the solid is balanced by the pressure in the liquid film. Other assumptions include: 1) the temperature of the solid remains at the initial temperature; 2) heat transfer is dominated by conduction in the liquid film; 3) the liquid film has uniform thickness; 4) the flow in the liquid film is primarily parallel to the solid surface and driven by pressure gradients; 5) the inertia terms in the governing equations are neglected.

Based on these assumptions, Chen et al. [21] developed an analytic solution for close contact melting in a vertical tube with isothermal heating both at the side wall and the bottom. However, these assumptions are only valid when the solid phase is much denser than the liquid. It was found that the analytical model by Chen et al. [21] always tends to under predict the melting time. One most probable cause is the air voids in the solid PCM (observable during the experiments) that may significantly lower the melting rate. The analytic model does not include the thickness of the glass tube and the heat transfer coefficient between the water and the tube, which slightly underestimates the

thermal resistance. The other possible cause is that the PCM ($CaCl_2 \cdot 6H_2O$) used in the experiment is of 98% purity. A sharp melting front may not be highly valid. Some transitional mushy zone could exist in the bottom liquid layer. Aiming at these situations that cannot be completely in accordance with the analytic model, a tuning parameter that can effectively adjust the thickness of the melt layer is introduced into the analytic solution. In this section, an analytic solution with a tuning parameter to adjust the thickness of the liquid layer is developed and its validation with experimental results is presented.

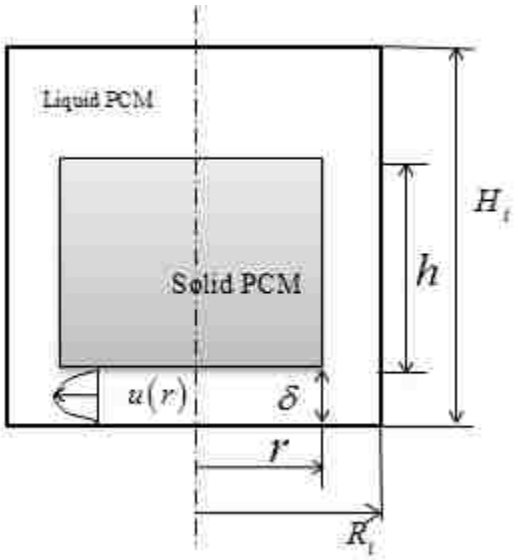

Figure 7.11 Schematic of unconstrained melting

Figure 7.11 shows the schematic of unconstrained melting in a cylinder. Assuming that the initial temperature is T_i everywhere, the PCM melting temperature is T_m and the cylinder is heated at the sides and the bottom with constant temperature T_w. The top boundary has zero heat flux.

First, a force balance acting on the solid PCM is considered. The momentum equation for the molten liquid layer at the bottom of the cylinder is:

$$\frac{dP}{dr} = \mu \frac{\partial^2 u(r)}{\partial z^2}. \tag{3.1}$$

With boundary conditions: $u(r)|_{z=0} = 0$ & $u(r)|_{z=\delta} = 0$, its velocity is:

$$u(r) = \frac{1}{2\mu}\frac{dP}{dr}(z^2 - \delta z). \tag{3.2}$$

Mass balance equation at the bottom liquid layer can be written as:

$$\rho_l 2\pi r \int_0^{\delta} u(r)\,\mathrm{dz} = -\rho_s \frac{dh}{dt}\pi r^2. \tag{3.3}$$

Integrating Eqn. (3.3) with respect to z, the pressure gradient is found to be:

$$\frac{dP}{dr} = \frac{6\mu}{\delta^3}\frac{\rho_s}{\rho_l}\frac{dh}{dt}r. \tag{3.4}$$

The pressure gradient in the bottom melt layer plays an important role. Its force balance with the solid PCM will determine the thickness of the melt layer. When considering that there is a transitional region (mushy zone) during melting, the velocity given by Eqn. (3.2) may no longer be valid. The existence of the mushy region will increase the flow resistance. Thus a tuning parameter can be introduced here to adjust the viscosity of the melt layer to mimic the extra flow resistance. The modified pressure gradient in the melt layer becomes:

$$\frac{dP}{dr} = \frac{6M\mu}{\delta^3}\frac{\rho_s}{\rho_l}\frac{dh}{dt} \tag{3.5}$$

where M is the tuning parameter. Letting $\Phi = \frac{6M\mu}{\delta^3}\frac{\rho_s}{\rho_l}\frac{dh}{dt}$, and integrating Eqn. (3.5) from 0 to r with respect to r:

$$\mathrm{P}(r) = \frac{\Phi}{2}r^2 + P(0). \tag{3.6}$$

The balance forces acting on the solid PCM can be described as:

$$\int_0^r 2\pi r P(r)\,dr = g(\rho_s - \rho_l)\pi r^2 h \tag{3.7}$$

Assuming $P(0) = 0$, Eqn. (3.7) becomes:

$$\int_0^r r\Phi\, r^2 dr = g(\rho_s - \rho_l) r^2 h. \tag{3.8}$$

Solving Eqn. (3.8) gives:

$$h = \frac{\Phi r^2}{4g(\rho_s - \rho_l)}. \tag{3.9}$$

Second, in terms of energy balance, a linear temperature distribution within the liquid layer is assumed:

$$T = \frac{T_m - T_w}{\delta} \mathrm{z} + T_w, \tag{3.10}$$

which gives:

$$\left.\frac{dT}{dz}\right|_{z=\delta} = \frac{T_m - T_w}{\delta}, \tag{3.11}$$

To account for the sensible energy, an 'effective' latent heat capacity, L_e, is defined as:

$$L_e = L_f + Cp_s(T_m - T_i) + 0.5Cp_l(T_w - T_m). \tag{3.12}$$

The first term is the latent energy of the PCM, the second term is the sensible energy for the PCM temperature to increase from its initial value to the melting point and the third term accounts for the sensible energy in the liquid PCM, where the factor 0.5 is used to approximate the temperature gradient within the liquid PCM. The local energy balance at the bottom solid PCM interface yields:

$$-k_l \left.\frac{dT}{dz}\right|_{z=\delta} = -\rho_s \frac{dh}{dt} L_e. \tag{3.13}$$

With Eqn. (3.11), the melt layer thickness can be obtained as:

$$\delta = \frac{k_l(T_w - T_m)}{-\rho_s \frac{dh}{dt} L_e}. \tag{3.14}$$

Substituting Eqn. (3.14) and the expression for Φ into Eqn. (3.9), a differential equation for the time dependent solid PCM height h is obtained:

$$h = 6M\mu \frac{\rho_s}{\rho_l} \frac{(\rho_s L_f)^3}{4g(\rho_s - \rho_l) k_l^3 (T_w - T_m)^3} r^2 \left(\frac{dh}{dt}\right)^4. \tag{3.15}$$

Let $\Theta = 6M\mu\frac{\rho_s}{\rho_l}\frac{(\rho_s L_f)^3}{4g(\rho_s-\rho_l)k_l^3(T_w-T_m)^3}$, and Eqn. (3.15) is simplified as:

$$h = r^2\Theta\left(\frac{dh}{dt}\right)^4. \tag{3.16}$$

Solving this differential equation by integration:

$$\int_{H_i}^{h} -(h)^{-1/4}dh = \int_0^t (r^2\Theta)^{-1/4}dt. \tag{3.17}$$

The final expression for the shrinking solid PCM height is:

$$h = \frac{3}{4}\left(\frac{4}{3}(H_i)^{3/4} - \int_0^t (r^2\Theta)^{-1/4}dt\right)^{4/3} \tag{3.18}$$

For melting through the side wall of the vertical tube, it is assumed that no convection in the melt is considered. Hence, heat transfer is based on pure conduction. The energy balance equation can be written as followings:

$$\rho_s L_f (R_i - r)\frac{dr}{dt} = -\frac{k_l(T_m-T_w)}{ln((R_i-r)/R_i)} \tag{3.19}$$

Solving the equation by integration, an implicit form for the r (shrinking radius of the solid PCM) is obtained:

$$(R_i - r)^2\left(2ln\left(\frac{R_i-r}{R_i}\right) - 1\right) = \frac{4k_l(T_w-T_m)t}{\rho_s L_f}. \tag{3.20}$$

The analytic solution is obtained by solving Eqns. (3.20) & (3.18) in discrete time space. At each time step, r is calculated using Eqn. (3.20) and is updated in Eqn. (3.18) to calculate h. Finally, the liquid fraction is calculated as following:

$$X = \frac{\pi R_i^2 H_i - \pi r^2 h}{\pi R_i^2 H_i}. \tag{3.21}$$

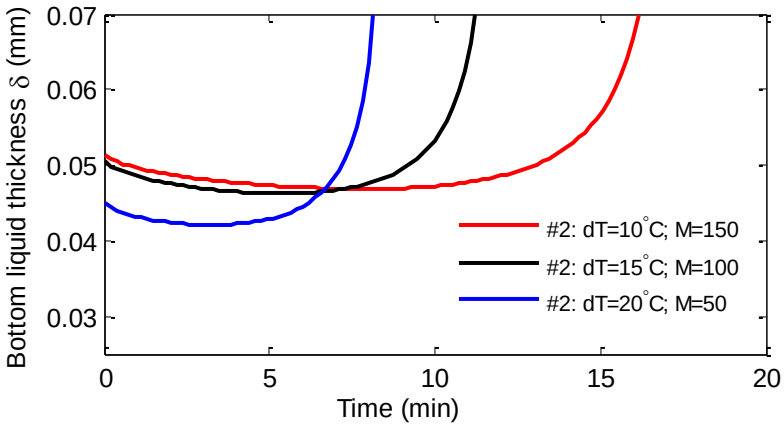

(a) δ for Case #2 under different dTs with different Ms

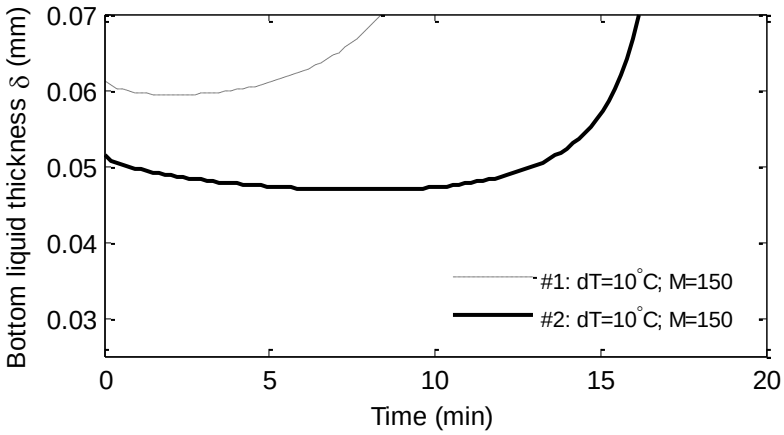

(b) δ for Case #1 and #2 under the same dT with the same M

Figure 7.12 Effect of the tuning parameter on the bottom liquid thickness

Figure 7.12 shows the effects of the tuning paramter M on the bottom liquid thickness (δ). Figure 7.12(a) shows that for the same case M can effectly control the thickness of δ. δ increases rapidly when all of the solid PCM is almost melted. Overall, a larger M tends to result in a thicker δ. Figure 7.12(b) shows that for the same value M and the same dT, when the solid PCM has a higher height (#2), δ is smaller, which is consistent with physical intuition. The square dot points in Figure 7.13 are the melting times estimated by the analtyic solutions for the cases investigated in the experiments. It can be seen that for a given drivng temperaure, the experimental results for the two

different geometries (#1 & #2) match the analytic solutions very well, with the same tuning parameter. The optimal tuning parameter has a strict linear relationship with the driving temperature differences ($M = 150$ for $dT = 10℃$; $M = 100$ for $dT = 15℃$; $M = 50$ for $dT = 20℃$). Within this temperature range, a linear correlation for the tuning parameter based on driving temperature differences is given as:

$$M(dT) = 50 - 10(dT - 20),\ \ 10℃ \leq\ dT \leq 20℃\,, \tag{3.22}$$

Finally, Figure 7.14 presents a comparison of the melting curves between the experimental, the analytic and the numerical results. The experimental time- dependent liquid fraction curves for the two driving temperature differences were obtained based on the mean values of the three sets of data of each case as shown in Figures 7.6 & 7.7. The numerical curves have a good agreement with the experimental ones. Especially for the larger dT case, there is a perfect match. Although the analytic curves match with the experimental ones in terms of the final melting time, there is deviation during the middle of the melting process. The analytic solution gives faster melting at the beginning, while the experimental melting curve shows more linearity. Thus improvement of the analytic solution is still required for future studies.

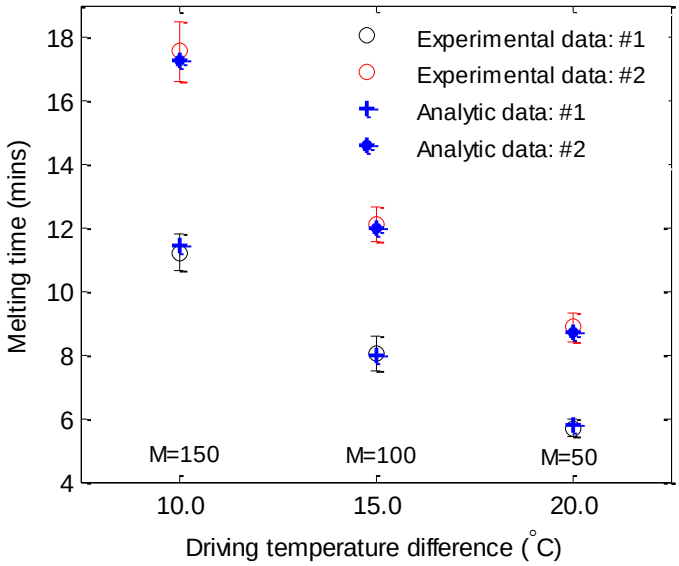

Figure 7.13 Comparison of the melting times predicted by the analytic solution with the experimental results

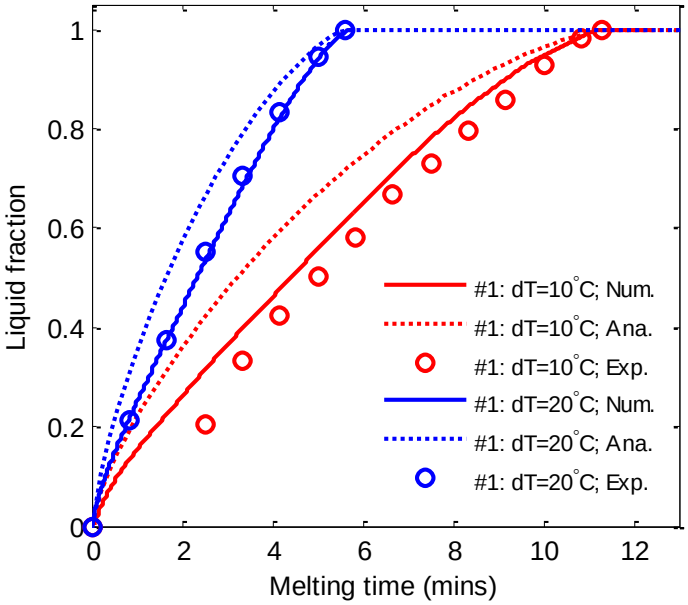

Figure 7.14 Comparison of melting curves from the analytic and numerical solutions

5. Conclusions

The mushy zone parameter within the source term used to modify the moment

equation for the enthalpy-porosity method is given more insight and discussion. In particular, the seeming contradiction that although, the enthalpy-porosity method in Fluent cannot model bulk solid sinking behavior, numerical solid sink behaviors are still reported in the literature. One possible explanation is that convection in the liquid phase can exert a downward shearing force on the solid. The other explanation is that within the mushy region, incompletely melted solids sink to the bottom by natural convection, which mimics the contact melting and enhances heat transfer. Moreover, in this paper, experiments demonstrating the melting of $\mathrm{Ca}Cl_2 \cdot 6H_2O$ in a vertical tube submerged in a water bath are conducted and used to calibrate numerical models. It is proposed for the first time in this paper that it is necessary to optimize the mushy zone parameter based on relevant driving temperature differences in order to achieve good agreement between numerical melting times and experimental ones. Finally, an analytic solution for unconstrained melting in a vertical tube with a tuning parameter to modify the viscosity of the mushy region was developed. A linear correlation for the tuning parameter based on driving temperature differences is given and experimentally validated.

Acknowledgement

This research is sponsored by the ARPA-e ARID Program under Contract No. DE-AR0000582. Any opinions, findings, and conclusions or recommendations expressed in this article are those of the authors and do not necessarily reflect the views of the Advanced Research Projects Agency-Energy.

References

[1] V.R. Voller, C. Prakash, A fixed grid numerical modeling methodology for convection-diffusion mushy region phase-change problems, Int. J. Heat Mass Transfer. 30 (1987) 1709-1719.

[2] V.R. Voller, M. Cross, N.C. Markatos, An enthalpy method for convection/diffusion phase change, Int. J. Numer. Methods Eng. 24 (1987) 271-284.

[3] Y. Kozak, G. Ziskind, Novel enthalpy method for modeling of PCM melting accompanied by sinking of the solid phase, Int. J. Heat Mass Transfer. 112 (2017) 568-586.

[4] M. Kumar, D. Jaya Krishna, Influence of Mushy Zone Constant on Thermohydraulics of a PCM, Energy Procedia. 109 (2017) 314-321.

[5] E. Assis, L. Katsman, G. Ziskind, R. Letan, Numerical and experimental study of melting in a spherical shell, Int. J. Heat Mass Transfer. 50 (9–10) (2007) 1790-1804.

[6] G. Ferrer, S. Gschwander, A. Solé, C. Barreneche, A. Inés Fernández, Peter Schossig, Luisa F. Cabeza, Empirical equation to estimate viscosity of paraffin, Journal of Energy Storage. 11 (2017) 154-161.

[7] S.F. Hosseinizadeh, A.A. Rabienataj Darzi, F.L.Tan, J.M. Khodadadi, Unconstrained melting inside a sphere, Int. J. Therm. Sci. 63 (2013) 55-64.

[8] A.R. Darzi, H.H. Afrouzi, M. Khaki, M. Abbasi. Unconstrained melting and solidification inside rectangular enclosure, J. Fundam. Appl. Sci. 7 (3) (2015) 436-451.

[9] R. Pakrouh, M.J. Hosseini, A.A. Ranjbar, R. Bahrampoury, A numerical method for PCM-based pin fin heat sinks optimization, Energ. Convers. Manage. 103 (2015) 542-552.

[10] A.A. Al-Abidi, S. Mat, K. Sopian, M.Y. Sulaiman, A. Th. Mohammad, Internal and external fin heat transfer enhancement technique for latent heat thermal energy storage in triplex tube heat exchangers, Appl. Therm. Eng. 53 (1) (2013) 147-156.

[11] H. Eslamnezhad, A. B. Rahimi, Enhance heat transfer for phase-change materials in triplex tube heat exchanger with selected arrangements of fins, Appl. Therm. Eng. 113 (2017) 813-821.

[12] N. Das, Y. Takata, M. Kohno, S. Harish, Melting of graphene based phase change nanocomposites in vertical latent heat thermal energy storage unit, Appl. Therm. Eng.

107 (2016) 101-113.

[13] N. Das, Y. Takata, M. Kohno, S. Harish, Effect of carbon nano inclusion dimensionality on the melting of phase change nanocomposites in vertical shell-tube thermal energy storage unit, Int. J. Heat Mass Transfer. 113 (2017) 423-431.

[14] S. Tiari, S. Qiu, M. Mahdavi, Numerical study of finned heat pipe-assisted thermal energy storage system with high temperature phase change material, Energ. Convers. Manage. 89 (2015) 833-842.

[15] R. Elbahjaoui, H. El Qarnia, Transient behavior analysis of the melting of nanoparticle-enhanced phase change material inside a rectangular latent heat storage unit, Appl. Therm. Eng. 112 (2017) 720-738.

[16] H. Shmueli, G. Ziskind, R. Letan, Melting in a vertical cylindrical tube: Numerical investigation and comparison with experiments, Int. J. Heat Mass Transfer. 53 (19–20) (2010) 4082-4091.

[17] B. Ghasemi, M. Molki, Melting of unfixed solids in square cavities, Int. J. Heat Fluid Flow. 20 (4) (1999) 446-452.

[18] A.D. Brent, V.R. Voller, K.J. Reid, Enthalpy-porosity technique for modeling convection-diffusion phase change: application to the melting of a pure metal, Num. Heat Transfer 13 (1988) 297-318.

[19] V. Shatikian, G. Ziskind, R. Letan, Numerical investigation of a PCM-based heat sink with internal fins, Int. J. Heat Mass Transfer. 48 (2005) 3689-3706.

[20] F. Moore, Y. Bayazitoglu, melting within a spherical enclosure, J. Heat Transfer 104 (1) (1982) 19-23.

[21] B.W. Webb, R. Viskanta, Natural-convection-dominated melting heat transfer in an tiltd rectangular enclosure, int. J. Heat Mass Trans. 34 (12) (1991) 3097-3106.

[22] W. Chen, S. Cheng, et al, Study of contact melting inside isothermally heated vertical cylindrical capsules. J. Therm. Sci. 2 (3) (1993) 190-195.

[23] W. Chen, S. Cheng, Z. Luo, et al., Analysis of close-contacting melting of phase change materials inside a heated rectangular capsule, Int. J. Energy Res. 19 (4) (1995) 337-345.

[24] H. Yoo, Analytical solutions to the unsteady close-contact melting on a flat plate, Int. J. Heat Mass Transfer. 43(8) (2000) 1457-1467.

[25] Y. Kozak, T. Rozenfeld, G. Ziskind, Close-contact melting in vertical annular enclosures with a non-isothermal base: Theoretical modeling and application to thermal storage, Int. J. Heat Mass Transfer. 72 (2014) 114-127.

[26] T. Rozenfeld, Y. Kozak, R. Hayat, G. Ziskind, Close-contact melting in a horizontal cylindrical enclosure with longitudinal plate fins: Demonstration, modeling and application to thermal storage, Int. J. Heat Mass Transfer. 86 (2015) 465-477.

[27] J. Zhao, J. Zhai, Y. Lu, N. Liu, Theory and experiment of contact melting of phase change materials in a rectangular cavity at different tilt angles Int. J. Heat Mass Transfer. 120 (2018) 241-249.

Chapter 8 Conclusions and Recommendations

A modeling and optimization framework that allows for both the detailed structural design of a finned heat pipe imbedded LTES system and the full-scale efficient simulation of the system with applications for operational research related to optimal flow path determination and sizing estimation has been developed. The key contributions and conclusions follow.

There are three main contributions from the dissertation in the area of modeling PCM-based heat exchangers. The first contribution is the idea and methodology of combining data-driven and physics-based models to develop a mathematical model for the efficient cost optimal design of finned PCM systems. The combined modeling approach (i) requires less sampling data (which is computationally expensive to obtain from a LTES unit with embedded fins) than that usually required by a full data-driven model to achieve high prediction accuracy and (ii) leverages the data-driven model schemes to reduce model complexity and avoid the difficulties of developing mathematical models based solely on the governing transient nonlinear partial differential equations for the physical problem. For finned PCM systems, results from Chapters 3 and 4 show that the proposed model can be efficiently used for the optimal design of multidimensional fins [1, 2]. With the proposed model, global sensitivity analysis is straightforward to carry out and provides estimates of how different parameters, such as system geometric dimensions as well as PCM and fin properties can affect the optimal unit cost [1].

The second contribution is the proposed modeling verification approach for these complex full-scale systems where (i) appropriate experimental measurements for validation purposes are prohibitively costly and/or unavailable, and (ii) even numerical

simulation approaches via CFD are computationally too expensive. For example, considering an embedded 3D finned heat pipe structure in a PCM cooling storage tank, fully coupled finite element modelling approaches are quite challenging to implement in terms of mesh generation and computational power and times. Moreover, such a simulation-based model is not suitable for the purposes of design optimization and operational studies. In contrast, the proposed iterative coupling method between the PCM behavior and the heat transfer process in the HTF channel, overcomes these difficulties by employing a strategy of modularization. In Chapter 6, a model in analytic form for a finned heat pipe supported PCM unit was developed (verified by comparison with CFD simulations) and was applied as a module to the full-scale system analysis [3].

Chapter 5 applies the same modeling approach in Chapter 6 to a shell-and-tube PCM-based heat exchanger unit for its convenient verification with traditional finite element approach (which in this case is tractable due to the simple geometry of the shell-and-tube PCM-based heat exchanger unit). In the shell-and-tube unit analysis, each module employs an analytic solution for PCM solidification in 1D annular coordinates. Thus Chapter 5 not only reports an efficient modeling approach for the optimal design of a shell-and-tube PCM-based heat exchanger, but also serves as an example for how verification for the more complicated geometry in Chapter 6 can be addressed. With this verification approach, it was shown that the total energy balance between the HTF and the PCM tank was very well matched for the complex system.

The experimentally validated analytic solution for unconstrained melting in a tube outlined in Chapter 7 constitutes the third contribution. This model captures the solid sinking behavior during the melting process that PCMs exhibit, which it was found is

critical to include because when a solid sinks to the bottom of the container, the thermal resistance is greatly reduced and enhances the melting process. This contribution has implications for the PCM-based CFD modeling and simulation community. The Melting & Solidification model in ANASYS Fluent, which is widely used to study the behavior of PCMs under heating or cooling conditions, is based on the enthalpy-porosity method. For this enthalpy-porosity method, there is a critical parameter called the mushy zone parameter that is commonly overlooked and applied without suitable consideration of issues related to experimental validation. Through a combination of experimental studies and numerical simulations using the default Melting & Solidification model in Fluent, it was confirmed that the mushy zone parameter values are dependent on driving temperature differences which was the first report of this finding [4]. Moreover, different values of this parameter have been reported in the literature for a same PCM and in similar physical models. It was determined that this contradiction comes from a particular limitation of the default enthalpy-porosity method in Fluent: Fluent does not have a mechanism to capture the solid sinking behavior during the melting process that PCMs exhibit [4]. However, it was also determined that a suitable mushy zone parameter can, to some degree, approximate the effects of the solid sinking behavior without its explicit inclusion. This emphasizes the importance of determining a suitable mushy zone parameter value when the popular numerical enthalpy-porosity models in CFD simulations are employed.

8.1 **Future Work**

Future work should concentrate on refining the proposed system level modeling approaches in order to create a reliable design software for practical applications. As the

representative power generation system analyzed in this dissertation is for condensing steam applications, an additional verified condensing steam model in the HTF channel is required to predict the heat absorbing performance of the PCM storage tank during the melting process. Currently the modeling component of the PCM tank was established and its interaction with water as the HTF was simulated. With the addition of a verified condensing steam model, optimal sizing of the PCM storage tank could be achieved for prescribed amounts of steam cooling loads during the daytime. Furthermore, sensitivity analyses for some of the model parameters, on the estimated sizing could be studied to increase the utility of results from the modified modeling design framework. As there are large uncertainties associated with important parameters in the proposed modeling approach (i.e., heat transfer coefficient for condensing steam, thermal resistances in the heat pipe, and PCM melting rates, etc.) sensitivity analysis is necessary and vital. Lastly at the system-level, operational research studies focused on the optimal distribution of steam in the PCM storage tanks under unknown steam loads should be studied and could result in smaller sizing and cost savings. Related to the steam cooling load, the steam mass flow rate, in reality, would probably not be constant (as is assumed throughout Chapters 5-6) due to temperature variations during the daytime. For example, the hottest daytime temperature may occur around 2:00 p.m., resulting in the largest amount of uncondensed steam coming from the air-cooled condensers in a power plant. Most probably, the steam mass flow rate would be similar to a Gaussian distribution with some associated uncertainty during the daytime.

Finally, at the modular level, Chapter 7 has introduced a way to develop an experimentally validated analytic model that captures the sinking behavior during PCM

melting in a tube. However, a similar model must be developed and experimentally validated for PCM melting in an annular tube and a non-isothermal heated base (representing the circular fin extended from the heated tube). Only then can the module be finally incorporated into the system level modeling in Chapter 6, to further enhance the fidelity and utility of the developed framework.

References

[1] Pan C., Vermaak N., Romero C., Neti S., et al. Cost estimation and sensitivity analysis of a latent thermal energy storage system for supplementary cooling of air cooled condensers. *Applied Energy*, 2018, (224): 52-68.

[2] Pan C., Vermaak N., Romero C. Neti S., et al. Efficient optimization of a longitudinal finned heat pipe structure for a latent thermal energy storage system, *Energy Conversion and Management* 2017, (153): 93-105.

[3] Pan C., Vermaak N., Romero C., Neti S., et al. A discrete-time dynamical model for a large scale latent thermal energy storage system and its operational research. Submitted to *Energy Conversion and Management*.

[4] Pan, C., Charles, J., Vermaak, N., Romero, C., Neti S., et al. Experimental, numerical and analytic study of unconstrained melting in a vertical cylinder with a focus on mushy region effects. *International Journal of Heat and Mass Transfer*, 124, p.1015-1024, 2018.

VITA

Chunjian Pan was born in November, 1986 in Shanghai, P. R. China. He earned a bachelor degree in 2010 at the Department of Thermal Engineering in University of Shanghai for Science and Technology. After graduation, he majored in Chemical Engineering for a master degree at East China University of Science and Technology (ECUST). In 2014, he went to Lehigh University in the U.S. for his PhD degree in Mechanical Engineering under the supervision of Dr. Natasha Vermaak with the thesis entitled “Efficient modeling of latent thermal energy storage systems for optimal design and operational research”.